

Carbon-based Electrode Materials for Application in the Electrochemical Water Splitting Process

Dissertation

zur Erlangung des akademischen Grades eines

Doktors der Naturwissenschaften

– Dr. rer. nat. –

vorgelegt von

Jan Willem Straten

geboren am 14.09.1987

Fakultät für Chemie
der Universität Duisburg-Essen

2018

For Ethel and my family

Die vorliegende Arbeit wurde im Zeitraum von Dezember 2013 bis Dezember 2017 im Arbeitskreis von Prof. Dr. Robert Schlögl am Max-Planck-Institut für Chemische Energiekonversion durchgeführt.

Tag der Disputation: 6. September 2018

Gutachter: Prof. Dr. Robert Schlögl

Prof. Dr. Malte Behrens

Vorsitzender: Prof. Dr. Stefan Rumann

Table of Contents

<i>Motivation</i>	6
<i>Abstract</i>	8
<i>Kurzzusammenfassung</i>	11
1. INTRODUCTION	15
1.1. Brief Historical Review of Hydrothermal Carbon	15
1.2. Hydrothermal Synthesis	18
1.3. Hydrothermal Carbonization (HTC) – Synthesis, Properties and Applications of HTC Chars	21
2. THEORETICAL FUNDAMENTALS	39
2.1. Postulated Reaction Mechanisms during Precursor Decomposition and Spherical Particle Formation	39
2.2. Chemical Energy Conversion using N-Functionalized/Doped Carbon-based Electrode Materials – A “Black” Prospect For a Bright Future	53
3. APPLIED CHARACTERIZATION METHODS	67
4. RESULTS AND DISCUSSION	72
4.1. Hydrothermal Synthesis of N-Functionalized HTC Chars	72
4.2. UV/VIS Spectroscopy	76
4.3. High-Performance Liquid Chromatography (HPLC)	79
4.4. Macroscopic and Microscopic Morphology of N-HTC Materials	82
4.5. Elemental Composition and Yields	88
4.6. Structural Composition of N-HTC	91
4.7. Computed FTIR Spectra	92
4.8. Computed and Experimental Gas Phase Infrared Spectra of Furan	93
4.9. Vibrational Spectra of α -Oligofurans and N-Free HTC (Pure HTC Originating from Glucose)	95
4.10. Comparison of the Vibrational Spectrum of N-Free HTC and Additional Structures	98
4.11. Thermal Analysis of HTC	100
4.12. Surface Analysis	105
4.13. Raman Spectroscopy	106
4.14. Electron Energy Loss Spectroscopy (EELS)	109
4.15. Structural Comparison of Different HTCs via Solid-State-NMR Spectroscopy	111
4.16. Structural Models	119
4.17. Concluding Remarks	122
4.18. Pyrolyzed HTC Chars: Disc Electrode Preparation and Characterization	126

4.19.	Electrochemical Approach: Composition of Commercial Pellet Holder, Nail Polish and Standardization Protocol	135
4.20.	Electrochemical Characterization in Alkaline Medium	138
4.21.	Carbon Corrosion and Activation as well as Deactivation of the Surface Area	153
4.22.	Post-Mortem Characterization: Analysis of Colored Electrolyte and Isolation of Residual of Colored Electrolyte after Electrochemical Stability Tests	155
4.23.	Concluding Remarks	163
5.	<i>CONCLUSIONS</i>	165
6.	<i>OUTLOOK</i>	166
7.	<i>REFERENCES</i>	167
8.	<i>APPENDIX</i>	187
8.1.	List of Abbreviations	187
8.2.	List of Publications	190
8.3.	Lebenslauf (Curriculum Vitae)	194
8.4.	Erklärung (Statement)	195
8.5.	Acknowledgments	196

Motivation

Hydrothermal carbonization (HTC) to produce “green” carbon materials is a promising, sustainable technique to get rid of depleting primary energy sources, in particular fossil fuels (oil, coal, natural gas). These carbonaceous materials are traced to inexhaustible, renewable energy sources (biomass) and thus preventing the evolution of greenhouse gases (e.g. CO₂) or other toxic, polluting emissions contributing to anthropogenic climate change and the related global warming which our planet is confronting with. In nature, carbon exists in various allotropes, that is to say diamond, graphite or amorphous carbon. As carbon is a natural product of coalification of every sort of biomass, mankind has been using it for millions of years exploiting it to a great extent. With modern technology the demand of fossil fuels is increasing to an alarming scale. Therefore, a sustainable feedstock to overcome the dependence on fossil fuel-derived energy is “green” HTC material. The HTCs are used for the application in the electrochemical water splitting process which is known to be a cheap and clean route to decompose water into its elements oxygen and hydrogen. With its highest energy density and its environmentally benign combustion in fuel cells among all fuels, hydrogen gas is considered to be the fuel of the future. The electrochemical water oxidation implies this opportunity towards an alternative and profitable way to produce hydrogen

Since the reserves of fossil fuels are finite and known to be exploited within the next couple of decades, major efforts need to be made in the context of renewable and alternative environmentally friendly resources. One of the concepts to replace primary energy with renewable energy sources is the solar refinery aiming a complete independence from primary energy carriers.

Water splitting into the components hydrogen and oxygen is crucial for a sustainable and renewable energy conversion technology. The electrochemical water splitting reaction as a simple, clean and economical process plays an

important role towards the production of hydrogen gas as chemical energy carrier. To date, several electrocatalysts have been investigated. Still, the leading anode materials are RuO₂ or IrO₂. The electrochemical reaction mechanism of RuO₂ or IrO₂ in the process of water electrolysis is not fully understood. In addition, RuO₂ or IrO₂ are expensive precious metal oxide catalysts. The oxygen evolution reaction at the anode is kinetically the most demanding and complicated step in the overall electrochemical water oxidation reaction compared to the hydrogen evolution at the cathode. Understanding the electrochemical water splitting process is therefore a key factor towards green production technologies and in particular the hydrogen-based energy economy.

Hydrothermal carbon as “green” carbon material is used in the electrochemical water oxidation. Synthetically, hydrothermal carbonization is one way to transform waste biomass into promising carbon materials. The simultaneous introduction of nitrogen is supposed to enhance the material properties and makes it an appealing object for electrochemical applications. The purpose of this thesis has been to synthesize and to characterize N-functionalized hydrothermal carbon materials. It also has been to significant importance to understand and to study the synergetic effect of carbon in conjunction with nitrogen through spectroscopic and electrochemical investigations, more specifically, the electrochemical water splitting process as a key application to obtain a better structure-property correlation.

Abstract

The synthesis and characterization of N-HTC materials for the application in the water electrolysis are the main focus of this work. N-incorporation is of fundamental importance throughout this work since, first of all, N is an n-type dopant by acting as electron-donor. The technique of N-doping tunes the physicochemical material properties. It is cheap, non-toxic and has the advantage to tailor the desired electrical, mechanical, optical, magnetic, structural, morphological or chemical properties. N-doping may improve conductivity, surface wettability, catalytic or storage characteristics. Besides, N-doping creates active sites and thus might enhance electrocatalytic activity as well as long-term electrochemical stability. The hydrothermal synthetic route has been applied based on the precursors glucose and urotropine. During hydrothermal synthesis, urotropine together with glucose undergoes a plethora of complex reaction pathways. Ammonia, in particular, the decomposition product of urotropine, contributes to a wide range of reaction mechanisms. The molar ratio of glucose and urotropine has been modified in order to achieve a steady increase of the N-content. Urotropine was proved to be a highly effective N-precursor. With raising the mass fraction of urotropine towards glucose, maximal N-proportion of 19 wt% can be achieved.

The pH plays a major role during synthesis and has a high impact in the reaction mechanisms of the corresponding reaction steps. Based on HTC chars, to date, no systematic pH investigations exist by modification of the molar ratios of the applied precursors. In this work, systematic studies on the pH have been performed. By variation of the molar ratio of urotropine to glucose the pH can be tuned due to the decomposition of the N-precursor urotropine into ammonia and formaldehyde. The pH changes to a more alkaline behavior if the molar ratio of urotropine to glucose is increased. Reversely, rising the molar ratio of glucose to urotropine or if only glucose is used as starting material, the pH tend

to be more acidic. In both cases $\leq C_6$ products are obtained. At $\text{pH} < 7$, the decomposition process via the intermediate HMF takes place. Herein, oxidative effects come into their own, such as dehydrations. Likewise, decarbonylations and decarboxylations occur more often. At $\text{pH} > 7$ the degradation via HMF is depressed and reducing effects yields deprotonations or benzylic acid-type rearrangements. Decarbonylations and decarboxylations arise only to a lesser extent. Besides, fragmentations are the predominant reactions enclosing β -elimination, retro-aldol fragmentation or hydrolytic β -dicarbonyl fragmentation. Throughout this work, both reaction pathways have been selected in order to analyze the degree of internal condensation of the polymeric carbon network, the preferential structural moieties or functional groups that have been formed. These special features are the main reason for the high diversity of organic compounds, functional groups and numerous structural motifs in the hydrochar.

A large variety of characterization techniques have been employed. It is the first comprehensive analytical study of a series of as-synthesized N-containing hydrothermal carbon (N-HTCs), consisting of analytical data of UV/VIS, HPLC, optical microscopy, SEM/(HR)TEM, BET, elemental analysis, FTIR, electronic structure calculations, TG-MS, zeta potential, acid-base titration, Raman, XRD, EELS and solid-state NMR. Due to the combination of these characterization techniques, scientific findings on the complex molecular structure could be gained. In N-free HTCs, solely O-functional groups exist, for the most part furan-based functions with aliphatic compounds acting as linkers. In contrast to it, N-HTCs consist of a large number of both, O- and N-functional groups. Only by adding higher amount urotropine, more temperature stable N-based structural elements such as pyrrole and pyridine are formed.

The N-HTC disc electrodes are subjected to electrocatalytic investigations with regard to water splitting process. Electrochemical characterization studies include cyclic voltammetry (CV), modular potentiometry (MP, stationary polarization), chronopotentiometry (CP) and chronoamperometry (CA) to

investigate electron transfer processes, electrochemical activity as well as stability. The pellets exhibit a remarkable mechanical stability. It is the very first approach in which no binder needed to be used to stabilize the material for electrochemical applications. Disc electrodes at high anodic-potentials are tested under oxygen evolution reaction (OER) conditions in alkaline media according to a standardization protocol.

N-free disc electrodes are most susceptible to carbon corrosion whereas the incorporation of N improves the material properties. The higher the amount of N is, the higher the electrochemical activity and stability.

Besides, the electrolyte undergoes a color change turning from colorless into dark brown. The brown substance was isolated and is presumed to be a polymeric humic acid-like organic compound.

Kurzzusammenfassung

Die Synthese und Charakterisierung von HTC-Materialien für die Anwendung in der Wasserelektrolyse stehen im Mittelpunkt dieser Arbeit. Im Verlauf dieser Arbeit ist der Einbau von N von grundlegender Bedeutung. Zunächst ist N ein Dotierstoff vom n-Typ, der als Elektronendonator fungiert. Die N-Dotierung ist ein Verfahren, das die physikalisch-chemischen Eigenschaften einstellt. Es ist billig, ungiftig und hat den Vorteil, dass die gewünschten elektrischen, mechanischen, optischen, magnetischen, strukturellen, morphologischen oder chemischen Eigenschaften zugeschnitten werden können. N-Dotierung kann ebenso die Leitfähigkeit, Oberflächenbenetzbarkeit, katalytische Eigenschaften oder Speichereigenschaften verbessern. Darüber hinaus erzeugt die N-Dotierung aktive Zentren und kann somit die elektrokatalytische Aktivität sowie die elektrochemische Langzeitstabilität erhöhen. Die hydrothermale Syntheseroute wurde auf Basis der Vorläufersubstanzen Glucose und Urotropin angewendet. Während der Hydrothermalsynthese durchläuft Urotropin, zusammen mit Glucose, eine Vielzahl komplexer Reaktionswege. Insbesondere Ammoniak, das Zersetzungsprodukt von Urotropin, trägt zu einer großen Bandbreite von Reaktionsmechanismen bei. Das Stoffmengenverhältnis von Glucose und Urotropin wurde variiert, um einen stetigen Anstieg des N-Gehalts zu erreichen. Urotropin erwies sich als äußerst wirkungsvoller N-Präkursor. Bei Erhöhung des Massenanteils von Urotropin gegenüber Glucose kann ein maximaler N-Anteil von 19 Gew.-% erzielt werden.

Der pH-Wert spielt eine große Rolle bei der Synthese und hat einen immensen Einfluss auf die Reaktionsmechanismen der entsprechenden Reaktionsschritte. Bisher existieren auf Basis von hydrothermalen Kohlenstoffmaterialien keine systematischen pH-Untersuchungen durch Änderung des Stoffmengenverhältnisses der verwendeten Präkursoren. In dieser

Arbeit wurden systematische Studien zum pH-Wert durchgeführt. Durch Variation des Stoffmengenverhältnisses von Urotropin zu Glucose kann der pH-Wert, aufgrund der Zersetzung des N-Präkursors zu Ammoniak und Formaldehyd, eingestellt werden. Der pH-Wert wird alkalischer, wenn das Stoffmengenverhältnis von Urotropin zu Glucose erhöht wird. Im umgekehrten Fall, wenn das Stoffmengenverhältnis von Glucose zu Urotropin oder falls ausschließlich Glucose als Ausgangsmaterial verwendet wird, neigt der pH-Wert zu einem acideren Verhalten. In beiden Fällen werden $\leq C_6$ Produkte erhalten. Bei $pH < 7$ findet der Zersetzungsprozess über das Zwischenprodukt HMF statt. Hier kommen oxidative Effekte zum Tragen. Ebenso treten Decarbonylierungen und Decarboxylierungen häufiger auf. Bei $pH > 7$ ist der Abbau über HMF unterdrückt. Reduzierende Effekte führen zu Deprotonierungen und Benzilsäure-artige Umlagerungen. Decarbonylierungen und Decarboxylierungen treten nur in geringerem Maße auf. Zudem sind Fragmentierungen die vorherrschenden Reaktionen, die β -Eliminierung, Retro-Aldol-Fragmentierung oder hydrolytische β -Dicarbonyl-Fragmentierung einschließen. In dieser Arbeit wurden beide Reaktionswege ausgewählt, um den internen Kondensationsgrad des polymeren Kohlenstoffnetzwerkes, der bevorzugten Struktureinheiten oder funktionellen Gruppen, die gebildet wurden, zu analysieren. Diese Besonderheiten sind der Hauptgrund für die große Vielfalt an organischen Verbindungen, funktionellen Gruppen und zahlreichen Strukturmerkmalen im hydrothermalen Kohlenstoff.

Eine große Vielzahl von Charakterisierungstechniken wurde verwendet. Es ist die erste umfassende analytische Studie einer Reihe von synthetisierten N-haltigen hydrothermalen Kohlenstoff (N-HTCs), bestehend aus analytischen Daten von UV/VIS, HPLC, optische Mikroskopie, SEM/(HR)TEM, BET, Elementaranalyse, FTIR, elektronische Strukturberechnungen, TG-MS, Zeta-Potential, Säure-Base-Titration, Raman, XRD, EELS und Festkörper-NMR. Nur durch die Kombination dieser Charakterisierungstechniken konnten

wissenschaftliche Erkenntnisse zur komplexen Molekülstruktur gewonnen werden. In N-freien HTC existieren ausschließlich O-funktionelle Gruppen, größtenteils Furan-basierte Strukturmerkmale mit aliphatischen Gruppen, die als Verknüpfer (Linker) wirken. Im Gegensatz dazu bestehen N-HTCs aus einer großen Anzahl von sowohl O- als auch N-funktionellen Gruppen. Nur durch die Zugabe an Urotropin höherer Menge werden meist temperaturstabilere N-basierter Strukturelemente wie Pyrrol und Pyridin gebildet.

Die N-HTC-Scheibenelektroden werden im Hinblick auf den Wasserspaltungsprozess elektrokatalytischen Studien unterzogen. Elektrochemische Charakterisierungsstudien umfassen Cyclovoltammetrie (CV), modulare Potentiometrie (MP, stationäre Polarisation), Chronopotentiometrie (CP) und Chronoamperometrie (CA) zur Untersuchung von Elektronentransferprozessen, elektrochemischer Aktivität und Stabilität. Die Pellets weisen eine bemerkenswerte mechanische Stabilität. Es ist die allererste Herangehensweise, bei dem kein Bindemittel zur Stabilisierung des Materials für elektrochemische Anwendungen benötigt wird. Die Scheibenelektroden werden bei hohen anodischen Potentialen unter Sauerstoffentwicklungsreaktionsbedingungen (OER) in alkalischer Elektrolytlösung gemäß einem Standardisierungsprotokoll getestet.

N-freie Pellets sind am anfälligsten gegenüber Kohlenstoffkorrosion, wohingegen N-Einbau die Materialeigenschaften verbessert. Je höher die Menge an N ist, desto höher ist die elektrochemische Aktivität und Stabilität.

Außerdem geht eine Farbänderung des Elektrolyten von farblos nach dunkelbraun einher. Die braune Substanz wurde isoliert und kann als polymeres huminsäureartige organische Verbindung angenommen werden.

ANÁLISIS

por Joaquín María Bartrina

*Juan tenía un diamante de valía,
y por querer saber lo que tenía
la química estudió, y ebrio, anhelante,
analizó el diamante.*

*Mas ¡oh! ¡qué horror! Aquella joya bella,
lágrima, al parecer, de alguna estrella,
halló con rabia y con profundo encono
que era sólo un poquito de carbono...*

*Si quieres ser feliz, como me dices
¡no analices, muchacho, no analices!*

1. INTRODUCTION

1.1. Brief Historical Review of Hydrothermal Carbon

Friedrich Bergius can be considered as the discoverer of hydrothermal carbon materials in the years of intense coalification research from 1911 to 1913 when reporting about the contribution of chemical high pressure processes applying biomass such as peat or cellulose in the high pressure reactor in the presence of aqueous environment at relatively mild temperatures over 300 °C. In both cases the coalification process succeeded and the outcome revealed that carbonaceous materials were obtained with the same elemental composition compared to natural coal. This led to his conclusion to examine the decomposition process of biomass-based precursors more in detail and stated the same process is similar to the process of formation into coal, which occurs over millions of years in nature [1].

Bergius was the very first one to overcome super-heating and the decomposition into great quantities of gases like CO₂. As a result the degradation of cellulose was suppressed by the addition of steam flow. Bergius discovered that if the plant-based precursor was suspended in water at mild temperatures in the high-pressure vessel, decomposition into gaseous products could be prevented [2].

By means of quantitative studies Bergius managed to publish the attained products in stoichiometric amounts. Using 2 moles of cellulose as starting material with the same high-pressure apparatus in a temperature window between 290 and 350 °C at pressures of about 200 bars in aqueous medium, 2 moles of CO₂, 5 moles of H₂O and a powdery carbonaceous product with an elemental composition of C₁₀H₈O were obtained. Approximately the same elemental composition was achieved using wood, peat, sugar or grass as starting

material. However, it turned out that hydrogen is a labile and unstable component in this artificial coal ^[1-2].

These groundbreaking discoveries were the go-ahead for numerous further experiments of Bergius in the field of hydrogenation of coal. The results of hydrogenation reactions of synthetic coal and natural coal were very similar. Based on these studies this process became the basis for the production of liquid and soluble compounds from coal which is nowadays considered as “coal liquefaction” ^[1-2, 3]. For all of these pioneering works, Friedrich Bergius together with Carl Bosch, were awarded the Nobel Prize in Chemistry for his discoveries in the field of chemical high pressure methods in 1931 ^[2b].

His fundamental research about these high pressure reactions based on biomass can be denoted as the very first attempts to get rid of primary energy carriers (fossil resources, e.g. coal or natural gas) and to find renewable, alternative energy sources. Bergius’ works were undoubtedly a landmark in the history of coal research and a laying of the foundation stone for a large number of further experimental investigations by many scientists.

In 1928, Berl and Schmidt imitated Bergius’ experimental conditions and pursued the decomposition process of cellulose systematically. The formed reaction products were closely investigated and characterized in order to gain deeper insights into the reaction processes ^[4].

Four years later, in 1932, the same authors published several papers on the emergence of carbon based on their studies in neutral and alkaline media. They utilized different plant-based starting materials (cellulose, lignin, resin, wax) and performed coalification studies in a temperature range between 150 and 400 °C. The carbonaceous end products were tested for their properties or their elemental composition with regard to C and H. The consistency varied in terms of their properties or elemental composition compared to the corresponding natural coal depending on the temperature or the reaction solution that was used ^[5]. In a further review Berl and Schmidt summarized not only their results but

also those from other authors the knowledge about the development of coal as things stood at that time ^[6]. A modern version on the theory of origin, formation or composition of coals and about coal structure research was published by Haenel in 1992 ^[7].

After World War II, on the basis of Bergius' studies, Schuhmacher resumed work about the chemical structure and properties of coal in the years of 1956 until 1960 ^[8]. In one of these publications Schuhmacher varied the pH and studied its influence on the overall hydrothermal carbonization reaction of plants, peat, cellulose, lignin and wood. As a consequence, substantial differences in the decomposition processes were encountered as the elemental composition of C, H and O changed at the same time ^[8b].

It took almost half a century, when in 2001 research on hydrothermal synthesis based on biomass was reported again. Syntheses of carbon spheres were carried out using sugar or glucose as starting materials at low temperatures. Sugar was hydrothermally treated at 190 °C ^[9] and glucose between 160 and 180 °C ^[10]. Simultaneously, Shu-Hong Yu figured out that the reaction time of hydrothermal synthesis of starch can be shortened significantly to only a couple of hours. Noble metal salts were added to the reaction solution and it seemed reasonable that they catalyze the speed of the hydrothermal carbon reaction at mild temperatures between 160 and 200 °C ^[11]. Furthermore, the syntheses in presence of metal ions lead to a structural diversity of end products since for instance metal/carbon (Ag@C or Te@C) nanocables ^[11-12], carbon nanofibers (CNFs) ^[12] or carbon spheres ^[9-10] were obtained.

Maria-Magdalena Titirici and Marta Sevilla can be regarded as one of the most prominent living scientists focusing intensely on hydrothermal carbonization research. Their research field embraces synthesis of (porous) hydrothermal carbons, composite materials, fluorescent carbon nanoparticles (carbon quantum dots, CQDs) and their application in electrochemical aspects, in particular for energy storage.

It is still an open question whether the hydrothermal carbon technology is going to be a firm part of the present environmental problems mankind is facing with respect to resource scarcity, environmental pollution, global warming or the high energy consumption.

1.2. Hydrothermal Synthesis

Hydrothermal synthesis is not to be confused with solvothermal synthesis. Upon hydrothermal synthesis, solely water is used as reaction medium by exceeding its boiling point ^[13]. In contrast, for solvothermal synthesis, organic solvents are utilized and treated at relatively high temperatures but critical temperatures and pressures are very often lower than in the case of water ^[13]. Nevertheless, both techniques are well-established synthesis strategies ^[14] and are important subareas of inorganic synthetic chemistry ^[13b].

Hydrothermal syntheses are heterogeneous reactions conducted in heated and sealed pressure vessels (autoclaves) employing aqueous environments beyond 100 °C, above the boiling point of water; in the temperature range 100-1000 °C, mostly 120-200 °C under autogenous pressures ^[13-14]. Typically, the pressures exceeds by far atmospheric pressures (1 bar) in the region 1-100 MPa (10-1000 bar), in general they range between 1 and 3 MPa (10 and 30 bar) ^[13-14]. Hydrothermal syntheses are performed under subcritical or supercritical conditions. Subcritical synthesis conditions imply the temperature in the range of 100-240 °C whereas in the supercritical regime, the temperature can reach 1000 °C with a pressure up to 300 MPa ^[13b]. Under hydrothermal conditions sparingly soluble reactants with high melting points dissolve as complex compounds in which water itself or highly soluble transport substances (“mineralizers”) can support their solubility. This process results in the formation of complexes. In this respect, conditions and laws are deemed to

chemical transport reactions. Hydrothermal synthesis can be referred to as a special case of chemical transport reaction ^[13a]. Therefore, hydrothermal reactions favor the self-assembly of the products from soluble precursors ^[14]. Hydrothermal synthesis implies the preparation of novel materials, the comprehension of hydrothermal reaction mechanisms and the development of new synthetic methods or techniques as well as strategies. Methods include crystal growing, structure-directing agent technique, mineralizing, templating, complexing, solvothermal routes, high temperature and pressure technique or redox environment control ^[13b, 15]. In principle, the hydrothermal reaction mechanism follows a liquid nucleation mechanism model and provides plenty of new complex and advanced solid materials or biomolecules ^[13b, 15].

A prominent example of hydrothermal processes is provided by nature itself. A large number of minerals have been formed under these conditions. Hydrothermal examinations are still indispensable in geological sciences for the contribution to the knowledge of geological processes. Hydrothermal processes play an important role in the context of hydrometallurgy, for instance, the Bayer process for the decomposition of bauxite. In heating and power stations hydrothermal conditions are the cause of numerous corrosion phenomena ^[13a].

After World War II hydrothermal synthesis was incorporated into solid state research. Inspired by the industrial cultivation of quartz oscillator crystals by Nacken^[16] interest focused on the growth of ultrapure crystals with significant physical properties and of sufficient size for the measurement and application of these features ^[13a].

Diverse solids have been attained by hydrothermal synthesis like superionic conductors ^[13b, 15a, 17], chemical sensors ^[13b, 15a, 18], electronically conducting solids ^[13b, 15a, 19], complex oxides and fluorides ^[13b, 15a, 20], magnetic materials ^[13b, 15a, 21], luminescence phosphors ^[13b, 15a, 22], open-framework compounds (e.g. zeolites, low-dimensional aluminophosphates) ^[13b, 23], inorganic-organic hybrid materials ^[13b, 15a, 24], metal-organic framework (MOF) materials ^[13b, 25], and

unique condensed materials such as nanoparticles^[13b, 15a, 26], gels^[13b, 15a, 27], thin films^[13b, 15a, 28], diamonds^[15a, 29], equilibrium defect solids^[13b, 15a, 30], distinguished helical and chiral structures^[13b, 15a, 31] or particularly stacking-sequence materials^[13b, 15a, 32]. Biological and environmental applications involve in the origin of life^[13b, 15a, 33] or in the supercritical water oxidation (SCWO) process for the decomposition of organic wastes^[13b, 15a, 34].

Unlike conventional, classical synthesis routes, hydrothermal syntheses offer a lot of advantages since reactions are accessible that under standard synthetic chemical techniques and approaches would not occur. It allows direct ion-doping in synthetic reaction and the control of morphology or particle size^[13b]. Sometimes, hydrothermal synthesis affords the opportunity – in contrast to some solid-state reactions – for an alternative and mild synthetic method by reducing the reaction temperature^[13]. These include the synthesis of compounds with oxidation states that in usual cases are difficult to achieve, e.g. ferromagnetic chromium(IV) dioxide. It is obtained in one step. Highly purified and uniform crystals are attained^[13a, 35]. The hydrothermal treatment also allows the production of low-temperature phases such like crystals of the zinc blende (γ)-phase of CuI which is an important optical-electronic material^[13a, 36]. Metastable compounds can be synthesized as well. Subiodides of tellurium TeI_2 and $\beta\text{-TeI}$ are formed by annealing of tellurium-rich samples. The structure of the needle-forming crystals is characterized by infinite chains of tellurium atoms^[13a, 37]. A further important application of hydrothermal syntheses is to grow perfect single crystals embracing all types of inorganic materials involving native elements (gold, silver or platinum), oxides, silicates, phosphates, chalcogenides, halides, germanates or carbonates^[13b, 38]. Commonly, hydrothermal syntheses are carried out in autoclaves that are required to withstand high pressures arising during a process or to protect the reaction vessel at high temperatures. However, low-temperature phases and metastable compounds are synthesized in glass or quartz glass ampoules^[13a].

Throughout this work, hydrothermal synthesis is the essential synthetic technique for the preparation of the carbonaceous materials. Those carbon materials are objects of investigation and are only accessible via hydrothermal synthesis. A variation of hydrothermal synthesis is used in this work, namely the so-called hydrothermal carbonization. In the next section a more detailed description and approach will be provided about this topic and the nature of the obtained carbon materials.

1.3. Hydrothermal Carbonization (HTC) – Synthesis, Properties and Applications of HTC Chars

Hydrothermal carbonization (HTC), also referred to as wet torrefaction, is a thermochemical process carried out in autoclaves converting natural organic renewable resources into a solid carbonaceous product ^[39]. It is a powerful method to synthesize “green” and novel carbon materials via hydrothermal one-pot synthesis of biomass (e.g. carbohydrates, agricultural resources, wood residues, crops), especially based on sugar compounds ^[40]. This synthetic technique allows a good control in morphology, chemical composition, surface functionality and structure ^[40b, 41]. The hydrothermal synthesis route is a cheap, simple, quick, non-toxic, environmentally friendly and highly efficient process which occurs in aqueous medium at mild temperatures in the range of 130-250 °C ^[40, 42] – other sources mention 180-260 °C ^[39]– under self-generated pressures ^[42a] at 2-6 MPa with reaction times of only a few minutes to hours, generally 5-240 min are sufficient depending on the starting materials ^[39, 43]. As the pressure is autogenic, this process is mainly controlled by the saturation vapor pressure of water (subcritical or superheated water) according to the reaction temperature. If the reaction temperature exceeds 260 °C, hydrothermal synthesis is then divided into hydrothermal liquefaction (HTL), hydrothermal

vaporization (HTV) or gasification (HTG) and supercritical water gasification (SCWG). In HTL and HTV gaseous or liquid products are obtained (Figure 1) [39, 44].

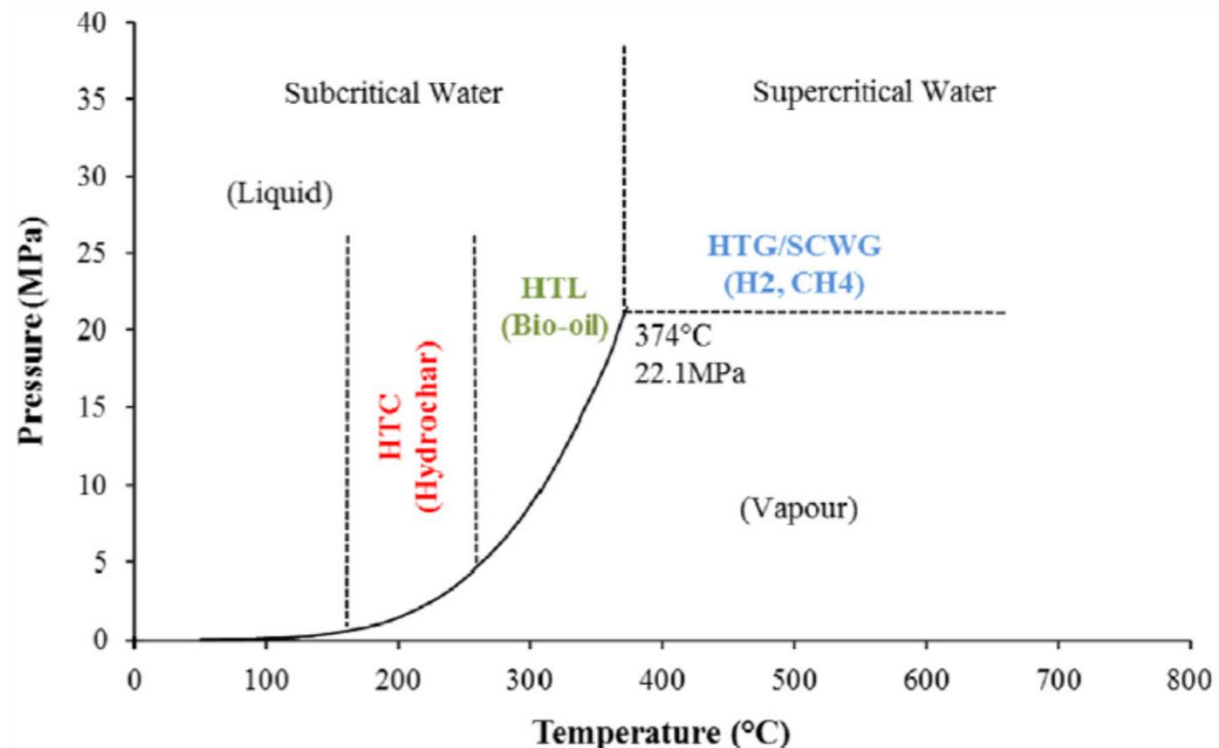


Figure 1: Pressure-temperature phase diagram of water classifying hydrothermal processing of biomass [39].

The presence of aqueous environment offers the advantage of using feedstock with high moisture content. Hence, energy-intensive pre-drying procedure of wet plant-based starting materials becomes superfluous when conducted under thermal treatments such as slow-pyrolysis or dry torrefaction [39, 45].

The HTC is a spontaneous, exothermic procedure. In principle, HTC is comparable with the natural coalification process of organic materials. The process of coalification can be diminished to only a few hours and, in addition, it generates climate-neutral renewable fuels. HTC synthesis produces carbonaceous solid (hydrochar or HTC char) as main end product and by-products like liquid supernatant (bio-oil/water emulsion) or small amounts of gaseous products, especially CO_2 [39, 46]. The physicochemical characteristics and relative distribution of the final end products strongly depend on the process

parameters such as reaction time and temperature. Usually, hydrochar is the most desired end product after hydrothermal synthesis with a mass yield between 40-70 %^[39, 46]. Taken glucose as a starting material, hydrothermal carbonization yields a HTC char in which one third of the combustion energy is stored. The final energy in carbonaceous glucose corresponds to a value of 2200 kJ·mol⁻¹^[47]. After the reaction has taken place, a suspension is formed with dispersed carbonaceous colloidal particles (hydrochar, HTC char)^[43a, 43c, 48], which are concerning elemental composition, structure, calorific value and color similar to lignite or peat (Figure 2)^[49].

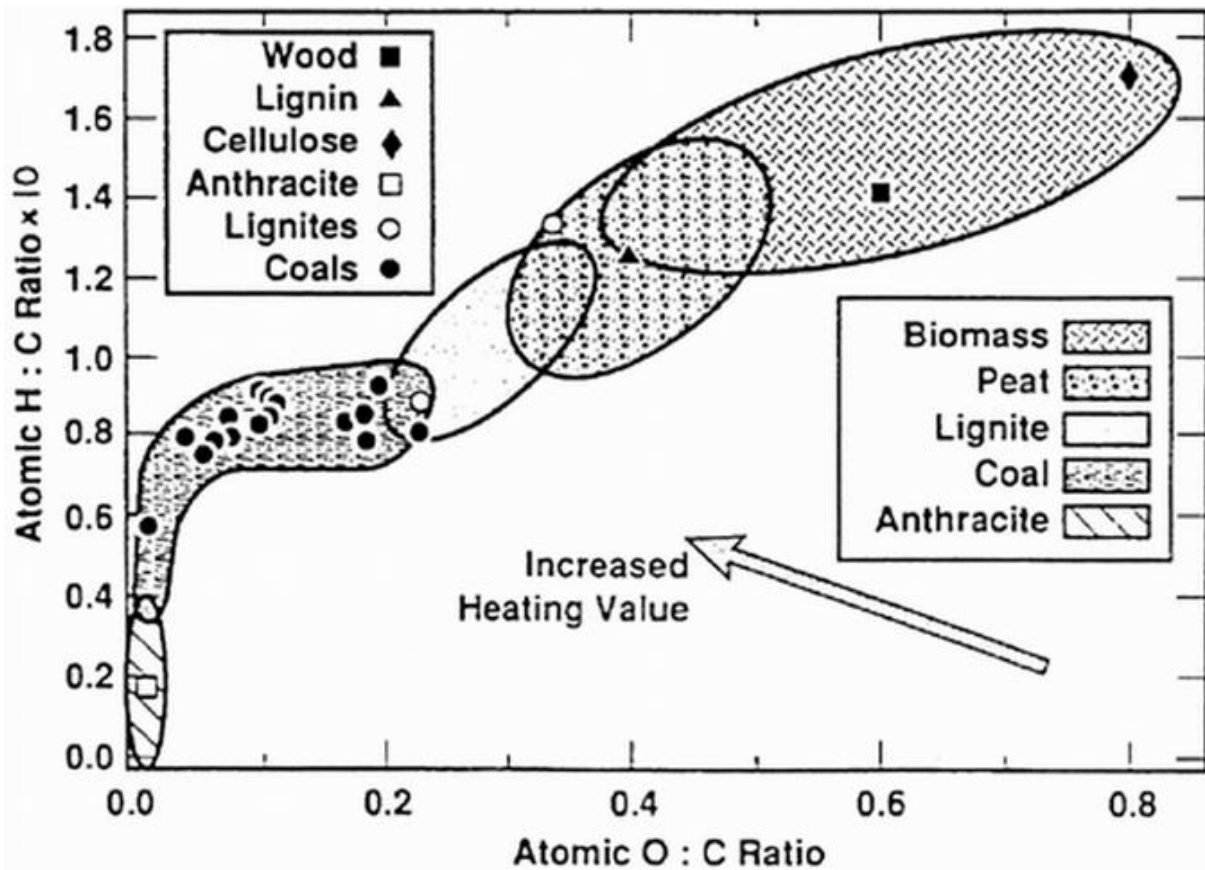


Figure 2: Van Krevelen diagram for various carbonaceous solid fuels^[50].

In the Van Krevelen diagram the biomass fuels are the highest in the H/C- and O/C-ratios in comparison with peat or coals (lignite, coal, anthracite)^[50]. The O/C-ratio is decisive for lowering the calorific value. Thus, biomass fuels are more volatile. The higher the volatility is the better the stability in the ignition process^[50]. The HTC process can be illustrated very well in this

diagram. During coalification, the process occurs starting from biomass (wood, cellulose) via the intermediate stage peat (lignin) and the different forms of coals (lignite) up to anthracite. Therefore, with increasing carbonization H/C- and O/C-ratios migrate as a result of dehydration and decarboxylation from biomass to anthracite. Consequently, in the Van Krevelen diagram, for any kind of HTC char, the degree of carbonization can be clearly visualized ^[49b].

The resulting HTC char is amorphous with only little aromatic domains but abundant in (oxygen) functional groups, is typically non-porous with a limited surface area, and has spherical morphology ^[42b, 51]. The spherical particles range in micrometer size. By means of solid-state NMR spectroscopy the structure of hydrochars has been analyzed (Figure 3) ^[51b]. It has been reasonable to suggest that the hydrothermal carbon is a complex and crosslinked organic polymeric network.

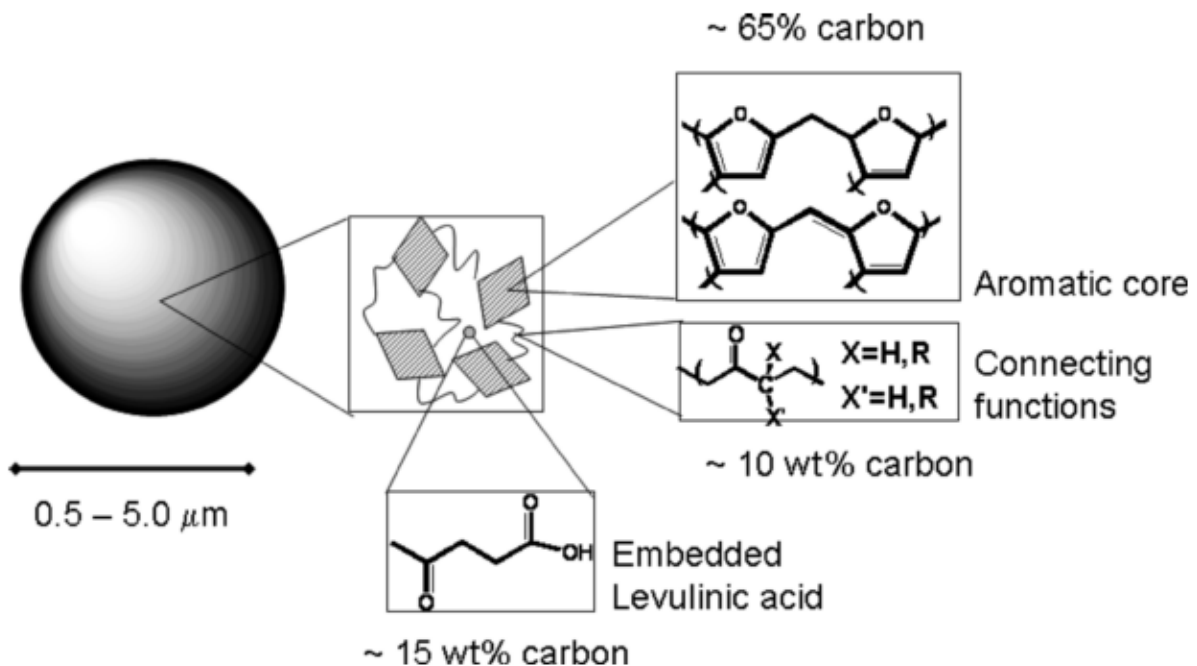


Figure 3: Structural model proposed for HTC chars ^[51b].

Using a 10 wt% glucose solution at 180 °C for 24 h, the obtained HTC char is built up of a sp^2 aromatic carbon core comprising furanic-based motifs which are the key structural element with a total share of around 65 % of the hydrothermal carbon. Approximately 23 % was attributed to sp^3 aliphatic carbon

and about 13 % consists of C=O groups (e.g. ketones or aldehydes). It was proposed that 10 % of the hydrothermal carbon is made of interconnecting chain functions, in particular keto groups linked to aliphatic compounds. Furthermore, it is suggested that 15 % of the hydrothermal carbon is composed of embedded levulinic acid-type moieties ^[51b].

Another chemical structure model based on elemental analysis and spectroscopic methods such as FTIR, Raman and XPS spectroscopy suggests a hydrophobic/hydrophilic core-shell model which highlights the different chemical structure between the core and the shell of these hydrochars stemming from hydrothermal carbonization (Figure 4) ^[52].

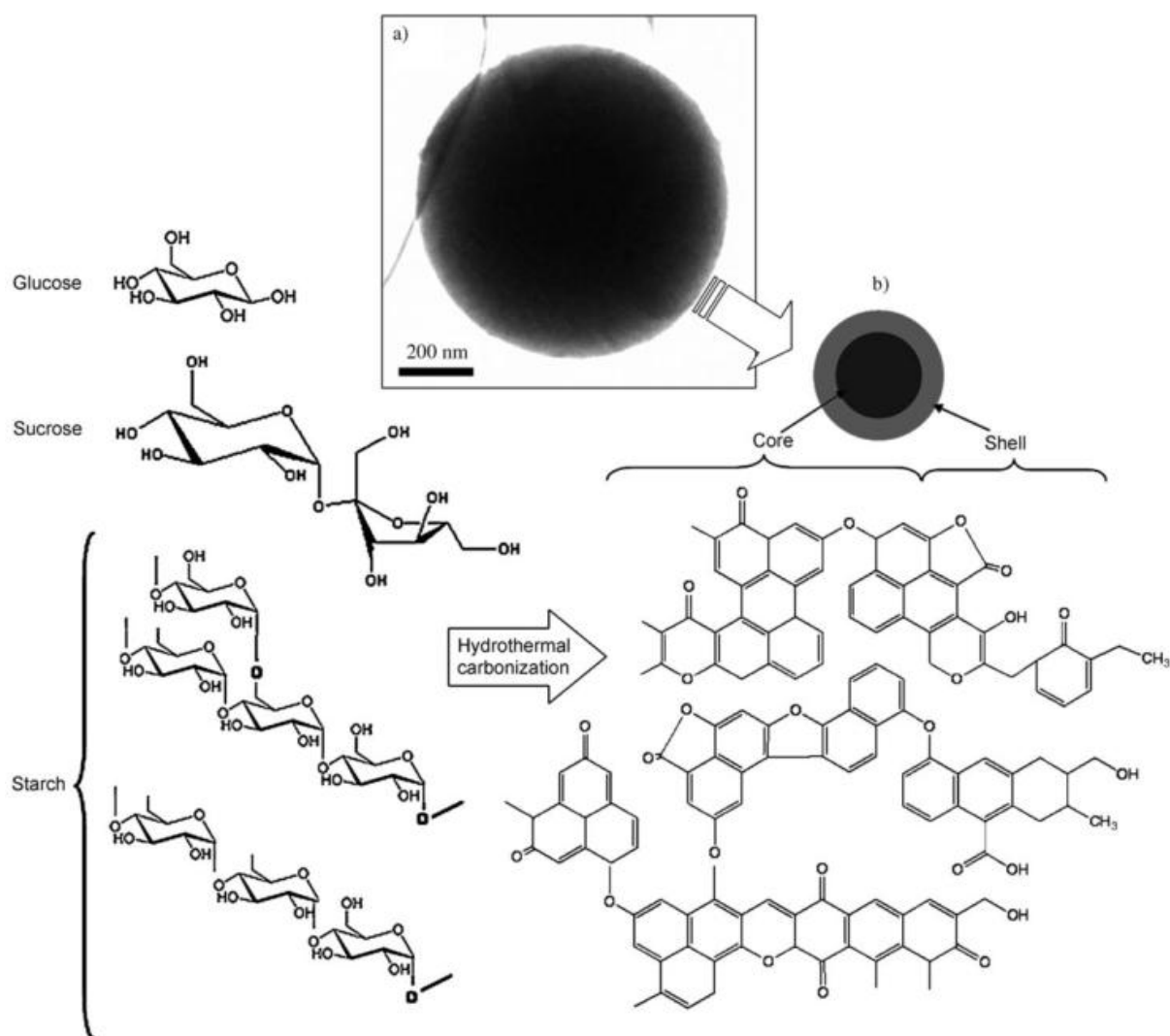


Figure 4: a) TEM micrograph of HTC chars originating from starch and b) schematic representation of the core-shell chemical structure model ^[52].

There are differences in terms of O-functionalities between the core and the shell. The core consists of stable, hydrophobic functions like ether, furan, pyran, lactone, keto, quinone or pyrone whereas the shell comprises reactive, hydrophilic groups such as hydroxyl, pyranol, carboxylic or ester (lactone). Both regions are interconnected by ether bonds and primarily consists of a polycyclic condensed aromatic structure [52].

HTC strongly depends on the applied starting material and the temperature as crucial parameter since it controls the degree of aromatization (Figure 5) [53].

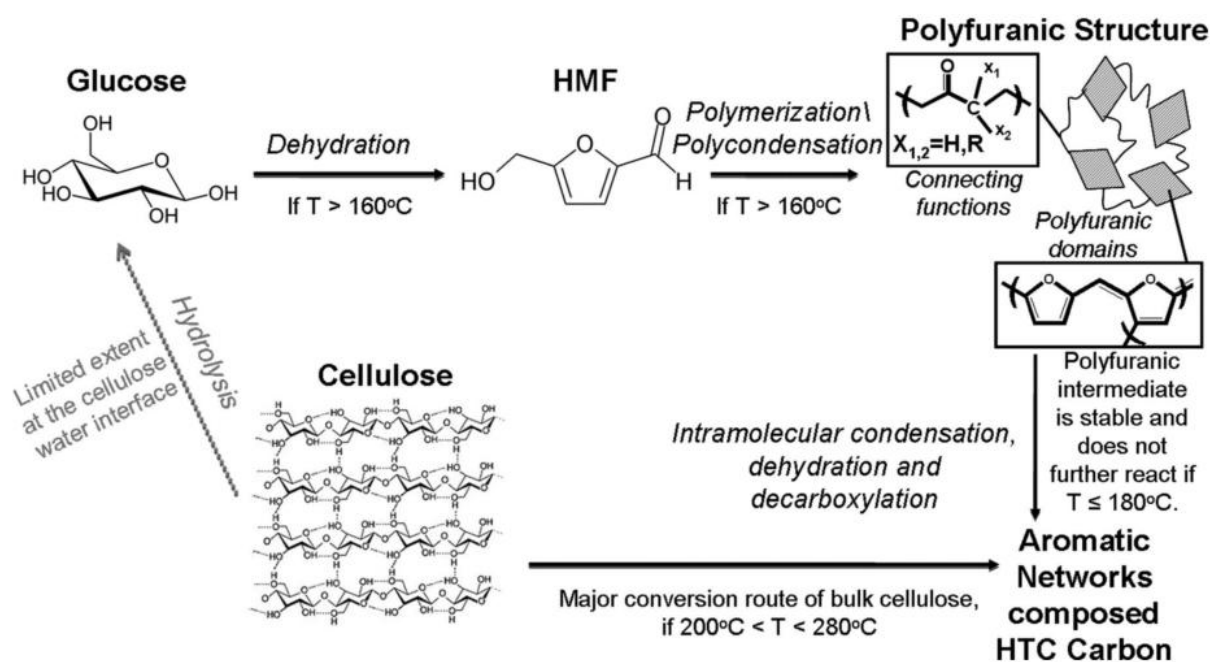


Figure 5: Postulated HTC degradation reaction pathway using cellulose or glucose as starting materials. Dotted lines depict a side reaction [53a].

If glucose is treated hydrothermally at temperatures beyond 160°C , 5-hydroxymethylfurfural (HMF) as intermediate is formed to a significant extent apart from decomposition products including levulinic acid, dihydroxyacetone and formic acid [51b, 53a, 54]. This degradation process is acid-catalyzed driven. HMF further undergoes polymerization (polycondensation) reactions resulting in domains of (poly)furan-based moieties in which levulinic acid-like functions act as linkers [51b, 53a, 55]. At temperatures higher than 180°C , intramolecular condensation, further dehydration and decarboxylation of (poly)furanic chains takes place producing an hydrochar with a pronounced

aromatic character with proportions of O-containing functional groups. In contrast to it, degradation mechanism of cellulose is postulated to hydrolyze by bond cleavage into single glucose units ^[53a, 56]. Stronger acid catalysts and harsher process conditions are needed meaning that, for instance, temperatures above 180 °C are indispensable ^[53a, 57]. It is believed that the HTC mechanism does not necessarily undergoes (poly)furanic-type intermediates as it yields in an extended aromatic network structure ^[53a, 58]. The intermediate is supposed to derive from cellulose being a polymeric compound, the so-called “intermediate cellulose” ^[53a, 59].

Basically, HTC chars are (poly)furanic-rich materials. The final structure depends on temperature, time and starting material (Figure 6). Another decisive process condition parameter is the pressure ^[44b, 60]. By rising the temperature or adding liquids, the reactor pressure increases isotropically ^[60b]. The reaction pressure influences the reaction network according to Le Chatelier’s principle ^[60b]. Increasing reaction pressure shifts reaction equilibrium to solid and liquid phases or to reactants with a lower amount of substance ^[60b]. Thus, at higher reaction pressures, dehydration and decarboxylation as main reactions are prevented ^[60b]. Next to temperature, pressure leads to the dissociation of macromolecules into water-soluble oligomers or monomers, e.g. glucose ^[60a]. Further hydrolysis and degradation of glucose (condensation or cleavage reactions) results in a wide range of decomposition products ^[44b, 60] and influences the yield as well as the composition of the end product ^[60a]. Apart from that, the hydrothermal conversion of biomass is not only controllable by varying the temperature but also by the pressure ^[44b, 60a]. The modifications in temperature and pressure can favor effective separations of product and by-product. In this way, it can decrease the required energy consumption to purify products ^[44b]. In addition, when water is heated at elevated pressures, the phase change to steam is impeded and thus hinders high expenditure of enthalpic energy which can provide advantages in terms of efficiency in hydrothermal

processes [44b]. The disadvantage of using higher pressure is that it involves higher investment costs for pressure equipment and higher energy consumption [60b]. Compared with this, elevated temperatures accelerate hydrothermal carbonization and might achieve a higher yield of the carbon content [60b].

In literature, no systematic investigation exists on the impact of pressure to the final structure of the HTC char. Therefore, in the following, main focus lies on temperature and time as process variables and their effect to the carbon structure (Figure 6).

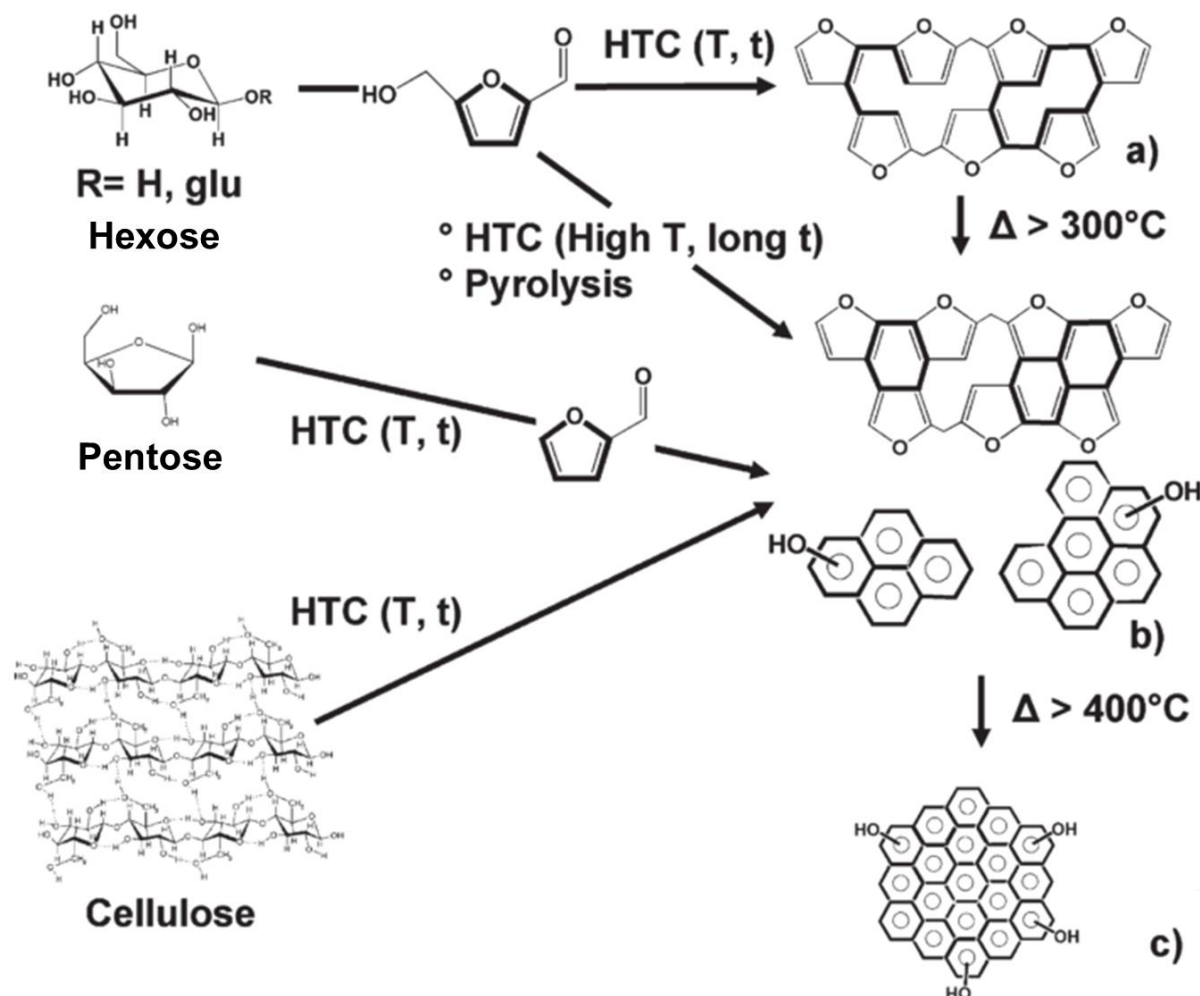


Figure 6: Different reaction pathways starting from carbohydrates describing the influence of process conditions such as temperature and time on the final structures [53b].

Structure (a) constitutes a crosslinked (poly)furanic chain structure which is observed on the hand at HTC temperatures below 200°C and on the other hand at low residence times. If hydrothermal synthesis is conducted at 180°C , this is the unalterable structure as it is also determined at a residence time of 72 h [53].

Interestingly, this structure is only found to a large scale if hexoses are used as a source. If pentoses or cellulose are utilized under mild process conditions (poly)furanic structures are not present abundantly anymore. Besides, furanic-type entities are not detected at all in pyrolyzed end products^[53].

Structure (b) illustrates a higher degree of internal condensation of the polymeric carbonaceous network. It can originate from (hetero)arenes such as furanic entities or from polycyclic aromatic hydrocarbons (PAHs)^[53b]. This structure phenomenon exists not only in HTC chars but also in pyrolyzed hydrochars. Moreover, coexistence between structure (a) and structure (b) is not unlikely^[53b]. Higher hydrothermal temperatures beyond 200 °C and longer residence times above 24 h are needed to achieve structure (b) for hexoses^[53b]. Pentoses prefer structure (b), too. It is formed under mild hydrothermal synthesis conditions and is probably controlled by the presence of furfural^[53b]. The same applies to cellulose that provides structure (b) under any temperature conditions^[53, 59d, 61].

At higher temperatures (>400 °C) the share of arene groups increases at simultaneous decrease of the number of furanic and phenolic moieties resulting in structure (c)^[53b].

Whereas O-functional groups and O-derived structure elements are formed spontaneously, N-type functionalities need to be induced because normally the contribution of N in carbon materials is negligibly small unless it forms part of the carbonaceous precursor. Traditionally, the incorporation of nitrogen is carried out in two ways^[62]. On the one hand, N-containing organic compounds or composites containing both, N-precursors and N-free materials are carbonized which typically lead to bulk structural modification (“in-situ doping”)^[62a, 62c, 62d]. “In-situ doping” is a powerful method to improve bulk material properties, especially structural and chemical features^[62a]. In-situ techniques include high-temperature processes such as arc-discharge^[62a, 62d, 63] and laser ablation^[62a, 62d, 64]. Low-temperature methods embrace chemical vapor deposition (CVD)^{[62a, 62d,}

^{65]}, modified CVD methods (aerosol assisted CVD ^[62d, 66], floating catalyst CVD ^[62d, 67], microwave plasma enhanced CVD ^[62d, 68], pyrolysis-type CVD ^[62d, 65a, 69]) as well as hydrothermal ^[70] or solvothermal synthesis ^[62a, 62d, 71]. N-precursors involve poly(acrylonitrile) ^[62a, 72], poly(aniline) ^[62a, 73], phthalocyanine ^[62a, 74], vinylpyridine ^[62a, 75], urea ^[62b, 76], melamine ^[62a, 77], acetonitrile ^[62a, 66a] and heterocycles such as pyridine ^[62a, 78] (Figure 7).

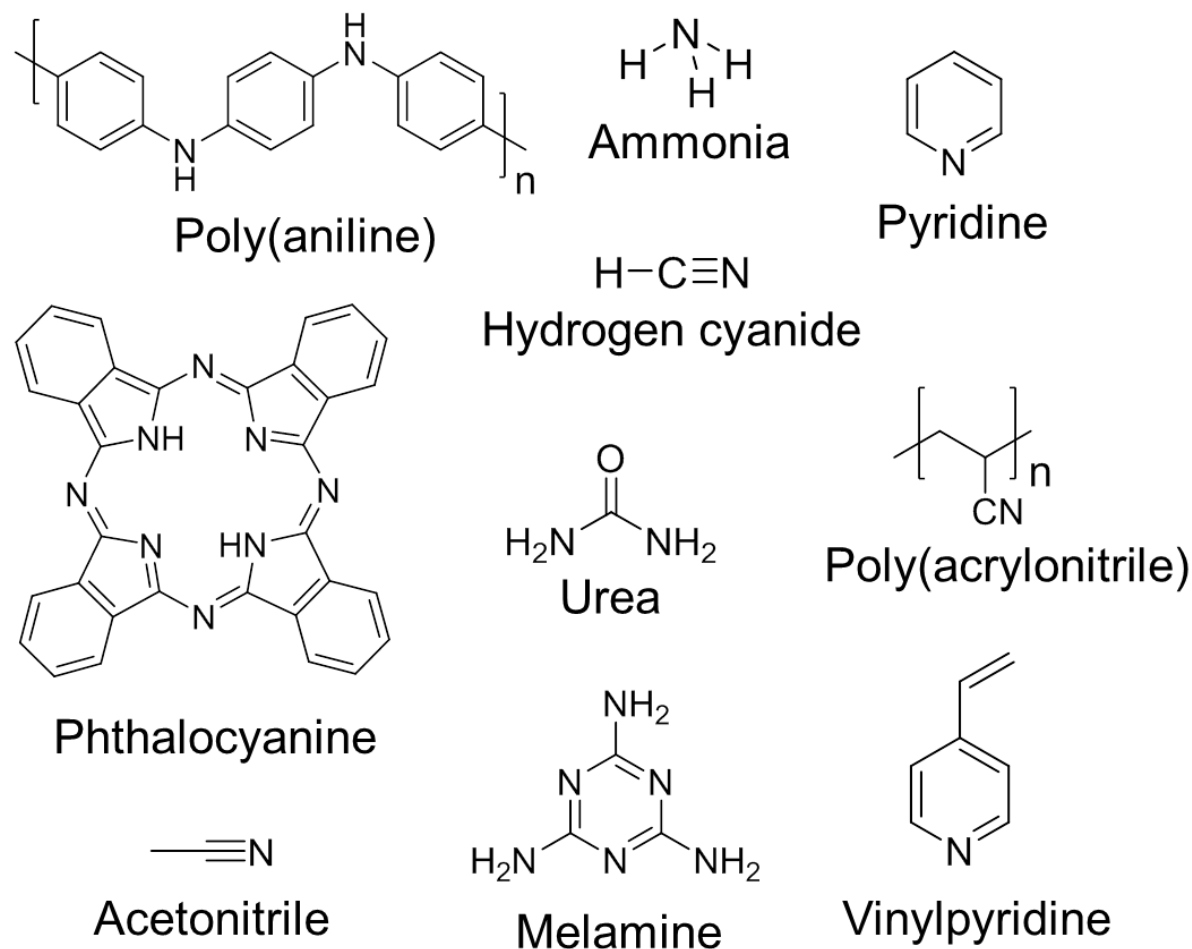


Figure 7: Common organic N-precursors for synthesis of N-functionalized carbon materials.

On the other hand, the as-synthesized carbon materials are treated at high temperatures with N-containing gases. The gases decompose with the evolution of highly reactive radicals ^[62c]. This approach leads to surface modification (“post-doping”) ^[62a]. In contrast to “in-situ doping”, the “post-doping” procedure offers less scope for significant modification. However, a well-known and typical approach for synthesis of N-containing carbons is the treatment of

activated carbons with NH_3 at temperatures up to approximately $600\text{-}900\text{ }^\circ\text{C}$ [62a, 62d, 79]. Another frequently used N-type gas is HCN (Figure 7) [62a, 79e, 79f].

Both approaches can tune the acid-base character of the carbon material and therefore tailor its surface reactivity or determine its catalytic activity [62a, 62b]. The N-containing carbon materials are characterized by their structural diversity. Depending on the type of N-precursor, the chemical activity of the carbon surface and, importantly, the temperature of heat treatment yields in a wide range of N-functional groups and N-based structural motifs can be detected on the carbon surface (Figure 8) [62a, 62b].

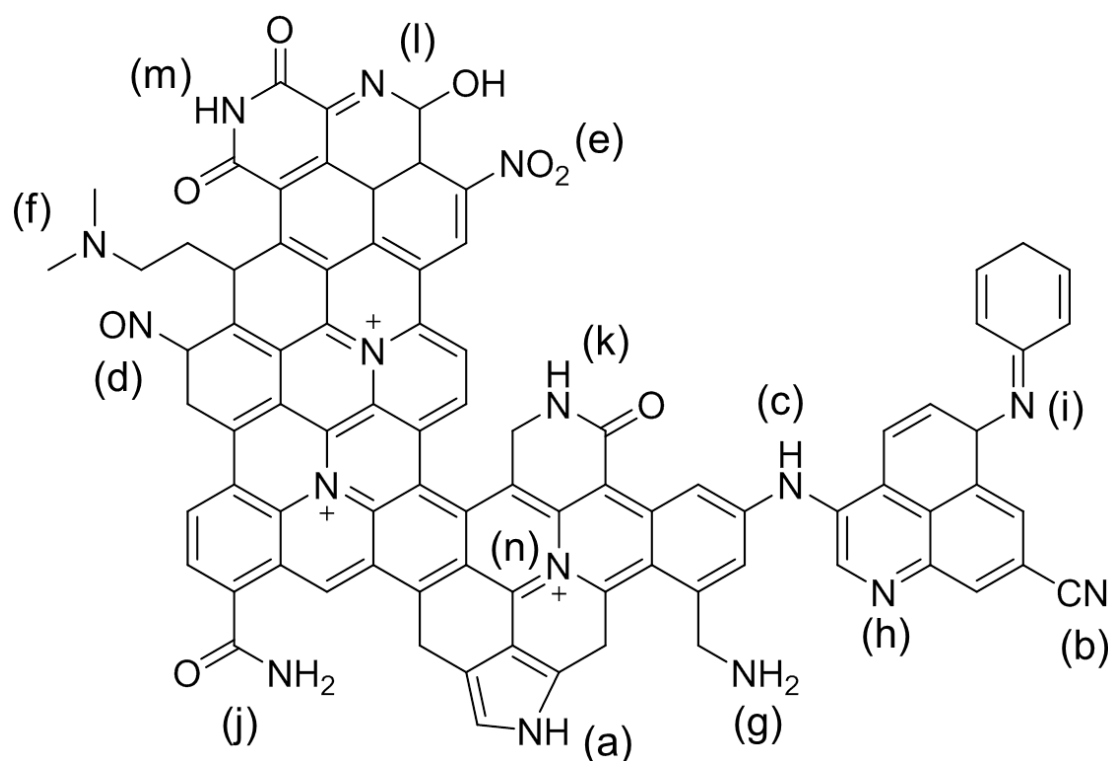


Figure 8: Types of N-functionalities on the carbon surface: (a) pyrrole, (b) nitrile group, (c) secondary amine, (d) nitroso group, (e) nitro group, (f) tertiary amine, (g) primary amine, (h) pyridine, (i) imine group, (j) amide group, (k) lactam, (l) pyridone, (m) imide, and (n) quaternary amine.

Heat treatment of carbon materials with N-precursors at temperatures lower than $530\text{ }^\circ\text{C}$ lead preferentially to lactams, imides or amines resulting in a carbon with slightly acidic behavior. Treatment at temperatures above $530\text{ }^\circ\text{C}$ yields in a higher amount of quaternary amines, pyridines and pyrroles [62b, 80]. The N-containing structures provoke a rise of surface polarity and for basicity of carbon since pyridine and pyrrole possess basic character [62b, 75, 81]. The overall

acid-base character is determined by the degree of heterogeneity of surface N-functional groups generated on the carbon surface ^[62b, 82].

The hydrochars can be subjected to, for instance, post-functionalization, thermal post-treatment or activation process, for example, by introducing porosity to achieve higher surface area in order to enhance material properties in terms of stability, catalytic activity or conductivity without changing the spherical morphology in a significant manner.

In general, HTC chars have widespread technological fields of application in our daily life making the hydrothermal carbonization a promising synthesis technique. Fields of application cover soil enrichment ^[43c, 83], in electrocatalysis as electrocatalysts for the oxygen reduction reaction (ORR) in fuel cell applications (e.g. direct methanol fuel cells) ^[84]. In the field of energy storage, they can act as electrode materials for rechargeable batteries ^[85] or as supercapacitors ^[86]. The hydrochars play an important role in heterogeneous catalysis as catalyst supports ^[87] or for photocatalytic purposes ^[88]. Apart from that, the HTC chars are suitable for gas storage involving CO₂ capture ^[89] or H₂ storage ^[90]. They can also be applied as adsorbents for the usage as sorption materials for water purification to remove heavy metals (Pb²⁺, Cd²⁺, Cu²⁺, U⁶⁺) ^[91] or organic pollutants (dyes) ^[92] from waste water. Furthermore, hydrochars are used as chemical ^[93] or gas sensors ^[94] as well as for medical aspects that include drug delivery ^[95] and bioimaging ^[96].

N-containing carbons have gained a lot of attraction since they play a major role for the application in environmental protection industry ^[42b, 97], pH-responsive adsorbents ^[62a, 98], as purifiers in particular as contaminant removal from gas or liquid phases ^[42b, 62a, 99], catalysts or catalyst supports ^[42b, 62a, 62b, 100], and for catalytic activity ^[62b, 79e]. They are also used in energy conversion or storage technologies like supercapacitors ^[42b, 62a, 101], fuel cells ^[62a, 62c, 102] and batteries ^[62a, 103] in which the addition of nitrogen enhances the electrochemical performance as well as for gas storage purposes (CO₂ capture) ^[42b, 62a, 89c, 104].

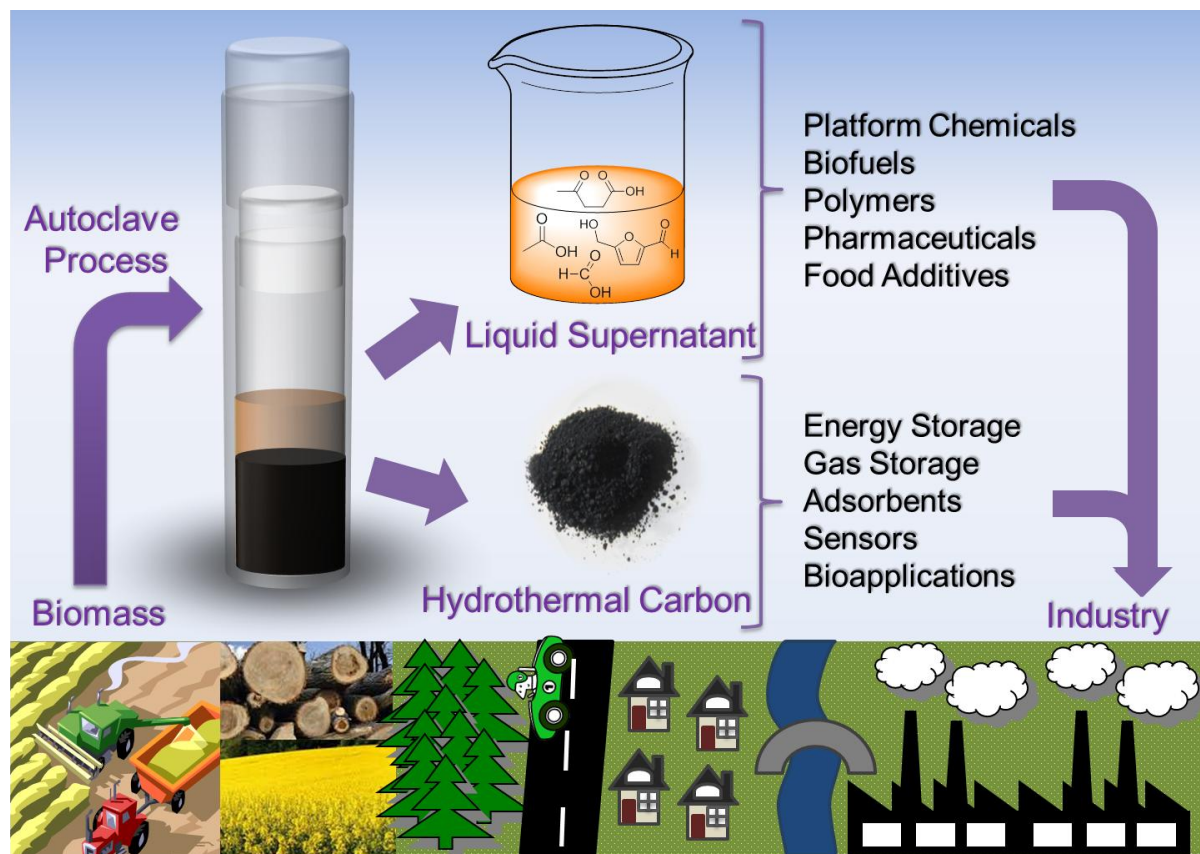


Figure 9: The concept of biorefinery starting from biomass via the production of hydrothermal carbon and liquid supernatant by means of autoclave synthesis up to versatile fields of application in industry.

In contrast to it, the liquid supernatant, which is a concurrent product after hydrothermal carbonization, is a valuable by-product as well (Figure 9). Without N-precursor, the supernatant has an orange-red color. By presence of a N-precursor during hydrothermal synthesis, it has a dark brown color containing organic acids such as formic acid, acetic acid or levulinic acid ^[105]. A further important chemical compound is 5-hydroxymethylfurfural (HMF). HMF is a bifunctional aromatic building block. It is a common key intermediate during acid-catalyzed degradation of carbohydrates ^[43c, 55, 106]. HMF is a crucial, versatile organic intermediate chemical and marketable product, which has the potential to replace oil-based products ^[39, 43c, 107]. Besides HMF, levulinic acid which is regarded among the top 12 most valuable chemicals from biomass ^[39]. All of these compounds are considered as typical platform chemicals in biorefineries and chemical industry for the production of valuable and diverse everyday products including pharmaceuticals, food additives or polymers (e.g.

polyester) but are also suitable for the use as liquid biofuels (Figure 9) ^[39, 105-106]. In terms of biofuel quality, HMF has been proven to be superior to ethanol on some points ^[39, 108].

Biomass or lignocellulosic biomass (e.g. wood, straw, grass, corn) is a natural, complex polymeric organic feedstock consisting of three key components which acts as building blocks, namely cellulose (hardwood: 39-54 %, softwood: 41-50 %, agricultural: 24-50 %), hemicellulose (hardwood: 15-36 %, softwood: 11-27 %, agricultural: 22-35 %) and lignin (hardwood: 17-29 %, softwood: 27-30 %, agricultural: 7-29 %) ^[39, 109].

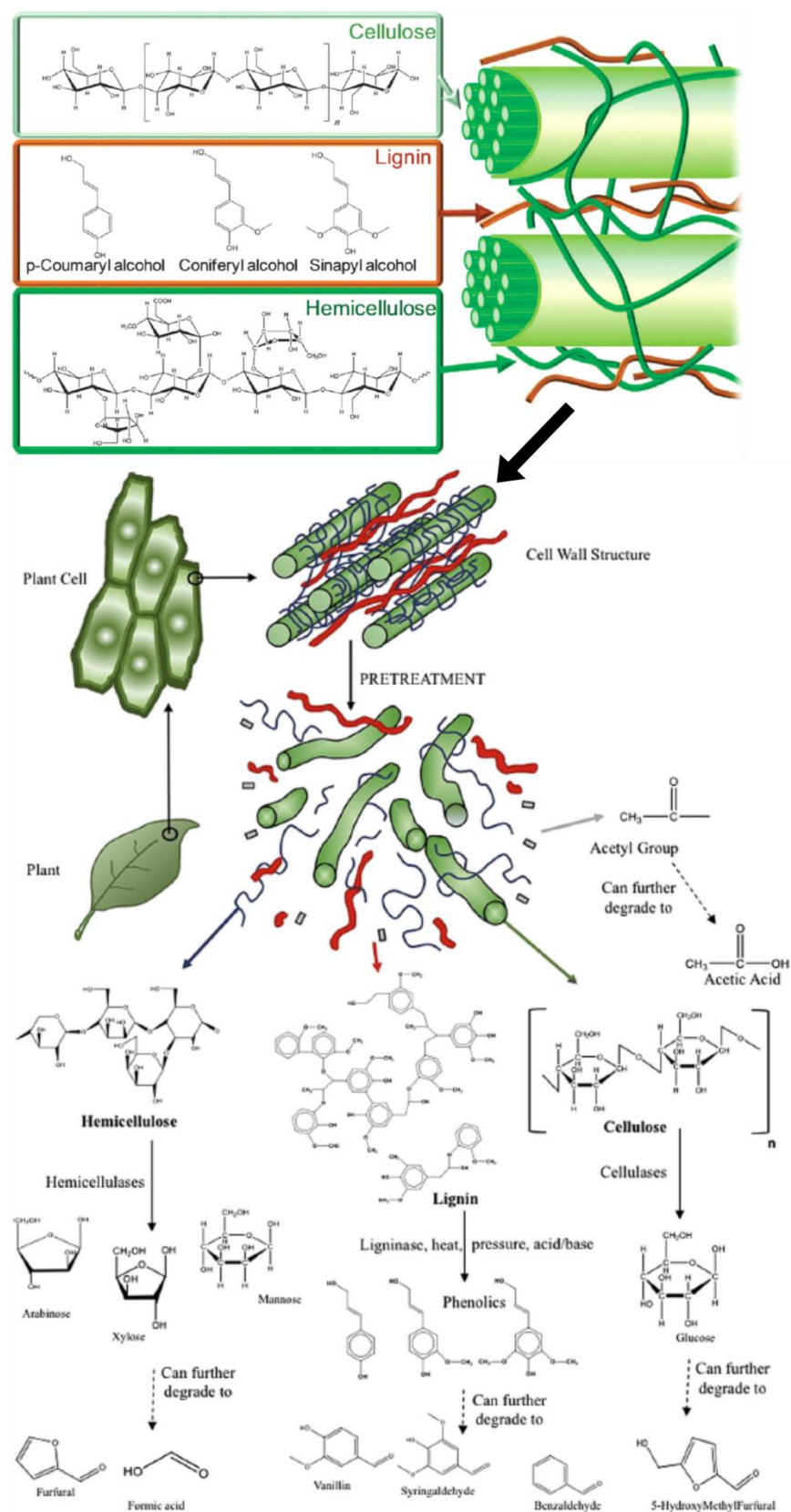


Figure 10: Schematic representation of secondary cell wall structure illustrating the main components cellulose, hemicellulose and lignin. Pretreatment and hydrolysis of cellulose, hemicellulose and lignin produce compounds covering mono-/oligosaccharides, phenolic compounds, furan derivatives and organic acids [39, 109-110].

Cellulose is the most abundant polysaccharide in nature and the main structural element of plants. In cellulose, glucose is the primary structural component linked via a linear homopolymeric chain by β -1,4 D-glycosidic bonds, also known as cellobiose unit. These chains are interconnected by hydrogen bridge bonds that transforms the chains into microfibrils featuring a crystalline character and an increased resistance to decomposition (Figure 10) [39, 109-111].

Hemicellulose is a heteropolymer comprising of pentoses (arabinose, xylose) and hexoses (galactose, glucose and mannose) in the form of polysaccharides xylan, galactan, mannan and arabinan. In hemicellulose, xylan is the most dominant polysaccharide whereby the units are bonded by β -(1 \rightarrow 4)-glycosidic or α -(1 \rightarrow 2)-4-*O*-methylglucuronic acids linkages (Figure 10) [39, 109, 112]. In plants, xylan is linked by hydrogen bonding with the cellulose forming an overlying layer. Moreover, it is covalently bonded with lignin which forms a protective sheath around the plant. Xylan is an essential component of plant cell walls. It is estimated to constitute 30-35 % of total dry weight [111, 112b].

Lignin is a complex, cross-linked heteropolymer of phenylpropanoid-based monomer building blocks including *p*-coumaryl alcohol, coniferyl alcohol and sinapyl alcohol (Figure 10). They are interconnected by alkoxy-bonds forming a macromolecular structure [39, 109]. Fully developed woody plants contain higher amount of lignin in cell walls imparting rigidity and strength. It further makes cell walls waterproof and offers effective protection against pathogens [111].

Pectin is another type of heteropolysaccharide with hydrophilic properties consisting of a highly diverse number of sugar compounds covering the main component galacturonic acid, but also arabinose, galactose, rhamnose as well as other monosaccharides such as fucose and apiose. Pectin retains water and exists in high concentrations in plant substances with high moisture content like fruits [109, 111, 113]. It forms a part of the intracellular network and gives flexibility to the cell by its interaction with water [111].

Besides hemicellulose and lignin, together with pectin they represent a matrix, which surrounds cellulose ^[109, 111, 114]. Lignin and hemicellulose are located in the gaps between cellulose microfibrils in primary and secondary cell walls as well as in middle lamellae ^[111, 114]. These components constitute the secondary cell wall found in plant cells of any kind of biomass ^[115]. This complex network of polymers are strongly interconnected and cross-linked. Additionally, they are chemically bonded by non-covalent physical interactions making the plant a structurally robust, rigid and resistant resource ^[39].

Glucose and urotropine (hexamethylenetetramine, HMTA) are used as model study precursors throughout the whole work. Glucose is used as carbon source whereby urotropine acts as nitrogen source. Whereas glucose is found abundantly in any type of renewable plant-based feedstock in nature, urotropine does not exist in nature. It is an artificial synthesized substance. Industrially, urotropine is formed by the condensation reaction of formaldehyde and ammonia, which are used as reactants either in liquid or in vapor phase (Figure 11) ^[116].

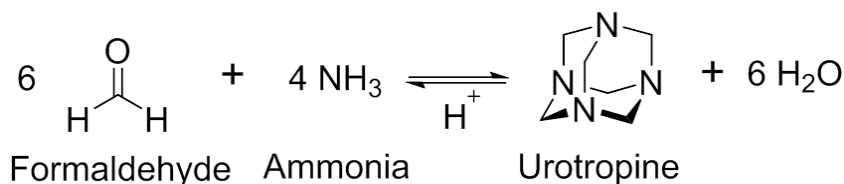


Figure 11: Formation of urotropine.

Urotropine is highly soluble in water, ethanol, chloroform and other organic solvents. It is stable in neutral, aqueous medium. However, in acidic solution it starts to hydrolyze into its starting materials ^[116]. Urotropine is a fourth-cycled, heterocyclic compound with a diamondoid-like geometry. It possesses a highly symmetrical, cage-like spherical shape with adamantane scaffold bonded to four N-atoms and linked to methylene bridges in between (Figure 11) ^[116a, 116c, 117]. Urotropine is inexpensive and commercially available at any time ^[117b]. Therefore, urotropine is manifoldly used in industrial and chemical applications ^[116a, 116b, 117b].

The main applications include its usage as additive in the rubber industry, as curing agent for thermosetting resins (phenol-formaldehyde and urea-formaldehyde resin). It is further used in foundry mold castings forming a part of binder resins, for the utilization in the fabrication of adhesives and coatings, in the manufacture as solid fuel for camping, or in flame-retardant materials. In addition, urotropine is used as a preservative (food additive) in food industry. Since under acidic pH conditions urotropine hydrolyzes into its reactants formaldehyde and ammonia, it has been used as a pharmaceutical for intestinal infection or for the treatment of urinary tract infection ^[116b, 118].

Synthetically, urotropine has become a crucial and versatile reagent, especially in the Duff, Sommelet or in the Delépine reaction ^[116a]. Moreover, it is an interesting building block for the design of coordination polymers ^[117b]. For example, it is applied in the production of chelating agents such as nitrilotriacetic acid (NTA) ^[116b]. Urotropine serves as a starting material for the production of nitroamines which are utilized as explosives, in particular hexogen (RDX) and octogen (HMX). In World War II they were used as explosive bombs or as additives in explosive mixtures ^[116a].

Throughout this work the use of urotropine as N-precursor turns out to be a powerful reagent due to its unique feature of hydrolyzing into its starting materials, formaldehyde and ammonia. This characteristic is an important factor as this opens up a variety of possible reaction pathways, especially in presence of ammonia. Together with the decomposition process of glucose widespread synthetic pathways are possible. Reaction mechanisms of the decomposition processes of both precursors – glucose and urotropine – and further reaction pathways of the degradation products will be in detail discussed in the next chapter.

2. THEORETICAL FUNDAMENTALS

2.1. Postulated Reaction Mechanisms during Precursor Decomposition and Spherical Particle Formation

Herein, we report the synthesis of nitrogen-functionalized carbonaceous materials by hydrothermal treatment using glucose as carbon source and urotropine as nitrogen source. Both starting materials are dissolved in aqueous medium, filled in Teflon lined autoclaves and treated hydrothermally at temperatures up to 180 °C for 6 h yielding the N-functionalized HTC material. As by-product, a liquid supernatant is obtained (Figure 12).

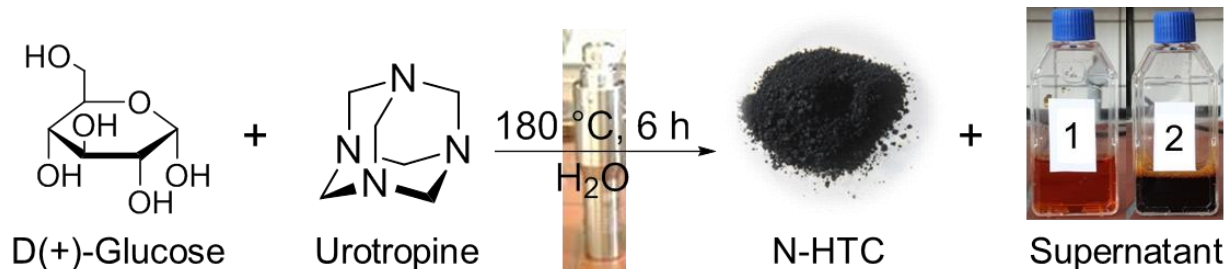


Figure 12: General reaction scheme of the hydrothermal synthesis of N-HTC chars (main product) and liquid supernatant (by-product) from glucose and urotropine. The liquid supernatant of pure glucose has an orange-red color (1) whereas the mixture of glucose and urotropine possesses a dark brown color (2).

At these hydrothermal synthesis conditions, urotropine presumably decomposes into formaldehyde and ammonia (Figure 13 (a))^[116b, 119], which are able to react with the decomposition products of glucose (Figure 13 (b)).

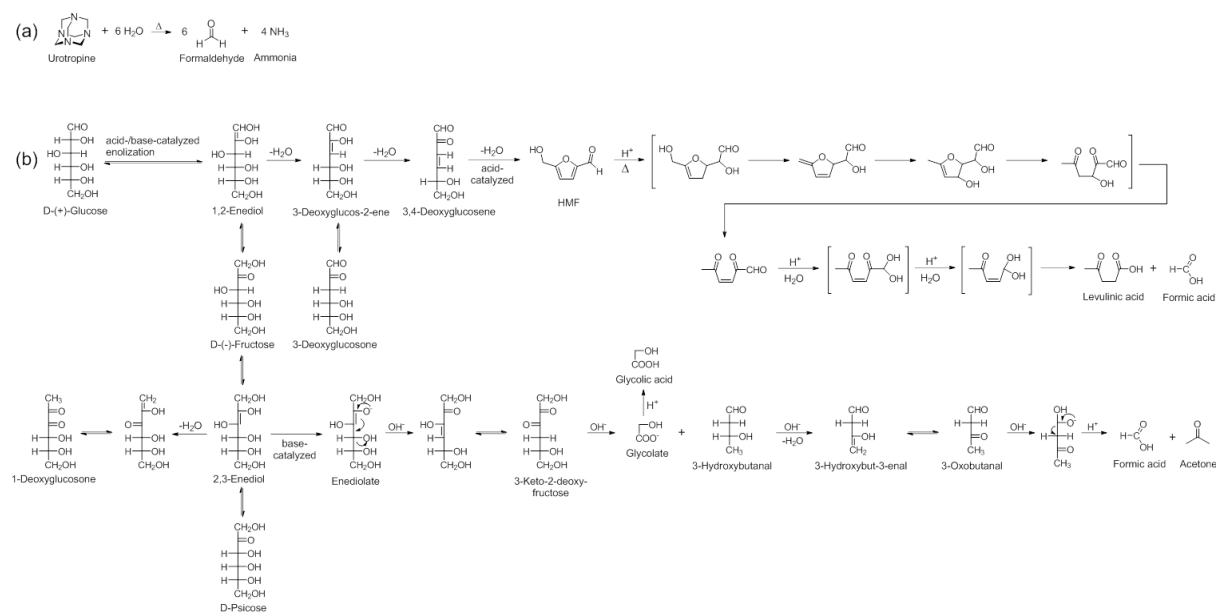


Figure 13: (a) Urotropine decomposes into formaldehyde and ammonia at high temperature. (b) Simplified scheme of the decomposition process of glucoses in acidic environment yielding into levulinic acid and formic acid as final decomposition products. The degradation products in brackets are proposed by means of ^{13}C NMR spectroscopy.

The acyclic pathway in the direct formation of 5-hydroxymethylfurfural (HMF) by acid-catalyzed dehydration of hexoses (e.g. glucose) is widely known ^[120]. Decomposition of the monosaccharide glucose occurs over initial acid- ^[120a] or base- ^[121] catalyzed aldose-ketose isomerization (Lobry de Bruyn-Alberda van Ekenstein transformation) and three times of dehydration forming the intermediate HMF ^[120a]. HMF further decomposes after several steps into levulinic acid and formic acid. The decomposition steps in brackets were proposed by means of ^{13}C NMR spectroscopy ^[122]. The decomposition process also includes a variety of side reactions leading for the most part to undesired polymeric by-products, called humins ^[120a, 122a, 123].

Several reaction pathways occur during the decomposition of the initial product glucose ^[120a, 124]. Considering the decomposition products of glucose, as well as ammonia and formaldehyde as additional reagents derived from urotropine, several N-containing structural motifs can be formed based on retro-synthetic ideas (Figure 14, Table 1).

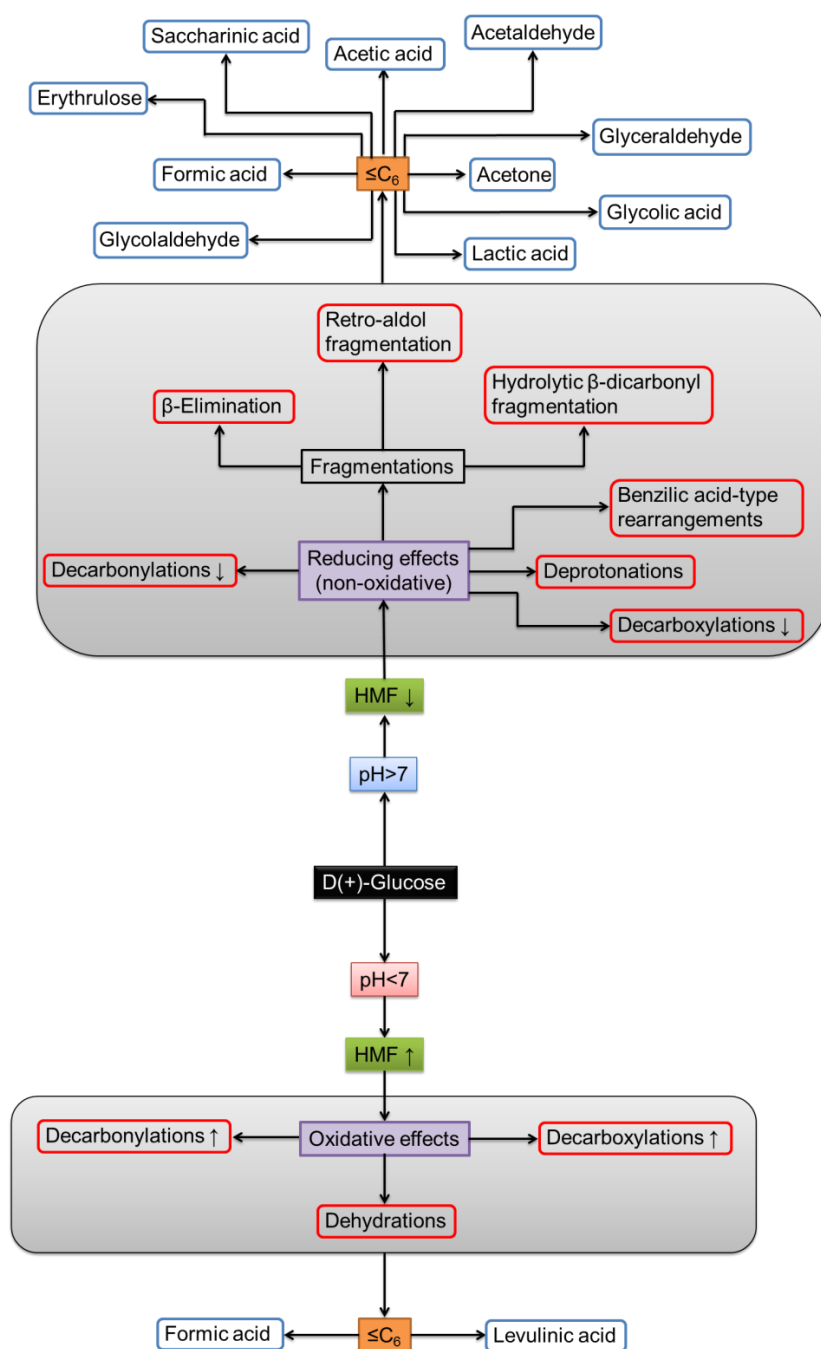
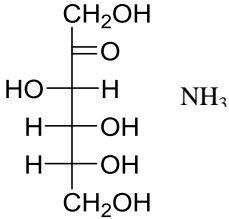
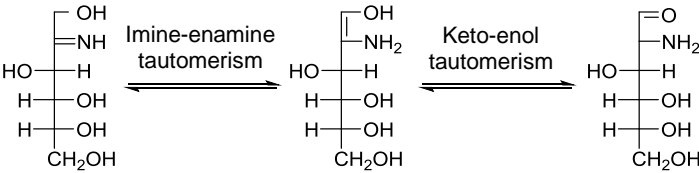
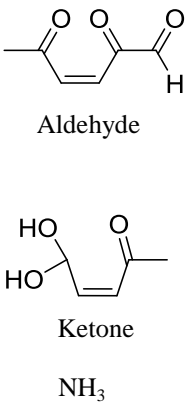
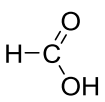
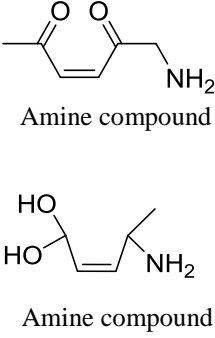
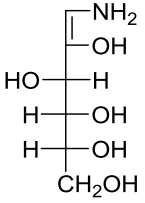
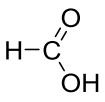
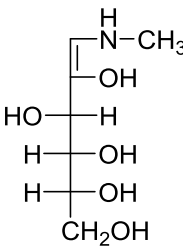
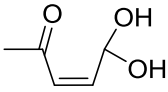
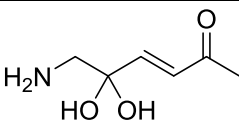
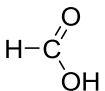
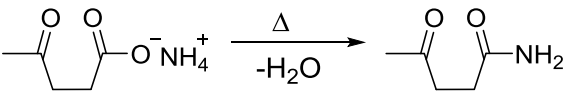
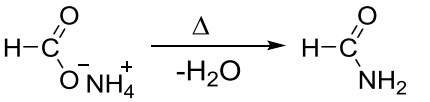
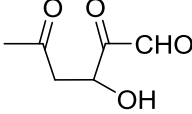
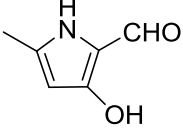
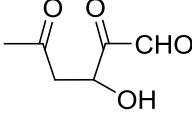
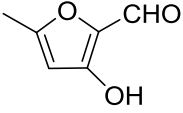
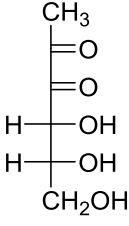
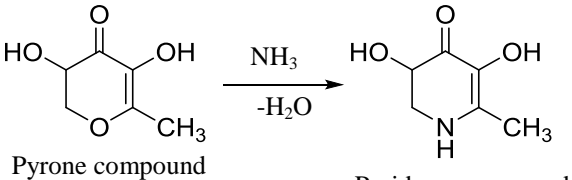
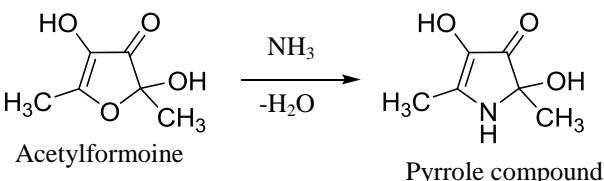


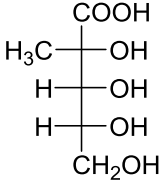
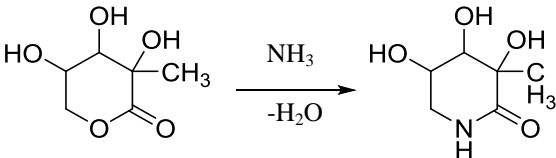
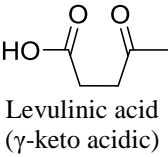
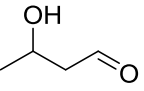
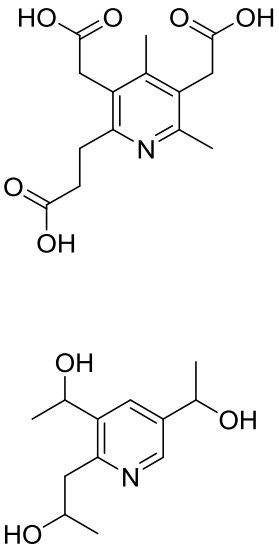
Figure 14: Schematic illustration of the pH-dependent synthetic pathways and their reaction mechanisms resulting in $\leq C_6$ decomposition products.

Table 1: Reaction pathways based on N-containing structural motifs.

Name reaction	Reagents and conditions	Products
Amadori rearrangement	$ \begin{array}{c} \text{H}-\text{C}=\text{O} \\ \\ \text{H}-\text{C}-\text{OH} \\ \\ \text{HO}-\text{C}-\text{H} \\ \\ \text{H}-\text{C}-\text{OH} \\ \\ \text{H}-\text{C}-\text{OH} \\ \\ \text{CH}_2\text{OH} \end{array} $ <p>NH_3</p> <p>D(+)-Glucose</p>	$ \begin{array}{c} \text{H}-\text{C}=\text{NH} \\ \\ \text{H}-\text{C}-\text{OH} \\ \\ \text{HO}-\text{C}-\text{H} \\ \\ \text{H}-\text{C}-\text{OH} \\ \\ \text{H}-\text{C}-\text{OH} \\ \\ \text{CH}_2\text{OH} \end{array} $ <p>Aldoimine (Schiff base)</p> <p>Imine-enamine tautomerism</p> $ \begin{array}{c} \text{H}-\text{C}-\text{NH}_2 \\ \\ \text{H}-\text{C}-\text{OH} \\ \\ \text{HO}-\text{C}-\text{H} \\ \\ \text{H}-\text{C}-\text{OH} \\ \\ \text{H}-\text{C}-\text{OH} \\ \\ \text{CH}_2\text{OH} \end{array} $ <p>Keto-enol tautomerism</p> $ \begin{array}{c} \text{H}-\text{C}-\text{NH}_2 \\ \\ \text{H}-\text{C}=\text{O} \\ \\ \text{HO}-\text{C}-\text{H} \\ \\ \text{H}-\text{C}-\text{OH} \\ \\ \text{H}-\text{C}-\text{OH} \\ \\ \text{CH}_2\text{OH} \end{array} $

<p>Heyns rearrangement</p>	 <p>D(+)-Fructose</p>	 <p>Ketoimine (Schiff base)</p>
<p>Leuckart-Wallach reaction (reductive amination)</p>	 <p>Aldehyde</p> <p>Ketone</p> <p>NH₃</p>  <p>Formic acid</p>	 <p>Amine compound</p> <p>Amine compound</p>
<p>Eschweiler-Clarke reaction (reductive amination)</p>	 <p>1,2-Enaminol</p>  <p>Formaldehyde</p> <p>NH₃</p>  <p>Formic acid</p>	 <p>Methylated enaminol</p>
<p>Mannich reaction (condensation)</p>	 <p>Formaldehyde</p>	

reaction)	NH_3  Ketone compound (α -CH acidic)	 β -amino carbonyl compound ("Mannich base")
"Schotten-Baumann"-type reaction	 Levulinic acid NH_3  Formic acid	 Ammonium carboxylate compound $\xrightarrow{-\text{H}_2\text{O}}$ Amide compound  Ammonium formate $\xrightarrow{-\text{H}_2\text{O}}$ Formamide
Paal-Knorr pyrrole synthesis	 1,4-Diketone NH_3 (alkaline)	 Pyrrole compound
Paal-Knorr furan synthesis	 1,4-Diketone H^+ (acidic)	 Furan compound
Cyclic follow-up products (Maillard reaction)	 1-Deoxyglucosone	 Pyrone compound $\xrightarrow{-\text{H}_2\text{O}}$ Pyridone compound  Acetylformine $\xrightarrow{-\text{H}_2\text{O}}$ Pyrrole compound

Cyclic follow-up products (Maillard reaction)	 Glucosaccharinic acid	 Lactone compound $\xrightarrow[\text{-H}_2\text{O}]{\text{NH}_3}$ Lactame compound
Chichibabin pyridine synthesis	<p>3 </p> <p>Levulinic acid (γ-keto acidic)</p> <p>3 </p> <p>3-Hydroxybutanal</p> <p>NH_3 Δp, Δ, [O] (oxidation)</p>	 Pyridine compounds

The decomposition processes of both precursors open up a multitude of possible reaction pathways in the presence of ammonia that will be discussed in the following.

The introduction of nitrogen into the carbon network during hydrothermal treatment is not fully understood. Indeed, it is accepted that Maillard reaction is one of the reaction pathway that takes place in presence of amine compounds or amino acids ^[27c, 70c, 124-125]. Briefly, it includes amination, imination (Schiff base), Amadori rearrangement, cyclization (cyclic/heterocyclic compounds), transformation into aromatic motifs (e.g. pyrazine, pyrrole, pyrone, furan) and further degradation reactions (Strecker degradation) ^[51b, 53a, 124-125, 126]. However, it rather occurs between reducing sugars (e.g. glucose) and amino acids. Reducing sugars in aqueous medium are stable within a pH range of 5-7. Nevertheless, it changes in more acidic and alkaline environment or in presence of amine compounds (Maillard reaction) ^[125b]. With increasing acidities the degradation of glucose are characterized by slow enolization due to unfavorable

protonation of the carbonyl group. The subsequent water elimination occurs rapidly. The intermediate of this decomposition process is 3-deoxyglucosone if glucose is used as starting material. Further dehydration, cyclization and aromatization can yield in HMF [125b].

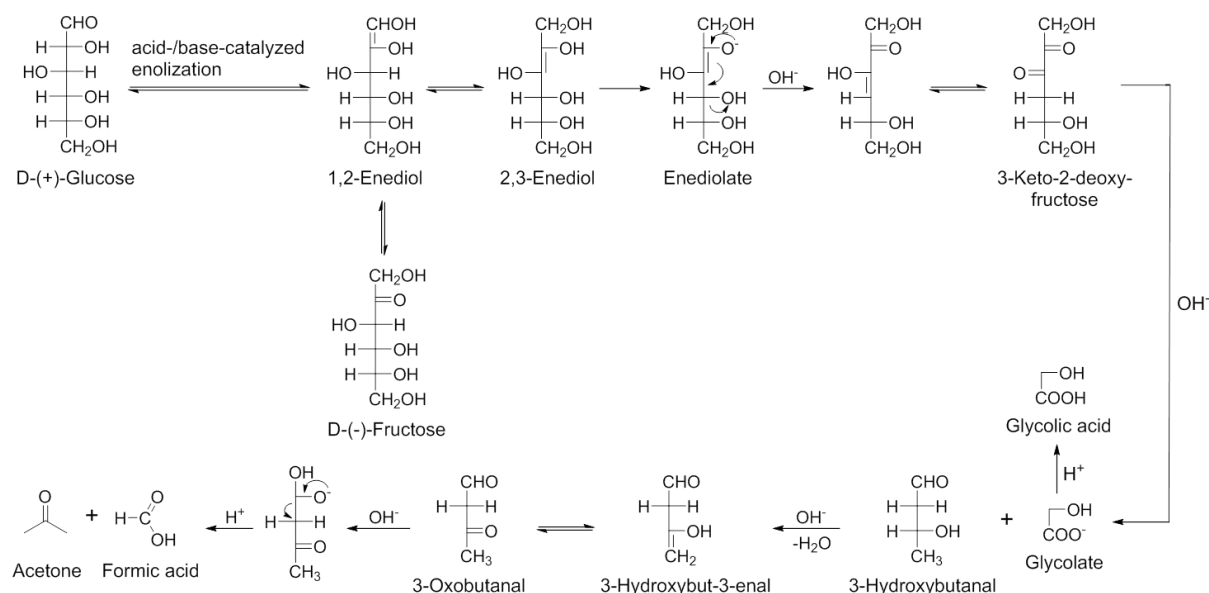


Figure 15: Simplified reaction scheme of the decomposition of glucose in alkaline medium.

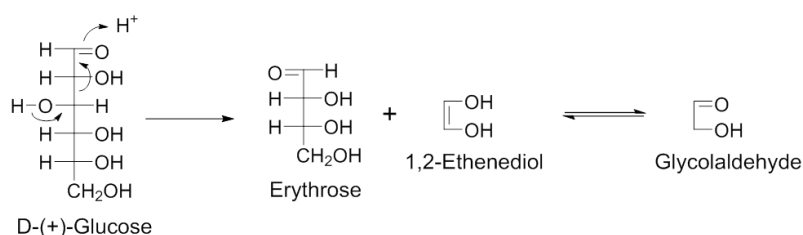
Both acid- and base-catalyzed decomposition processes were observed during hydrothermal synthesis of glucose [120a, 121, 125b]. In alkaline environment, the degradation of hexoses (e.g. glucose) yields in numerous lower molecular weight acidic products of $\leq C_6$ compounds (Figure 14 and Figure 15). C_6 acidic compounds include in particular deoxyaldonic acids (saccharinic acids) [121a, 125b, 127]. By-products such like higher molecular weight acidic compounds of $>C_6$ acids, non-acidic and cyclic unsaturated carbonyl compounds are identified in a less extent, too [121a, 128].

At $pH > 11$, the reaction pathway via HMF is suppressed [121b]. Instead the concentration of lactic acid, acetic acid and acetaldehyde can significantly increase, meaning that the reaction pathway over glyceraldehyde plays an important role in alkaline environment [121b]. Under alkaline conditions main products are glycolic acid and acetone (Figure 15). Glycolaldehyde has also been ascertained as considerable product [121b, 129]. After β -elimination of 2,3-

enediol keto-enol tautomerization can follow, converting into a α -dicarbonyl. It can further react to glycolic acid and 3-hydroxybutanal. Subsequent dehydration, keto-enol tautomerization and retro-aldol fragmentation of 3-hydroxybutanal may form formic acid and acetone ^[121b].

In alkaline conditions, the enolization occurs considerably faster due to the pronounced C-H acidity and the higher availability of the carbonyl groups in the open-chain form. Notwithstanding, the enolization goes through the whole sugar chain. For instance, via 2,3-enediol the psicose can be formed which has effects on all further decomposition reactions because it can lead to undesirable by-products (Figure 13 (b)) ^[125b]. The comparatively easier enolizability can create the conditions for β -elimination reactions. Starting from 1,2-enediol the cleavage of a water molecule leads to the formation of 3-deoxyglucosone (α -dicarbonyl) or 2,3-enediol to the generation of 1-deoxyglucosone (α -dicarbonyl) (Figure 13 (b)). It means the dehydration reactions of all enediol structures might result in α -dicarbonyl compounds which are deoxy sugars ^[125b]. Besides, in alkaline medium the enhanced carbonyl activity triggers fragmentations. Two non-oxidative mechanisms are known, the retro-aldol fragmentation and the hydrolytic β -dicarbonyl fragmentation (Figure 16).

(a) Retro-aldol fragmentation



(b) Hydrolytic β -dicarbonyl fragmentation

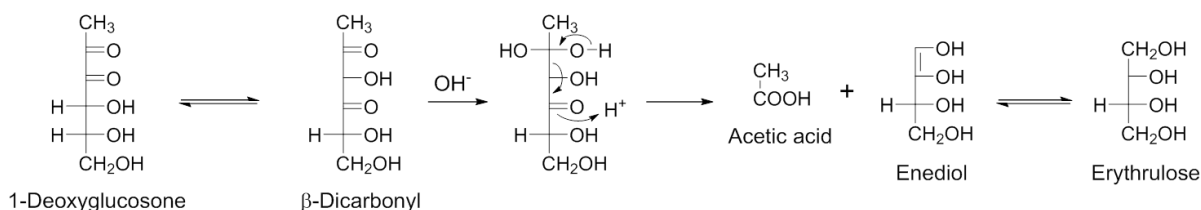


Figure 16: Non-oxidative fragmentation mechanisms in alkaline medium.

Retro-aldol reactions of glucose leads to glycolaldehyde and erythrose via 1,2-enolization (Figure 16 (a)). Those structures with high reductive force such as 1-deoxyglucosone or glucosone are prerequisite for tautomerization of sugars in a β -dicarbonyl structure. After hydratization of the β -dicarbonyl structure the carbonyl group causes the cleavage of the carbon skeleton yielding in acetic acid and erythrulose (Figure 16 (b)) [125b]. Reducing sugars exhibit a strong reducing capacity in alkaline medium. The reason for this is the facile deprotonation from enediols. In enediolates the negative charge is distributed over four centers meaning that the hydroxyl group chelates (Figure 17).

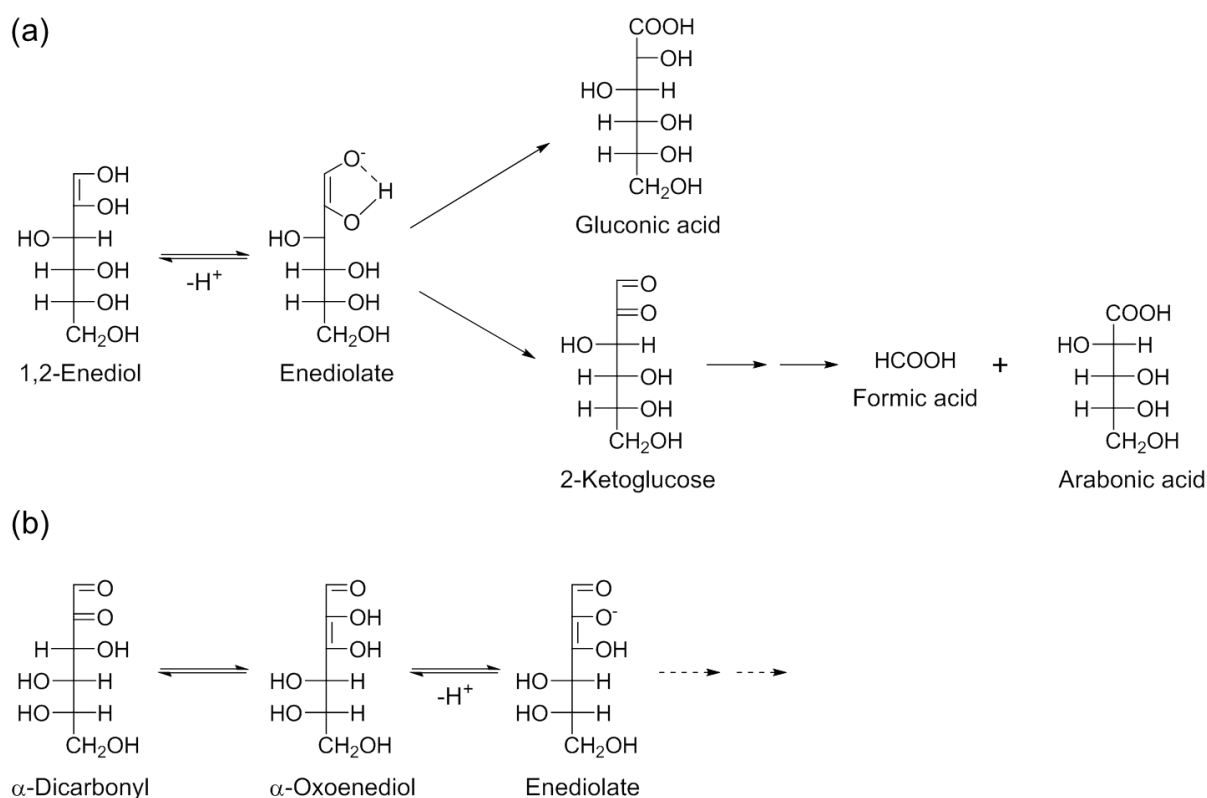


Figure 17: Enediolates and their reducing effect under alkaline conditions.

In fact, enediolates are the reducing species. Depending on the conditions used such as pH or temperature they can lead to oxidation while preserving or fragmenting the carbon skeleton [125b]. In case of working under strong alkaline medium, at $\text{pH} \geq 12$, not only the formation of lactic acid can increase but simultaneously also the production of saccharinic acid and their lactones typically occurs (Figure 18) [121a, 125b, 130]. However, the total amount of $< C_6$

acids decreases such as formic acid, glyceric acid or glycolic acid ^[121a, 129b, 131]. After hydratization of α -dicarbonyl compounds benzoic acid-type rearrangements occur ^[121a, 129b]. Consequently, these rearrangements involve the intramolecular disproportionation of Cannizzaro-type reactions (Figure 18) ^[125b].

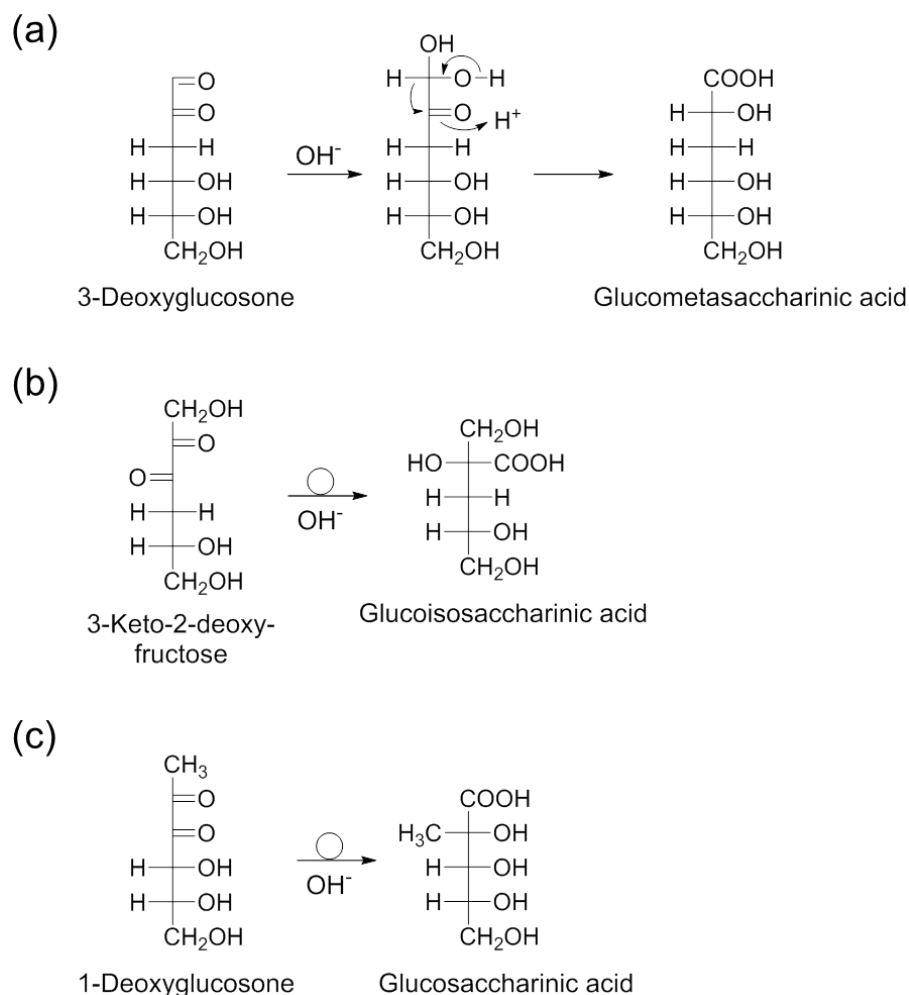


Figure 18: Formation of (a) metasaccharinic acid and (b) saccharinic acid in alkaline environment.

It has to be taken into account that it is not possible to define a certain mechanism for the formation of a nitrogen-containing HTC material due to the complexity of the decomposition process during hydrothermal synthesis ^[124, 132]. Also, plenty of other non-Maillard reaction mechanisms are occurring simultaneously to form N-HTC including Diels-Alder cycloaddition or imino-Diels-Alder, respectively yielding in the formation of heterocycles ^[91d, 124, 133].

Typical reaction mechanisms that may occur involve the Amadori rearrangement of aldoses ^[124, 125b]. It includes the nucleophilic attack of ammonia

on the aldehyde group of glucose to produce an hemiaminal that over dehydration yields in the aldimine (Schiff base ^[134]) (Table 1). Aldimine is in equilibrium with 1,2-enaminol (imine-enamine tautomerism). Keto-enol tautomerism of 1,2-enaminol leads to the aminoketose or so-called Amadori compound ^[124, 135]. Via Heyns rearrangement ketoses (e.g. D-fructose) react in presence of ammonia and over dehydration into ketoimines (Schiff base). Ketoimine is in equilibrium with 1,2-enaminol according to imine-enamine tautomerism. 1,2-Enaminol itself is converted into aminoaldose via keto-enol tautomerism ^[125b]. The Leuckart-Wallach reaction (reductive amination) describes the conversion of an aldehyde or a ketone compound to amine compounds using formic acid as reducing agent ^[136]. The Eschweiler-Clarke reaction can be considered as a special case of the Leuckart-Wallach reaction. The difference is that only formaldehyde is used that leads to a methylated amine compound ^[137]. The Mannich reaction is a condensation process in which formaldehyde, ammonia as well as a α -CH-acidic compound (aldehyde, ketone) react after several steps to the β -amino carbonyl compound (“Mannich base”) over dehydration ^[138]. The “Schotten-Baumann”-type reaction of carboxylic acids in presence ammonia generates ammonium carboxylate compounds. Upon temperature rise and simultaneous dehydration carboxylic acid amides are formed ^[139]. Cyclization reactions are also possible. The Paal-Knorr furan and pyrrole syntheses start from 1,4-diketone compounds in which two different cyclization reaction pathways are possible depending on the pH. Under alkaline conditions, in presence of ammonia, the pyrrole synthesis is preferred ^[140] whereas the furan synthesis occurs under acidic medium ^[141]. Due to its strong reductive force 1-deoxyglucosone are the most reactive Maillard-intermediates.

A plethora of follow-up products can occur like cyclic products. After intramolecular cyclization of 1-deoxyglucosone into a pyran-like compound it reacts after β -elimination into a pyrone compound ^[125b]. Further ring-opening reaction with ammonia and subsequent ring-closing reaction by dehydration the

pyridone compound can be obtained. 1-Deoxyglucosone may also form a furan-type compound after intramolecular cyclization. Dehydration can lead to the intermediate acetylformoine. In presence of ammonia pyrrole compounds are produced following the same ring-opening and ring-closing reactions as aforementioned ^[125b]. Lactones are one of the main products that can be found in alkaline medium ^[121a, 130]. Their formation can be attributed to intramolecular cyclization of saccharinic acids (e.g. glucosaccharinic acid) over dehydration. Lactame compounds can be attained by the reaction with ammonia via ring-opening and ring-closing reactions ^[142]. Pyridine compounds are accessible by the condensation reaction of keto acids or aldehydes with ammonia under high pressure and temperatures in an autoclave (Chichibabin pyridine synthesis) ^[143]. Pyrazine structural motifs can be formed during Strecker degradation. After keto-enol tautomerism to the α -amino carbonyl compound (e.g. Amadori compound), cyclization and oxidation pyrazine compounds can be synthesized, particularly at higher temperatures ^[125b]. This reaction can be assigned to a variant of the Staedel-Rügheimer pyrazine synthesis ^[144].

All in all, the hydrothermal synthesis results in hydrochars with spherical morphology. The carbon spheres are in micrometer size. The growth of the carbon microspheres occurs according to the LaMer model. It describes the formation of monodisperse particles from supersaturated solutions (Figure 19) ^[145].

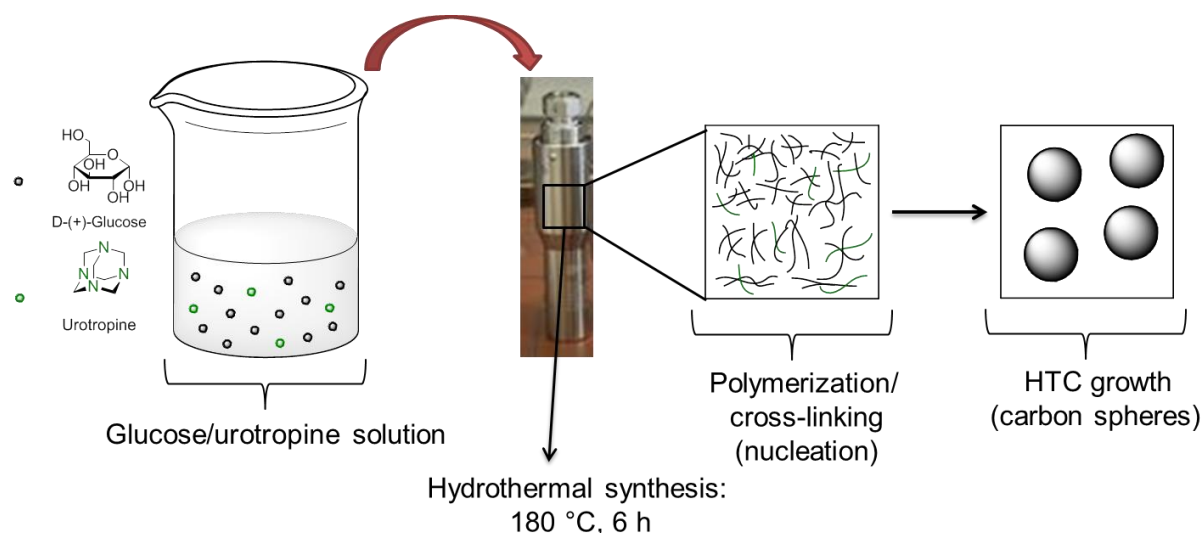


Figure 19: Simplified illustration of the hydrothermal carbon spheres formation process based on glucose and urotropine according to the LaMer model.

When the glucose/urotropine solution reaches a certain concentration (“critical supersaturation”) of both dissolved starting materials, a burst of nucleation takes place. This first nucleation stage occurs homogeneously. Via polymerization and cross-linking processes, first species form nuclei. In the next step, a solid growth phase follows. Herein, further monomer species nucleate heterogeneously in which they aggregate to the existing nuclei forming finally spherically shaped nuclei (spherical particles). These species finally determines the total number of particles as well as their size ^[10, 124, 145]. As the reactions occur in a quite complex manner inside the autoclave, the growth of particles yields in polydisperse and agglomerated spherically shaped particles rather than resulting in monodisperse particles ^[126d]. In literature, pure glucose treated hydrothermally at 180 °C yields in amorphous, nonporous carbon microspheres with a particle size of roughly 200 nm to 1 μm is attained ^[40b, 42b, 124]. Usually, N-containing HTC chars possess larger particle sizes. The change in particle sizes can be attributed to the reactants that have been used as well as the increased complexity of possible reaction pathways by adding urotropine forming a variety of organic compounds as aforementioned in the introduction and elsewhere ^[40b, 124].

Carbon materials of spherical particles were obtained with maximal N-percentage of 19 wt% that exceeds the N-content by far in comparison to other synthesis procedures ^[124]. Our group reported before on the role of synthesis pH on the material properties of the hydrochar in terms of color change, powder density, morphology particle size and specific functionalization ^[41]. Since the addition of N-precursor also increases the synthesis pH, pH-dependent structural changes are also discussed in this work. The liquid supernatant as co-product was investigated for the molecular compounds and its acid-basic character. As mentioned before, some reaction pathways (pyrrol synthesis vs. furan synthesis) occur in preferential pH regimes. Furthermore, the reaction parameters, such as temperature, play a major role on the potential reaction pathways. At high temperatures, different types of reactions occur such as cyclization, imination, amination or condensation reactions in which both crosslinking and N-doping are undergone ^[124]. Consequently, the N-functionalized HTC char includes a variety of functional groups and structural motifs. Particularly with regard to electrochemistry, N-functionalization has beneficial effects. The advantages of N-functionalized carbon materials in the context of electrochemical water splitting will be discussed in the next section.

2.2. Chemical Energy Conversion using N-Functionalized/Doped Carbon-based Electrode Materials – A “Black” Prospect For a Bright Future

Water can be electrochemically split into its elements oxygen (O₂) and hydrogen (H₂) (Figure 20).

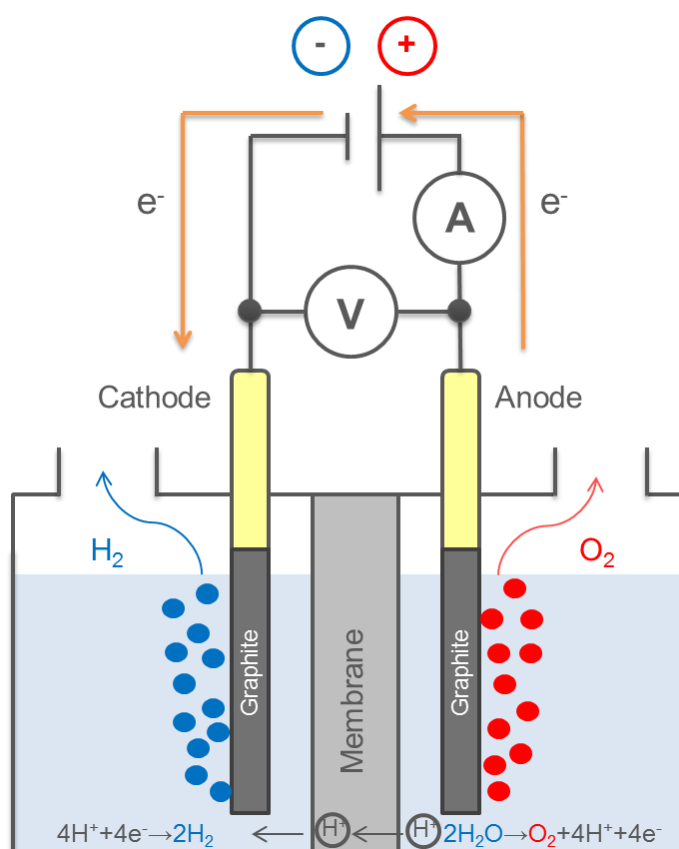
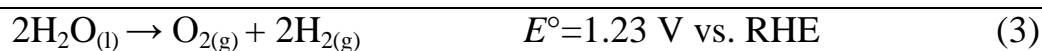
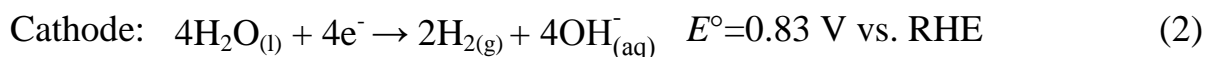
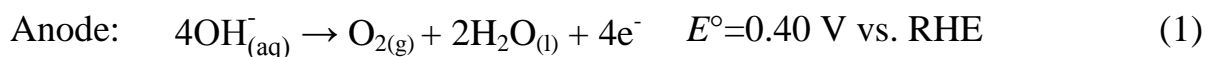
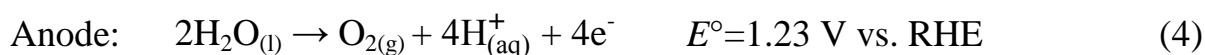


Figure 20: Water electrolysis with direct current in acidic medium.

Electrochemical water splitting occurs by two different half reactions which depend on the pH of the electrolyte ^[146]. On the anode, the half reaction is regarded as water oxidation or oxygen evolution reaction (OER) and on the cathode, the half reaction is considered as hydrogen evolution reaction (HER) ^[146-147]. In alkaline solution (pH=14), the following two electrochemical reactions take place ^[146, 147b]:



and in acidic electrolyte (pH=0) the corresponding electrochemical reactions are [146, 147b].



Hydrogen gas as feedstock is denoted as the most promising and valuable energy carrier for future fuel application since it is lightweight, highly efficient, it burns cleanly and is characterized by its high energy density [147b, 148]. Additionally, hydrogen is a sustainable, “green” energy as it can be generated from renewable sources and is environmentally friendly [148b, 148c, 149]. Hydrogen as alternative energy carrier has the potential to link renewable energy sources and zero-emission energy conversion technologies. It can be formed from renewable energy resources like solar, water, wind and biomass and converted to electricity or fuel directly at the point of use releasing just heat and vapor [150]. One appealing concept is combining electrochemical water splitting devices – the so-called water electrolyzers – with grid scale regenerative energy driven technologies, mainly intermittent energy sources such as wind turbines or solar panels. These would be alternative methods in connection with energy conversion from renewable energy sources (Figure 21) [147b, 151]. Herein, water electrolysis can act as a local energy storage system enabling the realization of these intermittent energy sources on a large and even global scale [147b, 152].

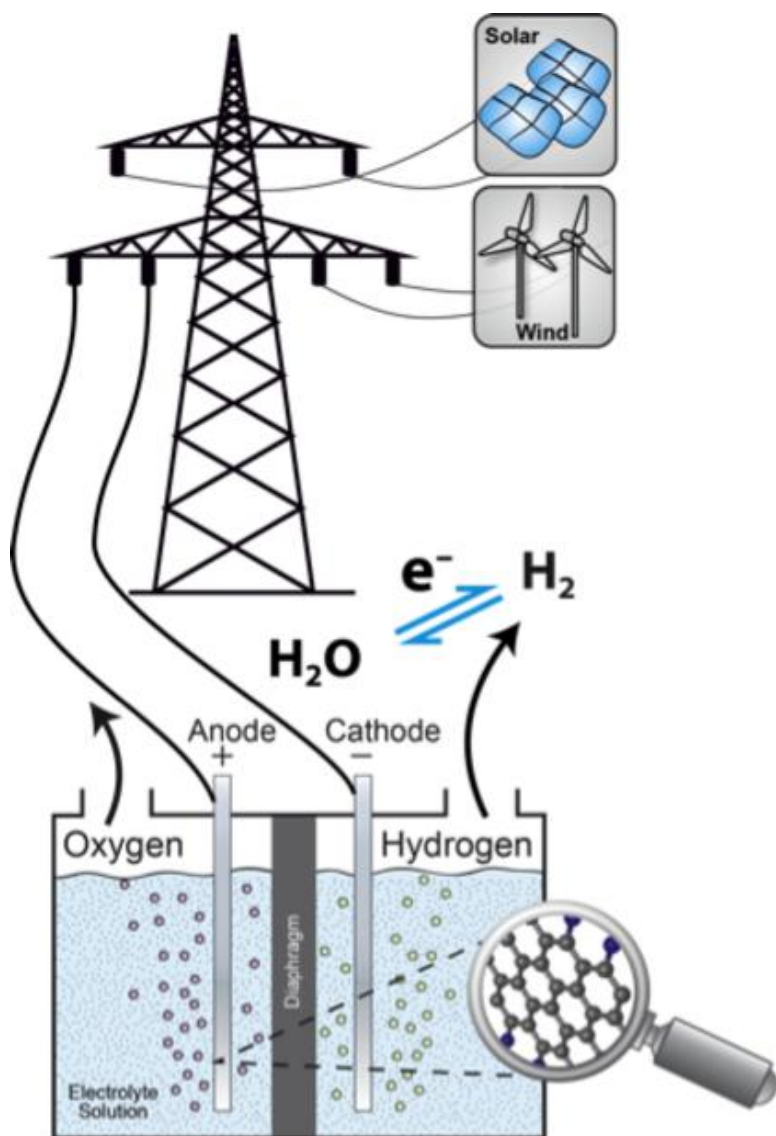


Figure 21: Process of energy conversion from renewable energy sources via water splitting.

Nevertheless, an industrial-scale hydrogen economy based on renewable processes does not exist. It is still produced on a large scale by steam reforming of natural gas meaning the dependence on fossil fuels is so far indispensable and harmful emissions of greenhouse gases (CO, CO₂) are still unavoidable^[147b, 148c]. Apart from that, hydrogen is unsafe and thus neither suitable for storage under mobile applications nor for bulk transportation over long distances^[153]. The efficient storage is fundamental for supporting the “hydrogen economy”. Drawbacks are its costliness, durability, refueling or availability of adequate high-pressure vessels which limits the idea of “hydrogen economy”^[148b].

The electrocatalytic water splitting (water electrolysis) offers one opportunity towards a “green”, clean, renewable, sustainable and in particular economical way to the generation of hydrogen gas ^[147b, 150, 154]. To establish this goal, still a lot of scientific problems need to be tackled. The OER at the anode is a four electron-transfer reaction – whereas the HER at the cathode is only a two-electron-transfer reaction – and thus the most energy-intensive step, which is attributed to higher overpotential, in the electrochemical water splitting process ^[147, 155]. HER can proceed with currents at potentials close to its equilibrium potential (or also referred to as Nernst potential) ^[147b, 156]. Unlike HER, the OER is limited by the large overpotential and necessitates a considerable anodic overpotential to cause measurable current densities ^[147b]. OER requires a higher overpotential to overcome the electrode kinetic barrier of the reaction ^[147]. Due to the slow kinetics of the reaction rates of OER, no water electrolyzer or any other functional electrolysis device can approximate the theoretical minimum operational voltage of 1.23 V ^[147b, 157]. In a similar way, the slow kinetics affect the sensible design of an electrolysis cell ^[147b]. This large anodic overpotential and relating thereto sluggish kinetics are the key points why a practical implementation is so far unprofitable ^[147].

The anode and the cathode themselves are electrocatalysts by favoring charge transfer, facilitating chemical reaction or reducing the activation energy of the electrochemical reaction. Consequently, the key role of the electrocatalyst is to lower the overpotential ^[154]. The function of an electrocatalyst is executed by its electronic structure. In case of HER, transition metals like Ni (electronic configuration: d^8s^2), Pd ($d^{10}s^0$) or Pt ($f^{14}d^9s^1$) depict minimum overpotentials whereas Zn ($d^{10}s^2$), Cd ($d^{10}s^2$) or Hg ($f^{14}d^{10}s^2$) exhibit maximal overpotential values ^[154]. In comparison with the cathode, in the last 50 years intense research has been dedicated to the design, synthesis and characterization of the anode, where the OER takes place to enhance electrode kinetics and stability varying the electrolyte solution ^[147]. Rutile-type precious metal oxides such as RuO₂ and

IrO_2 turned out to be the excellent heterogeneous catalysts for OER catalytic activity in acidic and alkaline electrolytes since they reveal the lowest overpotentials ^[146-147, 158]. In both electrolytes, RuO_2 is unstable at high anodic potential as it oxidizes to RuO_4 and dissolves ^[159]. Similarly, IrO_2 is oxidized as well into IrO_3 and dissolves during OER ^[160]. Comparing both electrocatalysts, IrO_2 is more stable than RuO_2 since it is more resistant against high anodic potential in acidic and acidic media ^[161]. Despite everything, owing to their low earth-abundance, high cost and their poor durability an industrial-scale production is impractical ^[146-147, 162].

Alternative cheap and at the same time excellent non-metal-based OER electrocatalysts for industrial-scale applications is a major concern. Developing highly active and cost-effective electrocatalysts is paramount to perhaps reach future large-scale production ^[163]. One approach is the use of carbon-based materials including carbon black, carbon nanotubes (CNTs), carbon nanofibers (CNFs), graphite, graphene or HTC chars ^[147a, 164]. The introduction of heteroatoms (N, O or S) via doping or functionalization is likely one way to cure the dependence on cost-intensive, exhaustible and scarce natural resources like the just mentioned precious metals (Ru, Ir) because among other beneficial properties they are highly electrically conductive or chemically inert to acidic or alkaline environments ^[147a, 162a]. In the following, main focus lies on the introduction of N as this is the topic of the present thesis.

N-functionalization has long been a natural and widely studied option ^[165]. Recently, main emphasis has been shifted on the sub-stoichiometric regime (e.g. doping) of N-modified carbons ^[165]. This modification is advantageous for the properties of the carbon by accurately tuning the desired electrical, morphological and chemical properties of the N-functionalized carbon network ^[165]. There is evidence that electrochemical and physical properties of carbon materials are very sensitive to doping by heteroatoms (N, B, S and P) into the carbon structure ^[166]. In this respect, metal-free N-containing carbon materials

have attracted interest in a large number of research topics over the past years as alternative to conventional metal-based catalysts due to their abundance, accessibility, low cost, low health risk, excellent reliability, environmental friendliness, high catalytic activity, abundant catalytic sites, high electrocatalytic selectivity, tolerance to poisoning and strong as well as long-term durability^[162b, 163, 164b, 165, 167]. N-containing carbon materials have the potential to replace expensive Pt-based catalyst for fuel cells and metal-air batteries^[168]. Moreover, it could be established for large-scale production and practical application due to its cost effectiveness^[168]. Additionally, the synthesis is conducted under mild preparation conditions^[167h, 167i]. The relatively easy synthesized N-doped carbon materials with proper porosity and good electrical conductivity are highly preferable^[164c]. As in the following, focus lies on graphene-like systems. Two approaches exist to chemically dope graphene; direct “*in situ*” synthesis and post-treatment^[62d, 165]. On the one hand by adsorption of gas, metal or organic molecules onto the graphene surface area and on the other hand by substitutional doping which leads to introduction of heteroatoms into the graphene lattice^[165].

N is the obvious choice for efficient and favorable modification. First of all, N is according to the periodic table of the elements one neighbor away from C and by substituting C with N in the carbon network the total number of electrons can be adapted in each case by one additional electron. Secondly, the atomic radius of N is similar in comparison with C and thus impeding substantial lattice mismatch. Thirdly, N-doping can cause an n-type semiconducting electronic modification to the carbon structure, enabling the possible utilization of these C-N structural networks in several important areas of application such as nanoscience, nanotechnology or nanoelectronics^[165, 169]. All in all, N-doping improves electrical, mechanical and structural properties of the carbon^[170].

Compared to other heteroatoms, N as an electron-donor and non-metallic dopant or functionality has been paid tremendous attention as it is not only cheap, feature competitive electrocatalytic activity, long-term electrochemical

stability as well as high thermal and mechanical stability or intercalation ability [162a, 164c, 167e, 169a, 171] but it also offers the opportunity to dope into different locations within the carbon structure which yields in several configurations [162b, 166d, 172]. The catalytic activity stems from the doping effect of N-atoms which perturbs the electroneutrality of neighboring C-atoms. N induces charge delocalization for adjacent C-atoms due to its strong electron affinity and generates positively charged sites meaning N is more electronegative than carbon and renders adjacent carbon atoms electron deficient [163, 167e, 172-173]. This promotes O₂ adsorption and reduction of O₂ on the carbon surface and occurs at the defect sites within the graphitic (graphene) edges or in the basal plane [163, 172]. Nonetheless, this process primarily happens at “pyridinic” N sites of the carbon edge plane [174]. The larger electronegativity of N also induces polarization in the carbon network and thus influencing the chemical, electronic, magnetic and optical properties of – for instance – graphene [175]. Besides, N can be viewed as n-type dopant because when it substitutes one C-atom in the graphite matrix, N donates its extra electron to the carbon plane [176]. N has one extra valence electron and can therefore modulate the electronic properties to an n-type semiconductor capable to suppress the density of states (DOS) near the Fermi level and shift the Fermi level above the Dirac point which evokes an increase of the band gap [165, 175a]. Simultaneously, N-doping pushes the Fermi level closer to conduction band which makes it more electronically conductive and disordered [67, 165, 171e, 172, 175a]. Adjusting the N-doping level is feasible to tune the electrical properties of a graphitic system (e.g. graphene) [175a, 177]. Likewise, it has been found that the nature of N functionalities is strongly affected by the structure of N-containing precursors and the pyrolysis temperature [164b, 167j, 168, 178]. Pyrolysis not only enhances the stability of the catalyst but also improves the catalytic activity [176, 179]. Hence, a sensible selection of a proper N-source is crucial to improve the catalytic activity [167j]. Due to the comparable atomic radius of nitrogen and carbon, together with five

available electrons in N, meaning three valence electrons (or bonding electrons) and one lone pair (non-bonding pair) permit the occurrence of strong covalent bonds. It has been revealed that the lone pair in the plane of a carbon matrix can increase the electron-donor property of the catalyst. This leads to an increase in the structural stability of N-doped carbons ^[162b, 172, 180]. Moreover, the lone pair can form a delocalized conjugated system with the sp^2 -hybridized carbon framework ^[167e, 181] yielding in significant improvement of the reactivity and electrocatalytic performance of graphene ^[181a]. The incorporation of N into carbon materials can additionally cause electron modulation to provide preferable electronic structures for a number of catalytic processes ^[171d, 182]. In particular, N can dope into carbon structures altering the surface structures and states of a carbon material as the robust carbon framework maintains and most of its intrinsic features ^[62d, 166a-c, 183]. Besides, N-doping into carbon exhibited a profound effect on surface chemical activity, electron-transfer rates and adsorption in redox reactions ^[166b, 166c, 183b-d]. Apart from this, N-doped carbon, as a support of metal particles, is beneficial as it provides nucleation sites for metal nanoparticles on N-adjacent C-atoms and it improves the dispersion and surface area of the metal nanoparticles yielding in good catalytic performances ^[170a, 184]. N-doping gives rise to an atomic-scale structural deformation ^[185], enhances surface wettability ^[164c, 186], conducting, field emission, catalytic or storage properties ^[169a, 187] as well as improves the capacitance of carbon materials with good conductivity and stability under harsh media. This latter characteristic has been taken advantage of multiple battery systems ^[170a, 188]. N-doped carbon shows oxygen reduction reaction (ORR) activity and has been examined as a cathode in fuel cells ^[167e, 170a, 181a, 185, 189]. The physicochemical properties of carbon materials are changed depending on the amount of N-doping ^[170a, 173a, 190]. By raising N-doping, the defect sites in the carbon increases but at the same time the degree of sp^2 -carbon decreases ^[170a, 173a, 190a]. These changes originating from the variations of the amount of N-doping determine the features of a carbon

material like capacitance and electron conductivity ^[170a, 190]. In general, the physicochemical characteristics of carbon materials are improved with increasing the content of N-doping but it should be taken into account an excessive amount of N-doping triggers a collapse in the carbon structure leading to dramatic performance degradation ^[170a, 173a, 190b]. Hence, reasonable amounts of N should be doped into the carbon according to the field of application. Therefore, controlling the amount of N-doping into carbon is a fastidious and critical technology ^[170a]. To summarize, the incorporation of N into a carbon matrix is fundamental to tailor the structural, chemical and electrical properties of the resulting carbon material ^[179a]. At the same time, N is essential to create the active sites necessary for any types of electrocatalytic application ^[191].

As aforementioned, the two main synthesis methods in connection with N-doping can effectively modulate the electronic band structure properties ^[181a, 192] of a carbon lattice (e.g. graphene) which means N-atoms can be doped into the basal plane of a graphitic carbon (graphene) sheet yielding in several bonding configurations ^[162b, 165, 166d, 182]. Their unique electronic properties derive from the conjugation between the N lone-pair electrons and the graphene π system ^[79b, 173b, 174c, 193]. In general, three different types of N-based structural elements are anchored diversely to the carbon matrix (e.g. graphene plane) according to different binding energies throughout XPS studies. These three bonding configurations include “pyridinic” N (sometimes oxidized N in the form of pyridinic oxide is also reported), “graphitic” (or quaternary) N and “pyrrolic” N (Figure 22) ^[165, 166d, 172, 175a, 179a, 181a, 191, 192b, 194]. It has to be mentioned that “graphitic” quaternary N is sometimes also referred to as “edge-valley” N or “bulk-like” N ^[163, 174a].

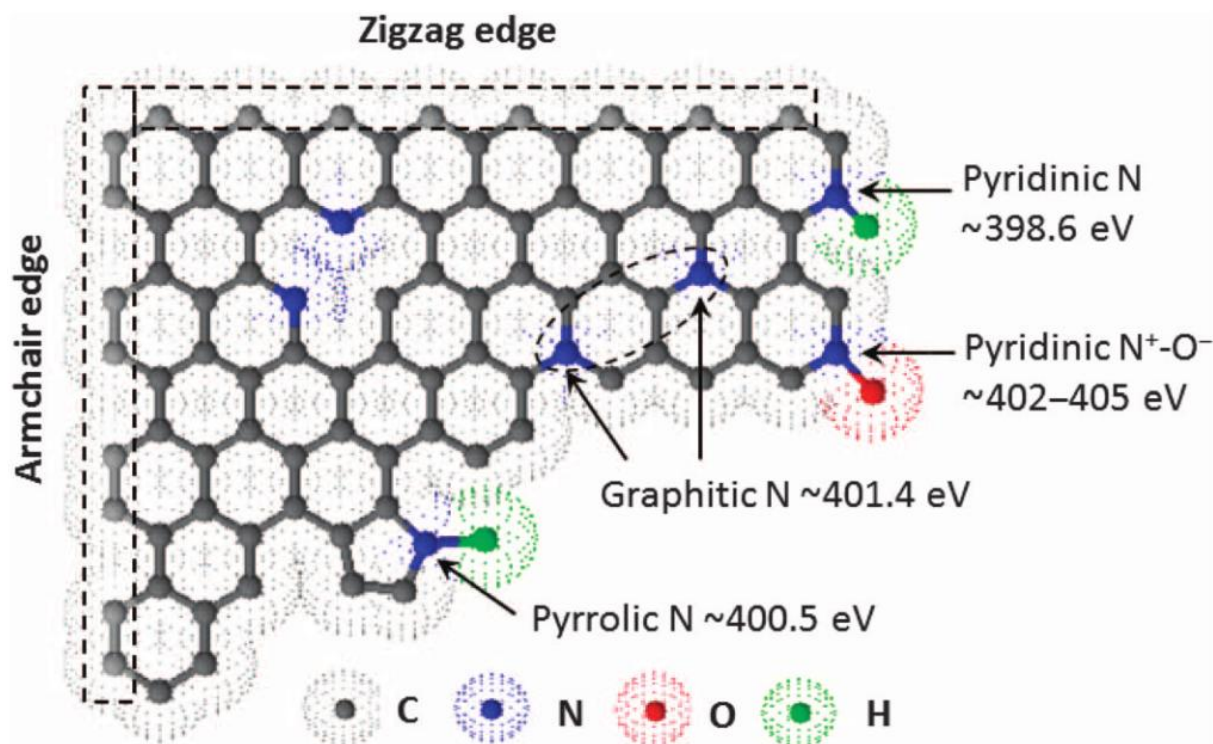


Figure 22: Schematic illustration of an N-doped graphitic carbon (graphene) plane ^[162b].

The ratio of these structural motifs depends on the N-precursor and thermal treatment ^[191]. Moreover, these distinct N-configurations can modify the electronic structure of adjacent carbon atoms and have an impact on physical and chemical properties, involving electrical conductivity and electrocatalytic activity ^[162b, 180]. It is known that the nature of N-functionalities affects the catalytic activity ^[164b]. Therefore, it is very important to achieve high percentage of desirable N-functionalities to optimize materials performance ^[168]. The exact catalytic role of these N-species is discussed controversial and studies show these structural entities to be main responsible for ORR activity ^[162b, 191, 194b] in alkaline ^[167e, 195] and acidic ^[195a, 196] electrolytes. Numerous research groups have claimed that “pyridinic” N is not only predicted to have higher reversible capacity in lithium ion battery by a theoretical study ^[168, 197] or that the localized lone pair of N-atoms are active in base-catalyzed reactions ^[183a, 194f] but would be also the essential active site to facilitate ORR activity ^[162b, 164d, 174b, 174c, 190a, 192a, 195d, 198] whereas other groups proposed that “graphitic” (or quaternary) N is the vital active site to enhance ORR activity of the N-doped carbon materials ^{[162b,}

^{173b, 199]} and – next to it – the most beneficial functionality for enhancing the capacitance of graphene in supercapacitor ^[168, 200]. To reconcile this controversy whether “pyridinic” N or “graphitic” N or even both structural moieties are active sites for ORR it has been suggested a mutual conversion of the “graphitic” N to “pyridinic” N sites (or vice versa) via ring-opening of a cyclic C-N bond ^[162b, 180]. Besides, especially the edge structure and doped N near the edge can substantially improve the ORR activity via the four-electron pathway (see next paragraph) ^[162b, 201]. Apart from that, the armchair and zigzag sites located at the edges with sp^2 hybridization are high energy sites meaning they can be functionalized with heteroatoms, in particular N, contributing to strong electrochemical activities (Figure 22) ^[162b]. Controllable N-doping in a graphene sheet makes graphene an excellent model for investigating the doping effect of “pyridinic” and “graphitic” (or quaternary) N on the physical and chemical features like electron and phonon transport properties, optical characteristics and chemical activity ^[192b, 195b].

Like OER, ORR plays a crucial role in electrochemical energy conversion and storage systems, involving fuel cells and metal air-batteries ^[162b]. It is also the most important reaction in life processes such as biological respiration ^[202]. In fuel cells, at the anode hydrogen oxidation reaction (HOR) occurs in which gaseous H_2 splits into protons and electrons whereas at the cathode, gaseous O_2 reacts with protons and electrons to form H_2O which is rate as ORR ^[175a]. Basically, ORR takes place in both alkaline and acidic electrolyte either via an indirect two-electron transfer process to form hydroperoxide anions (HO_2^-) as intermediate, followed by reduction to OH/H_2O or through the more efficient four-electron transfer which directly produces H_2O (Table 2) ^[162b, 171d, 202].

Table 2: Thermodynamic electrode potentials of ORR in alkaline and acidic media, respectively.

Alkaline electrolyte	$O_{2(g)} + 2H_2O_{(l)} + 4e^- \rightarrow$	(Four-electron	$E^\circ=0.401\text{ V}$	(7)
	$4OH^-_{(aq)}$	process)	vs. SHE	
	$O_{2(g)} + H_2O_{(l)} + 2e^- \rightarrow$		$E^\circ=-0.065\text{ V}$	(8)
$HO^-_{2(aq)} + OH^-_{(aq)}$		vs. SHE		
	$H_2O_{(l)} + HO^-_{2(aq)} + 2e^- \rightarrow$	(Two-electron	$E^\circ=0.867\text{ V}$	(9)
	$3OH^-_{(aq)}$	processes)	vs. SHE	
Acidic electrolyte	$O_{2(g)} + 4H^+_{(aq)} + 4e^- \rightarrow$	(Four-electron	$E^\circ=1.229\text{ V}$	(10)
	$2H_2O_{(l)}$	process)	vs. SHE	
	$O_{2(g)} + 2H^+_{(aq)} + 2e^- \rightarrow$		$E^\circ=0.70\text{ V}$	(11)
$H_2O_{2(l)}$		vs. SHE		
	$H_2O_{2(l)} + 2H^+_{(aq)} + 2e^- \rightarrow$	(Two-electron	$E^\circ=1.76\text{ V}$	(12)
	$2H_2O_{(l)}$	processes)	vs. SHE	

It has been published that the presence of N promotes the ability of e.g. a graphene carbon plane to donate electrons to the neighboring carbon atoms which is advantageous in terms of ORR [175a, 195c]. ORR over N-doped graphene is a four-electron pathway; nevertheless, pure graphene does not have these kind of catalytic activities [195a, 203]. “Pyridinic” N accelerates the ORR via a four-electron pathway whereas “graphitic” (or quaternary) N enhances the indirect reduction of O_2 via a two-electron pathway, through the formation of H_2O_2 [191, 194b]. It can be concluded that the catalytic active sites on the N-doped graphene depend on spin density distribution and atomic charge distribution on the adjacent C-atoms to the N-doping sites [195a, 203].

“Pyridinic” N, which is sp^2 hybridized is bonded to two carbon atoms and located at the edge sites or at defects of the graphene carbon plane. It provides one p electron to the π system of the graphitic layer. Furthermore, “pyridinic” N-

oxides, being also sp^2 hybridized, can be observed in which the N-atom is bonded with one O-atom and two C-atoms. In-plane “graphitic” (or quaternary) N is sp^2 hybridized as well. It can substitute carbon atoms within the hexagonal graphitic network and is capable to donate two p electrons to the π system. Quaternary N can also be located at the edge of the graphene system. “Pyrrolic” N is sp^3 hybridized and contributes two p electrons to the π system into a five-sided ring. The “pyrrolic N” atom in the five-membered ring is thermally unstable since at temperature beyond 800 °C it can be transformed into a “graphitic” (or quaternary) N within the graphene carbon plane [171e, 172, 175a, 191, 194b, 194c, 194f, 204].

Higher surface polarity of N-doped carbon materials was determined unlike carbons without any N-doping [75, 172]. This outcome substantiates N-doped graphitic or graphene layers, for instance during ORR, to reveal faster charge transfer rates than N-free carbon at the electrical double layer which results in a notable increase in the transfer of electrons and protons [166a, 166b, 167e, 172].

These investigations have demonstrated tailoring an electrocatalyst, e.g. a carbon material is an important tool to tune its structure-property relationship and hence enhance its activity for the ORR relative to undoped carbons [172]. To conclude briefly, N-doping is an effective way to tailor the properties of carbon and tune the N-containing carbon material for distinct applications of interest [165].

Within this work, electrochemical water splitting measurements are an integral part. These electrocatalytic measurements are carried out in a standard three electrode cell (Figure 23).

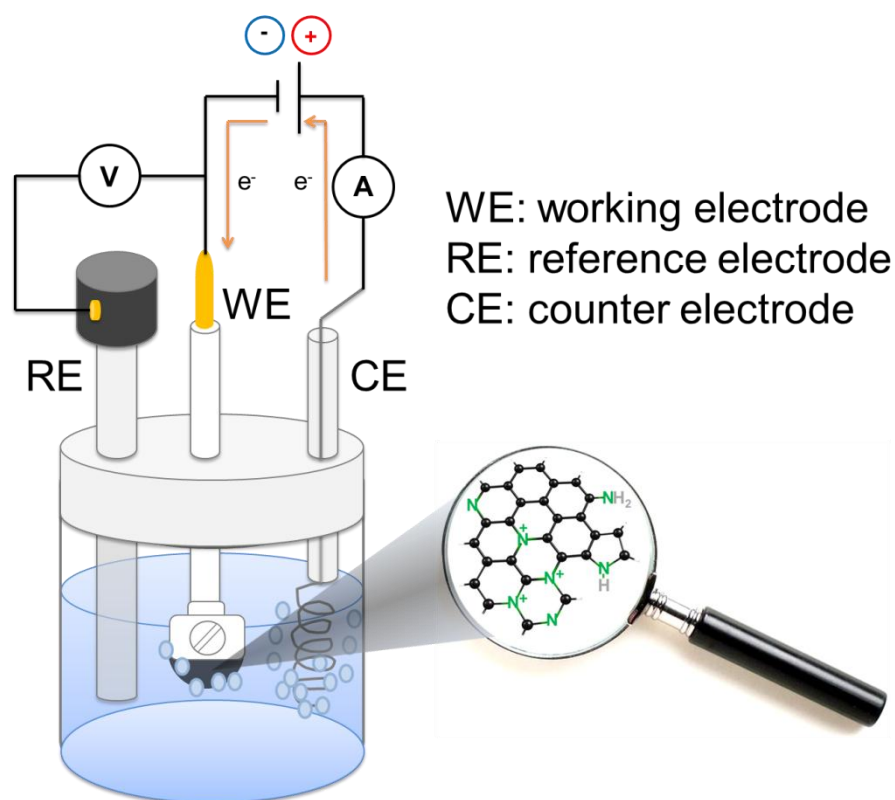


Figure 23: Schematic representation of the standard three electrode cell used for electrocatalytic water splitting measurements.

The whole apparatus will be discussed in detail in the next chapter of this thesis. Briefly, a cleverly devised standard protocol had to be prepared at first. Apart from this, a few optimizations needed to be done in order to guarantee a proper function of this cell. Taken as a whole, the executed optimizations were indispensable to facilitate reproducible measurements and data.

3. APPLIED CHARACTERIZATION METHODS

The liquid supernatant was analyzed by HPLC using an Agilent 1200 Series over an ion-exchange column based on styrene divinyl benzene (REZEX™, RHM-Monosaccharide, 80 °C, injection volume: 5 µL, 0.6 mL·min⁻¹, eluent: 0.005 M H₂SO₄). The measurements were automatically operated by the Agilent ChemStation software. Compounds with a more basic behavior such as ammonia or amine compounds cannot be detected by the HPLC column.

Potentiometric pH determination measurements from liquid supernatant were performed with a METTLER TOLEDO Titration Excellence T50 with a universal electrode METTLER TOLEDO DG 115-SC (reference: ARGENTHAL TM, 0–100 °C, 0–14 pH) for 60 s each measurement. A LabX light titration software v3.1 was used for operating automatically the pH determination.

In situ UV-visible diffuse reflectance (UV-VIS-NIR) spectra were measured on a Cary Model 5000 spectrometer (Agilent) equipped with a Harrick Praying Mantis diffuse reflectance attachment (Model DRP-P72) and a solid-state *in situ* sample holder. Spectralon[®] was used as a white standard. Spectra were taken in the range 200–2500 nm with a step size of 0.5 nm every 0.1 s (scan rate: 300 nm·min⁻¹) during the treatment of N-HTCs. The NIR region was measured with a step size of 1 nm every 0.1 s (scan rate: 600 nm·min⁻¹). Results were presented in the Kubelka–Munk function ($F(R_{\infty})$) and Tauc function ($(F(R_{\infty})) \cdot h\nu$)^{1/2} calculated from recorded reflectance data

The samples were characterized by a Thermo Scientific[®] Nicolet iS50 FTIR spectrometer using a monolithic diamond ATR crystal. In order to obtain a reasonable S/N ratio the samples were measured with 16 scans and a resolution of 4 cm⁻¹.

The elemental analysis was carried out by the external microanalytical laboratory Kolbe (Mikrolab Kolbe, Höhenweg 17, 45470 Mülheim an der Ruhr, Germany), using a Vario EL CHNOS-Analyzer from elementar company.

Raman spectra were recorded by a Thermo Scientific[®] DXR Raman Microscope with a 50x magnification and a 532 nm laser with a laser power in the range of 0.5–1.0 mW. The samples were measured within 2 s and an exposure rate of 20. For pyrolyzed HTCs, spectra were recorded with 50x magnification and a 532 nm laser applying a laser power in the range of 3.0–4.0 mW. At the same time, the scan rate has been adjusted by decreasing the value to 10 s with an exposure rate of 2 in order to avoid visual beam damage.

Scanning electron microscopy (SEM) micrographs were taken with a Hitachi S-4800 Field Emission Scanning Electron Microscope, working between 0.1–30 kV.

For (high-resolution) transmission electron microscopy [(HR)TEM] investigations a FEI TITAN 80-300 was used, working at acceleration voltages of 80, 200, 300 kV. A JEOL JEM-ARM200F was also applied, working at acceleration voltages of 80, 200 kV.

Thermogravimetric-mass spectrometric analyses (TG-MS) were performed at the NETZSCH STA 449 F3 Jupiter[®] thermobalance setup connected to a quadrupole mass spectrometer NETZSCH QMS 403 C Aëolos[®]. The sample was heated in Ar atmosphere with a constant gas flow of 50 mL·min⁻¹ in a temperature range of 40–1000 °C. For measurements, a temperature program with several isothermal steps was developed to separate the thermal decomposition events of the distinct functional groups. A heating rate of 20 K·min⁻¹ was chosen in order to enable good peak separation and to avoid any effect of overheating. The corundum crucibles were filled with 14 mg for the measurements. Only the N-free HTC was filled with another mass. Due to the low powder density the crucible was filled to the brim with 8 mg of the N-free HTC.

Solid acid-base potentiometric titrations were conducted using a METTLER TOLEDO Titration Excellence T50 with a burette DV1020 dosing 1 μL of standard solutions (acid or base) including an error margin of 0.2 %. A universal electrode METTLER TOLEDO DG 115-SC (reference: ARGENTHAL TM, 0–100 $^{\circ}\text{C}$, 0–14 pH) recorded the pH automatically. A LabX light titration software v3.1 was used for running automatically the potentiometric titration. At first, 100 mg of hydrothermal carbon material was dispersed in 100 mL of 0.001 M KCl solution and stirred overnight. The HTC sample was then titrated with 20 mL of 0.01 M HCl solution. Afterwards, the acidified solutions were titrated with 0.01 M NaOH solution.

N_2 sorption experiments were recorded with an Autosorb 6-MP (Quantachrome) at 77 K. The samples were outgassed between 7.5 h and 10.5 h at 120 $^{\circ}\text{C}$. The data were evaluated according to BET theory.

The X-ray diffraction (XRD) measurements were performed in Bragg-Brentano geometry on a Bruker AXS D8 Advance II theta/theta diffractometer, using Ni-filtered Cu $K_{\alpha 1}$ radiation and a position sensitive energy dispersive LynxEye silicon strip detector. The sample powder was filled into the recess of a cup-shaped sample holder, the surface of the powder bed being flush with the sample holder edge (front loading).

Zeta potential measurements were carried out by a ZetaPALS90 analyzer from Brookhaven Instruments Corporation, provided with an autotitrator. The phase analysis light scattering (PALS) is considerably more sensitive towards the electrophoretic light scattering (ELS) method that is measured by the conventional laser Doppler frequency shift. The PALS technique is able to detect the velocity of the moved particles 100 times lower than the traditional ELS method. Hence, a higher precision is achieved to record the electrophoretic mobility (EPM). The phase shift was measured by a 639 nm laser. The current of the cell was automatically adjusted to approximately 2 mA. 2 mg of hydrothermal carbon material was dispersed in 20 mL of distilled water in an

ultra-sonic bath for 10 min. In order to separate large particles the dispersion was filtered with a 0.22 μm Rotilabo[®]-syringe filter (PVDF, unsterile). The hydrothermal carbon materials were analyzed within a pH range of 3.2 to 10.2 adjusted by drops of 0.1 M KOH as well as 20 mM HNO₃ and 1 mM HNO₃, respectively

To simulate the fundamental IR transitions of various model structures, geometry optimization as well as subsequent harmonic vibrational analysis was performed by means of density functional theory (DFT) [205] employing the B3LYP [206] functional in conjunction with the def2-TZVP basis set [207]. D3 dispersion correction by Grimme [208] with Becke–Johnson (BJ) damping [209] was used in all computations. Additionally, the RIJCOSX [210] approximation with corresponding auxiliary basis set [211] was applied. Computed harmonic vibrational frequencies were scaled by 0.97 to take into account anharmonicity. Because of the satisfactory agreement between experimental and scaled theoretical infrared spectrum of furan the scaling factor of 0.97 has been applied to other calculated vibrational spectra. Tight criteria were used for geometry optimization and SCF convergence. All calculations based on model compounds were performed using the ORCA-4.0 suite of programs [212]. The visualization of the molecular structures and the Lorentzian band broadening for calculated spectra were prepared using ChemCraft (version 1.7, programming: G. A. Zhurko; design, additional support: D. A. Zhurko; <https://www.chemcraftprog.com>) with ca. 14 a.u. of band width at $\frac{1}{2}$ height.

All NMR experiments were performed on a Bruker Avance III HD 400 MHz spectrometer with a 1.3 mm double resonance MAS probe. The spinning frequency was 15 kHz for all the cross polarization (CP) experiments. For the single pulse 1D experiments on ¹H and ¹³C, excitation $\pi/2$ -pulses of 1.5 μs at 15 W and 70 W ($v_{\text{RF}}=166$ kHz) with relaxation delays of 5 s and 250 s were used, respectively. Ramped CP experiments with ¹H decoupling were able to achieve HH-matching with the same power levels as in the 1D experiments. The

number of accumulations was 8 and 128 for ^1H and ^{13}C , respectively. ^{15}N CP experiments were performed at a spinning frequency of 30 kHz, using 60 W of power and 2048 scans for sample 2 (G:Uro=1:0.17) and 9400 scans for sample 3 (G:Uro=1:4) with a delay of 5 s each.

^{13}C DP measurements were conducted applying 128 scans at a spinning frequency of 50 kHz in order to remove spinning side bands from the spectral region. The delay was set to 250 s to ensure complete relaxation.

^{13}C 2D SQ–DQ correlation experiments were performed utilizing the SC14 symmetry based sequence ^[125a] with simultaneous CP ^[125a]. The power level requirement was met using ^1H and ^{13}C RF fields of approximately 52 kHz and 100 kHz respectively. An additional Lee–Goldburg offset on the ^1H channel was used to avoid HH contact during DQ-generation and reconversion. Optimum signal was achieved by using 14 SC14 composite cycles for excitation and reconversion. Furthermore, 4096 and 128 points were used for the direct and indirect dimensions, respectively, and the number of accumulations was 400.

Both ^1H and ^{13}C chemical shifts were referenced to adamantane ($\geq 99\%$).

Electrical conductivity measurements of the carbonaceous disc electrodes were performed using the van der Pauw Method which is a four point probe measurement method. It was conducted on an ohmmeter (HIOKI 3541 RESISTANCE HiTESTER, Nagano, Japan) that is used for small resistances. The received resistivity values were converted to conductivity values.

4. RESULTS AND DISCUSSION

4.1. Hydrothermal Synthesis of N-Functionalized HTC Chars

All chemicals were of analytical grade. D-(+)-Glucose ($\geq 99.5\%$, GC) was purchased from Sigma Aldrich (Steinheim am Albuch, Germany). Hexamethylenetetramine ($\geq 99\%$) has been supplied by Carl Roth Chemicals GmbH (Karlsruhe, Germany).

In a series of experiment, pure glucose (20 wt%, 7.71 g, 42.8 mmol) and a mixture of glucose and urotropine were synthesized. In a first row, only the mass fraction of glucose was changed whereas the mass fraction of urotropine was kept constant. Glucose (20 wt%, 7.71 g, 42.8 mmol, 1 eq.) and urotropine (3 wt%, 1 g, 7.13 mmol, 0.17 eq.) as well as molar ratios of glucose to urotropine (G:Uro) of 1:0.2, 1:0.25, 1:0.33, 1:0.5 and 1:1 were synthesized. Additionally, in a second systematic row of experiments, only the mass fraction of urotropine was varied and the mass fraction of glucose was kept constant. Glucose (3 wt%, 1 g, 5.55 mmol, 1 eq.) and urotropine (4 wt%, 1.17 g, 8.33 mmol, 1.5 eq.), as well as molar ratios of glucose to urotropine (G:Uro) of 1:2, 1:3 and 1:4 were prepared. The starting materials were dissolved in distilled water (30 mL), respectively after intense stirring. The reaction mixtures were added into Teflon lined stainless steel autoclaves (50 mL volume). The autoclaves were then placed in a programmable laboratory oven preheated to 180 °C. After 6 h of reaction time, the autoclaves were cooled down to room temperature. After opening the autoclaves the supernatants were gently collected separately for further analyses. The HTC materials were removed from the autoclaves and recovered by filtration washing several times with distilled water until the filtrate got colorless. The filter cakes were dried in a heating stove at

100 °C overnight. In an agate mortar, the HTC materials were finally ground into powder materials.

Carbon materials of spherical particles are obtained with maximal N-percentage of 19 wt%, which by far exceeds the N-content in comparison to other synthesis procedures ^[124]. Our group reported before on the role of synthesis pH on the material properties of the hydrothermal carbon material in terms of specific functionalization, powder density, morphology, particle size and color change ^[41]. Since the addition of N-precursor also increases the synthesis pH, in this work pH-dependent structural changes are discussed. The liquid supernatant as by-product was investigated regarding the molecular compounds and its acid–base character. As mentioned before, some reaction pathways (pyrrol synthesis vs. furan synthesis) occur in preferential pH regimes. Furthermore, the reaction parameters, such as temperature, play a major role on the potential reaction pathways. At high temperatures applied for the preferential production of carbonaceous products, inevitably, multiple types of reactions occur simultaneously such as cyclization, imination, amination or condensation reactions in which both crosslinking and N-doping occur ^[124]. Since polyfuran or polypyrrole groups are prominent structural entities, further information of structural motifs and their properties were obtained by electronic structure calculations of model systems. Two systematic series of hydrothermal carbon materials were synthesized in autoclaves from pure glucose and from a mixture of glucose and urotropine at different molar ratios (G:Uro). In the first series, only the concentration of glucose was modified whereas the amount of urotropine was kept unchanged. Molar ratios of G:Uro of 1:0.17, 1:0.2, 1:0.25, 1:0.33, 1:0.5 and 1:1 were prepared. In the second series, only the mass fraction of urotropine was changed and the content of glucose was kept constant. Molar ratios of G:Uro of 1:2, 1:3 and 1:4 were synthesized. The glucose/urotropine reaction solutions before hydrothermal treatment as well as the colored liquid supernatants obtained after hydrothermal synthesis were tested for their pH

(Figure 24). Likewise, the C:N and C:H ratios as functions of N-content were determined.

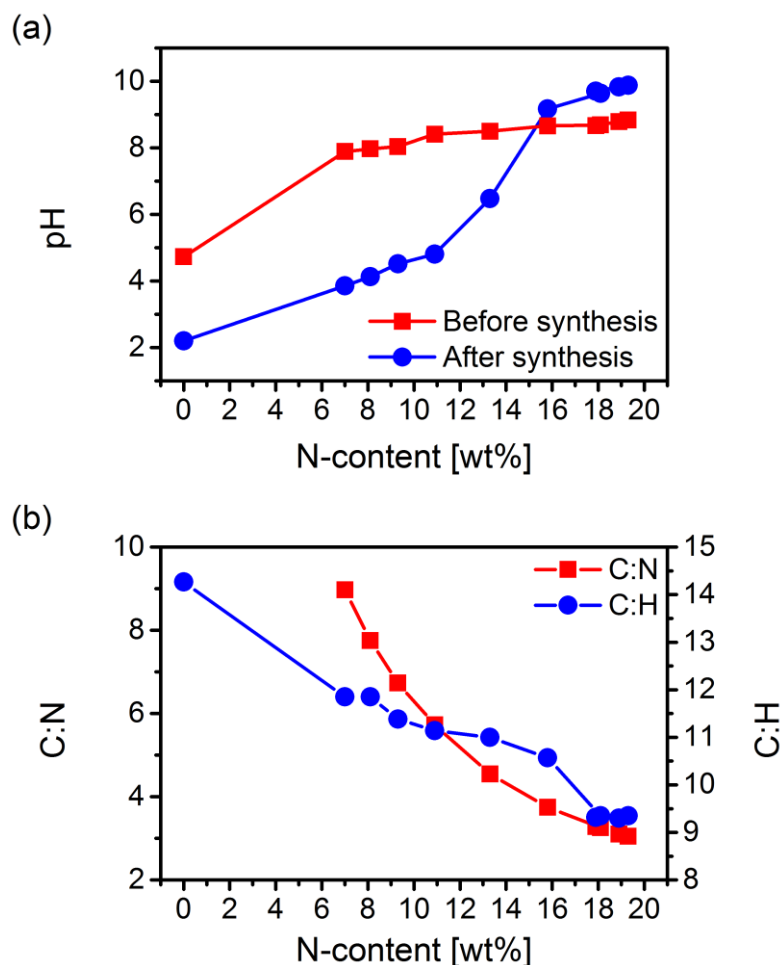


Figure 24: (a) pH values of the liquid supernatant of the glucose/urotropine reaction solution before and after hydrothermal synthesis. The pH values are plotted against the molar ratio of urotropine normalized to glucose. (b) C:N as well as C:H ratio as a function of the N-content.

The pH values of the initial solutions increase slightly with increasing urotropine concentrations from around pH 8 up to pH 9 in comparison to the pure glucose solution that has a pH of around 5. On the other hand the pH values after synthesis, determined by rehydration products of HMF such as levulinic acid, formic acid and acetic acid, show a drastic drop at the pivot point where the glucose to urotropine ratio reverses (Figure 24 (a)). Consequently, other reaction pathways and carbon formation processes take place. The C:N and C:H ratios decrease considerably with higher N-content (Figure 24 (b)). The N-HTCs showed color variations depending on the molar ratio of glucose to urotropine (Table 3).

Table 3: Color change from brown to black of N-HTC materials with increasing molar ratio of glucose to urotropine.

HTC sample	Color
G:Uro=1:0	 Brown
G:Uro=1:0.17-1:0.5	 Black
G:Uro=1:1-1:2	 Dark brown
G:Uro=1:3-1:4	 Brown

Briefly, for samples with a brown to dark brown color (G:Uro=1:4–1:1) similar C:N values of 3.7–3.1 and C:H values of 10.6–9.3 are obtained. There is a turning point when the sample starts to get black (G:Uro=1:0.5). At this point, not only the C:N and C:H ratios start to increase but also the pH value becomes more acidic. N-free HTC shows an acidic pH of 2.2 and, at the same time, exhibits quite a high C:H ratio with a value of 14.3. At lower pH values when the HTC material starts to turn from brown into black it changes to a more extensive degree of internal condensation of the polymeric carbonaceous network, and therefore an increasing amount of cross-linking bonds are observed. This phenomenon was observed before in the context of initial synthesis pH studies of HTC materials ^[41].

4.2. UV/VIS Spectroscopy

The materials synthesized at high urotropine mass fractions (G:Uro=1:4–1:3) reveal a brown color that turn into a dark brownish shade (G:Uro=1:2–1:1) until they completely become black (G:Uro=1:0.5–1:0.17). Nevertheless, a pure HTC material (G:Uro=1:0) depicts a brown color. Four of these colorful N-HTCs (G:Uro=1:1, G:Uro=1:1.5, G:Uro=1:3–1:4) were subjected to UV/VIS spectroscopic measurements (Figure 26-Figure 28).

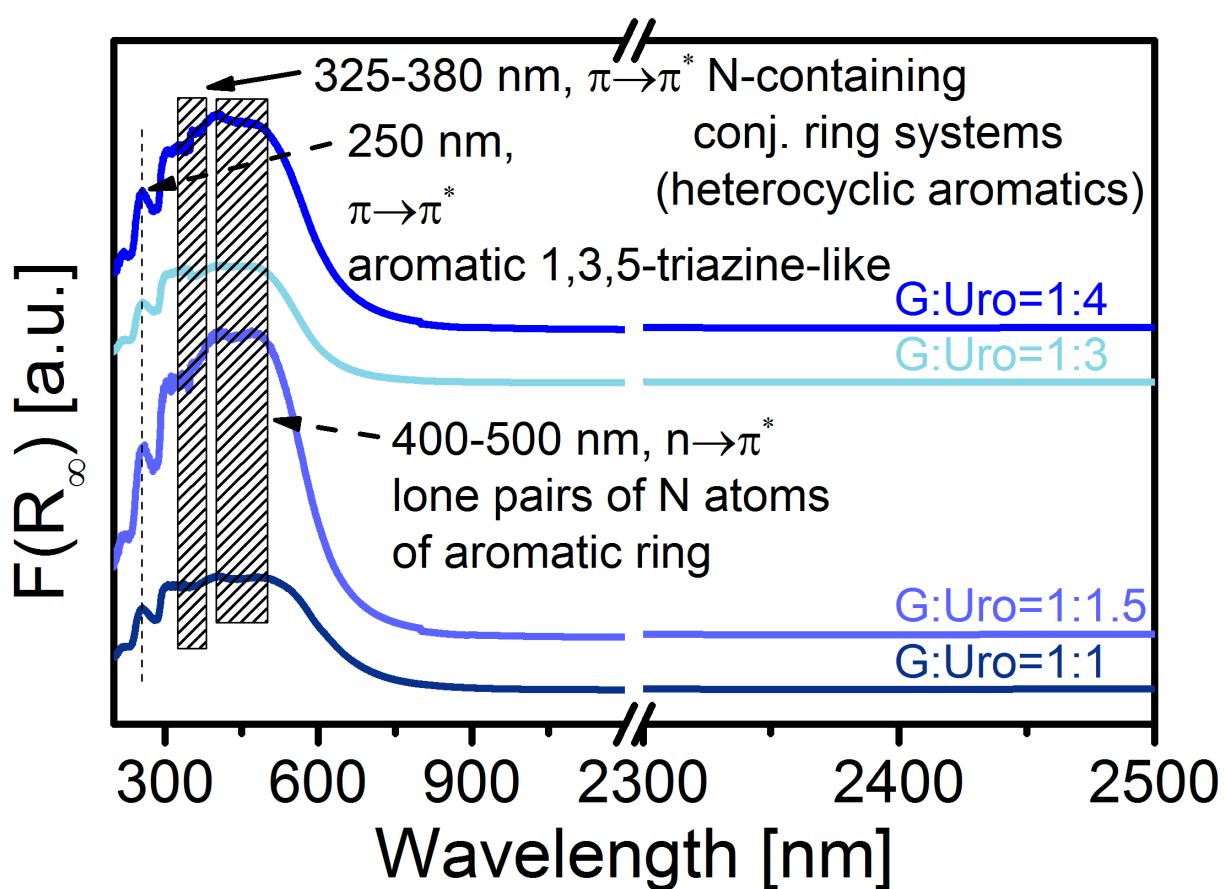


Figure 25: UV/VIS spectra of N-HTCs in the wavelength region of 200-2500 nm recalculated to Kubelka-Munk units.

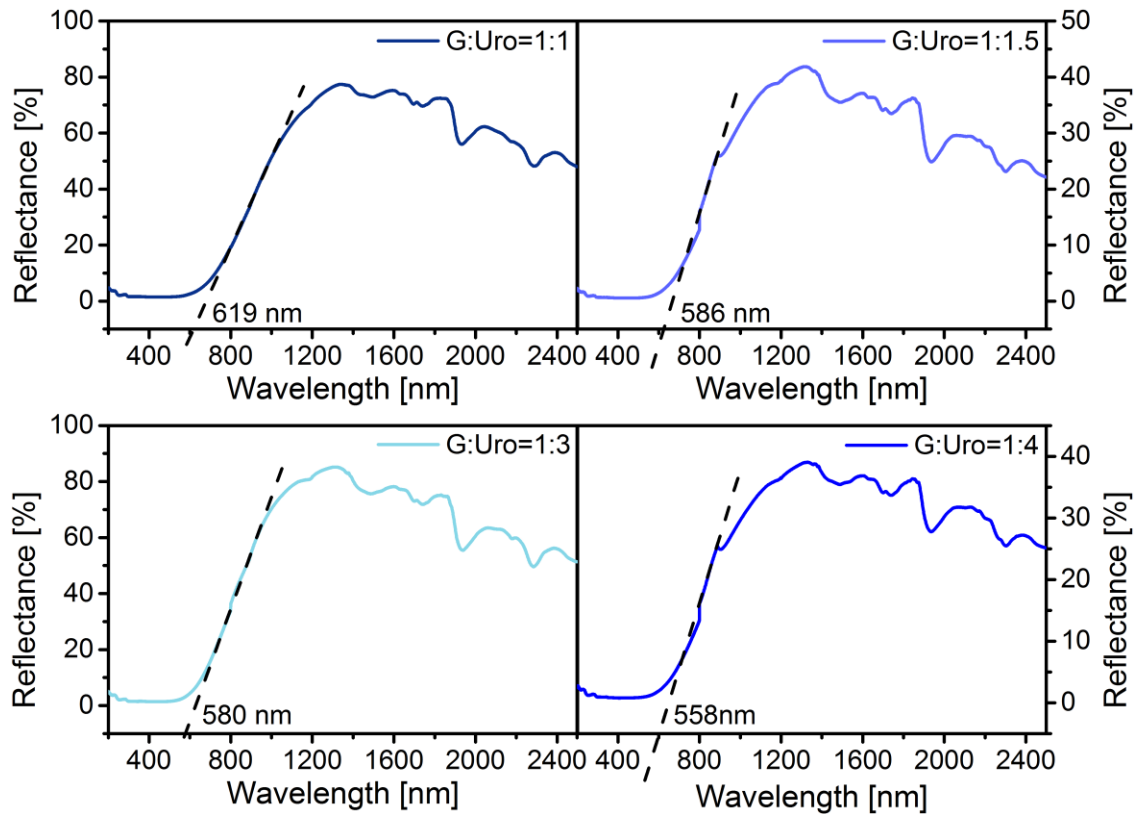


Figure 26: UV/VIS spectra of N-HTCs in the range of 200-2500 nm. By means of a regression line (tangent) on the turning point of the curves allows to determine the value of the wavelength on the point of intersection of the x-axis.

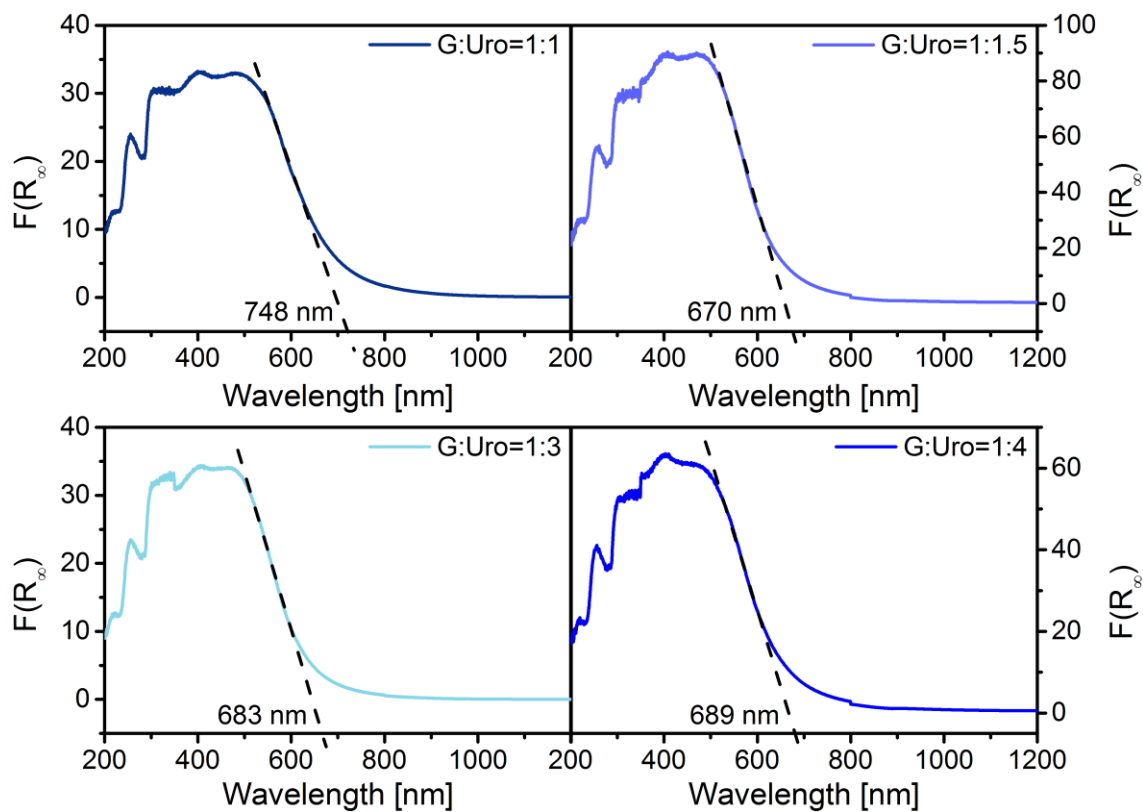


Figure 27: UV/VIS spectra of N-HTCs in the wavelength range of 200-1200 nm recalculated to Kubelka-Munk units. By means of a regression line (tangent) on the turning point of the curves allows to determine the value of the wavelength on the point of intersection of the x-axis.

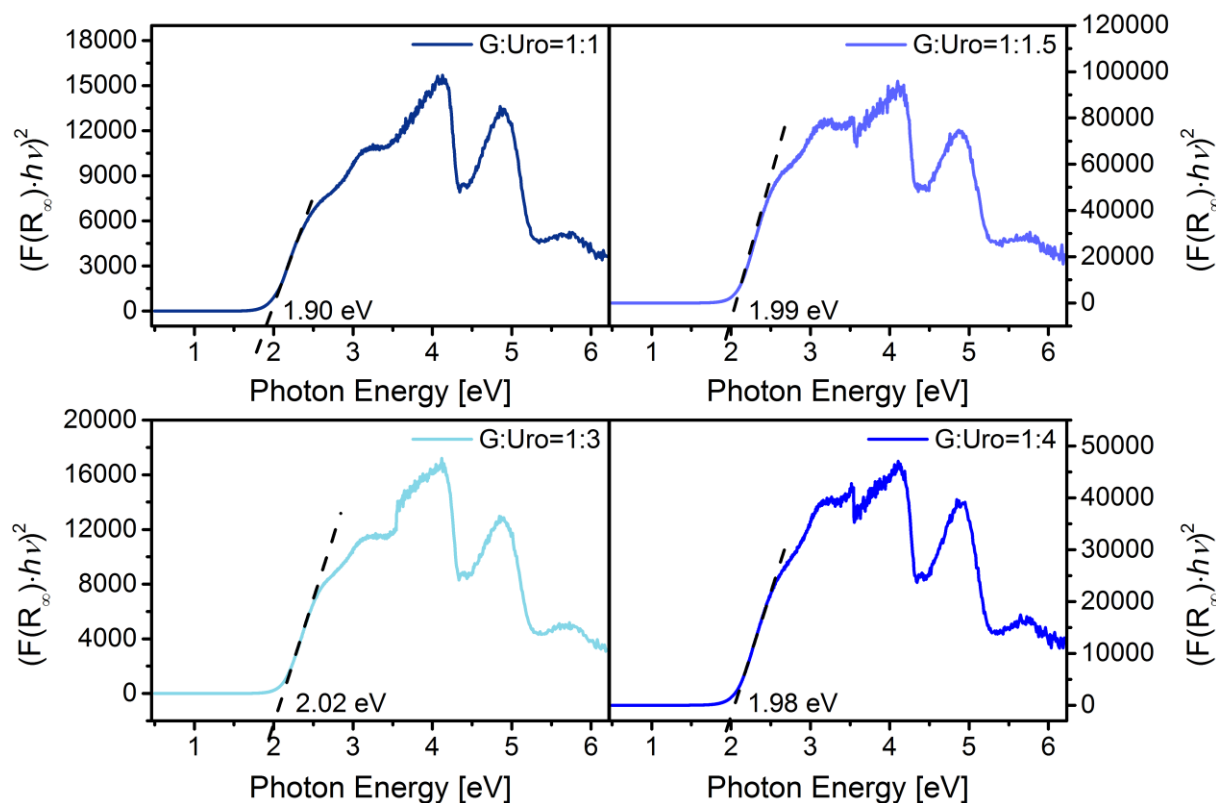


Figure 28: Tauc plots as a function of photon energy recalculated from UV/VIS spectra of N-HTCs. By means of a regression line (tangent) on the turning point of the curves allows to determine the value of the photon energy on the point of intersection of the x-axis.

The UV/VIS spectra of N-HTCs illustrate a maximum between 325–380 nm (Figure 25) in the blue to violet-UV region of the electromagnetic spectrum, resembling a semiconductor bandgap in the region 2.0–2.2 eV (Figure 26) ^[213]. In contrast, graphitic carbon nitride (g-C₃N₄) has a bandgap of approximately 2.7 eV ^[214]. Applying Kubelka–Munk functions and Tauc plots, similar intrinsic band gaps are obtained ranging between 1.7–1.8 eV (Figure 27) and 1.9–2.0 eV (Figure 28), respectively. In each case, the N-HTC with lowest N-content exhibits lowest band gap and with raising N-content the band gap increases, which suggests a trend that the higher the N-content the brighter the color of the N-HTC and the larger the band gap. Increasing the N-content to 19 wt% evoked the absorption edge to shift to slightly shorter wavelength. The additional absorption band around 400–500 nm underlines the feature of the N-HTCs to absorb wavelengths in the visible range ^[213a]. The absorption band at 250 nm can be ascribed to $\pi \rightarrow \pi^*$ electronic transition in an aromatic 1,3,5-triazine-like

compound [213b, 215]. However, this statement and the following interpretations should be treated with caution since the assignments refer to $g\text{-C}_3\text{N}_4$ [213, 215]. The intense band at 325–380 nm can be attributed to $\pi \rightarrow \pi^*$ transitions present in N-containing conjugated aromatic ring systems, e.g. heterocyclic aromatics [213]. Around 400–500 nm, the absorption band can be assigned to $n \rightarrow \pi^*$ transitions including lone pairs of N atoms of aromatic rings [213, 215c].

4.3. High-Performance Liquid Chromatography (HPLC)

HPLC measurements confirm the presence of fructose, HMF, as well as levulinic and formic acid (Figure 29).

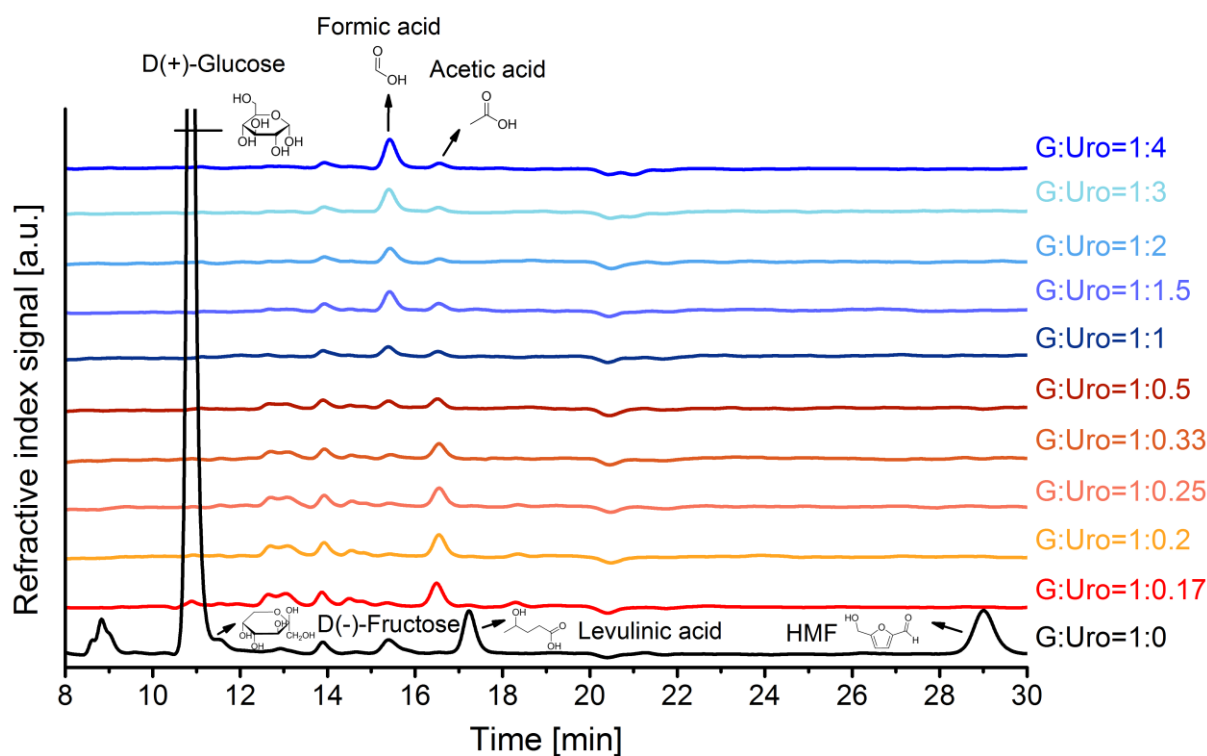


Figure 29: HPLC measurements on dark brown supernatant liquid after hydrothermal synthesis of glucose and urotropine.

Increasing amounts of formic acid and decreasing concentrations of acetic acid can be observed with rising urotropine amount, as depicted in Figure 30.

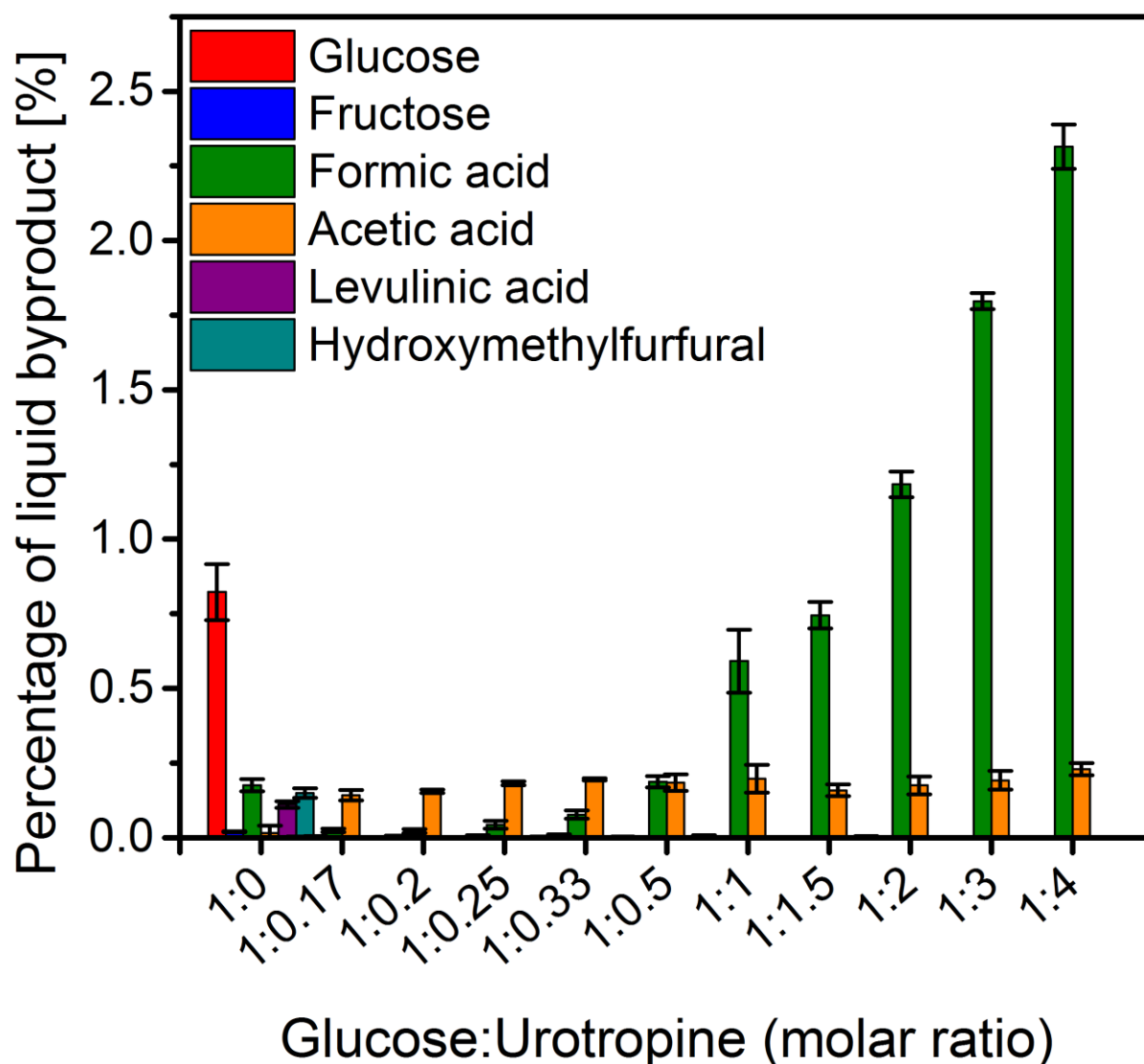


Figure 30: Percentage of liquid byproducts in the supernatant, normalized to initial glucose concentration, as a function of the molar ratio between glucose and urotropine, determined by HPLC.

The HMF band in the chromatogram is only visible if pure glucose was used as starting material and if glucose itself was completely consumed in the case of high glucose to urotropine ($G:Uro > 1:0.5$) ratios. The complex chromatogram indicates that other by-products than levulinic and formic acid are present in the liquid phase after rehydration. An increase of the amount of acidic by-product in the supernatant with raising molar ratio of urotropine to glucose was obtained by HPLC. At first glance, this is in contradiction to the pH measurements that show a higher basicity when the amount of urotropine to glucose increases. The decomposition of urotropine is thermodynamically and acid- or base-catalysis driven, yielding in the decomposition products formaldehyde and ammonia ^[216].

Formaldehyde itself gets oxidized and is converted into formic acid. Ammonia leads in total to an increase in basicity of the supernatant. NH_3 ($\text{p}K_{\text{b}}=4.75$, strong base) raises the pH basicity and thus suppresses the acidity of formic acid ($\text{p}K_{\text{a}}=3.75$, strong acid), acetic acid ($\text{p}K_{\text{a}}=4.75$, medium-strong acid) and levulinic acid ($\text{p}K_{\text{a}}=4.78$, medium-strong acid). With higher molar ratio of urotropine to glucose, more formic acid is catalyzing the decomposition of urotropine, increasing the ammonia concentration. According to the HPLC chromatogram, only at higher molar ratio of urotropine to glucose a higher percentage of formic acid is still left after hydrothermal synthesis. Due to the higher pH it is likely that consecutive reactions involving formic acid get prevented. However, compounds with a more basic behavior such as ammonia or amine could not be separated by the HPLC column. The HPLC column used for this application is only able to separate monosaccharides in combination with organic acids, fatty acids, alcohols, ketones, neutral compounds or inorganic salts.

4.4. Macroscopic and Microscopic Morphology of N-HTC Materials

SEM and TEM images reveal spherical morphology of the obtained N-containing hydrothermal carbonaceous materials (Figure 31).

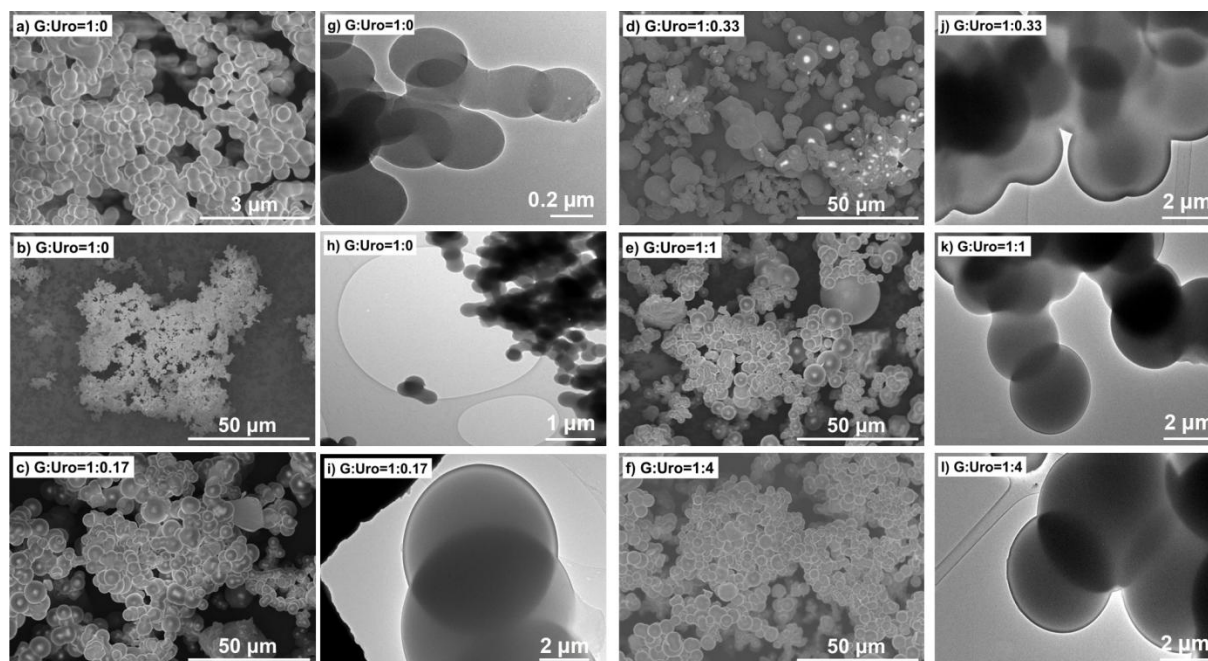


Figure 31: (a)-(f) Scanning electron micrographs and (g)-(l) transmission electron micrographs of N-HTC materials with different compositions, illustrating spherical particle shapes.

Moreover, all HTC materials exhibit regions of aggregated particles. Particle sizes were determined by optical microscope images after the materials were pressed to pellets (Figure 32).

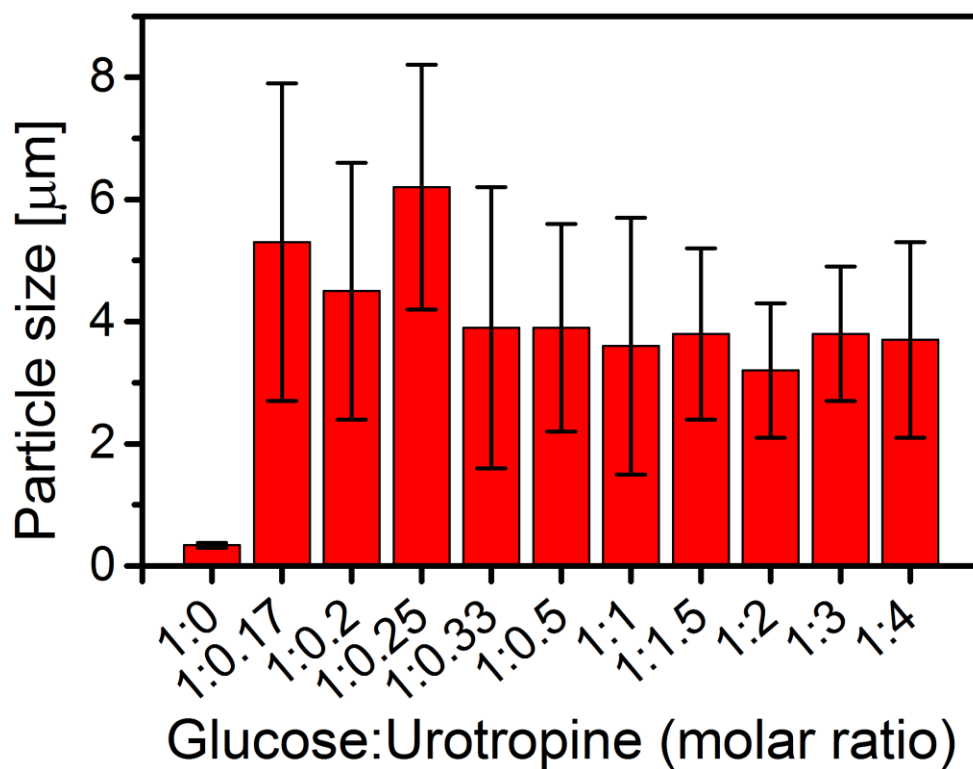


Figure 32: Particle sizes of the synthesized HTC samples as a function of the molar ratio between glucose and urotropine.

The average particle size is around 3 to 6 μm for the N-containing HTC materials, showing a broader particle size distribution for the samples with higher glucose content. In comparison, pure HTC particles are smaller by a factor of ten with an average particle size of 0.34 μm (Figure 32 and Figure 33).

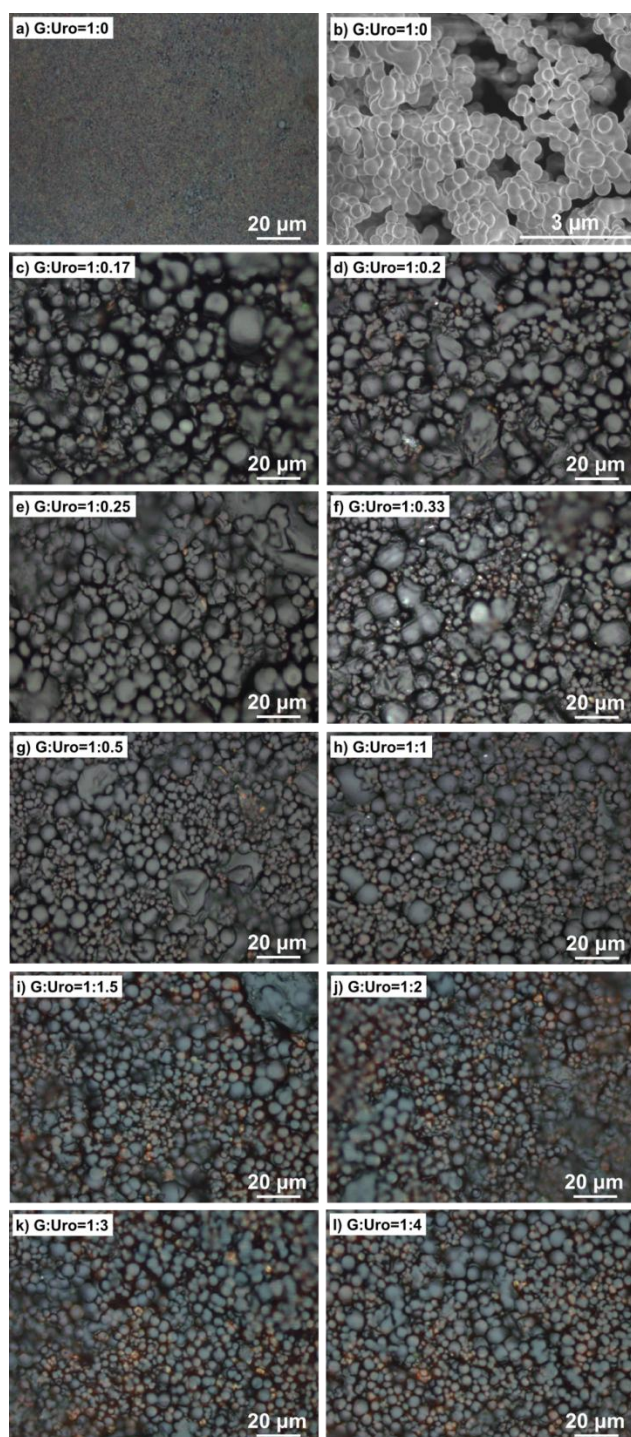


Figure 33: (a) and (c)-(l) optical microscopic images and (b) scanning electron micrograph of N-HTC materials pressed to pellets.

This change in particle size can be attributed to the different kinds of mass fractions of the reactants that have been used as well as the increased complexity of possible reaction pathways by adding urotropine, forming a variety of organic compounds as mentioned in the introduction. The growth of the carbon microspheres occurs according to the LaMer model^[145]. Via polymerization and

cross-linking processes, first species form nuclei followed by their spherically shaped growth ^[10, 145]. As the reactions occur in a quite complex manner inside the autoclave, the growth of particles occurs in polydisperse and agglomerated spherically shaped particles rather than in monodisperse particles ^[40b]. The LaMer model does not take the pH behavior into account that is crucial according to the decomposition behavior of the used reactants (Figure 34).

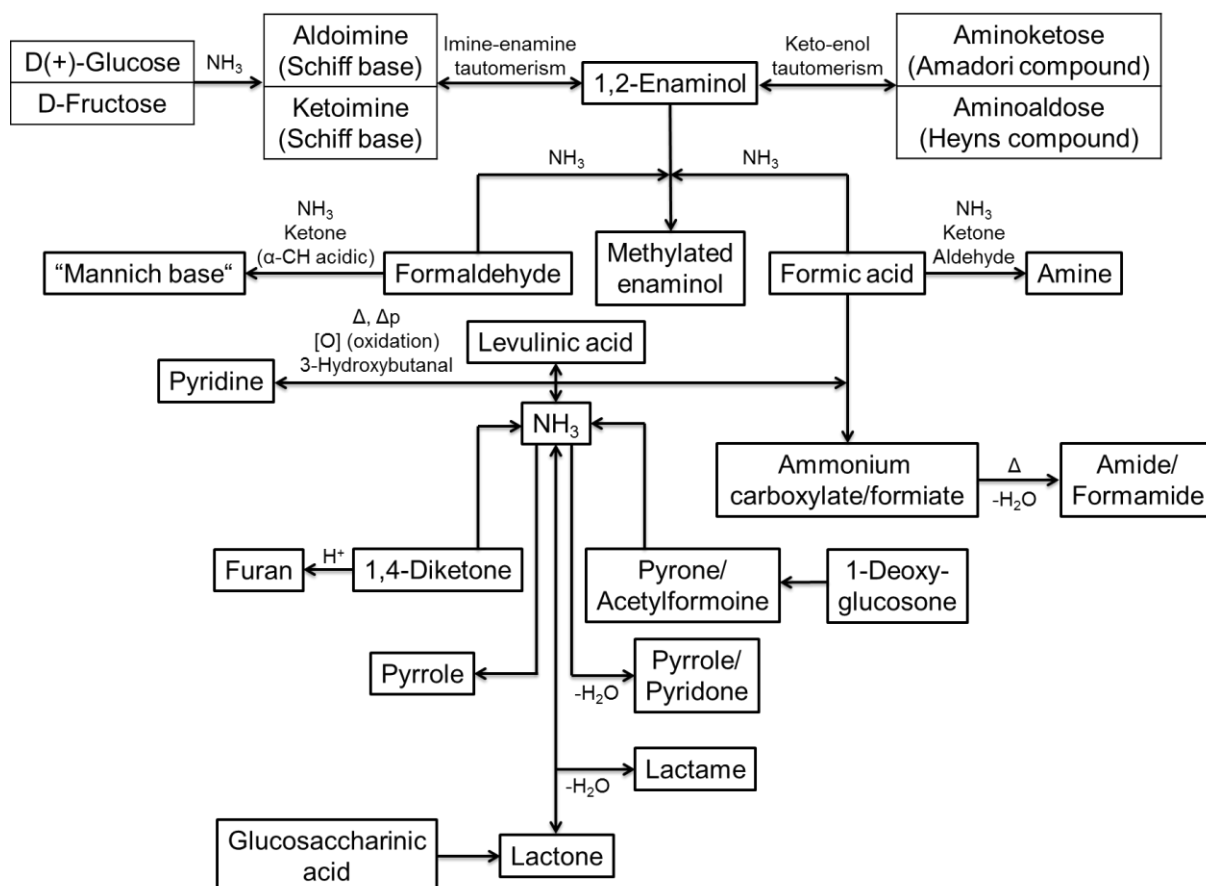


Figure 34: Schematic representation of the various reaction steps and the conditions during precursor decomposition leading to a diversity of structural motifs.

Recent pH dependent studies on hydrothermal carbons investigated the influence of the initial pH from pH 0 to pH 6, revealing a change in particle size from 15 to 0.5 μm , respectively ^[41]. At lower pH values, when the HTC material starts to turn from brown into black, the formed carbons have a higher degree of internal condensation of the polymeric carbonaceous network and therefore an increasing amount of cross-linking bonds. By hydrothermal synthesis of a pH-basic amino sugar such as glucosamine, smaller particle sizes than for a pure

glucose sample have been obtained ^[70b]. The addition of a basic comonomer like ethylenediamine has not only an impact on the particle size that decreases, but also, depending on the concentration of ethylenediamine, the morphology changes abruptly into a net-cross structure ^[217].

Specific surface areas were determined by nitrogen adsorption experiments and BET analysis. The synthesized N-HTCs provide negligibly small surface areas below $1 \text{ m}^2 \cdot \text{g}^{-1}$, solely pure HTC has a larger specific surface of around $9 \text{ m}^2 \cdot \text{g}^{-1}$ (Table 4).

Table 4: BET surface area of hydrothermal carbon materials.

G:Uro [mol]	Surface area [$\text{m}^2 \cdot \text{g}^{-1}$]
1:0	9.34
1:0.17	0.62
1:0.33	0.64
1:1	0.46
1:4	0.75

The structural texture of the N-HTCs was investigated using HRTEM (Figure 35).

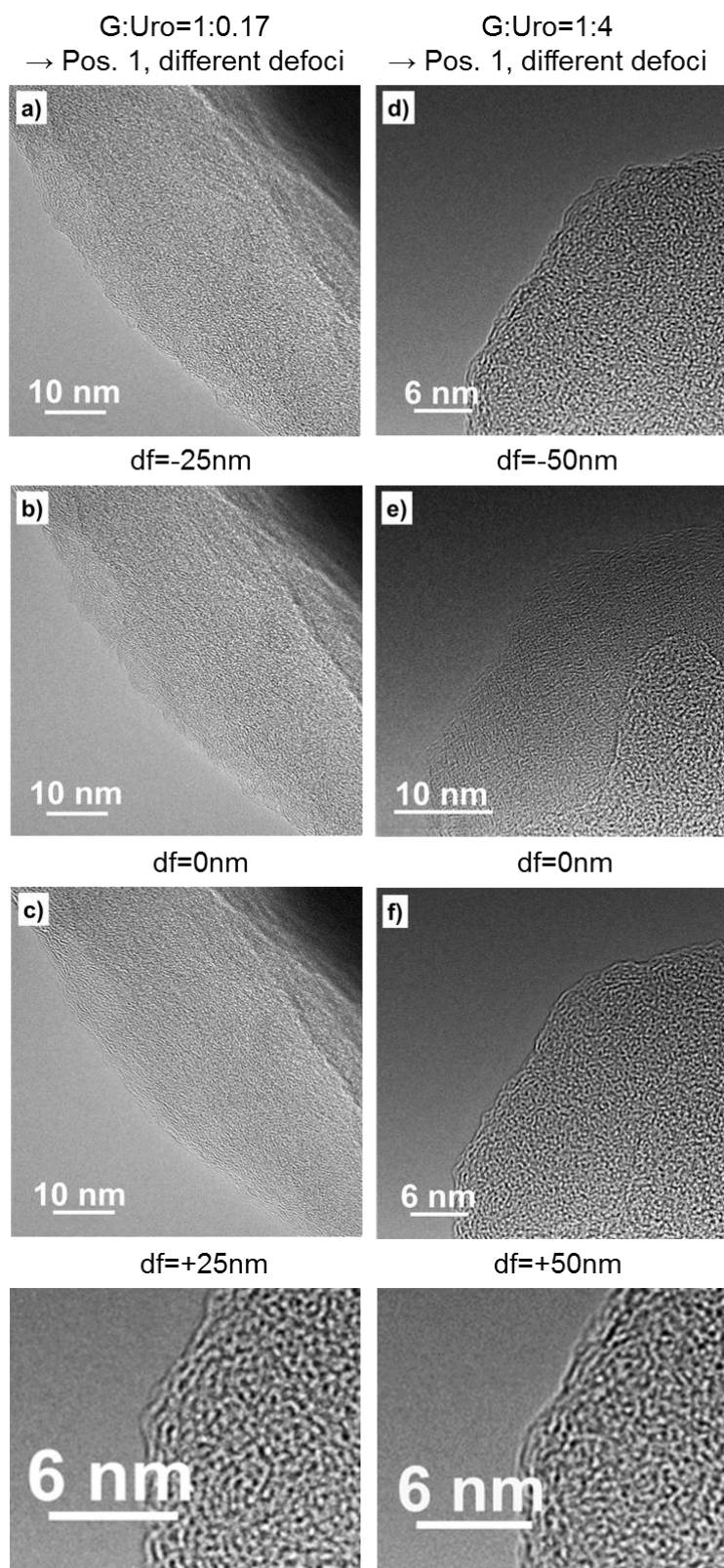


Figure 35: HRTEM images of N-HTCs using G:Uro=1:0.17 (a-c) and G:Uro=1:4 (d-f), applying different defoci. The bottom row panels are cropped HRTEM images to highlight isotropicity of carbon structures.

In the outer part of the carbon sphere surface, walls depict a surface roughness that can be accounted for by the irregular arrangement of 8–12 curved atom

chains (e.g. C) caused by defect sites (e.g. O, N). As a result, there is no preferred direction. The highly curved texturing profile leads to isotropic orientation of the carbon structure [27c, 42a].

4.5. Elemental Composition and Yields

The determination of elemental composition of the N-HTC samples was carried out by total organic carbon (TOC) combustion analysis. The results in wt% of different molar ratios of glucose to urotropine are visualized in Figure 36.

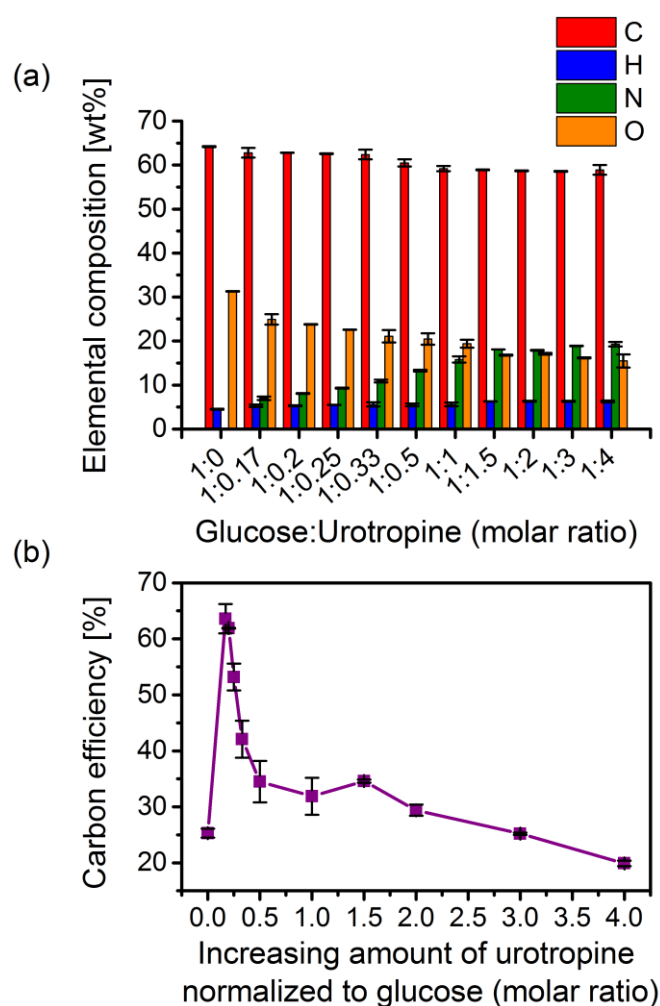


Figure 36: (a) Elemental composition plotted against the molar ratio between glucose and urotropine and (b) carbon efficiency of all synthesized hydrothermal carbon samples as a function of the increasing amount of urotropine normalized to glucose.

With increasing molar ratio of urotropine to glucose maximal N-content of about 19 wt% can be achieved with a simultaneous decrease of the carbon and oxygen fraction. It has to be noted that standard deviations were calculated from at least two experiments running separately, using the same molar ratio of glucose to urotropine. Oxygen was calculated by subtracting the amount of C, H, and N from 100 %.

The carbon efficiency ^[53a] was determined as

$$\text{Carbon efficiency [\%]} = \frac{\text{Amount of carbon in the solid after hydrothermal synthesis}}{\text{Initial amount of carbon in the reactants}} \quad \text{Eq. (1)}$$

If only glucose is used as starting material the carbon efficiency is very low at around 25 %, which is consistent with the high glucose peak in the HPLC experiments. Maximum carbon efficiency of approximately 64 % could be achieved with the lowest amount of urotropine to glucose at the applied synthesis conditions. The carbon loss can be explained by the transformation of glucose into degradation products, e.g. levulinic acid, acetic and formic acid or dihydroxyacetone, which is also in accordance with the HPLC measurements. The formation of liquid supernatant (liquefaction) and volatile side products (gasification), which are concurrent parallel reactions to the formation of hydrothermal carbon, are formed at a greater or lesser extent depending on the preferential synthetic pathway ^[218]. Furthermore, higher pH of the solvent is unfavorable for internal degree of condensation as urotropine very quickly releases ammonia whereby the pH raises too high and too fast (Figure 14). The reaction conditions at high urotropine concentration favor fragmentation reactions over condensation reactions. Alternatively, more stable N-sources or non-aqueous polar reaction medium could be applied for hydrothermal synthesis.

The yields of all the HTC solid materials were calculated according to formula (2) ^[53a, 126d]

$$\text{HTC yield [\%]} = \frac{\text{Amount of attained solid after hydrothermal synthesis [g]}}{\text{Initial amount of glucose and urotropine [g]}} \quad \text{Eq. (2)}$$

By normalizing the elemental composition to the HTC yield the mass loss as function of the different molar ratios of glucose to urotropine and their composing elements can be followed. Major part of the diminishing of HTC yield is not only accompanied by a decrease of the carbon content but also by oxygen loss. The loss of the carbon content can be explained by the transformation of glucose into the final degradation products levulinic, acetic and formic acid or dihydroxyacetone that is in accordance with the HPLC measurements ^[51b, 53a, 54a]. The liquid supernatant (liquefaction) and volatile side products (gasification), which are concurrent parallel reactions to the hydrothermal carbon process, are formed in a greater or lesser extent ^[218]. If only glucose is used as starting material, theoretically a yield of about 60 % could be reached due to the dehydration steps of the decomposition process of glucose to form HTC since a molecule of glucose eliminates four water molecules, which make up 40 % of the starting mass as explained in the introduction and elsewhere ^[41, 53a, 54b, 219]. However, a yield of only 16 % was obtained for a hydrothermal carbon material based on pure glucose. Maximal HTC yield of ca. 42 % was obtained for a glucose/urotropine mixture.

4.6. Structural Composition of N-HTC

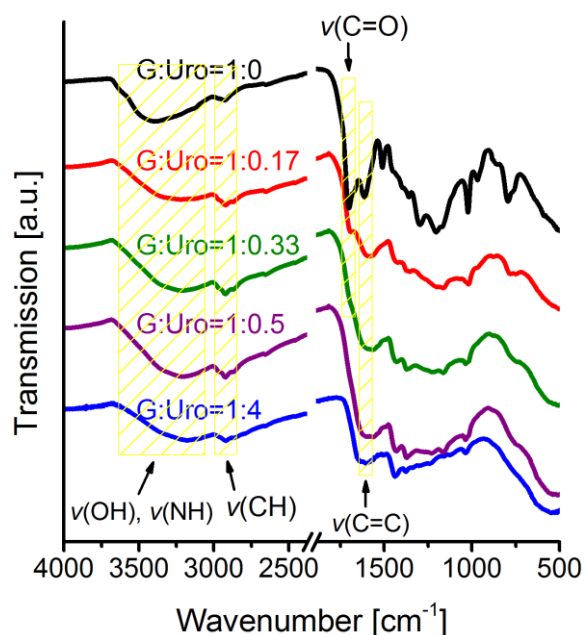


Figure 37: FTIR (ATR) spectra of the synthesized HTC samples with different molar ratios of glucose to urotropine. Higher glucose to urotropine ratio is depicted on top and higher urotropine to glucose ratio below.

The structural compositions of N-HTC materials were investigated by spectroscopic methods supported by electronic structure calculations. Fourier transform infrared spectroscopy (FTIR) was performed in attenuated total reflection mode (ATR). The collected spectra of selected samples are shown in Figure 37.

The broad absorption band between 3650 and 3060 cm^{-1} corresponds to $\nu(\text{O-H})$ stretching vibration as well as to the $\nu(\text{N-H})$ stretching vibration. The overlap of both functional groups excludes their exact determination. The aliphatic methylene-type group $\nu(\text{C-H})_{\text{stretch}}$ is observed at around 2923 cm^{-1} for all synthesized materials. The $\nu(\text{C=O})$ band at 1700 cm^{-1} is only visible at higher molar ratio of glucose to urotropine, starting from $\text{G:Uro}=1:0.33$. The carbonyl group can probably be ascribed to a higher degree of internal condensation of the polymeric carbonaceous network structures since these HTC chars are characterized by an acidic pH behavior, a higher HTC yield and in the same way a higher carbon efficiency rendering these materials compact and robust. The

band between $1630\text{--}1550\text{ cm}^{-1}$ is attributed to $\nu(\text{C}=\text{C})_{\text{stretch}}$ vibration, pointing to graphitic structures in the HTC materials. The evaluation of the bands in the fingerprint region becomes more complicated. Theoretical studies of the IR spectra of carbon materials were carried out by Fuente and co-workers for different O-functional groups (carboxyls, lactones, anhydrides, phenoles, quinones and pyrones) that were suitable for the description of the surface chemistry of graphene layers ^[220]. To our knowledge no efforts have been made so far to calculate IR spectra of hydrothermal carbon materials, especially in the fingerprint region, due to the fact that the exact structure of the HTC remains unclear. In the fingerprint region, however, it is only known that for pure HTC originating from xylose, highly intense bands at 880 and 752 cm^{-1} ($\delta(\text{C-H})_{\text{oop}}$) were confirmed to stem from aromatic structure motifs ^[42a, 221].

4.7. Computed FTIR Spectra

The interpretation of the vibrational and deformation modes at these lower wavenumbers is supported by utilizing polyfuran and polypyrrole as model compounds for quantum-chemical calculations, since oligomeric ring structures such as polyfuran was successfully verified as a major part of the structural motifs of the HTC network ^[51b, 53a, 125a, 126a]. In terms of N-functionalization it was proven that polypyrrole is one of the important structural motifs ^[125a] and hexameric pyrrole has therefore been chosen next to hexameric furan for calculations. For details on the electronic structure calculations see supporting information. For a series of model compounds such as hexameric furan and hexameric pyrrole, features of the vibrational spectra were evaluated by normal mode analysis using Density Functional Theory (DFT) methods (Figure 38).

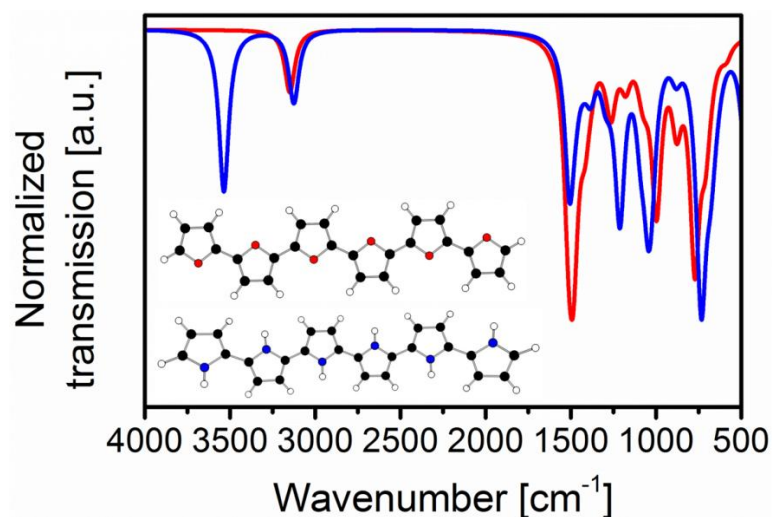


Figure 38: Calculated FTIR spectra for hexameric furan (red) and hexameric pyrrole (blue).

4.8. Computed and Experimental Gas Phase Infrared Spectra of Furan

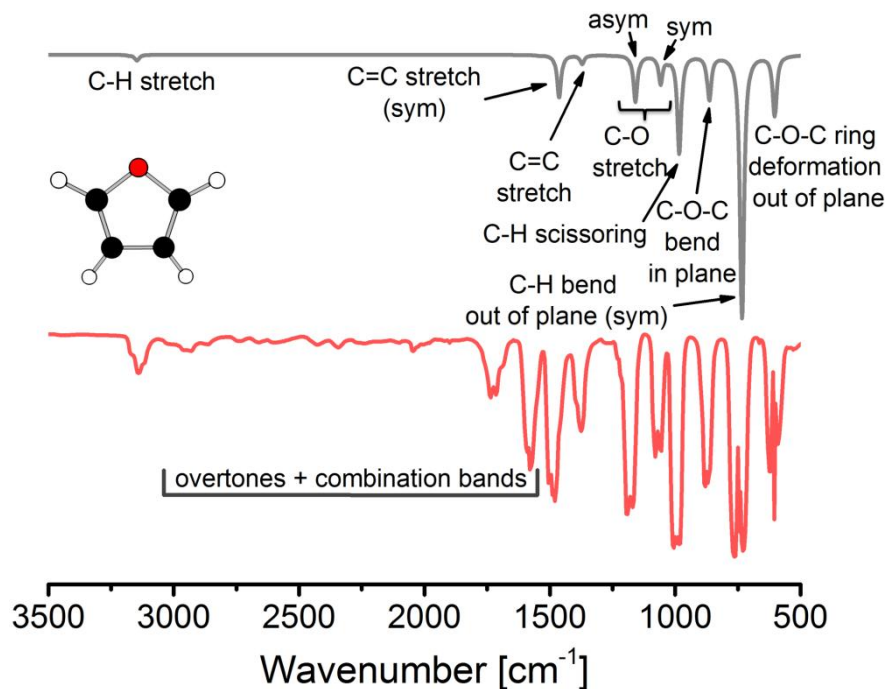


Figure 39: Experimental gas phase (red line) and calculated (B3LYP+D3/def2-TZVP with scaling factor of 0.97, grey line) infrared spectrum of furan. Experimental IR spectrum of furan was obtained from NIST Chemistry WebBook ^[222].

The discrepancy between the positions of computed and experimental IR bands is smaller than 30 cm^{-1} (for most bands the difference is in the range of $2\text{--}15\text{ cm}^{-1}$). Computed intensities of the IR bands reproduce experimental intensities well. The bands of the experimental gas phase IR spectrum exhibit the rotational structure with clearly visible Q, P, and R branches of the lowest two bands (Figure 39). In addition to fundamental bands found in the experimental spectrum, overtones and combination bands are present in the region of $1500\text{--}3000\text{ cm}^{-1}$. The band at about 605 cm^{-1} of high intensity (calc. 603 cm^{-1}) is the out-of-plane ring bending (C-O-C bend out of plane). The next very strong band at 745 cm^{-1} (calc. 734 cm^{-1}) corresponds to symmetric C-H bend out of plane of all hydrogen atoms. The band at about 870 cm^{-1} (calc. 863 cm^{-1}) is the in-plane C-O-C ring bending. Another strong band appears at about 995 cm^{-1} (calc. 984 cm^{-1}) and indicates C-H bend in plane (C-H scissoring). Two bands at 1070 cm^{-1} (calc. 1057 cm^{-1}) and 1180 cm^{-1} (calc. 1158 cm^{-1}) correspond to symmetric and asymmetric C-O bond stretching, respectively. A weaker band is found at about 1380 cm^{-1} (calc. 1370 cm^{-1}) and it corresponds to aromatic C3=C4 bond stretching. At about 1490 cm^{-1} (calc. 1461 cm^{-1}) lies the band that can be assigned to symmetric C₂=C₃ bond stretching. The highest lying band of low intensity (exp. 3140 cm^{-1} , calc. 3143 cm^{-1}) is the asymmetric aromatic C-H bond stretching. These benchmark simulations of the vibrational spectrum of furan show that the computed DFT spectra are in good agreement with experiment.

4.9. Vibrational Spectra of α -Oligofurans and N-Free HTC (Pure HTC Originating from Glucose)

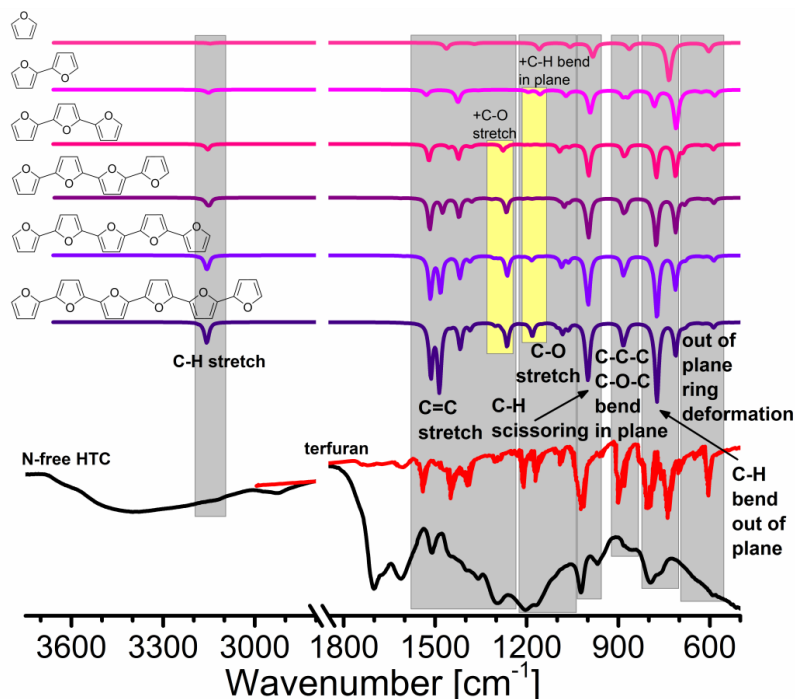


Figure 40: Computed (B3LYP-D3/def2-TZVP) IR spectra of linear oligofurans (one to six furan units, see schemes), experimental spectrum of terfuran^[223] (red line), and experimental FTIR spectrum of N-free HTC (black line). IR spectra are divided into regions according to the type of vibrations. Additional lines that appear conjointly with main vibration are marked with yellow boxes.

In order to assess the quality of simulated spectra for a well characterized compound, the vibrational spectrum of furan was computed. Calculated harmonic vibrational frequencies of furan scaled by 0.97 are in good agreement with the experimentally obtained gas phase spectrum (Figure 39). It is known that HTC networks contain polyfuran motifs^[51b, 53a, 125a, 126a]. Linear oligofurans containing two to six furan rings were chosen as model compounds that are supposed to match with furanic-type structural units to examine their match with calculated spectra (Figure 40). It has then been investigated how accurate the IR spectra of HTC materials can be described by polyfuranic models and what influence the number of furan rings in α -oligofurans have on their vibrational spectra. Additionally, the experimental infrared spectrum of terfuran (red line)^[223] was compared with the computed spectra of α -oligofuran models and with

the IR spectrum of the N-free HTC material (black line). Theoretical vibrational spectra of furan and α -oligofurans can be divided into seven regions according to the type of vibration they represent. These include out-of-plane ring deformation ($<700\text{ cm}^{-1}$), C-H bend out of plane (ca. $680\text{--}820\text{ cm}^{-1}$), C-C-C and C-O-C bend in plane (ca. $820\text{--}920\text{ cm}^{-1}$), C-H scissoring, C-O stretch, aromatic C=C stretch, and aromatic (or sp^2) C-H stretch. Increasing the number of furan rings influences the vibrational spectra of α -oligofurans considerably. Additional bands appear already in the spectrum of 2,2'-bifuran compared to the spectrum of furan and either corresponding bands shift or their intensities change. To some of the bands two or more types of vibrations can be assigned. Increased number of furan rings causes for instance that the C-O-C bend out-of-plane band shifts from 603 cm^{-1} (furan) to $615\text{--}630\text{ cm}^{-1}$ (hexameric furan) and its intensity significantly decreases. Additionally, two other bands appear. One appears at about 590 cm^{-1} with a very low intensity that represents out-of-plane C-C-C ring deformation, and another one at about $680\text{--}690\text{ cm}^{-1}$ (depending on the oligomer length), which is described by the combination of C-O-C bending with asymmetric C-H bending out of plane. In the area of C-H bend out of plane, a further band occurs. This band corresponds to C-H bending out of plane of inner furan rings and its intensity increases with increasing number of rings. The lower lying band in this region corresponds to the C-H bend out of plane in the two outer furan rings. The intensity of the bands in the regions of in-plane ring bending and C-H scissoring increases when the oligofuran chain elongates. In the wider regions of aromatic C=C and C-O stretching more new bands appear that grow in intensity. These are mainly the combinations of symmetric and asymmetric bond stretches of individual rings and also other vibration types, i.e. C-H bending in plane in case of bands in the area of C-O stretching or mixture of C=C and C-O stretching in the C=C stretch area. The last band at about 3155 cm^{-1} represents combination of aromatic symmetric and asymmetric C-H bond stretching.

Many common features can be recognized in the spectra of N-free HTC and α -oligofurans. The vibrational spectrum of N-free HTC can be partially explained by the computed spectra of oligofurans up to 1600 cm^{-1} and in the region of aromatic C-H stretching. These findings are in agreement with the analysis of infrared spectra of several HTC materials [42a, 224]. For example, the sharp strong band at about 1020 cm^{-1} could be assigned to aromatic C-H scissoring as it is the case in α -oligofurans. Also, a weak band in the spectrum of nitrogen-free HTC at about 860 cm^{-1} could be assigned to ring bending in plane which has a comparable position in the computed spectra of oligofurans. A wide group of bands in the region of $1070\text{--}1470\text{ cm}^{-1}$ in the spectrum of HTC could consist of a mixture of C=C and C-O stretching vibrations, and of C-H in-plane bending. However, the area in the range of $1600\text{--}1800\text{ cm}^{-1}$, the band at about 2950 cm^{-1} , and a broad band above 3150 cm^{-1} in the spectrum of N-free HTC cannot be explained by the pure oligofuranic structure. Despite many similarities between the computed oligofuran spectra and the experimental spectrum of N-free HTC the intensities of corresponding bands cannot be compared as the spectrum of HTC is a combination of many overlapping vibrations. Furthermore, the bands of the N-free HTC spectrum are in general broader, indicating the richness in molecular entities and functional groups. Large parts of the observed N-free HTC spectrum are not accounted for by the heterocyclic model structures. Hence, aliphatic (hydrocarbons) moieties need to be present in addition.

4.10. Comparison of the Vibrational Spectrum of N-Free HTC and Additional Structures

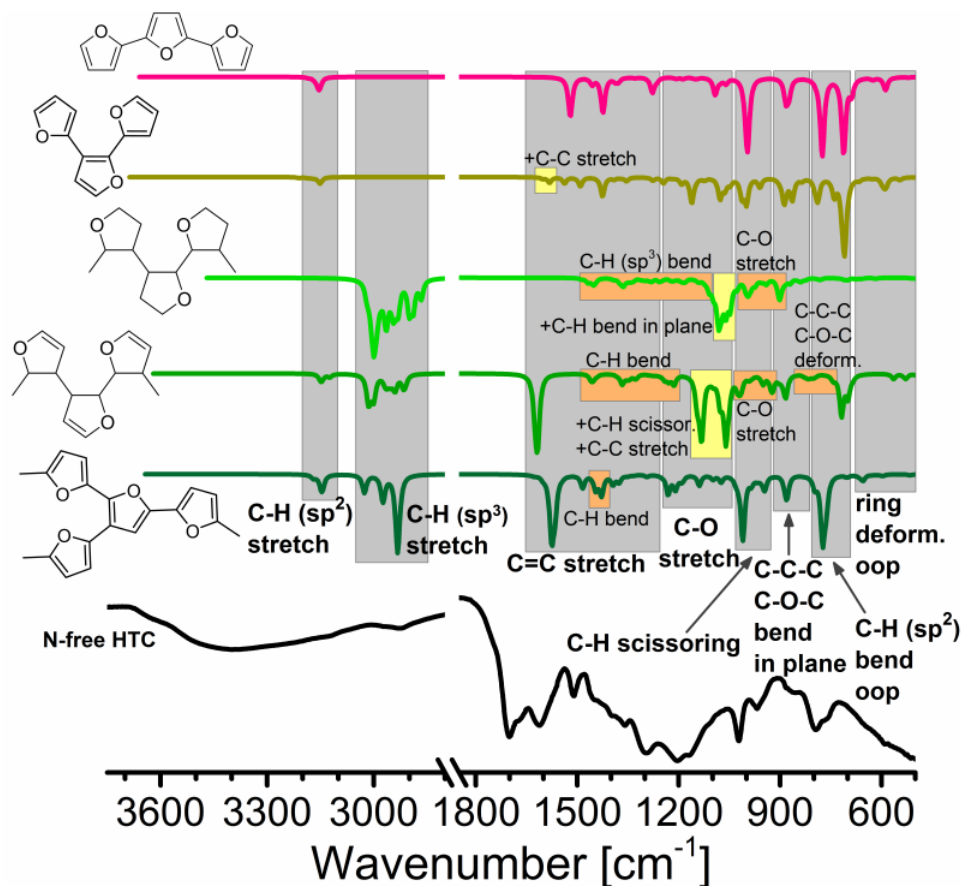


Figure 41: Computed vibrational spectra of additional structural motifs found in polyfurans and experimental FTIR spectrum of N-free HTC (black line).

Polyfurans can contain additional structural motifs other than furan chains that are described in detailed elsewhere ^[225]. Similar motifs might be present in HTC materials. Therefore, in order to assess how different functional groups will influence the IR spectra of furans, we performed the vibrational analysis on structures found in the review ^[225] and compared them with the experimental spectrum of terfuran and N-free HTC (Figure 41 and Figure 42).

carbons. But also carbonyl group stretching bands of ketone and lactone may be present.

4.11. Thermal Analysis of HTC

Thermal analysis of the synthesized HTC materials was performed in Ar atmosphere with a heating rate of $20 \text{ K}\cdot\text{min}^{-1}$.

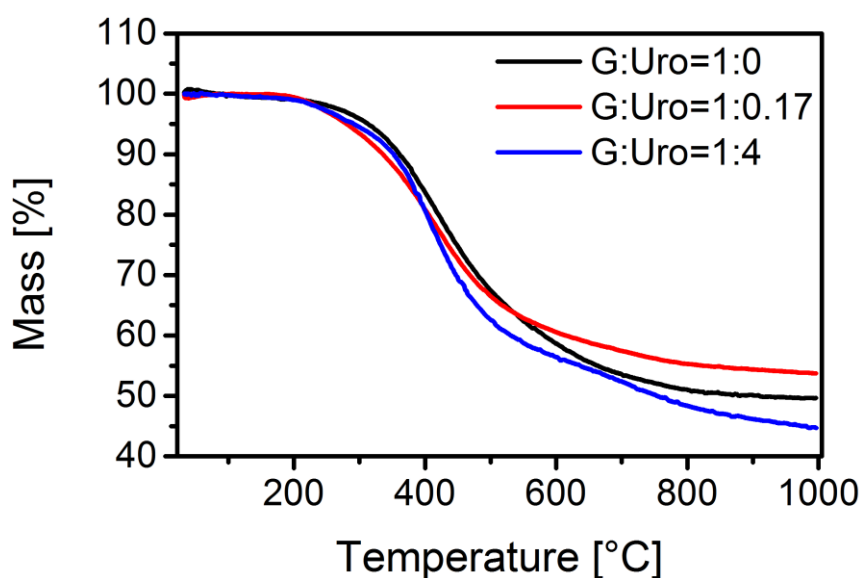


Figure 43: TG curves plotted as a function of the temperature for G:Uro=1:0, G:Uro=1:0.17 and G:Uro=1:4.

Thermogravimetric studies of the HTCs are shown in Figure 43. For an N-free HTC char approximately 50 % mass loss can be observed. Highest mass loss of around 55 % was determined for the sample with highest N-content (G:Uro=1:4) and 46 % for the sample with lowest N-content (G:Uro=1:0.17). Among the synthesized HTC samples, the one with the lowest N-content is more resistant against thermal decomposition. Reversely, HTC sample with highest N-content is the one with lowest resistance against thermal degradation. All HTC chars denote the same curve progression with a similar decomposition process. It seems the mass loss depends on the one hand on the degree of

internal condensation of the polymeric carbonaceous network structures and on the other hand on the functional groups (Figure 44).

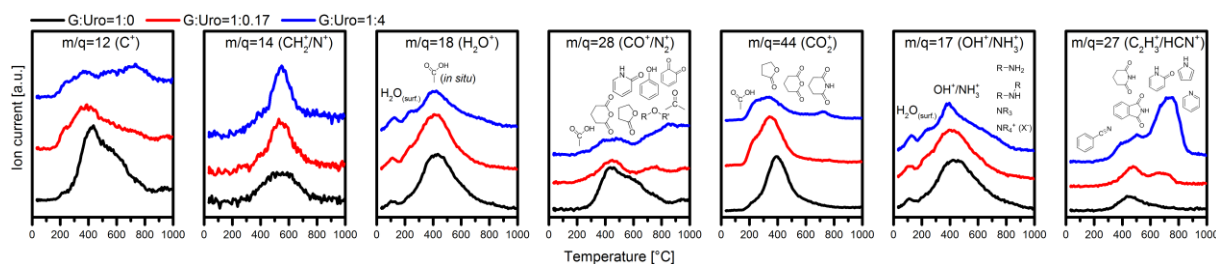


Figure 44: MS signals of TG-MS experiments plotted against the temperature. A vertical offset was applied for better comparability of N-free (black) and N-containing HTC, depicting molar ratios of glucose and urotrpine with lowest (red) and highest N-content (blue).

The higher the degree of internal condensation the more thermally stable the HTC chars as proved by the N-free sample. The N-HTC material with highest N-content exhibits the highest mass loss, which is accounted for by the multitude of more thermostable N-functional groups that evolve strongly at approximately 800 °C. The recorded mass spectra (MS) of the decomposition products are shown in Figure 44.

An unambiguous evaluation is aggravated by the fact that MS signals of N-functional groups overlap with the signals of the O-functional groups. The recently developed isothermal segregation procedure and the semi-quantitative analysis of the O-functional groups could therefore not be applied [226]. Nevertheless, trends within the synthesized HTC materials can be determined. In accordance with the IR spectra, N-containing HTC materials point to lower abundance of oxygen containing functional groups, seen by a decrease of total peak intensities of the CO, CO₂ and H₂O MS signals in comparison to pure HTC. CO₂ (m/q=44) MS signals are caused by the thermal decomposition of carboxylic, lactone and anhydride groups. They are present in all synthesized HTC materials but the total amount decreases with increasing N-content and their ratio changes, too. A peak shift from around 389 °C for pure HTC to around 341 °C and the appearance of a second peak at around 210 °C for the N-HTC materials can be observed. The ratio shifts towards more carboxylic and lactone groups than anhydrides.

This corresponds very well with the detected water signals ($m/q=18$). Caused by the abundance of hydrophilic functional groups, surface water is bonded that desorbs at around 125 °C. Here again, the total water signal is higher in the case of pure HTC than for the N-containing samples. The signal of physisorbed water is superimposed by an intense water signal that arises at higher temperatures, around 411 °C, due to the evolution of water from neighboring carboxylic acid functional groups and the formation of anhydrides. Due to the intense water signal it can be assumed that a high fraction of the anhydride groups was formed during the heating process from adjacent carboxylic groups instead of being present directly after the synthesis. Therefore, the higher ratio of carboxylic groups in the N-HTC determined by the CO₂ signal is only ostensible due to the broad distribution, meaning dehydration and transformation into anhydrides are hindered.

The detected mass of $m/q=28$ is representative for CO as well as N₂. The peak maxima of pure and low N-containing HTC correspond very well with the peak maxima observed at mass 18 (H₂O) and mass 44 (CO₂), pointing again to anhydride groups. Further CO releasing functional groups with higher thermal stability are phenols, ether and carbonyls. They cause the shoulders at higher temperatures observable in the pure HTC material. With increasing N-content of the HTC materials two fused peaks at 380 °C and 500 °C become dominant, most likely they can be attributed to N-containing functional groups as they do not appear in the pure HTC sample. In combination with the mass signals of $m/q=27$ they can be related to aromatic N-heterocycles, aromatic amines or nitriles. Increasing peak intensities with increasing N-content indicate that these are N-containing functional groups rather than terminal vinyl derivatives (-C₂H₃). An indication for the existence of lactams is the *in situ* decarbonylation to pyrrole groups, which can be found in the mass spectrum of CO⁺ at approximately 450–540 °C [142, 227]. The CO peak at 500 °C can be ascribed to this conversion. The stable intermediate, pyrrole, is supposed to decompose at

around 680 °C under the release of HCN as seen in the mass $m/q=27$ [142a, 228]. Degradation of imide occurs via decarboxylation ($m/q=44$) of phthalimide at 450 °C [142a, 229], yielding benzonitrile. Subsequently, benzonitrile decomposes to HCN at 500 °C as inferred from the detection of a signal at $m/q=27$ in the MS spectrum [142a, 230]. In contrast, pyrolysis of succinimide leads to the evolution not only of CO_2 and HCN, but also to the generation of isocyanic acid (HNCO) or isocyanate (NCO^-) as key gaseous compound [142a, 231]. The CO_2 evolution can be found at a temperature of approximately 450 °C, by analogy to imide decarboxylation. Exact determination is therefore complicated. The degradation to HNCO or NCO^- happens at around 510 °C. In the mass spectra of HNCO^+ ($m/q=43$) and NCO^+ ($m/q=42$) at 510 °C it seems reasonable to suppose that the evolution of these gas products occurs (Figure 45).

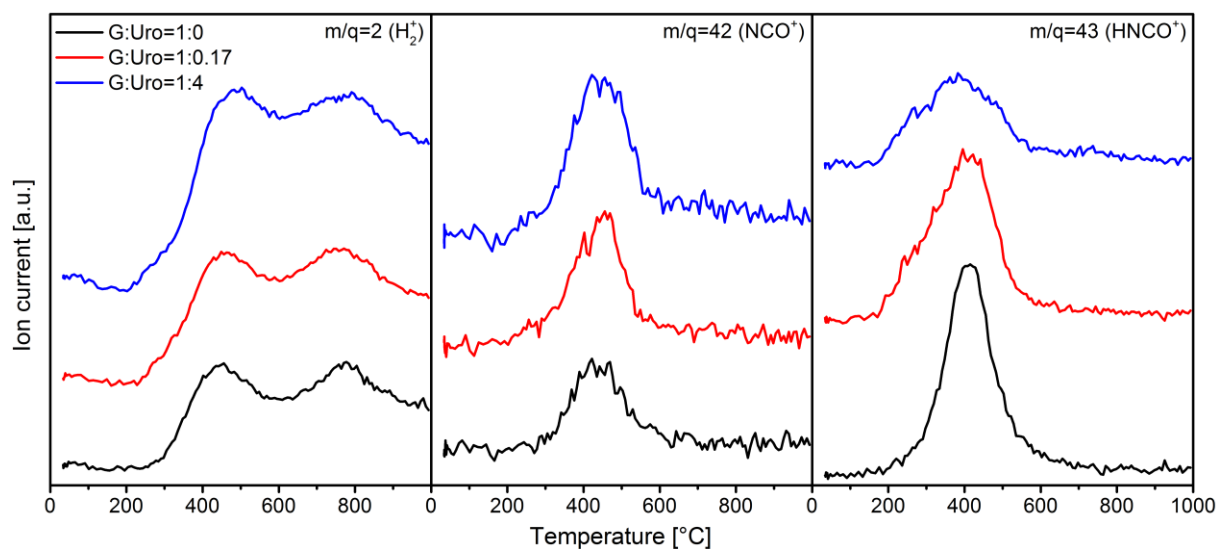


Figure 45: MS signals of G:Uro=1:0 (black), G:Uro=1:0.17 (red) and G:Uro=1:4 (blue) as a function of temperature for $m/q=2$, $m/q=42$ and $m/q=43$ at a heating rate of $20 \text{ K}\cdot\text{min}^{-1}$.

If the molar ratio of urotropine to glucose is increasing (G:Uro=1:0.17 and G:Uro=1:4), HCN and H_2 are released as gaseous pyrolysis products of pyrrole, seen in the mass spectrum of HCN^+ at 785 °C and in the H_2^+ curves ($m/q=2$) at 805 °C (Figure 45). Likewise, the decomposition of pyridinic groups generates HCN and H_2 , which are formed at 905 °C and 920 °C, respectively [232]. However, a clear proof cannot be given for the origin of these bumps,

considering that pyrroles and pyridines are only generated by samples containing a significant amount of nitrogen.

The detected MS signals of $m/q=17$ support the previous conclusions. The first peak maxima correlate with the signals of $m/q=18$ in terms of temperature and intensity and are therefore attributed to OH^+ resulting from water fragments. Additional peak intensities determined for mass 17 at around $400\text{ }^\circ\text{C}$ are associated to an overlap of OH^+ ions and N-containing fragments. With increasing N-content the signals caused by H_2O become less dominant. The peak shapes develop into sharper peaks and shift slightly to lower temperatures. The peak shoulder at around $680\text{ }^\circ\text{C}$ becomes pronounced with increasing N-content and can thus be ascribed to NH_3^+ of amines.

The mass spectrum at $m/q=12$ of a N-free HTC sample exhibits a broad and a sharp peak between $175\text{ }^\circ\text{C}$ and $845\text{ }^\circ\text{C}$. With increasing N-content this channel becomes less intense since N becomes the dominant species. This is confirmed by the MS signal of $m/q=14$. In case of an N-free HTC char the peak is broad but small within a temperature window between 309 and $761\text{ }^\circ\text{C}$. Herein, only methylene-type linkages (CH_2^+) occur. As the N-content rises this peak shortens and at the same time gets more pronounced. This can be accounted for by a synergetic interaction of N- and methylene-like connectivities.

4.12. Surface Analysis

Zeta potential measurements were performed as a function of pH for the synthesized HTC materials in aqueous solution (Figure 46).

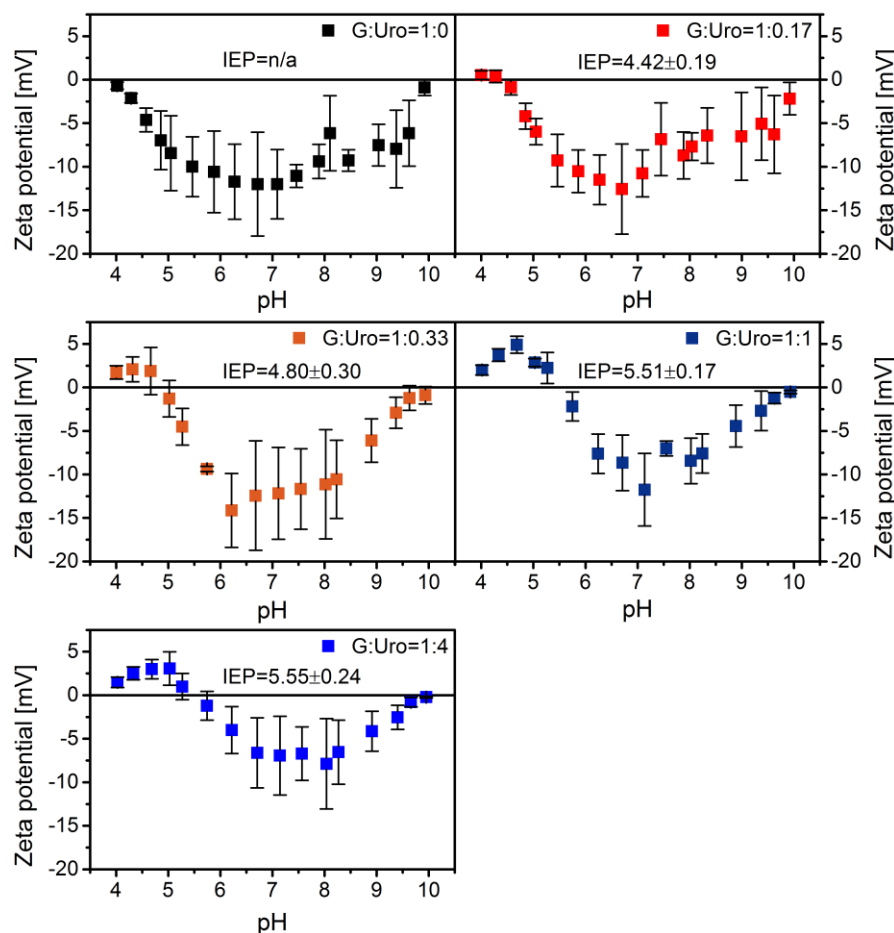


Figure 46: Zeta potential measurement for HTC materials derived from G:Uro=1:0 (pure HTC, black), G:Uro=1:0.17 (low N-content, red), G:Uro=1:0.33 (orange), G:Uro=1:1 (dark blue) and G:Uro=1:4 (high N-content, blue) as a function of the pH.

Pure HTC shows completely negative zeta potential values and no isoelectric point (IEP) over the measured pH range, which is caused by the richness of acidic oxygen functional groups. The lowest negative zeta potential value is around -12 mV at around pH 6.7. With increasing incorporation of nitrogen an increase of the isoelectric point (IEP) from 4.42 ± 0.19 to 5.55 ± 0.24 can be observed. Simultaneously, the negative zeta potential values raise to more positive values from -12 mV to -6.6 mV at pH 6.7, indicating that more basic functional groups or more functional groups with positive charge exist on the

surface. This observation supports all aforementioned conclusions from FTIR and TG-MS, including acid–base titrations (Figure 47).

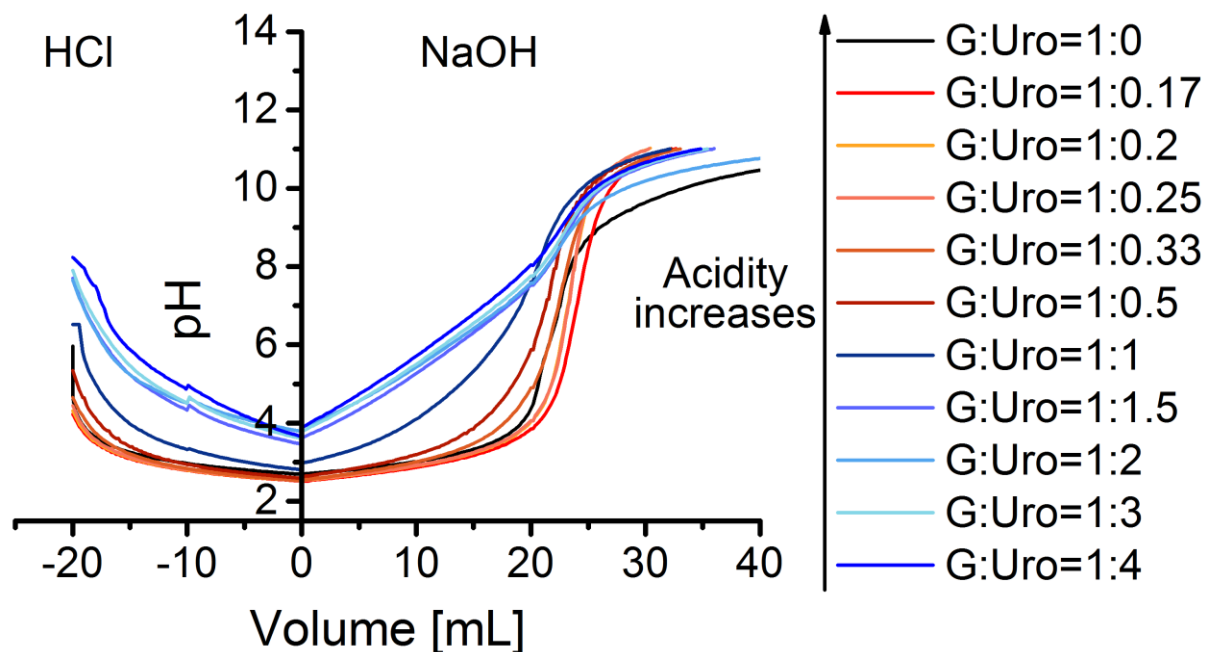


Figure 47: Titration curves of a HTC-derived glucose material and of all N-HTC carbons.

4.13. Raman Spectroscopy

The amorphous nature of the polymeric carbonaceous network of the HTC materials broadens the two characteristic bands in the Raman spectra at 1358 cm^{-1} and 1577 cm^{-1} by molecular excitations (Figure 48) ^[41].

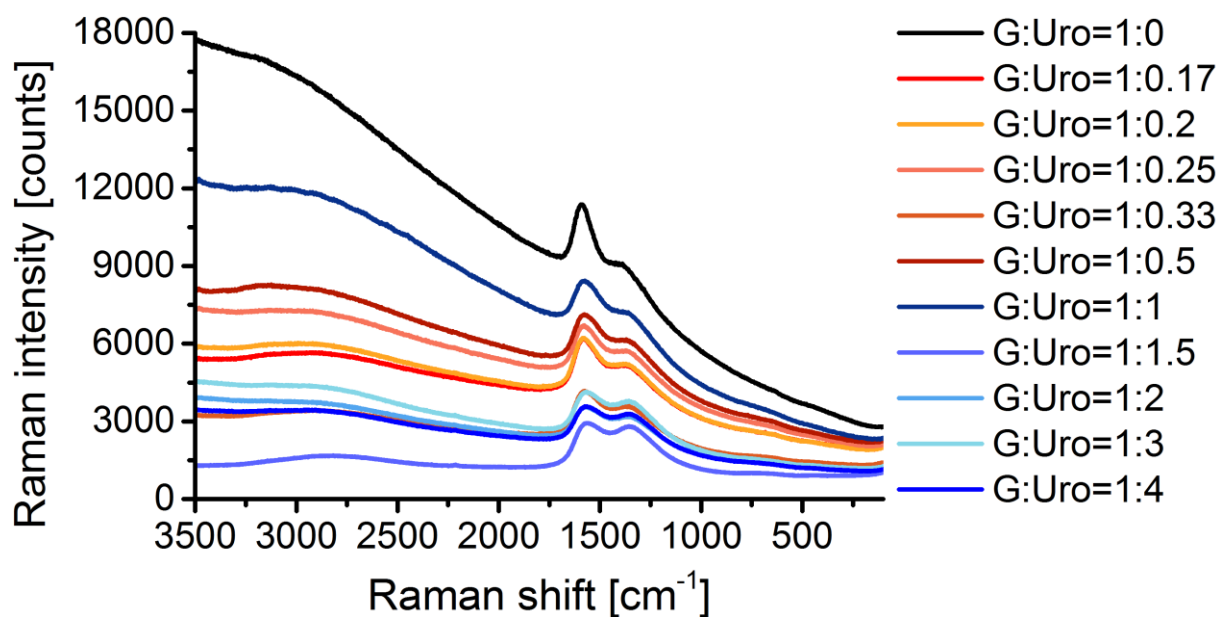


Figure 48: Raman spectra of all synthesized HTC materials at different molar ratio of glucose to urotropine, showing the whole wavenumber region from 100 to 3500 cm^{-1} . Fluorescence background indicates the polycyclic molecular structure of the HTC carbons.

Although in literature it is common to assign these two representative bands to the first-order Raman peaks – the D and G band ^[233] – this is in this case not possible as HTC chars are not of graphitic or graphene origin. The origin of soot can also be excluded as it can be denoted as highly disordered graphitic structures ^[234]. Hexabenzocoronene which is referred to as polycyclic aromatic hydrocarbon, cannot be compared as well since it is described as a graphene layer section and serves as a model for the building blocks of tiny graphitic domains, e.g. in soot ^[234]. Usually, the D band occurs from the breathing modes of six-membered aromatic rings of phonons of A_{1g} symmetry with disorder and defects in the graphitic or graphene lattice (e.g. edges/boundaries, sp^3 carbon bonds, bonding disorders, vacancies or heteroatoms) ^[233-235]. So, it highlights structural defects in the graphene layer ^[233]. In contrast, the G band is ascribed to an “ideal”, ordered undisturbed sp^2 bonded graphitic carbon lattice (chain or ring configurations) ^[234, 235c] stemming from the doubly degenerate zone center phonon E_{2g} mode ^[233]. Likewise, the broad and weak peak around 2834 cm^{-1} (Figure 48) is neither attributed to a second-order 2D band (D-band overtone), which normally features few-layered graphene ^[233], nor accounted for

combinations of the G and D (G+D) graphitic lattice vibration modes, which is characteristic for disturbed graphitic structures^[233-234]. All in all, D, G, 2D and combination (G+D) bands provide information about structural defects within graphitic systems^[233-234]. Therefore, detailed analyses by applying different fitting methods to obtain insights about the defect entities were not successful as these fitting methods were developed for graphitic or soot materials^[226, 234]. X-ray diffraction patterns of the measured hydrothermal carbon samples support the absence of highly structured domains due to a very broad band around 10–20° (Figure 49).

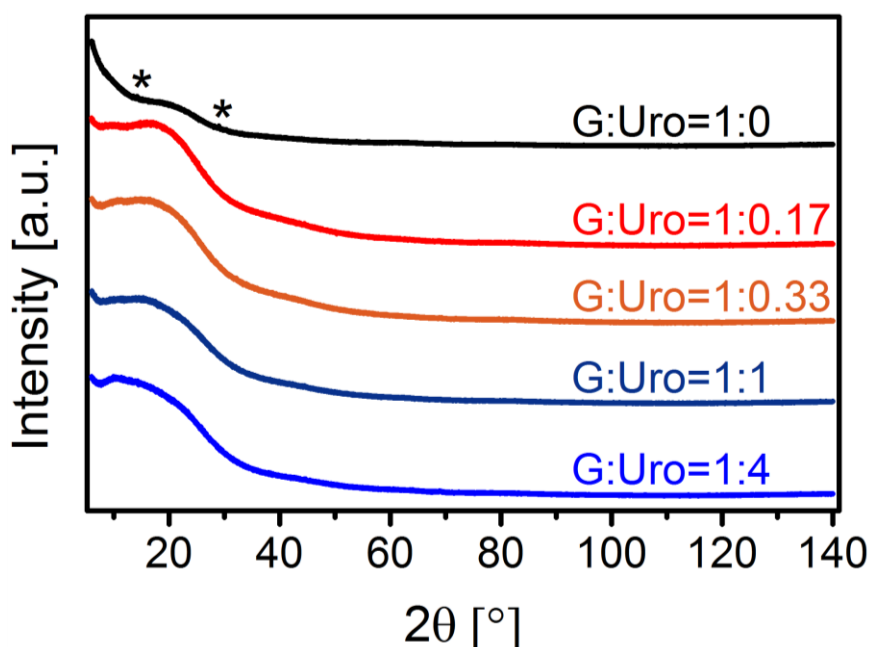


Figure 49: XRD powder pattern of all measured hydrothermal carbonaceous materials. Very small reflexes derived from the sample carrier are marked by an asterisk (*).

There is also the effect that due to fluorescence background a reasonable evaluation of the Raman spectrum is tremendously complicated. This phenomenon has been described before as an indication of the polycyclic molecular structure of the carbon materials^[41]. Raman measurements were performed on different spots of the surface of the pellets. Low laser power between 0.5 and 1.0 mW was applied in order to avoid beam damage on the material surface. Depending on the spots that were measured the intensity of the fluorescence changed, which is a hint for the inhomogeneity of the carbon

structure of the hydrothermal carbon materials. Annealing experiments would be appropriate to overcome this, but at the same time the amount of desired functional groups would be reduced. Nevertheless, for HTC materials exhibiting an acidic behavior and thus showing uniformly black color there is a change in the peak ratio of both bands. The band at 1577 cm^{-1} is sharper in contrast to the band at 1358 cm^{-1} , which can be considered as an evidence for a more condensed polymeric carbon network ^[41].

4.14. Electron Energy Loss Spectroscopy (EELS)

EELS is an efficient analytical characterization method for the N-HTCs (Figure 50).

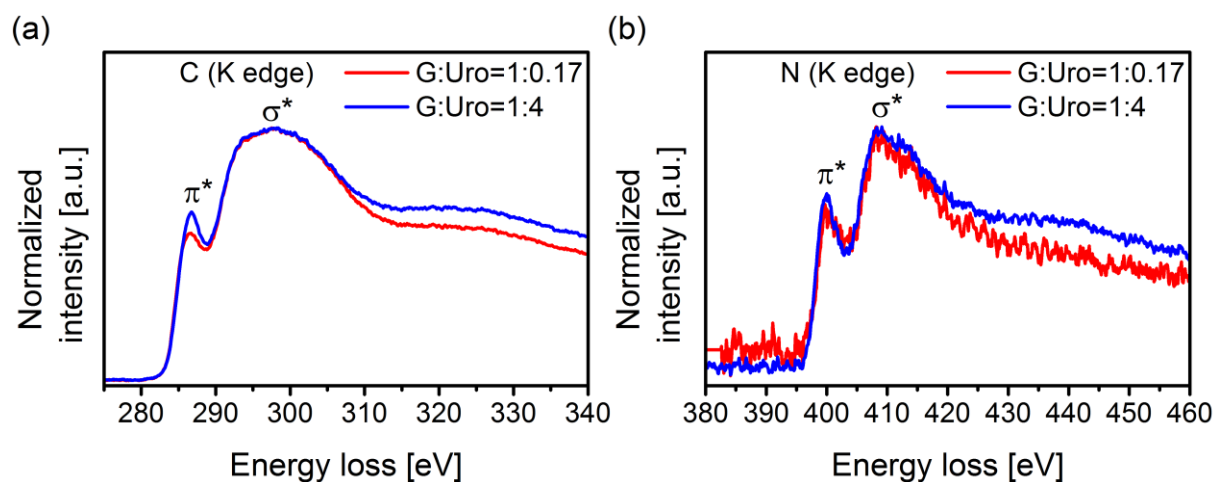


Figure 50: EELS spectra of N-HTCs with G:Uro=1:0.17 and G:Uro=1:4. (a) Carbon K-edge. (b) Nitrogen K-edge.

The fine structure of the absorption peak is related to the bonding and local electronic state ^[236]. The spectrum depicts the representative excitation of the C1s and N1s shell electrons to the empty conduction band. The carbon K-edge for both samples illustrate a sharp and defined peak at 286.8 eV which correspond to the excitation of 1s shell electrons to empty π^* orbitals ^[236b, 237]. Over the following energy losses above 286.8 eV the spectrum gets smooth and

featureless, characteristic for amorphous carbon [237a]. It means the loss of long-range order leads to a collapse in dipole selection rules and a blurring of the energy levels [237b]. In addition, interatomic distances and linkages or cross-linking cannot be determined anymore [237a]. The N-HTC material can be rather referred to as an isotropic mixture of polycyclic compounds [237a]. Transitions between 287 and 298 eV indicate a C-H σ^* orbital and therefore a high hydrogen content of both N-HTCs [237a, 238]. These finding was corroborated by Gaussian fitting curves to the π^* and σ^* peaks [237a, 238a]. Hence, the broad band at 293.4–301.8 eV cannot be ascribed to transitions to the π^* orbital interfusing partially with transitions to the σ^* orbital [237b]. At this stage, the σ^* orbital is not yet fully defined [237a]. It only occurs if the carbon materials are treated at higher temperatures, starting from around 750 °C [237a]. However, the ratio between π^* peak and σ^* peak is often referred to as the degree of graphitization of the sample [236b]. Consistent with this, the carbon K-edge suggests an amorphous state with a mixture of both sp^2 and sp^3 hybridization for the N-HTCs. The EELS profile of carbon and nitrogen K-edges are similar, which features the introduction of nitrogen atoms within the amorphous polymeric carbonaceous network. At around 399.9 eV the π^* peak in the nitrogen K-edge is assigned to the sp^2 hybridization state of N incorporated in the sp^2 bonded carbon network [239]. The σ^* peak at approximately 408.5 eV is not only ascribed to the sp^3 bonding nature with the carbon material but also to defect sites within the sp^3 bonding, such as pentagonal defects or corrugations within the structure [236a, 240].

4.15. Structural Comparison of Different HTCs via Solid-State-NMR Spectroscopy

N-free HTC material (G:Uro=1:0, N: 0 wt%), a sample with highest N-content (G:Uro=1:4, N: 19 wt%) and a sample with lowest N-content (G:Uro=1:0.17, N: 7 wt%) have been selected for NMR measurements. $^{13}\text{C}_6$ -labeled glucose and $^{13}\text{C}_6, ^{15}\text{N}_4$ -labeled urotropine were used as starting materials. Quantitative single pulse direct polarization (DP) ^{13}C magic angle spinning (MAS) NMR experiments were recorded for all three samples (Figure 51) [241].

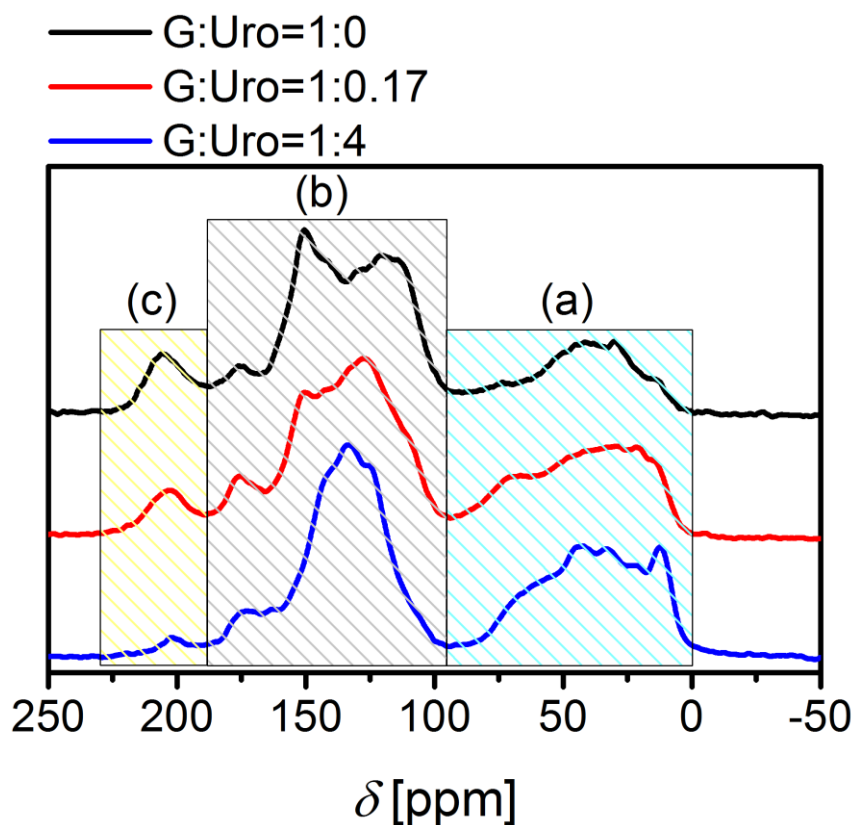


Figure 51: Quantitative DP ^{13}C NMR spectra of HTC materials based on $^{13}\text{C}_6$ -labeled glucose and $^{13}\text{C}_6, ^{15}\text{N}_4$ -labeled urotropine with regions (a) 0-95 ppm (b) 95-188 ppm and (c) 188-230 ppm. Black: N-free HTC, red: lowest N-containing HTC, blue: highest N-containing HTC.

The spectra can be divided coarsely into three regions. The sp^3 aliphatic carbons cover the chemical shift range from 0 to 95 ppm (region (a)). Resonances of sp^2 carbons (C=C bonds), including aromatic and carboxylic groups, appear between 95 and 188 ppm (region (b)). From 188 to 230 ppm

carbonyl groups, especially ketones and aldehydes, can be assigned (region (c)) [51b, 53a, 242]. The quantification of the different regions for the three samples is summarized in Table 5.

Table 5: Band assignments for the DP ^{13}C NMR spectra of the HTCs based on $^{13}\text{C}_6$ -labeled glucose and $^{13}\text{C}_6$, $^{15}\text{N}_4$ -labeled urotropine.

G:Uro	δ (ppm)	Functional group	Relative share [%]
1:0	188-230	Ketone	9
	95-188	Aromatic, carboxylic	65
	0-95	Aliphatic	26
1:0.17	188-230	Ketone	6
	95-188	Aromatic, carboxylic	58
	0-95	Aliphatic	36
1:4	188-230	Ketone	2
	95-188	Aromatic, carboxylic	55
	0-95	Aliphatic	43

The presence of aliphatic groups (region (a)) in the HTC structure increases from 26 to 43 % with increasing N content. This can be explained presumably on the one hand by the introduction of secondary amine groups, which show a resonance at around 53 ppm (Figure 51), and on the other hand by the overall reductive synthesis conditions. At the same time, several resonances that correspond to sp^3 aliphatic carbon atoms are rather well resolved at high N content, which points towards fairly well-defined structural features. In particular, a resonance at 10 ppm, which corresponds essentially to methyl groups connected to a carbon, shows an amplitude that indicates a relative share of about 5 %. At low N content this resonance is poorly resolved and shows less than half the intensity, and in the sample without N its amplitude is reduced further. In addition, between 60 and 90 ppm there are overlapping resonances of different types of alkyl ether groups. Unreacted glucose would show resonances in this region as well, yet the absence of noticeable signals between 90 and 100 ppm indicates very low glucose content below about 1% relative share even for N-free HTC.

The overall fraction of aromatic sp^2 carbons and C=C double bonds (region (b)) diminishes slightly from 65 to 55 % with increasing N content, yet individual features change considerably. This region also includes sp^2 carbons with oxygen bonds such as O-C=C or C=O groups (carboxylic acid moieties, carbonate, ester, amide) between 165 and 185 ppm, heteroatom-bonded aromatic compounds (145–165 ppm) and aromatic compounds/acetals (95–145 ppm). The N-free HTC material contains a small quantity of carboxylic acids. The proportion of furans is high and can be described by the signals at 110 ppm and at 145 ppm. By addition of urotropine (G:Uro=1:0.17) the share of carbon-based aromatic components rises, which corresponds to the resonance at 128 ppm. Also, a high amount of methyl furan species can be identified at 152 ppm. For G:Uro=1:4, the aromatic nature of the sample is by far the highest, as confirmed by the sharp signal at 134 ppm. The furan character of this HTC material is quite low, probably due to substitution of O-functional groups with N-containing functional groups.

In region (c) C=O groups, especially ketones and aldehydes (200–220 ppm), can be detected. The ratio of carbonyls is highest for N-free HTC with a share of 9% and lowest for N-HTC with highest N-content with a relative share of 2 %, which can be accounted for by the reductive conditions during synthesis.

Cross-polarization (CP) MAS measurements with varying contact times were carried out for all three samples to determine C-H connectivities and to identify the chemical environment of ^{13}C as well as ^1H nuclei (Figure 52).

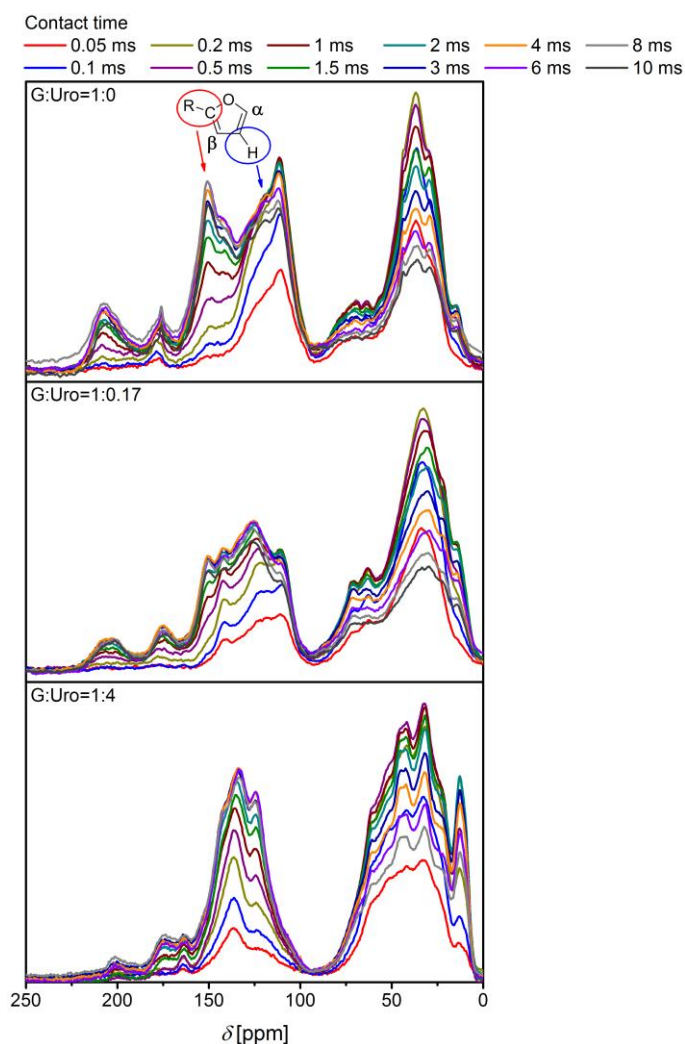


Figure 52: Variable contact time ^{13}C CP NMR spectra for G:Uro=1:0, G:Uro=1:0.17 and G:Uro=1:4.

For the N-free HTC material weaker resonances are obtained beyond 170 ppm, indicating a smaller concentration of aldehydes. In particular HMF can be regarded as aldehyde source. In the structural network, most heteroaromatic compounds are linked by the C_α of a furan whereas the C_β features a high share of connected protons (Figure 52).

For the lowest N-containing HTC the presence of aldehydes can be excluded since the resonances at characteristic frequencies do not show an enhancement at short contact times. For the peak at 151 ppm the absence of bonded protons can be detected, pointing to a crosslinking between C_α of the furan ring with, most likely, aliphatic carbons. Just as for G:Uro=1:0.17, in the highly N-containing HTC (G:Uro=1:4) the presence of aldehydes can be excluded, too.

In order to identify carbon environments within a C-C network in the different structural motifs, 2D CP MAS homonuclear single-quantum double-quantum (SQ-DQ) ^{13}C correlation experiments were performed (Figure 53).

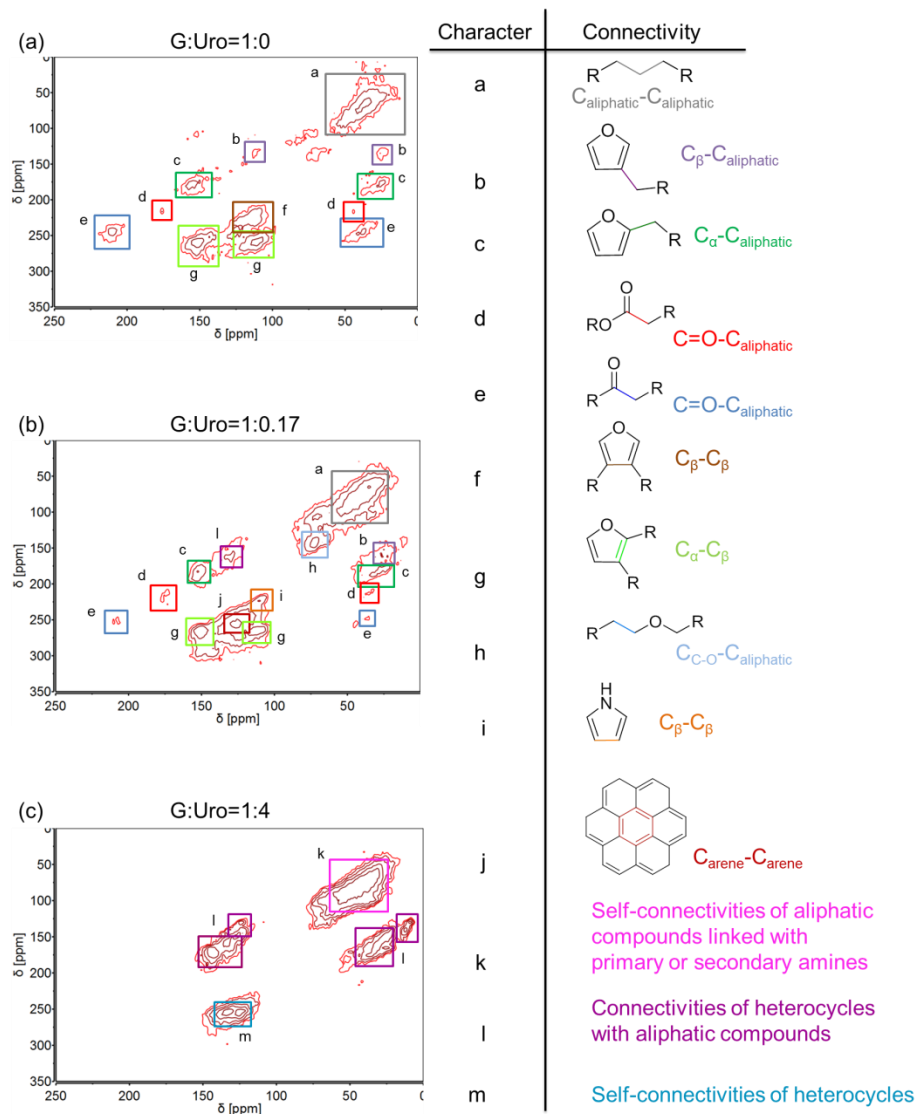


Figure 53: 2D CP MAS SQ-DQ ^{13}C correlation spectra with 15 kHz spinning frequency for (a) G:Uro=1:0, (b) G:Uro=1:0.17 and (c) G:Uro=1:4. Different resonances are marked with letters **a-m**. The corresponding structural motifs are shown on the right.

The projection along SQ and DQ projections are compiled in the following (Figure 54).

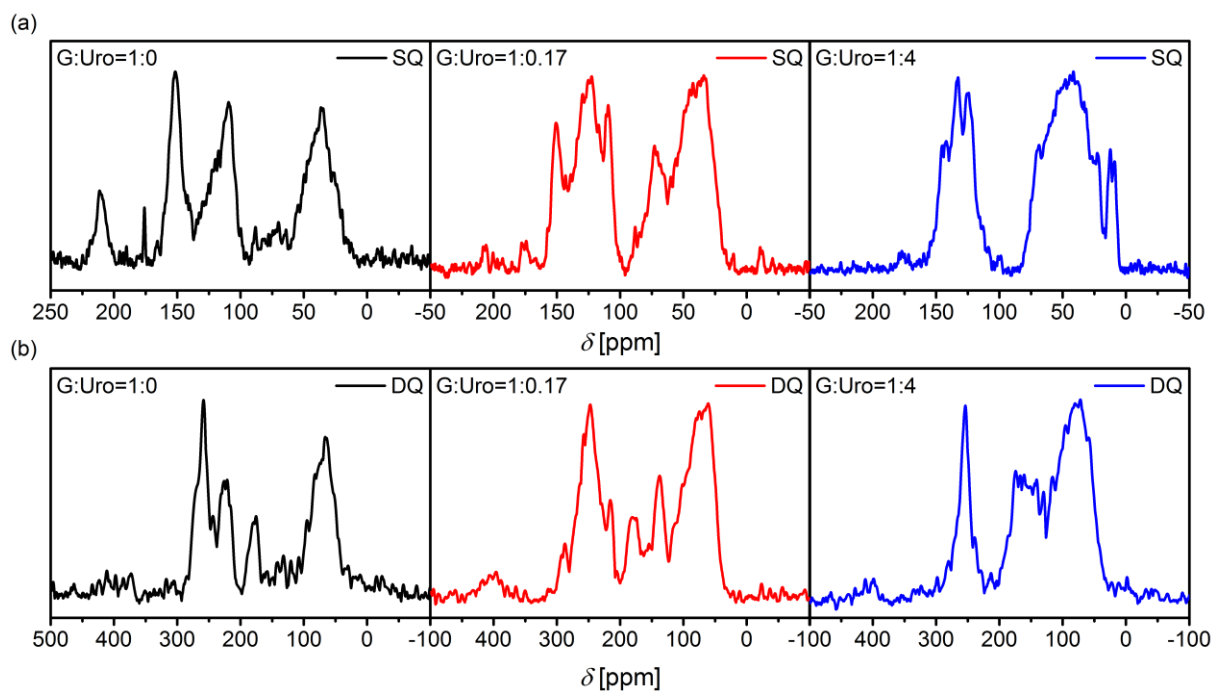


Figure 54: (a) SQ projection and (b) DQ projection of 2D CP MAS SQ-DQ ^{13}C correlation spectrum with 15 kHz MAS frequency for G:Uro=1:0, G:Uro=1:0.17 and G:Uro=1:4.

The assignment of the cross-peaks of the correlation patterns to the corresponding C-C connectivity based on glucose or cellulose as starting material was done in accordance with the literature [51b, 53b, 242].

For the N-free HTC material the broad cross-peak at 12–60 ppm (a) derives from aliphatic carbons, showing various C-C correlations among the aliphatic carbon atoms. Sharp correlation peaks of $\text{C}_\alpha\text{-C}_\beta$ and $\text{C}_\beta\text{-C}_\beta$ of furanic linkages are observed (f–g), but also furanic rings linked with aliphatic groups (b–c) as well as keto groups bonded with aliphatic compounds (d–e). The weak signals at approximately 176 ppm (d) corroborate the presence of aliphatic carboxylic acids or esters. However, they can also be attributed to embedded or crosslinked levulinic acid-type functions within the organic polymer-like carbonaceous network [51b, 242a].

With respect to N-containing HTC materials, additionally ether-like functions (h) or pyrrolic-like groups can be proposed (i). In general, by gradual increase of the N-content, changes occur in the correlation spectra when comparing (a) with (b) and (c) in Figure 55.

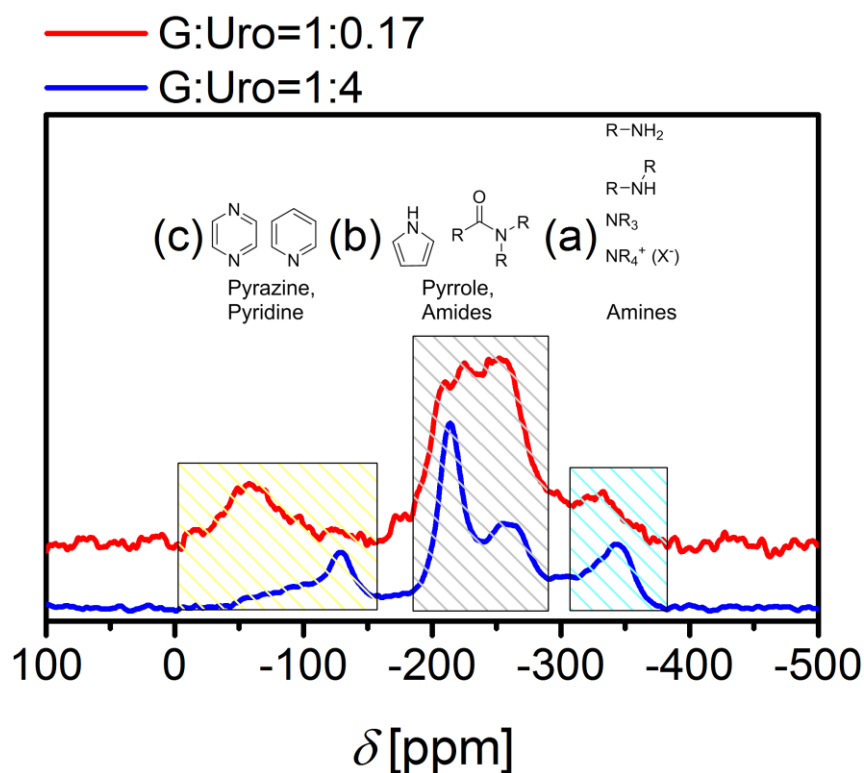


Figure 55: ^{15}N CP MAS NMR spectrum with 30 kHz spinning frequency for G:Uro=1:0.17 (red) and G:Uro=1:4 (blue).

In particular, O-functional groups or atoms are substituted by N-groups, which are observed from the occurrence of correlation peaks such as (i). The correlation spectrum of the N-HTC with G:Uro=1:0.17 reveals a rise of the aromatic carbon density, and an increase of aromatic self-connectivities into a polycyclic aromatic-like structure can be observed (j). Furthermore, connectivities of heterocyclic compounds with aliphatic compounds can be identified (l).

The correlation spectrum of the N-HTC with G:Uro=1:4 shows self-connectivities (C-C) of aliphatic compounds bonded to primary or secondary amines (k). Likewise, the percentage of self-connectivities of heterocycles grows as well (m). On the other hand, the cross-connectivities between carbonyl-based and aliphatic carbons as well as furanic rings disappear completely. Instead, the share of N-functional groups and structural motifs rises. In addition to the structural motifs such as pyrazine, pyridine, pyrrole, amides or amines shown in Figure 55, further N-based compounds are possible.

Since the cross-peak (**m**) encloses a chemical shift between 121 ppm and 137 ppm, according to literature various structural motifs could be responsible. These include mainly five- and six-membered heterocyclic compounds. Among other heterocycles, imidazole is assumed to be a representative candidate but further studies are necessary ^[243]. Taken as a whole, the results prove that in the absence of N, furanic structures are the essential structural motifs in which aliphatic compounds act as linkers within the polymeric carbon network. However, by increasing the molar ratio of urotropine to glucose, furanic groups disappear due to the more reductive synthesis conditions and are substituted by N-containing entities.

The N-HTCs (G:Uro=1:0.17 and G:Uro=1:4) were subjected to ¹⁵N CP MAS NMR measurements (Figure 55) to get a detailed insight into N-functional moieties. As a chemical shift reference the nitromethane scale was applied ($\delta_{\text{NH}_3} = \delta_{\text{CH}_3\text{NO}_2} + 380.5$ ppm).

Several N-containing structural motifs such as amines, pyrrole and amides, or pyrazine and pyridine (Table 6) can be assigned to the resonances contained in three distinct regions (a)–(c) (Figure 55).

Table 6: Peak assignments and structural motifs of the ¹⁵N CP MAS NMR spectrum for G:Uro=1:0.17 and G:Uro=1:4.

G:Uro	δ (ppm)	Structural motif	Region
1:0.17	-369 – -307	Amines	(a)
	-290 – -185	Pyrrole, amides	(b)
	-112 – -3	Pyrazine, pyridine	(c)
1:4	-383 – -307	Amines	(a)
	-290 – -185	Pyrrole, amides	(b)
	-158 – -39	Pyrazine, pyridine	(c)

Mainly in regions (b) and (c), considerable differences in the positions and the shape of the resonances are visible for the two investigated N-HTCs. In general, for G:Uro=1:0.17 the resonances are less clearly resolved than for G:Uro=1:4, consistent with a higher structural ordering with increasing N content, as already observed in the ¹³C NMR spectra. In region (b) fewer

resonances are visible for G:Uro=1:4, indicating a smaller number of distinct N-containing structural motifs. In region (c) the main signal for G:Uro=1:4 appears at a lower resonance frequency than for G:Uro=1:0.17, indicating a decrease of pyrazines and a simultaneous increase of pyridines with increasing N content. In region (a), a distinction between primary, secondary or tertiary amines is not unambiguously possible. As a rough trend, a small shift towards lower frequency for G:Uro=1:4 may hint towards amides with more directly bound hydrogens with increasing N. For the N-HTC with highest N-content most probably the quaternary amine with its resonance at -343 ppm can be assigned to an ammonium ion (NH_4^+)^[244].

4.16. Structural Models

Drawn from the obtained results of elemental analysis, experimental and calculated FTIR spectra, TG-MS measurements as well as solid-state NMR experiments three different prototypical structural models are proposed to describe nitrogen-free (0 wt% N), lowest nitrogen-containing (7 wt% N) and highest nitrogen-containing (19 wt% N) hydrothermal carbons (Figure 56).

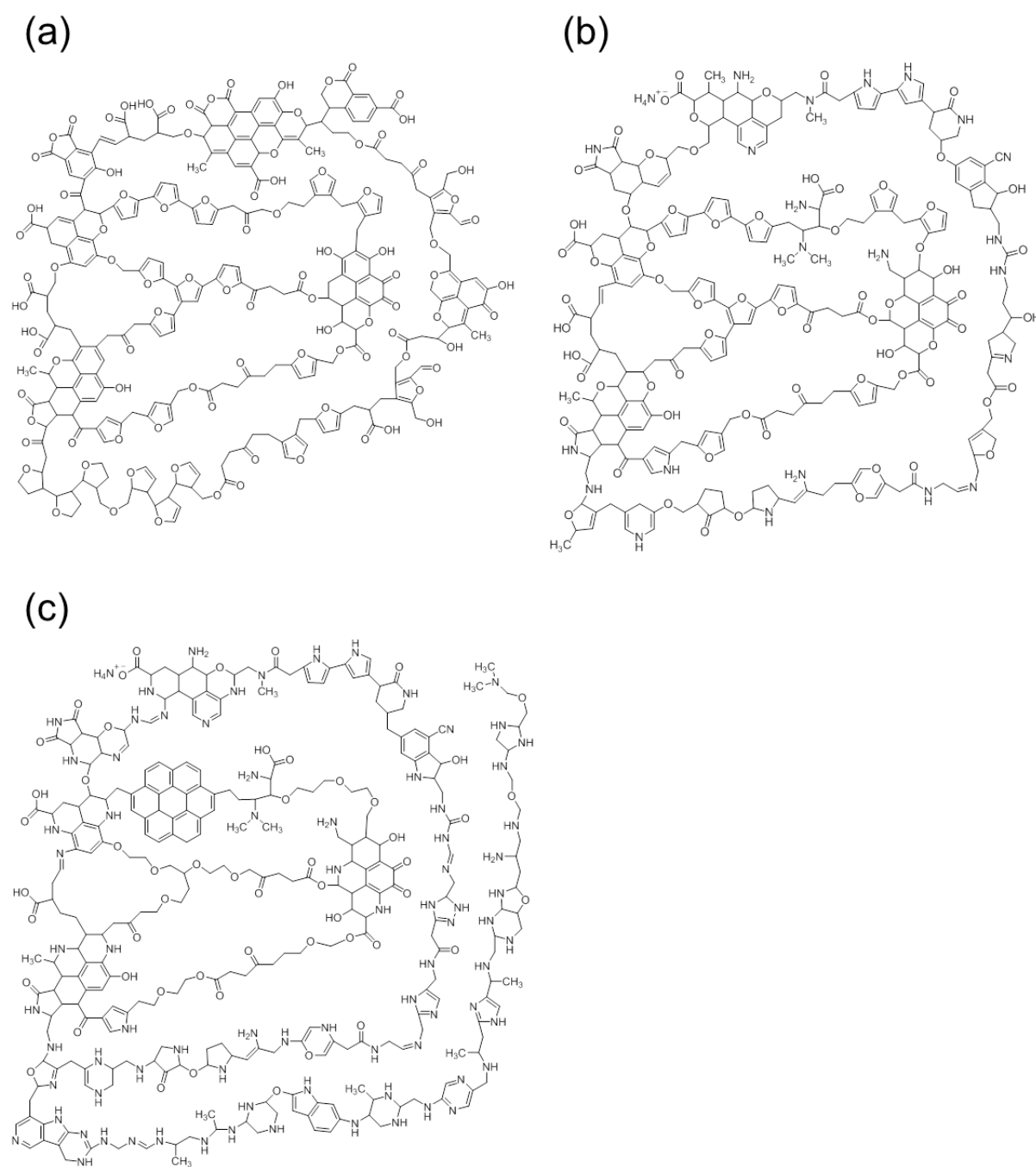


Figure 56: Structural models proposed for hydrothermal carbons with (a) N-free, (b) lowest N-containing (7 wt%) and (c) highest N-containing (19 wt%) scaffold.

First of all, the carbon scaffold has been considered as a polymer-like structure, consisting of condensed cyclohexane and linear structures as well as polyfuranic chain entities showing only a few domains of aromaticity. Based on solid-state NMR spectroscopy the sp^2 bonding character increases gradually with raising N-content, implying that the aromatic nature of G:Uro=1:4 is highest. Simultaneously, aliphatic sp^3 carbons rise by increasing the amount of

N. Hence, N-HTC with highest N-content (G:Uro=1:4) has the highest sp^3 character. The functional groups and structural motifs are taken on the basis of the findings of FTIR spectra and TG-MS as well as solid-state NMR spectroscopy. Hydroxy, amine, methylene-type and carbonyl groups as well as aromatic alkene-like structures are taken from FTIR spectroscopy. Further O-functional groups such as carboxylic, anhydride, lactone, phenolic, ether, quinone or keto groups are based on TG-MS. N-functional groups embracing nitrile, imide, lactam, amine (prim./sec./tert./quat.), pyrrolic and pyridinic groups are also attributed to TG-MS. Both characterization techniques are surface-sensitive. Most information about functionalities or structural motifs is gained from solid-state NMR, which is a bulk-sensitive analytical method. These involve aliphatic compounds (hydrocarbons), furanic entities (linked with aliphatic structures), aliphatic carboxylic acids or esters (embedded or cross-linked levulinic acid-type functions), keto groups (bonded with aliphatic moieties), ether-like functionalities as well as polycyclic condensed structures. In the presence of N, amide, amines (prim./sec./tert./quat.), pyrazine, pyrrolic and pyridinic groups can be identified. Additionally, aliphatic carbons bonded to primary or secondary amines and heterocycles (linked with aliphatic groups) can be detected. Based on the analysis for an N-free HTC material, solely O-functional groups and O-related structural motifs are incorporated. Mainly furan-based entities are introduced that are bonded with aliphatic chains containing O atoms or groups such as levulinic acid-type linkers. In addition, condensed cyclohexane rings or HMF moieties are taken into account (Figure 56 (a)). N-HTC with lowest N-content denotes a mixture of both O- and N-functional groups. Structural motifs include amine, amide, ammonium carboxylate, nitrile, amino acid, imide, lactam, and pyrrolic compounds (Figure 56 (b)). N-HTC with the highest N-containing scaffold exhibits a stronger percentage of the aforementioned N-functional groups, especially pyrrolic and pyridinic groups come into full effect (Figure 56 (c)). So we can conclude a

successive exchange of O-functional groups by N-functional groups. While carbonyl functional groups form furanic entities in the absence of N, the reaction pathways change with increasing abundance of NH_3 in the reaction mixture. For instance, pyrrol or pyridine syntheses are favored. Hence, only with the addition of a large amount of N-precursor, more temperature-stable N-functional groups such as pyrrol or pyridinic groups are formed.

4.17. Concluding Remarks

In this work, the hydrothermal synthetic route was applied based on the precursors glucose and urotropine. Urotropine turns out to be a powerful N-precursor due to the multitude of possible reaction pathways it can undergo. Especially its decomposition product ammonia contributes various reaction mechanisms leading to numerous different structural motifs.

The HTC chars are semiconductor-like materials. The materials feature an extended degree of internal condensation of the polymeric carbonaceous network. Also, these materials possess a high powder density. It can be concluded that the combination of nitrogen and oxygen strengthen the stability of the structural network. Furthermore, the pronounced presence of the carbonyl group ($\text{C}=\text{O}$) is presumably an important factor for stabilization.

HTC materials of spherical morphology with high N-content of about 19 wt% were achieved. Precursor decomposition during hydrothermal synthesis occurs over a wide range of complex reaction pathways, yielding a multitude of organic compounds, structural motifs and functional groups especially in the presence of an N-precursor. The preparative success results in HTC chars with a high number of N- and O-functional groups. They are able to bind positively and negatively charged ions. The HTC materials can be therefore used as adsorbents or for the application as support catalysts. By increasing the molar ratio of

urotropine to glucose, the color of the materials turns from black to brown. Likewise, the HTC yield, carbon efficiency and the powder density of these N-HTCs diminish dramatically. The pH changes to a more alkaline behavior, too, which causes an increase of pyrrolic and pyridinic structural motifs according to TG-MS experiments. Features such as the macroscopic morphology or the internal polymeric structural network, which play a crucial role for the material properties, are drastically changed. By only adding a urotropine mass fraction of about 3 wt%, the carbon efficiency could be increased to a maximum value of 64 % and a HTC yield of 42 % could be reached.

This is the first comprehensive analytical investigation of a series of N-containing HTCs, comprising analytical data of UV/VIS, HPLC, optical microscopy, SEM/(HR)TEM, BET, elemental analysis, FTIR, electronic structure calculations, TG-MS, zeta potential, acid-base titration, Raman, XRD, EELS and solid-state NMR. Only with the combination of these methods, scientific findings on the complex structure could be gained.

In order to assess the presence of certain functional groups or structural motifs from vibrational spectra, electronic structure calculations can be applied. Even though the whole system is by far too complex to simulate, the cooperative effects of different vibrational modes allow the estimation of the most abundant structural features of the carbonaceous network.

Solid-state NMR measurements confirm that furan-based moieties are the key structural motifs in which aliphatic compounds act as linkers within the polymeric carbonaceous network. By increasing the molar ratio of urotropine to glucose, furanic structures disappear due to the more reductive synthesis conditions and are substituted by N-containing entities.

The mechanistic success reflects on the three samples (Sample 1: G:Uro=1:0, sample 2: G:Uro=1:0.17 and sample 3: G:Uro=1:4) that were subjected to solid-state NMR. Sample 1 follows the oxidative synthetic pathway as described in Figure 14.

Consequently, furan-based functions and condensed entities are obtained. Under these conditions, HTC chars with relatively low carbon efficiency are produced. Sample 2 underwent during the synthesis probably first reductive and then oxidative synthesis routes. The final overall pH value is acidic. O-functional groups are substituted by N-functional groups but do not condense extensively to pyrrolic or pyridinic groups. The alkaline additive urotropine seems to trigger an activating effect in terms of chemical cross-linking of the polymeric carbonaceous network yielding higher carbon efficiencies. Sample 3 only went through alkaline medium during synthesis. Under these reductive conditions, a high proportion of fragmentation reactions occur, such as β -elimination, retro-aldol fragmentation, hydrolytic β -dicarbonyl fragmentation, benzylic acid-type rearrangements or deprotonations. These fragmentation reactions presumably cause again lower carbon efficiencies.

Three different structural models are proposed to describe N-free (0 wt% N), lowest N-containing (7 wt% N) and highest N-containing (19 wt% N) hydrothermal carbons based on the findings of elemental analysis, experimental and calculated FTIR spectra, TG-MS measurements as well as solid-state NMR experiments. With raising the molar ratio of urotropine to glucose a gradual exchange of O-functional groups by N-functional groups can be concluded. In the absence of N, mostly furanic entities linked with aliphatic groups are proposed. By the addition of N-precursor, a multitude of parallel reactions occurs, forming several types of N-functional groups and N-based structural motifs due to the increasing presence of NH_3 in the reaction mixture. Only with high addition of N, more temperature stable N-functional groups such as pyrrol or pyridine are formed.

The suggested structural models are coal structure models, which are inspired by the diversity of existing coal structure models ^[7, 245]. Coal itself is one of the most heterogeneous organic sedimentary rock of vegetal origin with a complex chemical and physical structure, containing for the most part carbon, hydrogen,

(hydro)aromatic rings, heteroatoms (O, N or S), heterocycles (furan, quinone, pyridine, pyrrole, thiophene), aliphatic/ether bridges and other elements including mineral matter which are cross-linked in a macromolecular three-dimensional network [7, 245a-d, 246]. The structural models are therefore neither graphite nor a macromolecule. Although HTC chars are somewhat similar to polymers, they can better be described as the lowest rank of coal. The rank of coal is correlated with the carbon content, heating value and the amount of volatiles. Lowest rank of coals are characterized by their lowest carbon content, lowest heating value but at the same time highest amount of volatiles [247]. Hence, HTC chars can be classified as lignite [49].

In carbon materials, heteroatoms such as O or N provide various advantages. In N-containing carbon, improved π -bonding, electrical conductivity and Lewis basicity are present, simplifying reductive processes such as reductive oxygen adsorption on the carbon surface. Structural defects in the carbon lattice caused by heteroatoms yield more edge-active sites. It is accepted that edge-bound heteroatoms (e.g. pyridine) have an enhanced catalytic importance. Main advantage of the synthesized N-HTCs is the fact that they were synthesized at mild reaction conditions, providing them with polar surface functional groups that are responsible for their hydrophilic material property. This factor can modify their selectivity or can offer the possibility for further modifications by means of simple chemical functionalization.

Since HTC chars are regarded as green and sustainable renewable energy sources one promising application is the utilization in storage technologies, such as power-to-gas, converting electricity to hydrogen as feedstock or fuel via water electrolysis, or producing carbon dioxide to generate synthetic natural gas (methanation) [148a]. Among other application fields, N-HTCs are promising candidates for the utilization as sorption materials for the removal of heavy metals (Pb^{2+} , Cd^{2+} , Cu^{2+} , U^{6+}) or organic pollutants (e.g. dyes) from waste water due to their abundance in surface functional groups. The low surface area of

these materials does not present any problems. By variation of the pH values the selectivity towards a certain heavy metal could be increased by improving the binding capacity. Also, the removal of an organic dye pollutant from water can be achieved at a certain pH range. Overall, the obtained HTC carbons appear to be promising candidates for widespread applications where the already mentioned advantageous properties of the materials might be of crucial importance. The materials are currently tested for such applications. Ongoing works include further pressing the powder to pellets and subject them to pyrolysis in order to obtain disc electrode materials for electrochemical applications. Investigations include the application in the water splitting process within the oxygen evolution reaction (OER) or for fuel cell application in the oxygen reduction reaction (ORR).

The results of the previous chapters were recently successfully published in Chemistry – A European Journal (DOI: [10.1002/chem.201800341](https://doi.org/10.1002/chem.201800341)).

4.18. Pyrolyzed HTC Chars: Disc Electrode Preparation and Characterization

The HTCs were pelletized with a pressure of 10 t within 2-3 min and thermally annealed at 900 °C for 5 h in inert atmosphere with a nitrogen flow of 520 mL·min⁻¹. A preparation scheme is shown in Figure 57. The hydrothermal synthesis of N-HTCs was in detail described in chapter 3.1.

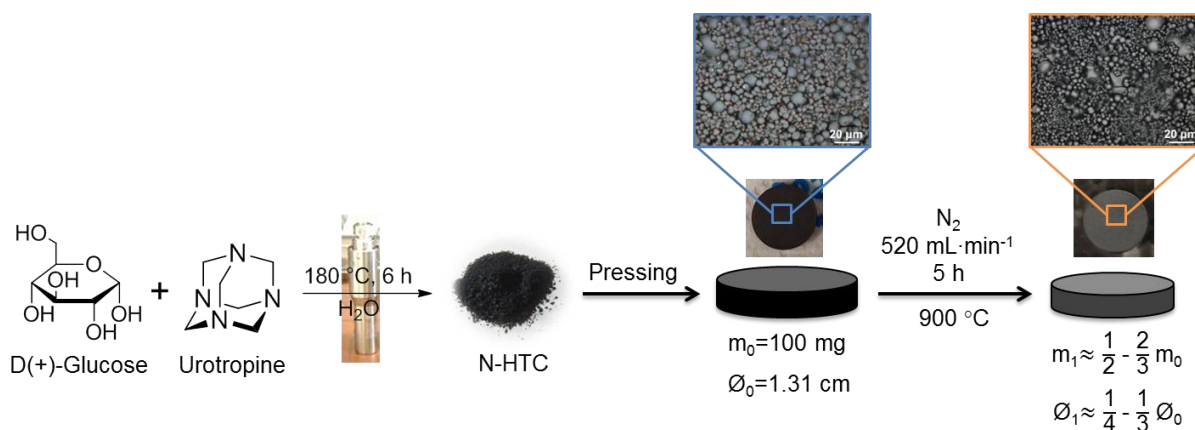


Figure 57: Schematic illustration of the preparation of disc electrodes and subsequent pyrolysis accompanied by a mass and diameter loss as well as by shrinkage of the spherical particles.

SEM micrographs of the powder materials confirm microspherule particles of all samples illustrating domains of together merged particles and, importantly, spherical morphology maintains upon thermal annealing (Figure 58).

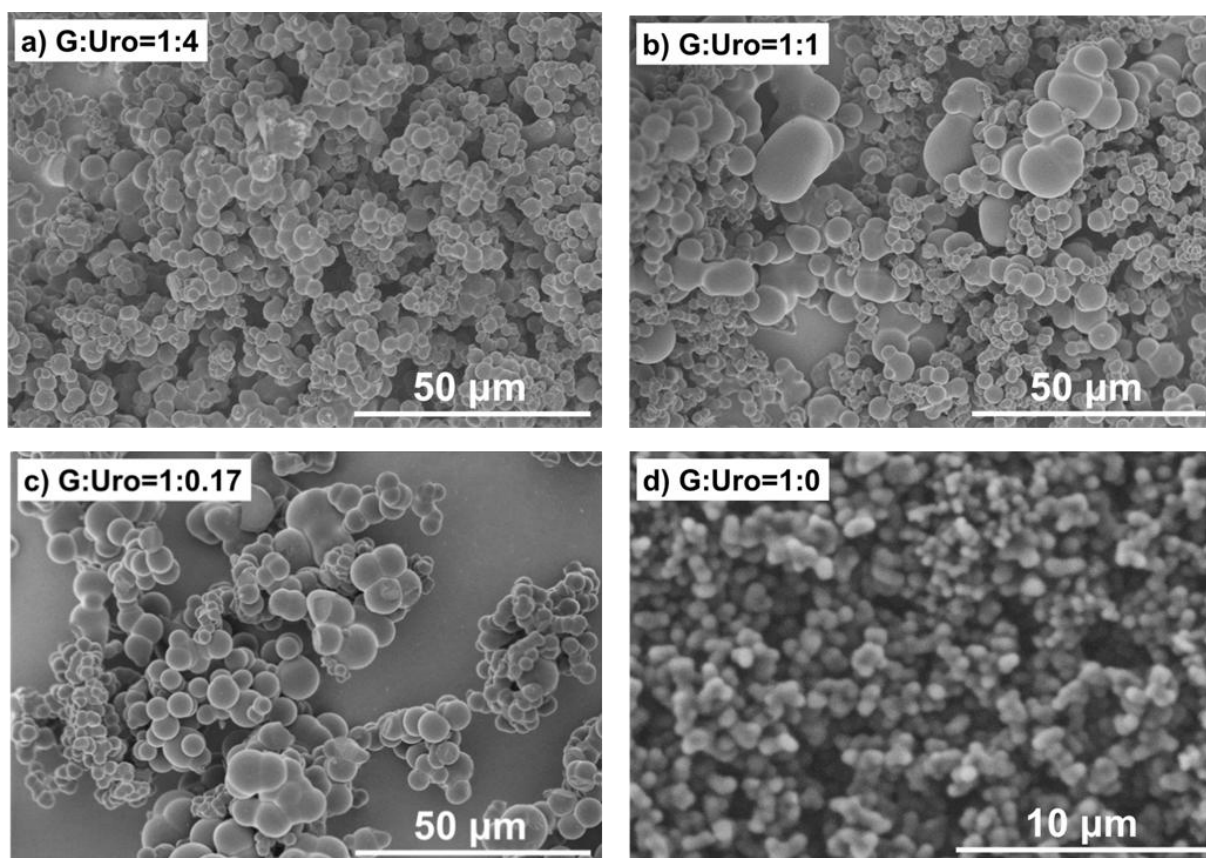


Figure 58: (a)-(c) Scanning electron micrographs of thermally annealed HTC powder materials with (a) highest, (b) medium and (c) lowest N-content, as well as (d) N-free HTC as reference material. All samples have spherical morphology.

From optical microscopic images the size of spherical particles can be measured (Figure 59, and Figure 60).

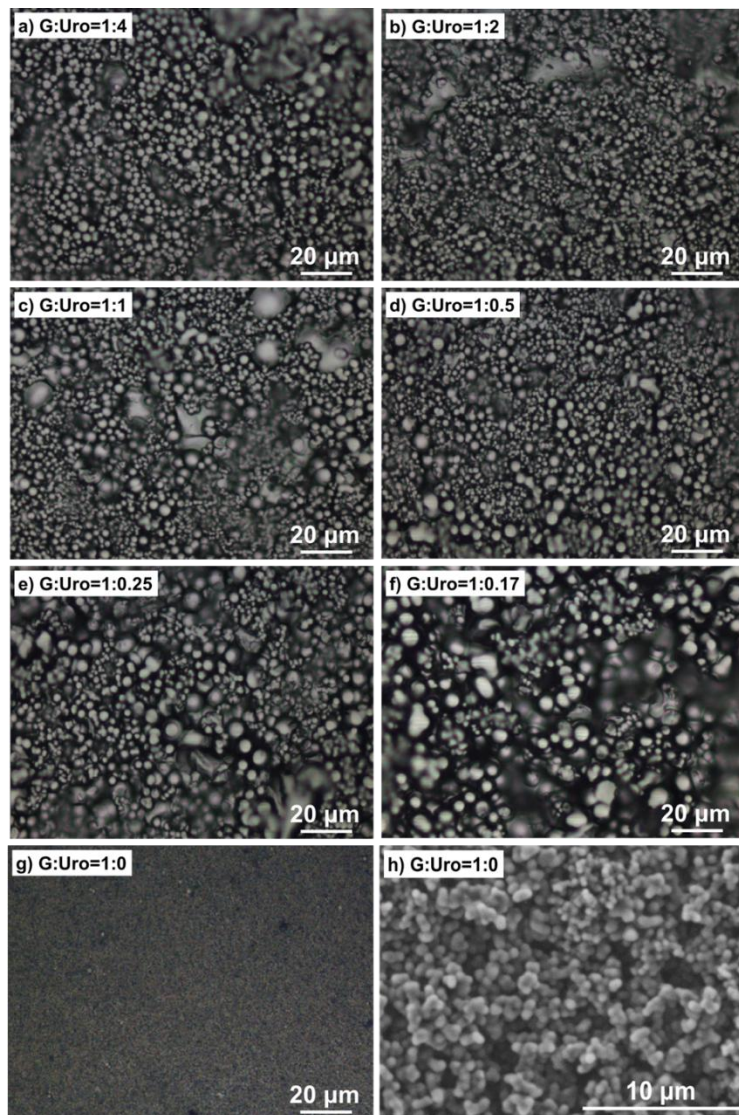


Figure 59: (a)-(f) Optical microscopic images of pyrolyzed HTC discs.

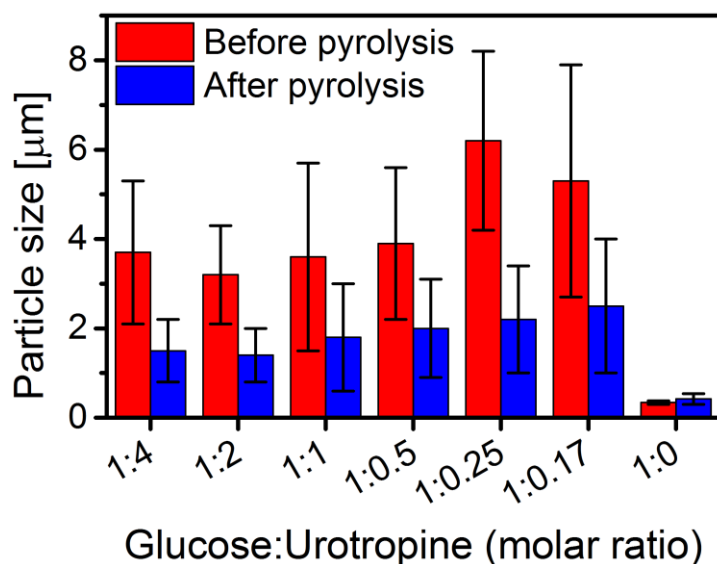


Figure 60: Comparison of particle sizes of HTC discs before and after pyrolysis.

In case of N-containing HTCs, the average particle size ranges between 3.2 μm and 6.2 μm but can be regarded as similar. On the one hand due to the inhomogeneity and on the other hand because of the high standard deviation. In contrast to it, the average particle size of an N-free HTC is substantially smaller and has a value of only 0.34 μm . Thermal annealing is accompanied by reduction of the particle size (Figure 60). Comparing the N-HTCs among each other, the average particle size encloses 1.4-2.5 μm . Besides, the average particle size of an N-free HTC seems unaffected. The shrinkage of the particles results as well in a significant shrinkage of the pressed and pyrolyzed pellets (Figure 61).

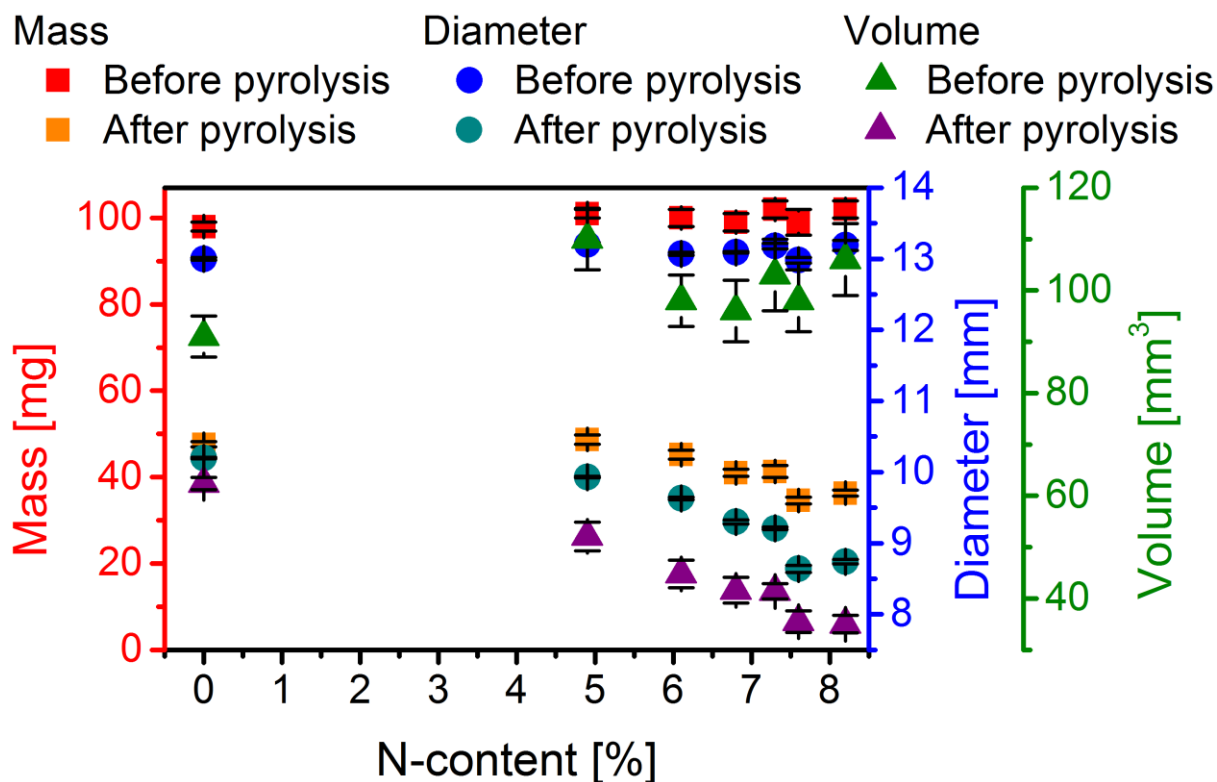


Figure 61: Geometrical analyses of HTC disc electrodes before and after pyrolysis.

Geometrical analyses of the disc electrodes have been carried out before and after pyrolysis, respectively. Mass and diameter as well as the height and the volume reduce. There are some trends visible indicating that higher N-content yields in a more pronounced mass and diameter loss (including decrease of the height and the volume). Around 2/3 of the initial mass diminishes depending on the molar ratio of urotropine towards glucose. Analogously, the diameter shrinks to a value of 1/3 of the initial diameter. Linked to this, there is a reduction of the height and the volume of the pellets. The height falls to maximal values of 1/4 of the initial height and the volume drops to 2/3 of the starting volume. Independent from the N-content, the geometric density of all disc electrodes is around $1 \text{ g}\cdot\text{cm}^{-3}$, while the diameter was measured to be 13 mm.

After pyrolysis, the amount of nitrogen decreases from 19 wt% down to 8 wt% at simultaneous increase of the carbon content up to 91 wt% which points to the fact that the materials possess a pronounced carbonized character. The

low H-content of below 1 wt% points to the highly condensed nature of the carbonaceous material (Figure 62).

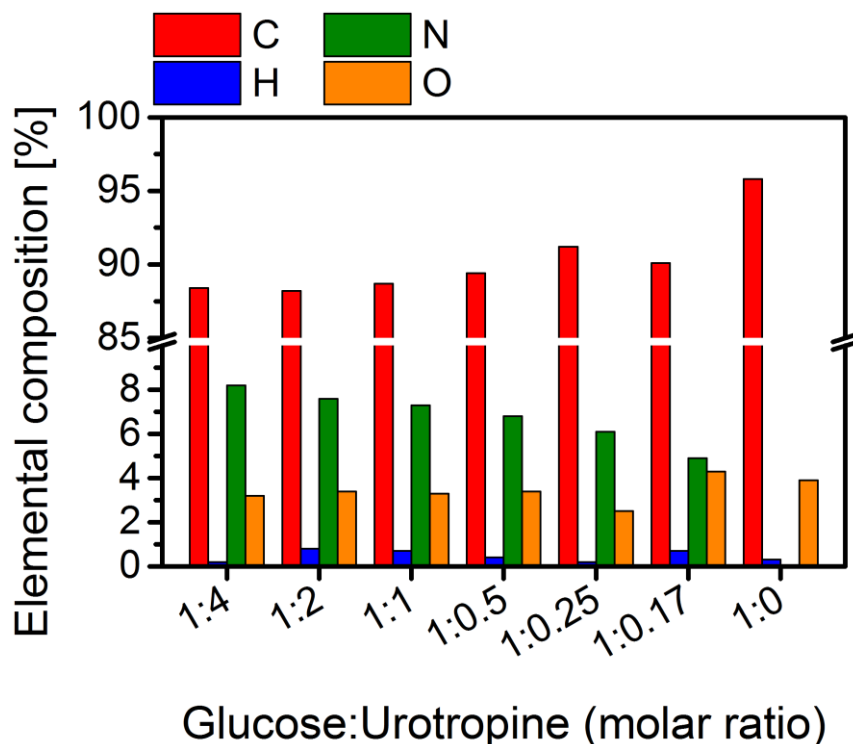


Figure 62: Elemental composition of thermally annealed HTCs.

The BET surface area of the measured pyrolyzed N-HTC materials verifies low surface area of around $1 \text{ m}^2 \cdot \text{g}^{-1}$. Surprisingly, an N-free HTC possesses a significantly higher surface area with $347 \text{ m}^2 \cdot \text{g}^{-1}$ (Table 7).

Table 7: BET surface area of pyrolyzed HTCs.

G:Uro [mol]	Surface area [$\text{m}^2 \cdot \text{g}^{-1}$]
1:4	1
1:1	1
1:0.17	1
1:0	347

Although it is reported that thermal annealing of HTC leads to rising degree of structural order (long-range order) in which aromatized domains are formed suggesting a more turbostratic-like structure ^[126d], the Raman spectra of our HTC electrode materials show broad bands of the representative bands at 1355 cm^{-1} and 1584 cm^{-1} (Figure 63).

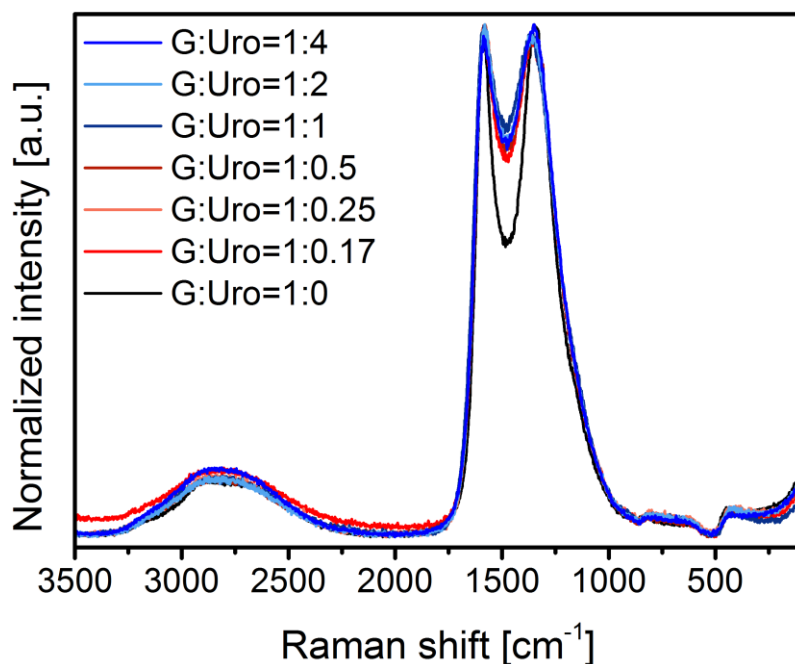


Figure 63: Raman spectra of thermally annealed HTC pellets at distinct molar ratio of glucose towards urotropine. Compared to non-pyrolyzed HTCs no fluorescence background is observed.

The broadening is mainly attributed to molecular excitations of the carbonaceous network ^[41]. In comparison with non-pyrolyzed HTCs, no fluorescence background is observed. It means pyrolyzed HTCs treated at 900 °C are not abundant in functional groups in contrast to non-pyrolyzed HTCs ^[41]. Pyrolyzed HTCs at 900 °C are still somewhat related to amorphous carbon. Thus, they are not of graphitic or graphene origin. Soot can also be excluded as it can be described as a material containing highly disordered graphitic structures ^[234]. Polycyclic aromatic hydrocarbon compounds such as hexabenzocoronene are not comparable either as this material is comparable with a section of a graphene layer ^[234]. To conclude, these two bands are not referred to first-order Raman D and G peaks ^[233]. The D band originates from the breathing modes of six-membered aromatic rings of phonons of A_{1g} symmetry with disorder and defects in the graphitic or graphene lattice (e.g. edges/boundaries, sp^3 carbon bonds, bonding disorders, vacancies or heteroatoms) ^[233-235]. So, it suggests structural defects in the graphene layer ^[233]. On the other hand, the G band can be accounted for a perfectly ordered undisturbed sp^2 bonded graphitic carbon lattice (chain or ring configurations)

[234, 235c] arising from the doubly degenerate zone center phonon E_{2g} mode [233]. Besides, the broad and less intense peak around 2828 cm^{-1} (Figure 63) is neither ascribed to a second-order 2D band (D-band overtone) which outlines few-layered graphene [233] nor attributed to combinations of the G and D (G+D) graphitic lattice vibration modes which are typical for disturbed graphitic structures [233-234]. Taken as a whole, D, G, 2D and combination (G+D) bands provide information about structural defects within graphitic sheets [233-234]. Consequently, in-depth analyses by applying various fitting methods to gain insights about defect structures were not effective since these fitting methods were developed for graphitic or soot materials [226, 234]. Raman spectra were recorded on different spots of the surface area of the pyrolyzed HTC discs with a laser power between 3.0-4.0 mW. In case of an N-free disc, the amorphous region seems not be as pronounced as the N-containing pellets. It is probably due to the fact that N-functional groups enhance the structural diversity. XRD patterns support the presence of disordered and amorphous structures as well as the presence of high molecular entities of all N-HTC samples since the X-ray reflections are broad. Nevertheless, the amount of molecular moieties of an N-free material seems to be a little smaller because the X-ray reflection at approximately 24° is not as intense as the N-HTCs. However, the broad 002 reflection at around 24° is found in amorphous polymer-related carbon materials [42a, 248] but could be also attributed to a highly disturbed interlayer carbon packing reflection [42a, 70b]. The combined 100 and 101 reflections at 44° typically found in turbostratic-like carbons are observable and refer to in-plane scattering demonstrating increasing structural order by means of condensation and aromatization (Figure 64) [42a, 70b, 126d, 249].

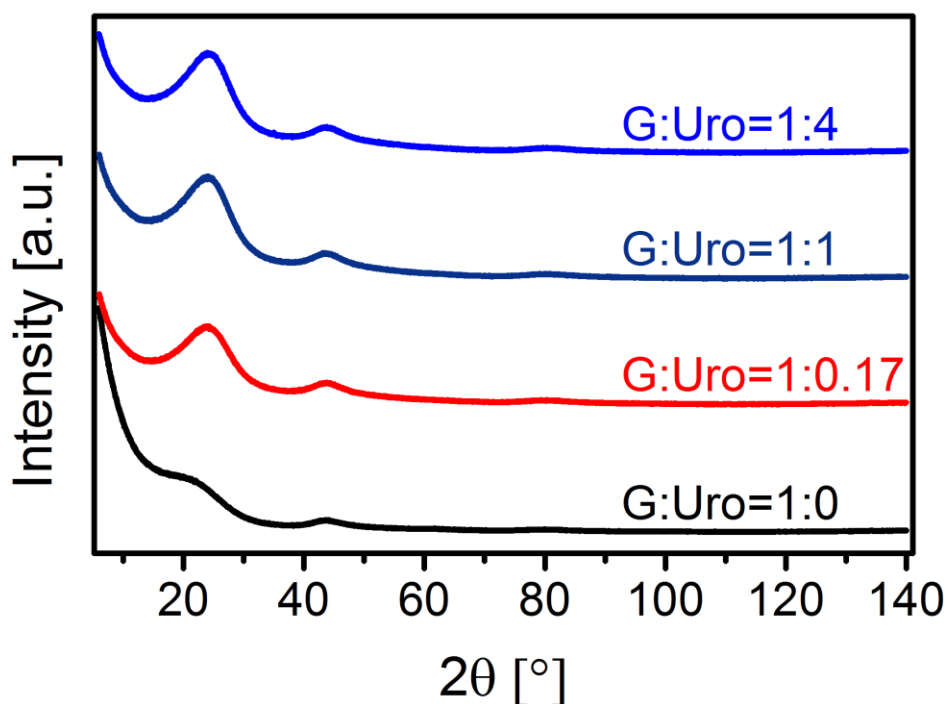


Figure 64: X-ray diffractogram of the measured HTC samples.

At ca. 80° a small bump is visible which can be assigned to the 110 reflection describing also in-plane scattering [42a, 249b]. As the pyrolysis temperature is 900°C an ordering of graphitic domains occurs by forming small but badly oriented graphenic sheets [42a, 250].

The disc electrodes were submitted to electrical conductivity measurements and the effect of the amount of nitrogen was investigated. Electrical conductivity measurements were conducted according to the van der Pauw Method revealing values around $45\text{ S}\cdot\text{cm}^{-1}$ (Figure 65).

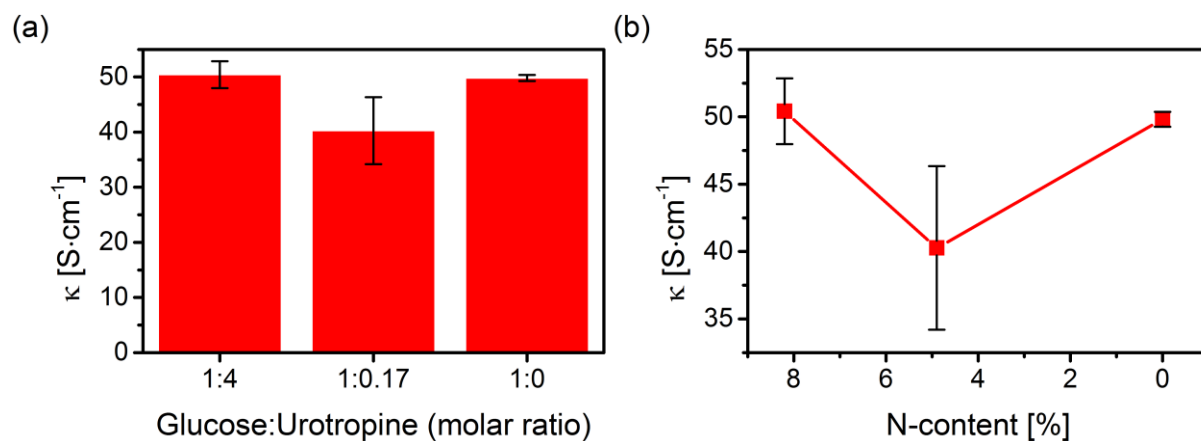


Figure 65: (a) Electrical conductivity values for the measured carbon disc electrode materials and (b) effect of N-introduction on the electrical conductivity.

Due to the high standard deviation no clear trend is evident by comparing three different discs with rising N-content. Therefore, compared to other carbonaceous materials such like graphite, CNT or glassy carbon, at pyrolysis temperature of 900 °C nitrogen does not reveal yet preferential bulk properties with respect to conductivity meaning that electron transfer properties are not favored. Another reason is still the amorphousness and the heterogeneity of these materials which results in an isotropy of the electrical properties.

4.19. Electrochemical Approach: Composition of Commercial Pellet Holder, Nail Polish and Standardization Protocol

All electrochemical measurements were conducted on a multichannel potentiostat (VMP3, BioLogic) using the EC-Lab[®] software V10.34. In a standard three-electrode configuration, Pt-foil was utilized as counter (CE) and a mercury/mercury oxide electrode (Hg/HgO) as reference electrode (RE). The reference potential was calibrated against a standard Ag/AgCl (3 M KCl, Metrohm), which is only used for this purpose and not applied for measurements to insure a stable potential. For a better comparison all potentials are given versus the reversible hydrogen electrode (RHE). As working electrode (WE), the hydrothermal carbon or glassy carbon disc electrodes were fixed in a commercial pellet holder (J110, Tianjin Aida Hengsheng Technology Development C., Ltd., Tianjin, China, Figure 66).

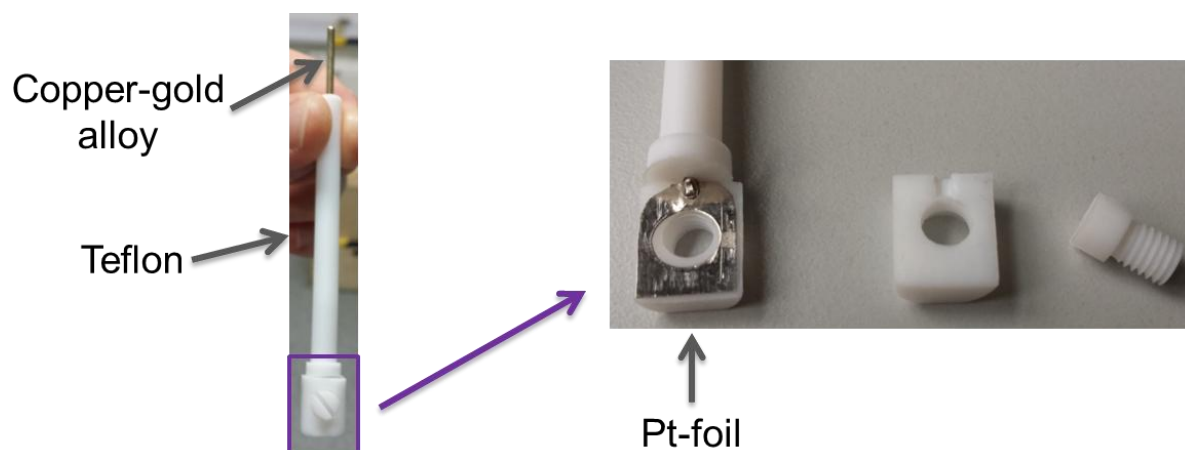


Figure 66: Design of the commercial pellet holder.

As current collector a Pt-foil connected by a copper-gold alloy is utilized in this holder. To define the surface area and prevent contact of the electrolyte with the current collector, half of the surface area of the pellet as well as the pellet holder itself were coated with nail polish (Gel-look nail colour 24 ruby red, Dirk Rossmann GmbH, Burgwedel, Germany) and dried in an upside down position for at least 3 h in air before it was immersed carefully into the electrolyte (Figure 67).

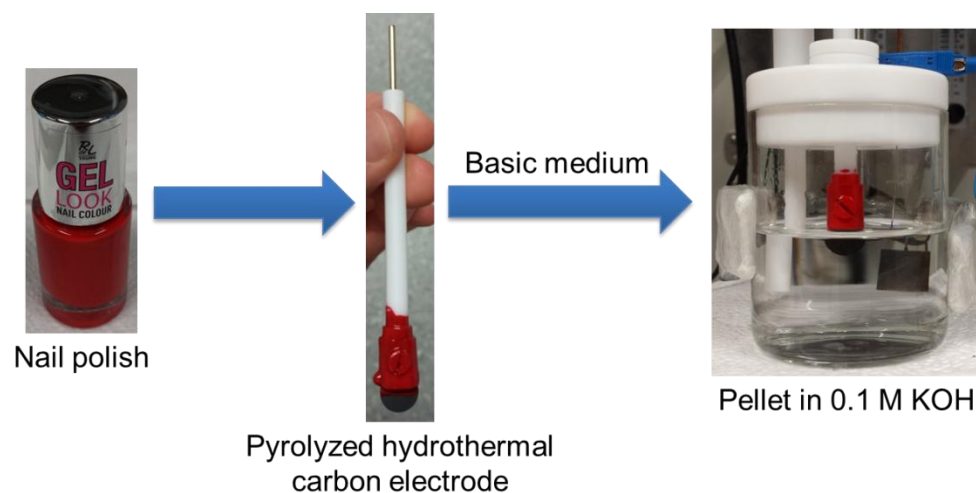


Figure 67: Nail polish was used to coat half of the electrode in order to prevent electrolyte diffusion into the Pt-foil of the pellet holder.

Potassium hydroxide concentrate (1 mol for 1 L standard solution, Sigma-Aldrich, Steinheim am Albuch, Germany) as electrolyte was diluted to 0.1 M KOH with deionized water obtained from a Millipore (Milli-Q[®]) water system ($18.2 \text{ M}\Omega\cdot\text{cm}^{-1}$). The electrolyte was purged with argon for 30 min before and

continuously during each experiment. Electrochemical tests have been pursued according to the standard protocol as defined in the MANGAN project ^[251], with the following variations; instead of powder materials, deposited on an RDE tip, the aforementioned carbon pellets were utilized. This omits the use of a binder, but also no rotation or stirring was applied. Additionally the electrolyte concentration was 0.1 M KOH (instead of 1 M KOH). All measurements were corrected for the internal resistance (iR). A scheme of the full measurement procedure can be found in Figure 68.

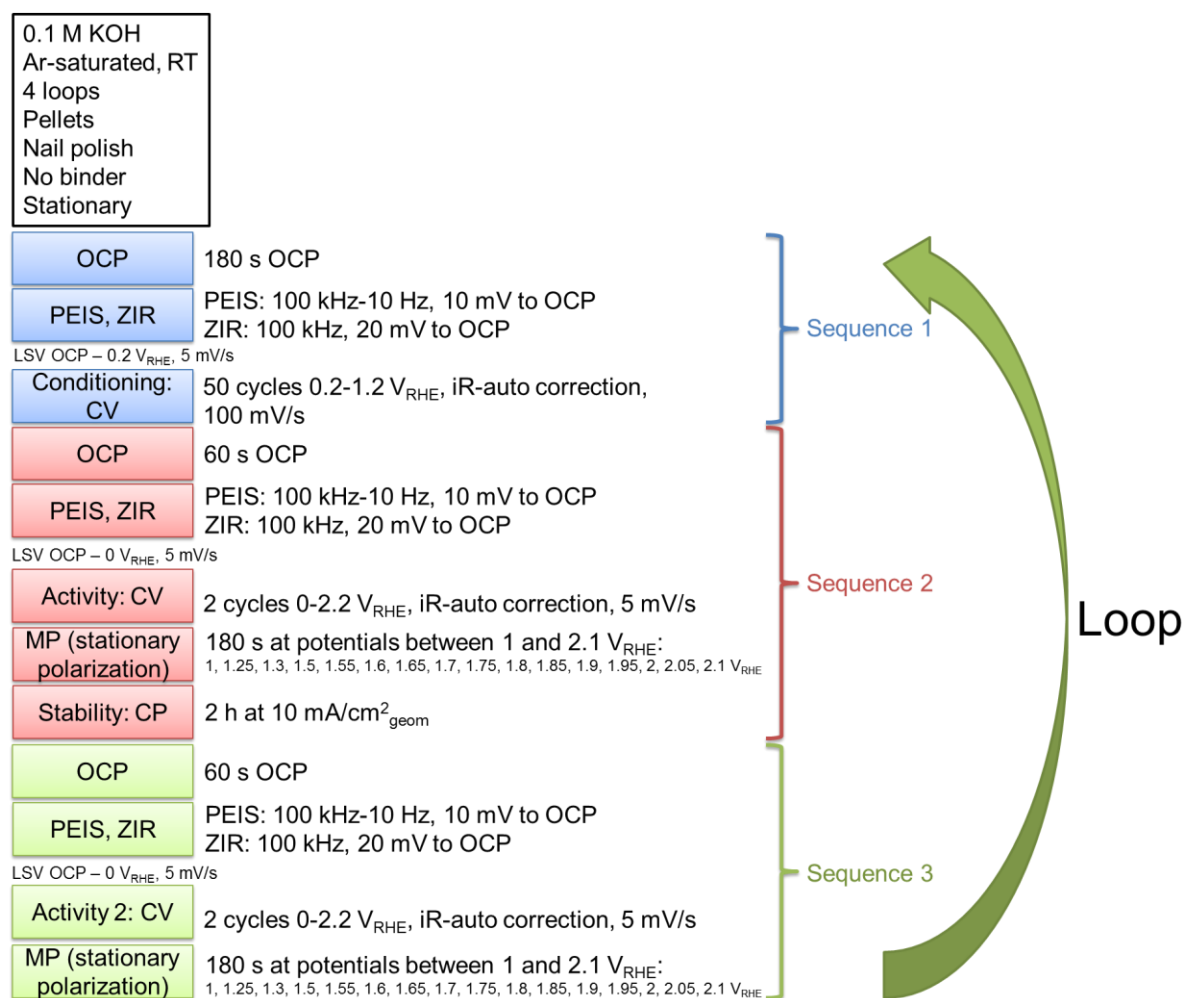


Figure 68: Conditioning (sequence 1) and activity, stability as well as OER measurements (sequence 2 and 3).

In brief, the electrochemical measurements are divided into three sequential parts. OER studies starts with pre-analysis (sequence 1) containing open circuit potential (OCP) and impedance measurements. Preconditioning is used to activate the disc electrode, by applying 50 cyclic voltammograms (CV) between

0.2 and 1.2 V_{RHE}. Preconditioning will affect the properties of the surface area by redox processes occurring in the electrode which might already result in an improvement of the activity.^[251-252] Sequence 2 addresses the catalytic activity and stability. The activity is tested by CVs up to 2.2 V_{RHE} as well as by stationary polarization (steps of 50 mV with a dwell time of 180 s, up to 2.1 V_{RHE}), to reduce influences of the capacitive current. Stability is evaluated by means of chronopotentiometry (CP), applying 10 mA·cm⁻² for 2 h. The activity is again tested after the stability (sequence 3). To observe some long-term stability, all sequences were repeated in total four times, which accumulated to a total measurement time of 24 h (thereof 8 h of CP).

4.20. Electrochemical Characterization in Alkaline Medium

For the electrochemical characterization three different HTC disc electrodes were selected involving the sample with highest N-content (G:Uro=1:4, N: 8 wt%), lowest N-content (G:Uro=1:0.17, N: 5 wt%) and with N-free HTC as reference. These are used to characterize the influence of N-incorporation within the carbon disc electrodes on electrochemical activity and stability towards the OER. All three samples were measured for their reproducibility (Figure 69-Figure 74).

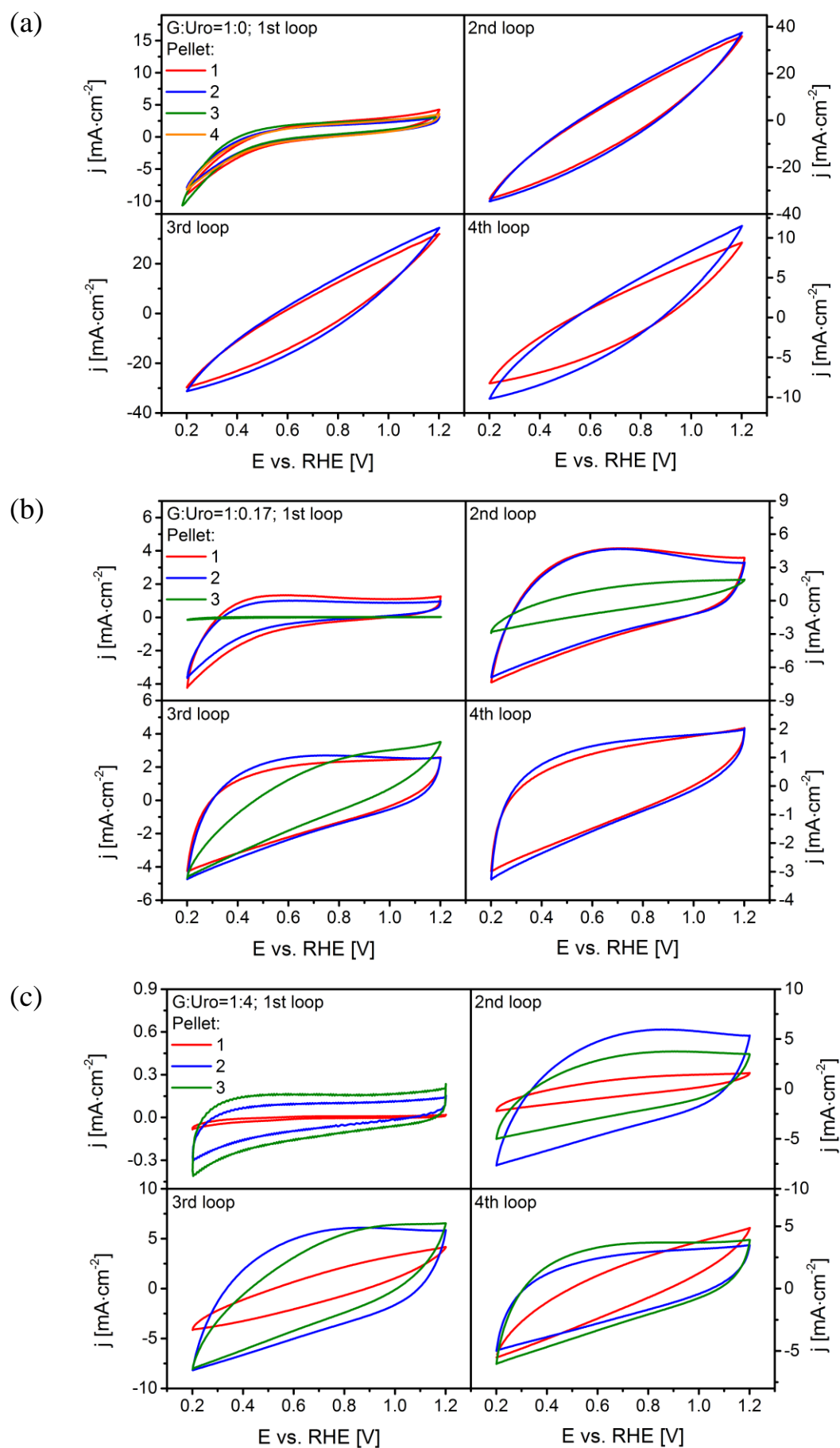


Figure 69: Conditioning for at least three different pellets of (a) G:Uro=1:0, (b) G:Uro=1:0.17 and (c) G:Uro=1:4 during all four loops.

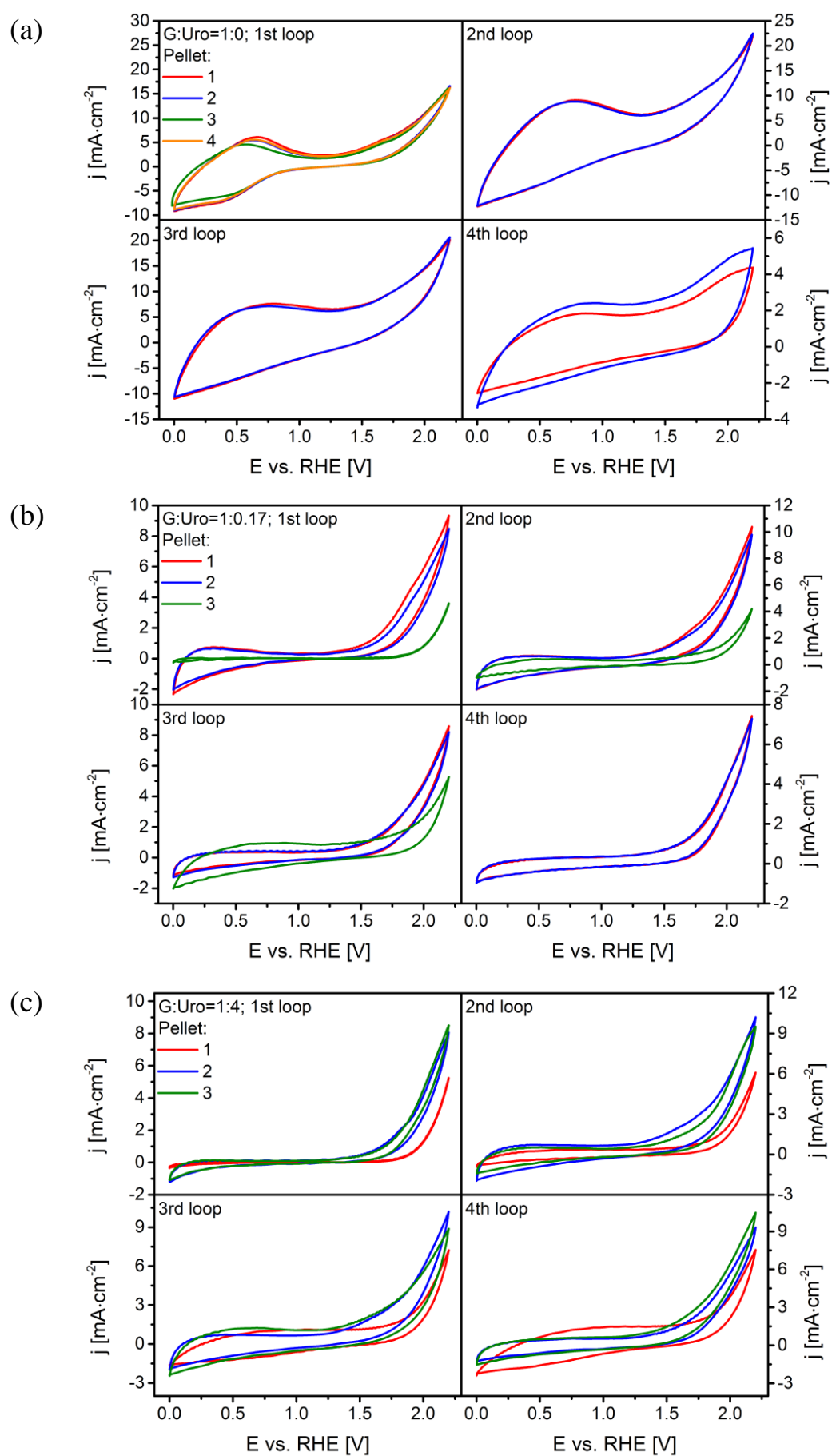


Figure 70: Activity CVs for the sequential loops for at least three different pellets of (a) G:Uro=1:0, (b) G:Uro=1:0.17 and (c) G:Uro=1:4.

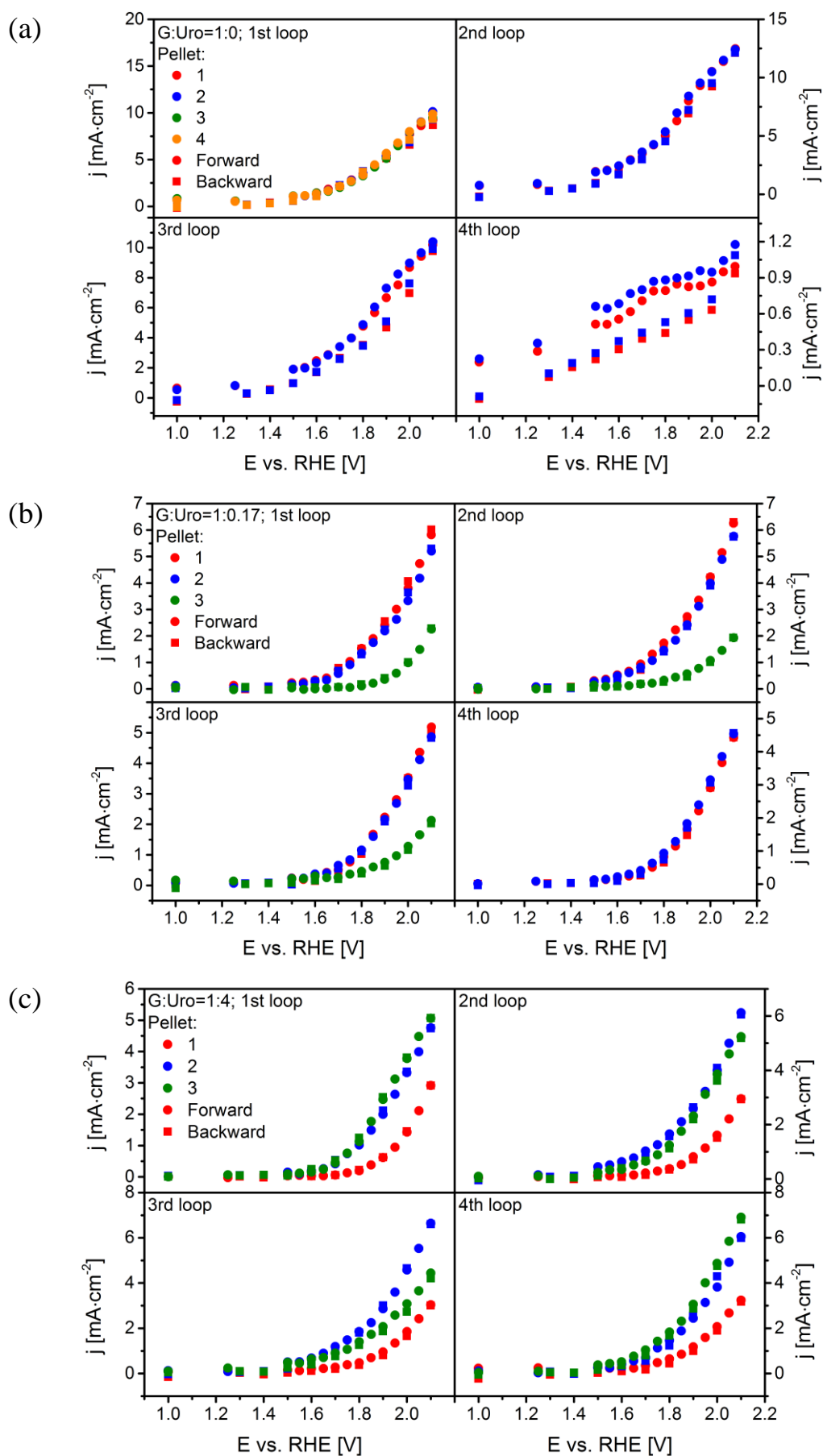


Figure 71: Stationary polarization for at least three different pellets of (a) G:Uro=1:0, (b) G:Uro=1:0.17 and (c) G:Uro=1:4 for four loops.

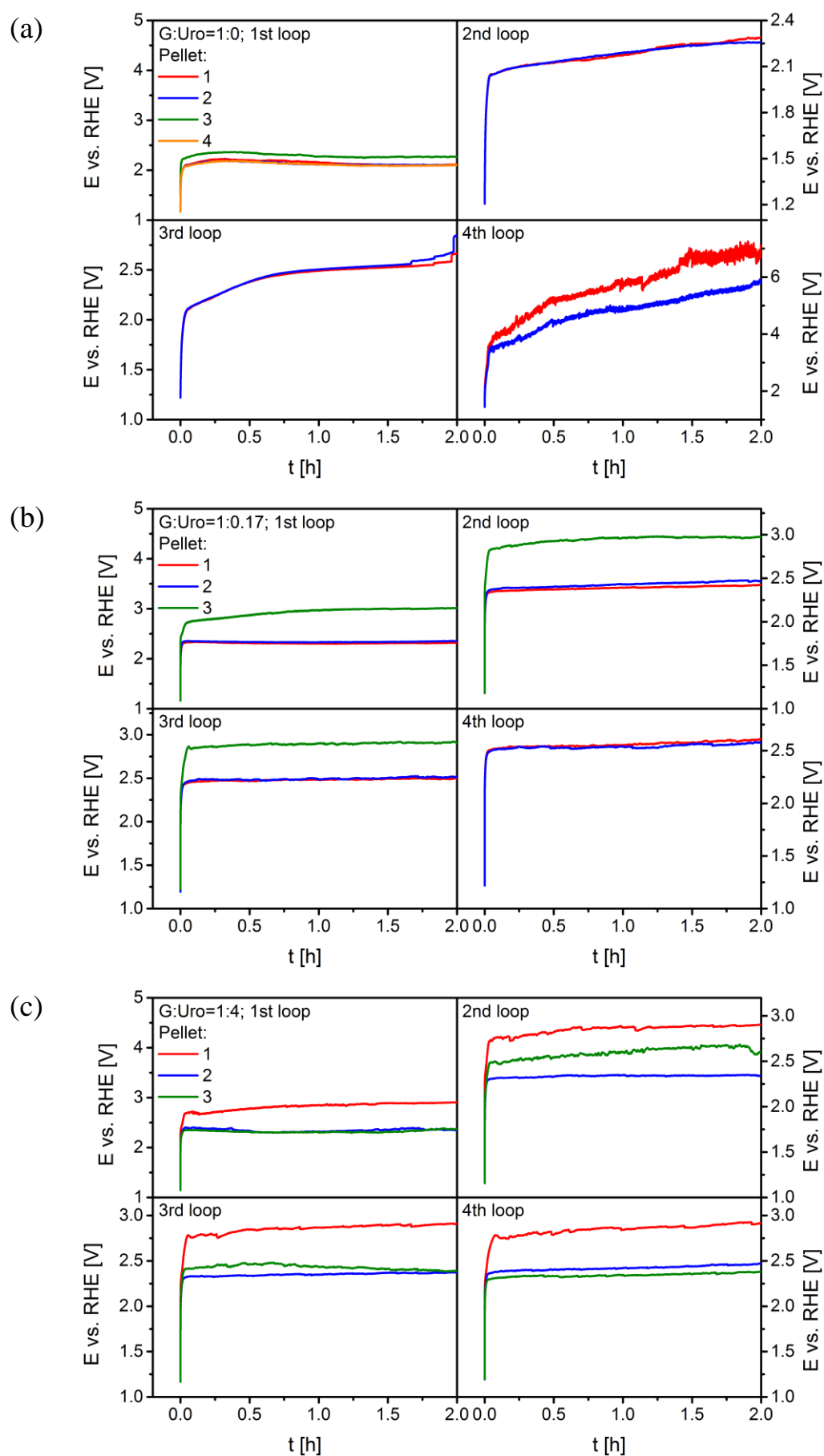


Figure 72: Chronopotentiogram for at least three different pellets of (a) G:Uro=1:0, (b) G:Uro=1:0.17 and (c) G:Uro=1:4 for four loops.

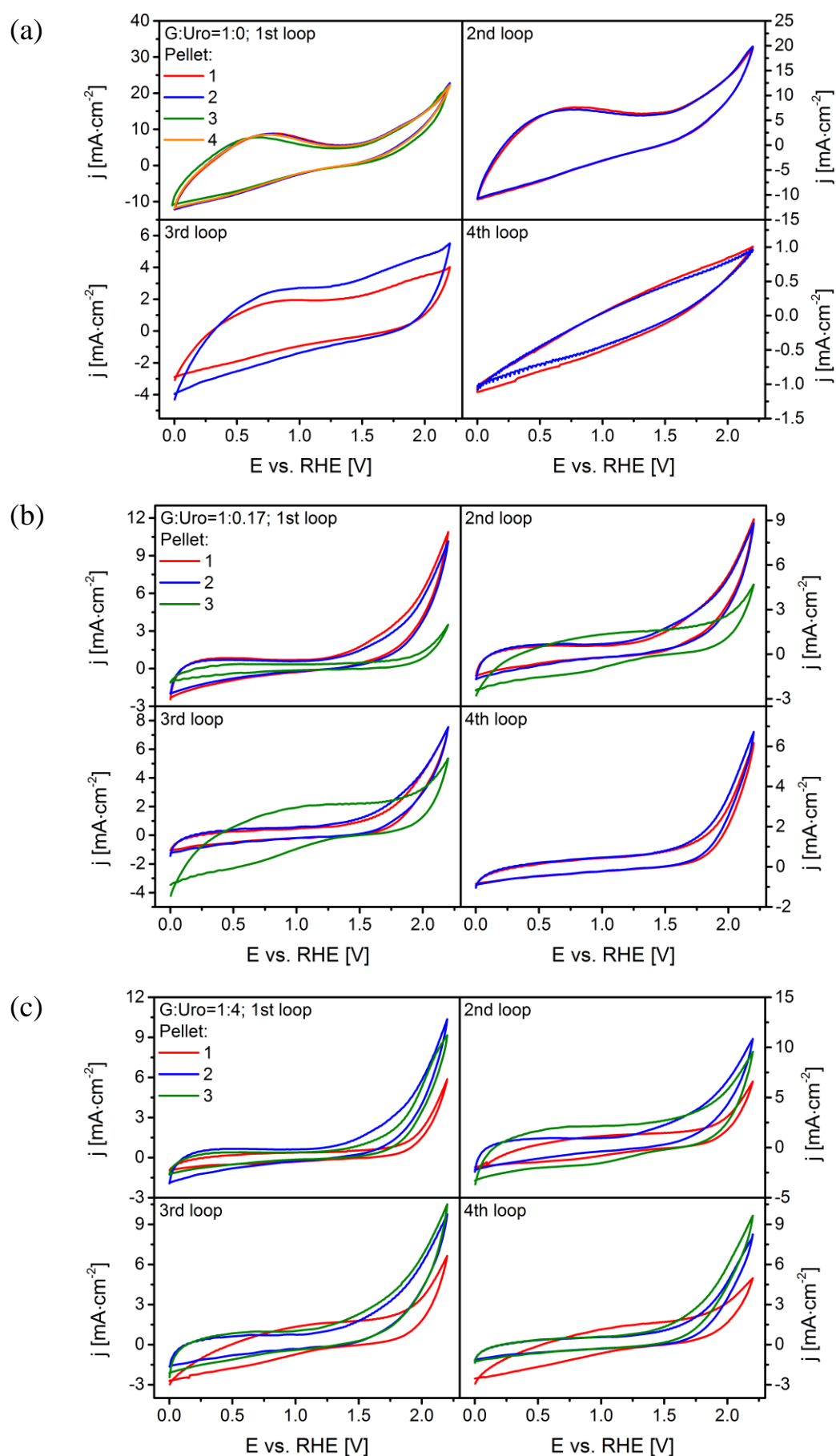


Figure 73: Activity CVs for the sequential loops for at least three different pellets of (a) G:Uro=1:0, (b) G:Uro=1:0.17 and G:Uro=1:4.

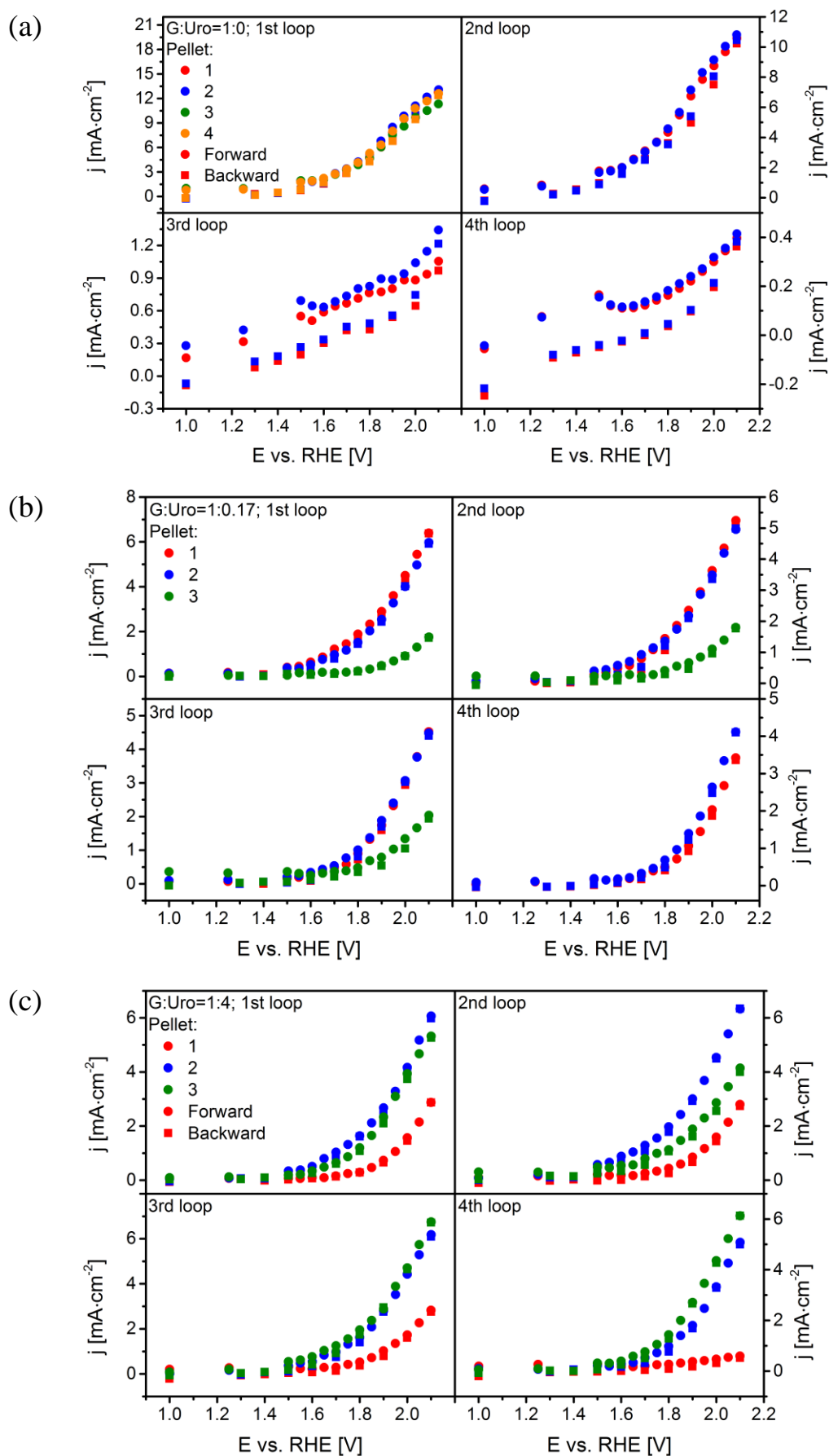


Figure 74: Second stationary polarization for at least three different pellets of (a) G:Uro=1:0, (b) G:Uro=1:0.17 and (c) G:Uro=1:4 for four loops.

Already the grade of reproducibility depends on the N-content, probably indicating differences in the homogeneity of the prepared samples. While for the N-free HTC the reproducibility is excellent, the standard deviation significantly increases for G:Uro=1:4. Nevertheless, identical trends can still be deduced from all series.

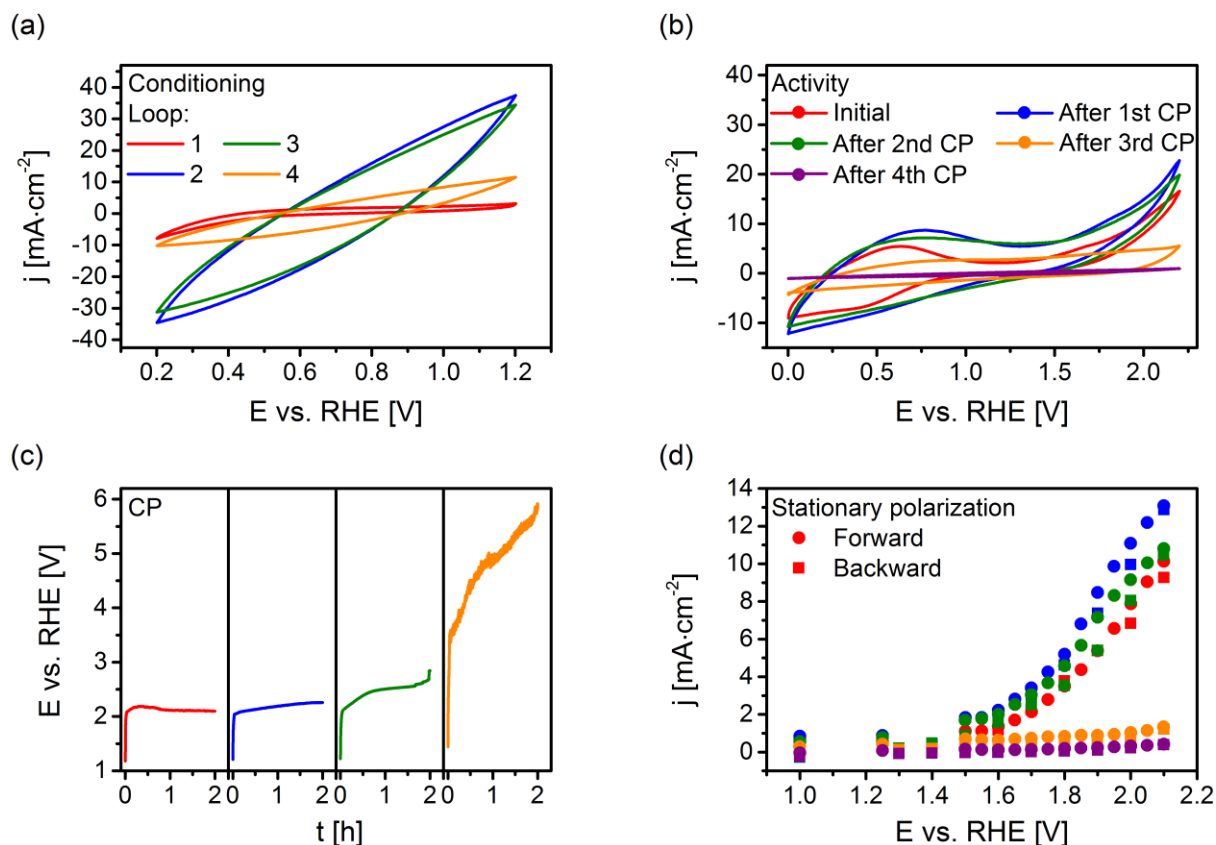


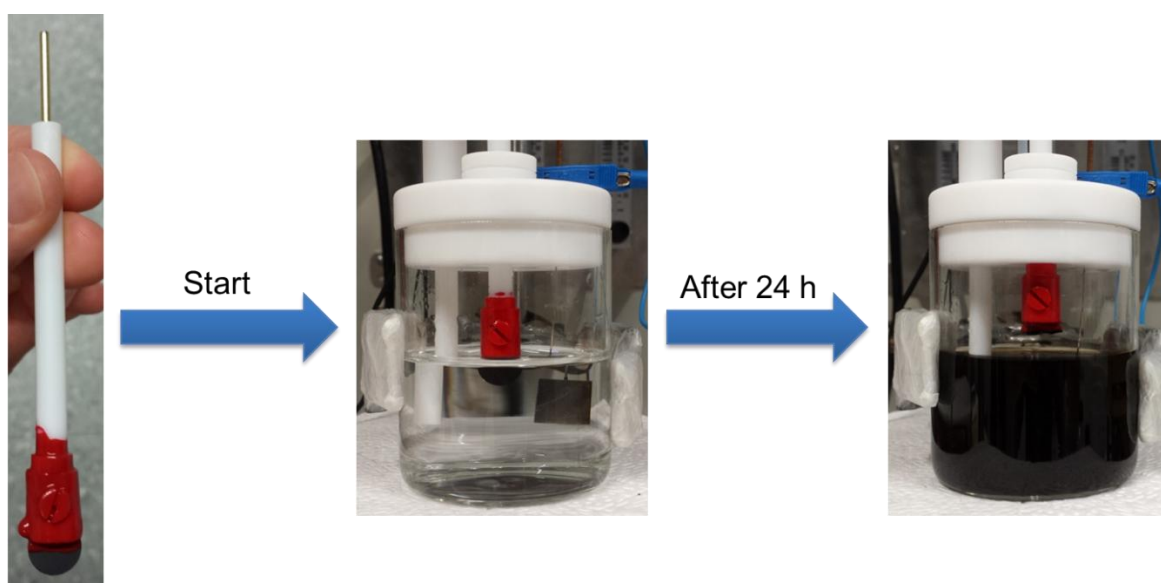
Figure 75: (a) CVs, (b) activity CVs, (c) CPs and (d) MPs for G:Uro=1:0.

Figure 75 summarizes the electrochemical responses for N-free HTC during the different sequences of the electrochemical protocol (Figure 68) and their development during several loops. The cyclic voltammograms (CVs) of the conditioning exhibit mainly capacitive current, which increases from the 1st to the 2nd loop (Figure 75 (a)). This can be explained by a higher surface area or a change of functional groups. Similarly, the sudden drop of capacitive current in the 4th loop (i.e. after the 3rd stability sequence) can be attributed to a significant loss of surface area. During sequence 2 and 3 the activity is determined by CVs with up to 2.2 V (Figure 75 (b)). In spite the slow scan rate (5 mV·s⁻¹), still a high capacitive current overlays the onset of the OER, which increases

according to the conditioning CVs with increasing loop numbers. Additionally, a new redox peak can be observed around 0.5-0.8 V. This might originate from a quinone/hydroquinone couple which probably is activated by raising the potential ranges ^[253].

In the 4th loop this redox peak disappears due to the overall surface area loss.

As a measure of stability, a constant current of $10 \text{ mA}\cdot\text{cm}^{-2}$ was applied for 2 h per loop (chronopotentiometry, CP, Figure 75 (c)). During the 1st loop, the potential slightly decreases but increases again during the 2nd and 3rd loop, indicating a loss of active sites, e.g. by corrosion. Also optically, the electrolyte slowly changes from colorless to dark brown, which shows the continuous carbon corrosion. At the end of the 3rd CP, the potential increases to above 2.5 V. This probably induces higher corrosion rates, leading to the significant drop of surface area, as seen in the CVs (Figure 75 (a) and (b)). The loss in surface area further increases the potential during the 4th CP, thereby self-amplifying the carbon corrosion. In fact, after this 4th loop, the part of the pellet that was immersed into the electrolyte dissolves completely for the N-free material (Figure 76).



G:Uro=1:0

Figure 76: Long-term electrochemical measurements are accompanied by color change from colorless into dark brown and a complete carbon corrosion for G:Uro=1:0 after 24 h.

Figure 75 (d) shows the stationary polarization results. By applying potential steps with a dwell time of 180 s, and averaging the current only over the last 30 s, the high capacitive currents of the CVs can be suppressed. Still, multiple processes can contribute to the measured current while mainly carbon corrosion and oxygen evolution are expected in this case. As already indicated by the potential drop in the 1st CP, a slight activation (i.e. current increase) can be observed initially. However, while no significant drop of the surface area could be detected in the CVs during the 3rd loop, the activity already slightly drops, especially at high potentials. Also, although still a capacitive current is measurable after the 3rd CP, the activity almost drops to zero. Finally, no current is measurable after the 4th CP, which is a logical consequence of the complete loss of active material.

All three different disc electrodes seem to activate after 1st CP. Even if the electrochemical measurements were conducted with potentials up to 2.1 V any influence by means of gas bubble formation on the measurements cannot be excluded since gas bubble formation on the surface area of the pellets was very small.

For the HTC material with lowest amount of N (G:Uro=1:0.17) similar behavior as for the N-free HTC electrode can be observed during the first two loops. For instance, after the 1st loop also an increase in the capacitive current can be observed that is followed by a decrease in the 3rd and 4th loop (Figure 77 (a)).

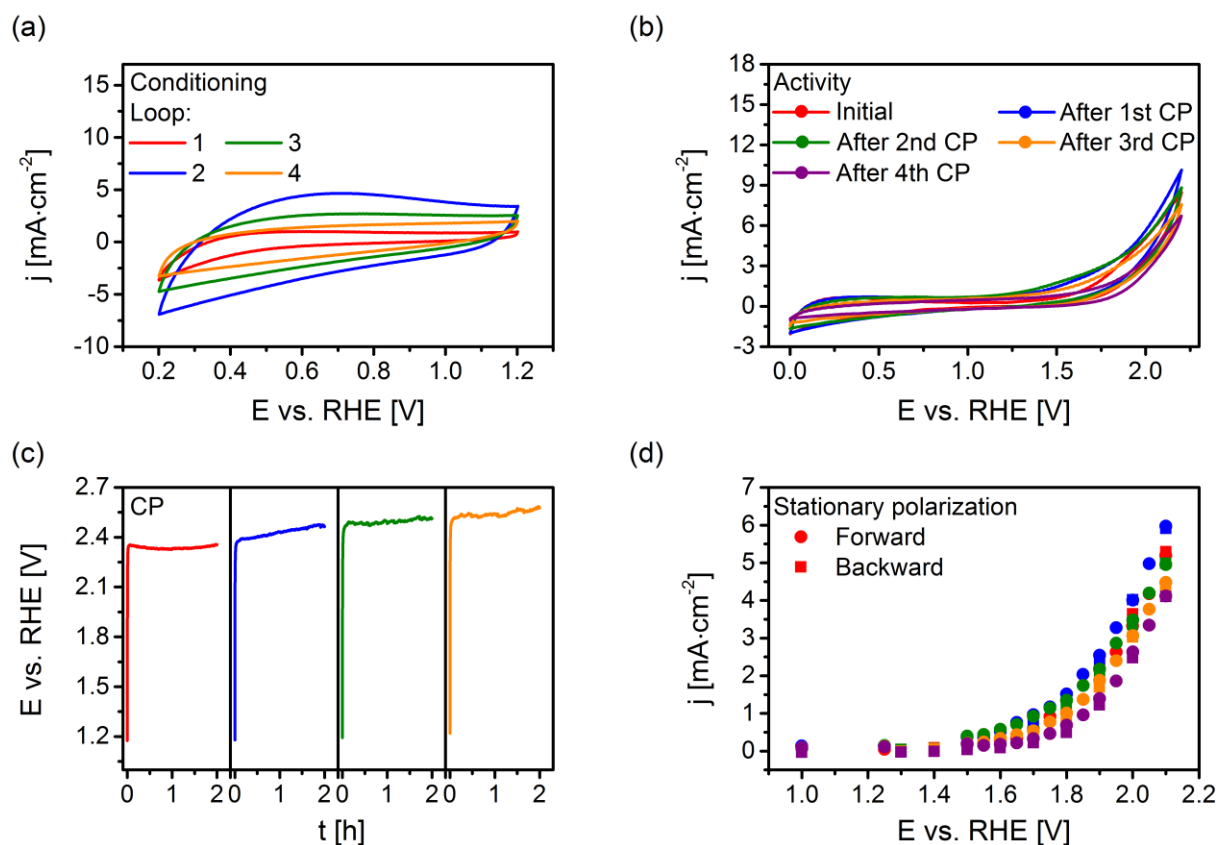
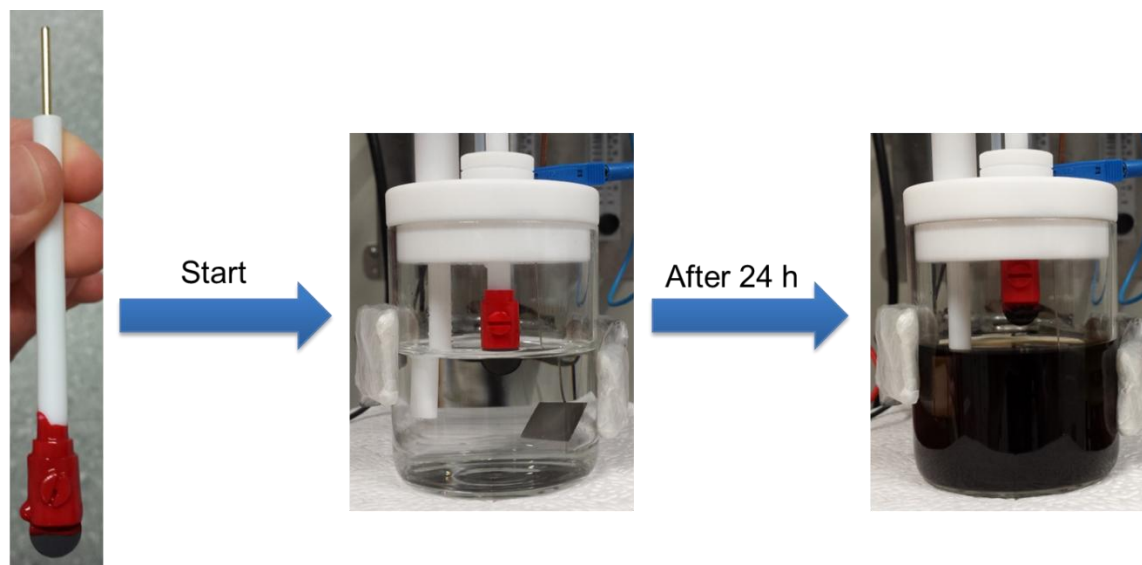


Figure 77: (a) CVs, (b) activity CVs, (c) CPs and (d) MPs for G:Uro=1:0.17.

It, however, needs to be mentioned that in contrast to N-free HTC, the initial and maximal capacitive current are significantly smaller as the BET surface area of N-containing HTCs in comparison with the current density are only around $1 \text{ m}^2\cdot\text{g}^{-1}$ compared to the N-free discs with $347 \text{ m}^2\cdot\text{g}^{-1}$ (Table 7). Furthermore, the drop is more continuous and even after the 4th CP still a significant capacitive current is measurable (Figure 77 (b)). This already indicates a higher retention of surface area of surface area during the whole protocol. During the CVs of the 2nd sequence also no redox peak arises, which indicates different surface functionalization than on N-free HTC electrode (Figure 77 (b)). Furthermore, the potential during the CPs increases from initially around 2.35 V to only 2.57 V after 4th CP; in strong contrast to more than 5 V in the N-free HTC electrode (Figure 77 (c)). This is also resembled in Figure 77 (d), where the stationary polarization curves show only a small loss of the current density even after the 4th CP. Nevertheless, even after a total measurement time of 24 h

a stationary state is not reached, implying a constant corrosion rate also for longer operation.

Optical investigation of the electrolyte for the lowest N-containing HTC electrode also reveals a color change of the electrolyte from colorless into dark brown. But in contrast to N-free HTC, the pellet remains structurally stable and does not dissolve completely in the electrolyte (Figure 78).



G:Uro=1:0.17

Figure 78: Carbon dissolution for G:Uro=1:0.17.

With an even higher N-content (G:Uro=1:4) the initial CV is even smaller than for lowest N-containing HTC (Figure 79).

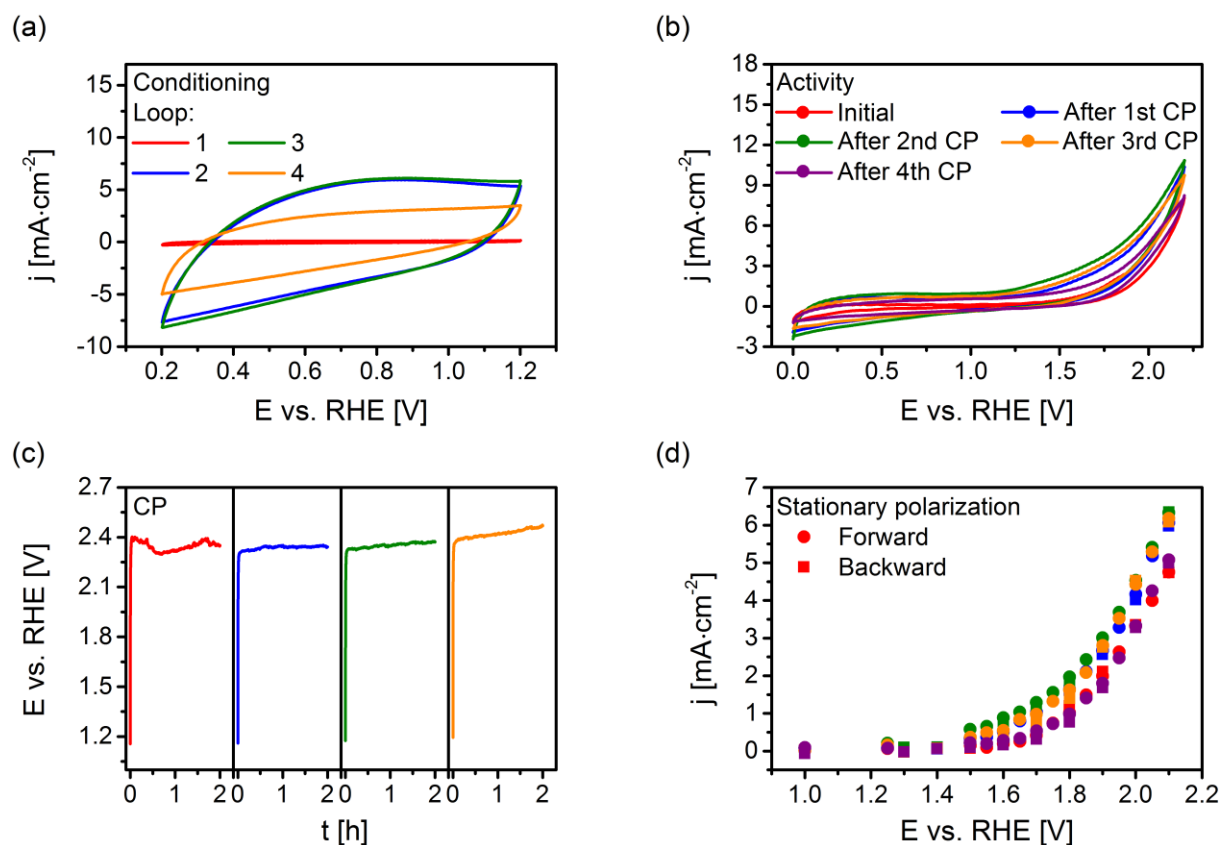
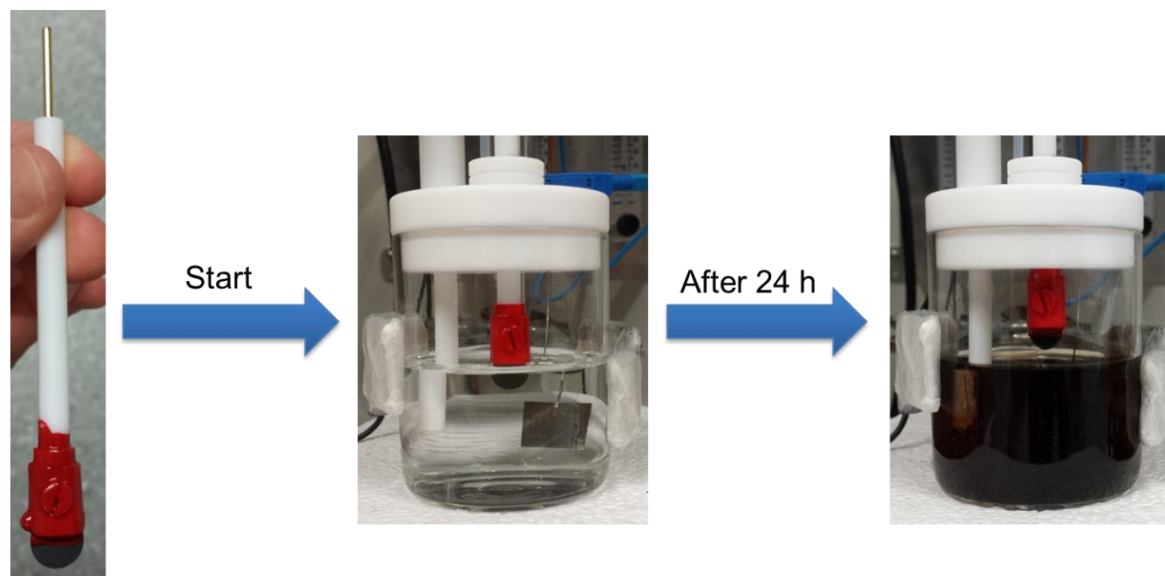


Figure 79: (a) CVs, (b) activity CVs, (c) CPs and (d) MPs for G:Uro=1:4.

However, after the 1st loop, CV increases as expected and even remains completely stable for the 3rd loop. The CV of the last loop only slightly decreases. This indicates a higher stability and is confirmed by the CPs, where the potential increase is limited to 0.12 V over the entire measurement time. Also optically, the pellet remains structurally stable (Figure 80). With this behavior, the highest N-containing HTC pellet exhibits the best stability of all three samples.



G:Uro=1:4

Figure 80: Carbon dissolution for G:Uro=1:4.

For the disc with highest N-content the same observations can be made as in the previous case. A color change occurs from colorless to dark brown and the electrode remains stable after long-term electrochemical measurement 24 h (Figure 80).

Figure 81 directly compares the performance of all three different pellets.

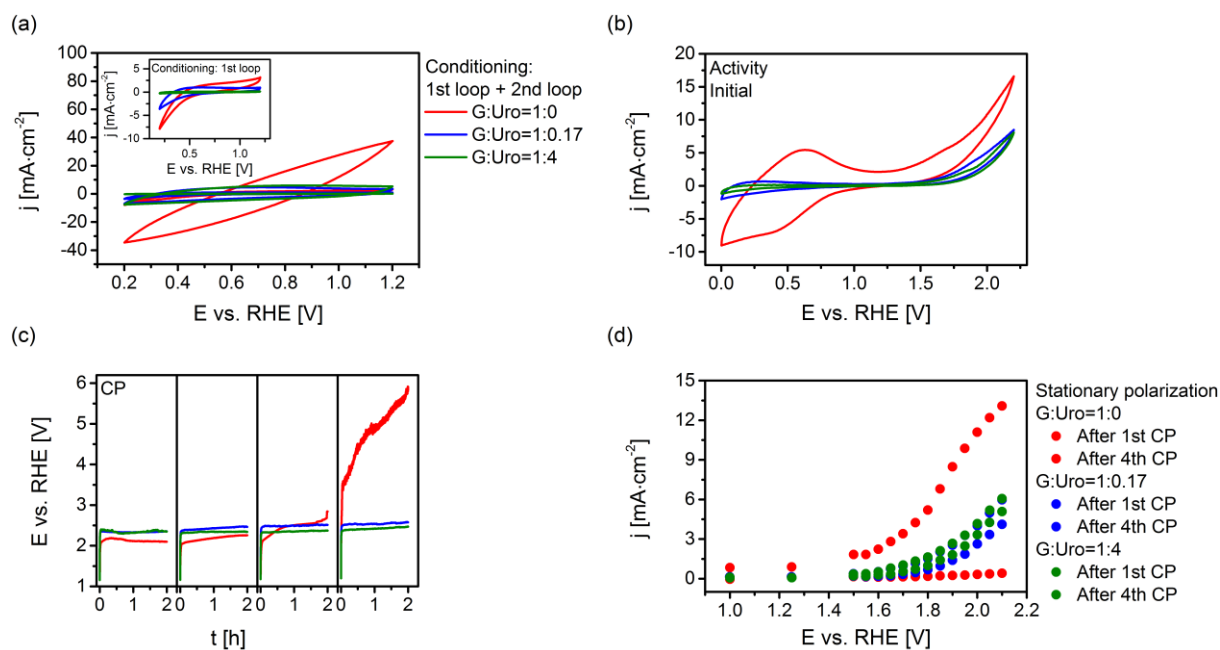


Figure 81: Comparison of all the disc electrodes (G:Uro=1:0, G:Uro=1:0.17 and G:Uro=1:4) including (a) CVs, (b) activity CVs, (c) CPs and (d) MPs (only forward).

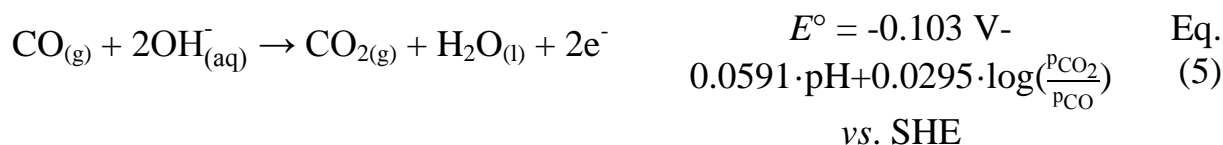
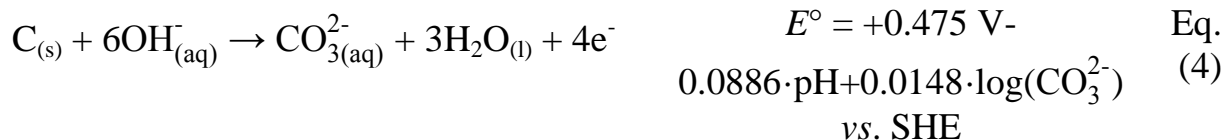
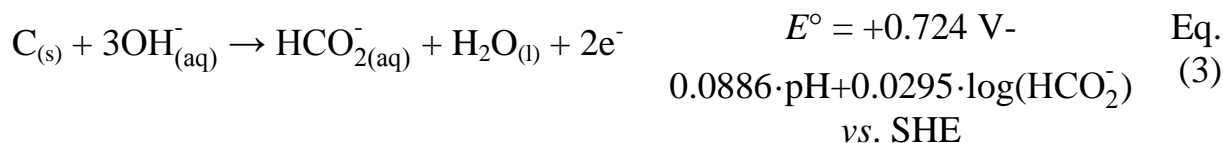
A clear trend of decreasing initial capacity with increasing N-content is visible in the conditioning cycles. As initially an effect of corrosion can nearly be excluded, this can probably be explained by a different hydrophilicity or wettability of all three disc electrodes attributed to the surface termination with varying N-content. After the 1st CP, the capacity of the two N-containing HTC pellets has equalized while N-free HTC still exhibits a considerably higher capacitance. Besides, the redox peak around 0.5-0.8 V, which is only observed for N-free HTC indicates electrochemical active surface functional groups that are not present in the N-containing HTC materials. Moreover, the direct comparison reveals that the initial activity – as deduced from the stationary polarization – is substantially lower for the N-containing pellets but does not vary with growing N-content. As already estimated before, the stability of the N-containing HTC pellets is significantly increased and with raising N-content, a higher current density can be sustained at the end of the electrochemical test (i.e. after four times 2 h of CP measurements). This is not only evident from the curves of the stationary polarizations but also from the stability curves. Therein, the crossing point, where the higher initial activity is conducted by its strong corrosion, occurs approximately halfway through the 3rd CP after a total of 7 h of constant exposure (i.e. 15 h of total operating time).

In conclusion, in terms of activity, the N-containing samples have initially a drawback over N-free HTC pellets. Nevertheless, this is strongly balanced by their higher corrosion resistance, which makes them more powerful candidates for long-term operation.

After electrochemical corrosion tests of all HTC discs further post-characterization have been performed for the pellets and for the electrolyte.

4.21. Carbon Corrosion and Activation as well as Deactivation of the Surface Area

In theory, the process of carbon corrosion during chronopotentiometric experiments at high and constant anodic-current densities of $10 \text{ mA}\cdot\text{cm}^{-2}$ is a complex degradation mechanism ^[254]. Upon these harsh conditions electrochemical oxidation takes place in which morphological and structural changes occur. In the presence of KOH, surface oxides or hydroxides and organic-carbon are formed to a large extent ^[255]. The N-free electrode denotes a low activation during the first 2 h of CP at roughly 2.10 V (red curve, Figure 75 (c)). Thermodynamically, at 1.23 V_{RHE} not only oxygen evolution is possible but also carbon oxidation is in progress and moreover surface changes cannot be excluded ^[256]. In alkaline electrolytes, the two main reactions that describe the electrochemical degradation or oxidation (“cold combustion”) of carbon are the formation of gaseous CO which further reacts to gaseous CO₂ (equation (5)). However, carbon corrosion in neutral or alkaline media leads CO₂ to convert into aqueous HCO₂⁻ (equation (3)). It is reasonable to suggest that CO₂ exists in the form of aqueous HCO₂⁻. Apart from that, the formation of carbonate ions is of considerably importance (equation (4)) ^[255, 257].



The electrochemical measurements are performed at pH=13. According to the Pourbaix diagram at pH=13, main reaction is the formation of CO_3^{2-} ions (equation (4))^[257].

After initial potential rise up to a maximum of all chronopotentiograms which is attributed to charging of the double-layer capacitance the curves activate to lower oxidation potentials. The activation in the oxidation potential during chronopotentiometry can occur due to surface functionalization on the carbonaceous electrode^[256, 258]. In theory, this process is also accompanied by the evolution of gaseous products including CO_2 , CO and O_2 in basic environment. Herein, no head-space analyses could be carried out to prove gaseous products. Nonetheless, gas evolution of CO_2 in KOH leads to the formation of CO_3^{2-} ions^[259]. Furthermore, surface oxides are formed in alkaline medium^[254]. The deactivation process to higher potentials for a N-free disc or the oxidation potential which gradually decrease to a 2.10 V during the first 2 h of the CP (Figure 75 (c)) is presumably a result of a protective surface oxide layer (passivating oxide film) that is caused by further surface oxide coverage on the carbon electrode^[260]. The passive oxide film on the carbon surface inhibits further formation of oxides. Reversely, the presence of this protective layer oxide has in theory no effect towards gas evolution (CO_2 , CO , O_2). In fact, CO_2 formation becomes the dominant electrochemical reaction^[261] (equation 5) as this reaction is the prerequisite for the existence of CO_3^{2-} ions^[255, 257]. However, the passivating oxide layer decelerates the reaction kinetics of gas evolution^[255]. Both types of reaction, gas evolution and the formation of surface oxides on the carbon electrode are susceptible to changes in reaction rate with time, and occur probably on active sites that are located at edges, defects or at dislocations^[255-256]. Nonetheless, the active sites are not known in the context of the used N-HTC samples. In the course of the long-term electrochemical measurement, the N-free pellet strongly deactivates from 2.26 V (blue curve, Figure 75 (c)) via 2.85 V (green curve) up to a potential of 5.90 V (orange curve). In alkaline

electrolyte, the decomposition of carbon occurs presumably following a radical mechanistic pathway^[254]. By radical substitution of alkyl site chains at the edges of small graphitic regions with hydroxyl radicals these groups are oxidized forming typical surface O-functional groups like aldehydes or carboxylic acids. Therefore, the graphitic layer gets more hydrophilic and thus loses the π - π interaction between the agglomerates which leads to a dissolution of the carbon material following the principle of the sacrificial electrode.

4.22. Post-Mortem Characterization: Analysis of Colored Electrolyte and Isolation of Residual of Colored Electrolyte after Electrochemical Stability Tests

Overall, the electrochemical corrosion tests of the N-HTC discs (G:Uro=1:0, G:Uro=1:4 and G:Uro=1:0.17) result in color changes. The electrolyte turns from colorless to dark brown. As the electrochemical corrosion tests are accompanied by a color change, in particular, by a brown coloration (Figure 76, Figure 78 and Figure 80) the electrolyte solutions were analyzed by means of UV/VIS spectroscopy in order to gain information about their UV activity (Figure 82).

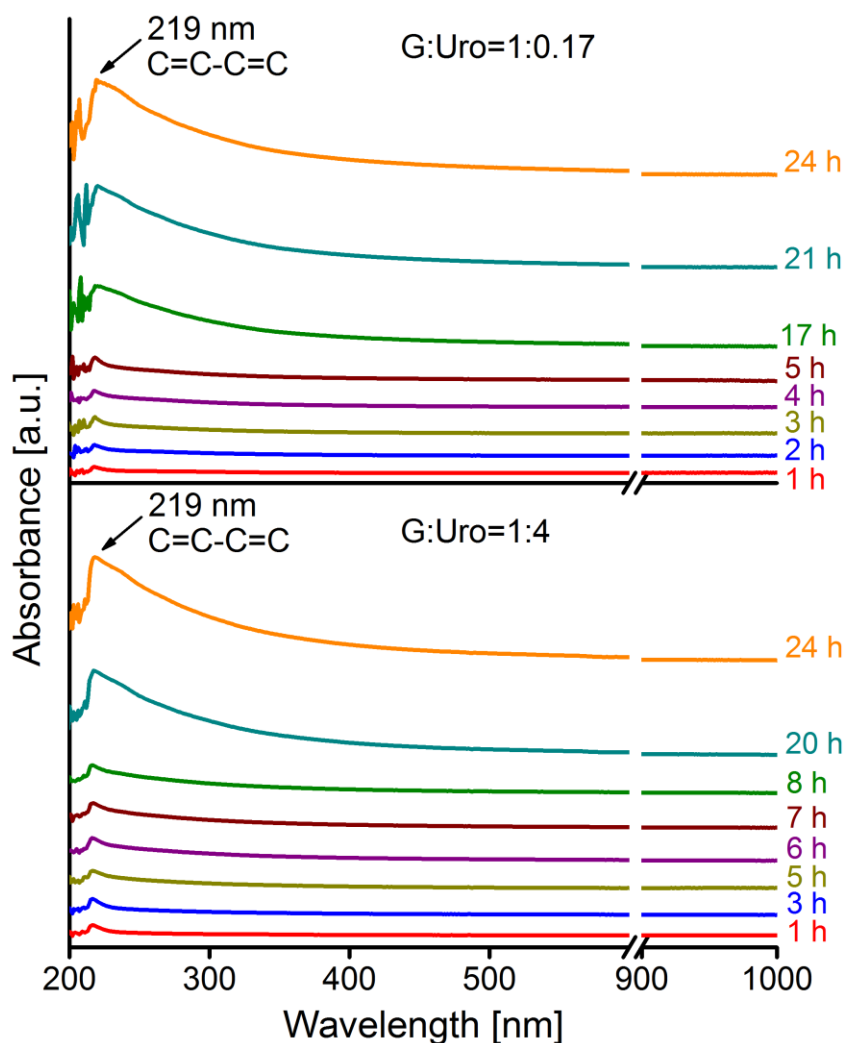


Figure 82: UV/VIS spectra of electrolytes from G:Uro=1:0.17 and G:Uro=1:4 in 0.1 M KOH.

At different points in time an aliquot of the electrolyte solutions were taken and UV/VIS spectroscopic measurements were recorded. Peaks at 219 nm are typically found in polyene-like compounds. In literature, the brown coloration is referred to humic acid-like compounds ^[262].

Furthermore, the dark brown electrolyte solutions of G:Uro=1:4 and G:Uro=1:0.17 were directly submitted to lyophilization (freeze-drying). The residual brown mixed phase of G:Uro=1:4 was added to EtOH (ca. 50 mL). Still a little amount of the brown solid remained in the solution. Indicator paper turned to a blue color indicating KOH is fully dissolved in EtOH. The suspension was sonicated for ca. 10 min before the brown solid has been filtered

and washed with EtOH. After drying in a heating stove at 110 °C overnight for approximately 15 h the brown solid (yield: m=6 mg) has been isolated.

The dark brown electrolyte solution of the N-HTC of G:Uro=1:4 obtained after electrochemical stability test was further analyzed. The electrolyte was lyophilized overnight and a brown mixed solid phase was obtained consisting of the brown unknown material and KOH. The mixed phase was partially dissolved by addition of EtOH. Data of elemental analysis before and after isolation of brown solid was compared. However, only a small increase up to 10 wt% of C-content was observed (Table 8).

Table 8: Elemental analysis before and after isolation of brown solid for G:Uro=1:4.

Sample	C [wt%]	H [wt%]	N [wt%]	K [wt%]
G:Uro=1:4 (before isolation)	2.8	6.9	0.4	42.8
G:Uro=1:4 (after isolation)	10.5	2.1	0.4	39.3

The remaining brown solid was dissolved in D₂O and ¹H NMR as well as ¹³C NMR spectra were recorded (Figure 83).

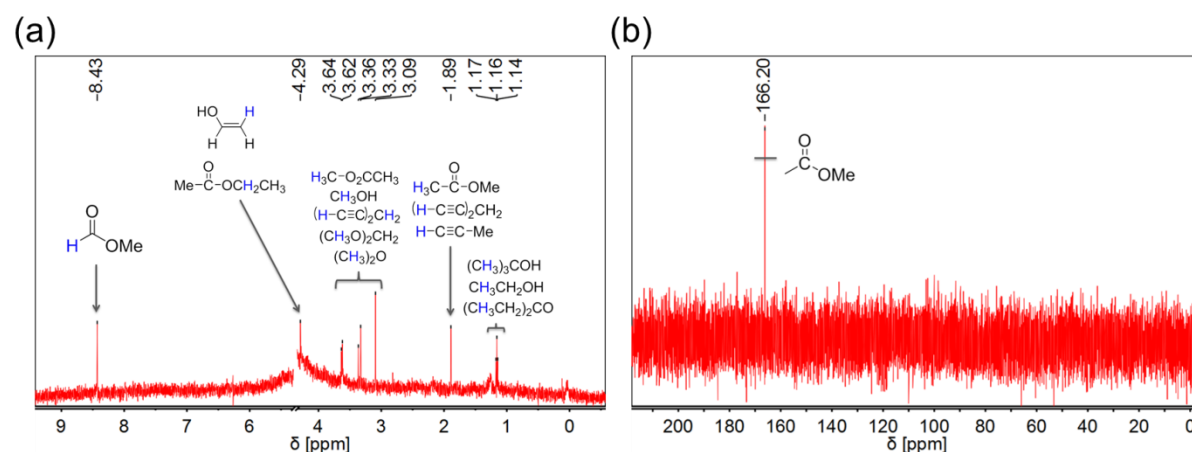


Figure 83: (a) ¹H NMR spectrum of the isolated brown solid and (b) the corresponding ¹³C NMR spectrum dissolved in D₂O.

¹H NMR spectrum reveals a material which is abundant in hydroxyl, ether-, ester-, or keto- like groups. Besides, the structure contains alkene- or alkyne-type bonds. ¹³C NMR spectrum confirms the presence of an ester-like group.

In a further approach, a saturated solution of barium hydroxide (1.75 g, 10.2 mmol) was prepared with distilled water (100 mL). The as-prepared

saturated Barium hydroxide (anhydrous, 94-98 %, Alfa Aesar, Karlsruhe, Germany) solution was added to the obtained dark brown electrolyte solutions of G:Uro=1:4 and G:Uro=1:0.17. After the addition, the electrolyte solutions got less turbid and sedimentation was observed after 2 minutes (Figure 84).

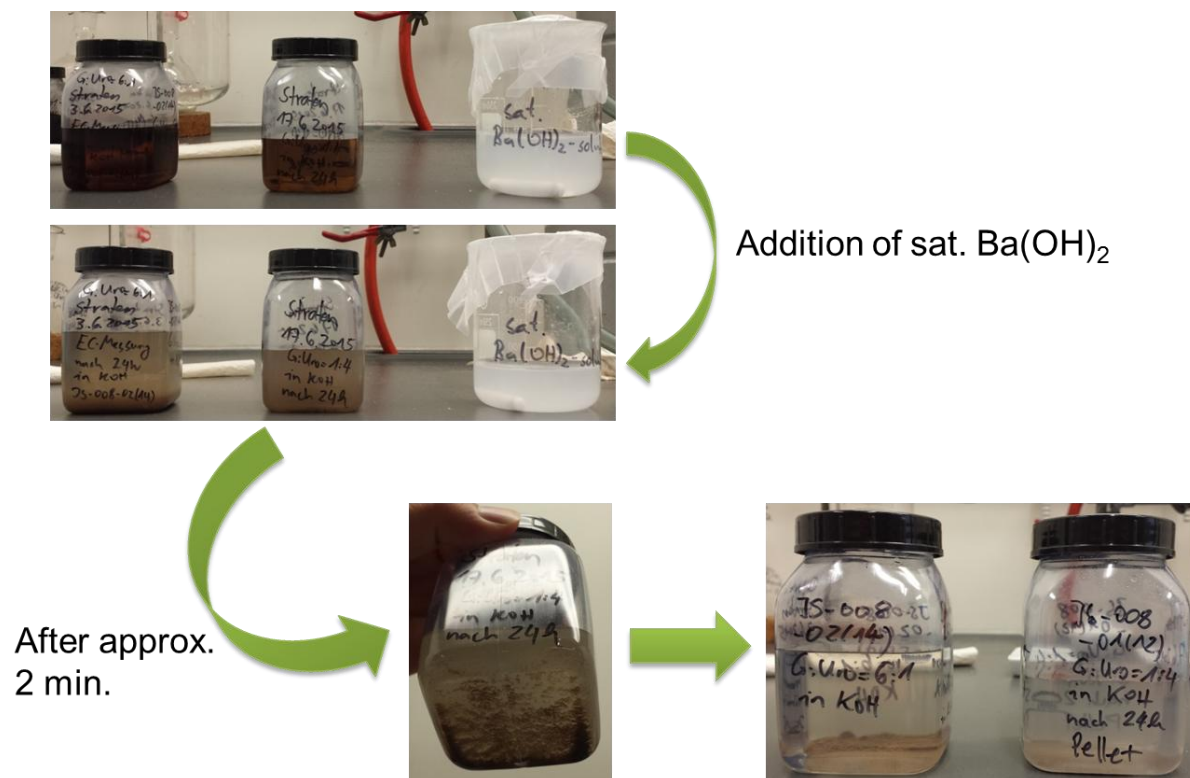


Figure 84: Precipitation of the electrolyte with saturated $\text{Ba}(\text{OH})_2$ solution.

A mixed phase of BaCO_3 and a brown substance precipitated suggesting the brown material polar characteristics. The precipitates were filtrated and washed a few times with distilled water. After drying in a vacuum drying oven at $125\text{ }^\circ\text{C}$ for 1 h the brownish mixed phases (G:Uro=1:0.17, yield: 91 mg; G:Uro=1:4, yield: 17 mg) were obtained.

According to equation (4) and equation (5) the corrosion of carbon leads to the formation of CO_2 which dissociates in water to CO_3^{2-} ions. Hence, the dark brown electrolyte after CA of lowest (G:Uro=1:0.17) and highest (G:Uro=1:4) amount of nitrogen was precipitated with saturated $\text{Ba}(\text{OH})_2$ solution (Figure 84).

The precipitation process occurs following the chemical equation (6):



Again, a solid mixed phase precipitated which is composed of a colorless and a brown-colored phase. Main component of this type of mixed phase – ca. 95 % (86.78 mg) and 86 % (14.60 mg) – are made of BaCO_3 for G:Uro=1:0.17 and G:Uro=1:4, respectively. BaCO_3 is the colorless phase of the mixed phase. The content of BaCO_3 was calculated by means of the data of elemental analysis (Table 9).

Table 9: Elemental composition of brownish mixed phase.

Sample	C [wt%]	H [wt%]	N [wt%]	K [wt%]	Ba [wt%]	O [wt%]
G:Uro=1:4	7.32	0.83	0.02	0.29	55.47	36.07
G:Uro=1:0.17	9.15	0.59	0.24	0.74	65.43	23.85
BaCO_3	6.09	-	-	-	69.59	24.32

The brown phase itself comprises 5 % (4.22 mg) and 16 % (2.40 mg) for G:Uro=1:0.17 and G:Uro=1:4, respectively. The values are almost conformed with the mass loss of the N-HTC for G:Uro=1:0.17 and G:Uro=1:4. In case of N-HTC disc electrode for G:Uro=1:0.17 experimentally 4.02 mg of mass loss occurred whereas for G:Uro=1:4 experimentally a mass loss of 1.92 mg resulted. The deviations between experimental and calculated data are thus around 5 % (G:Uro=1:0.17) and 25 % (G:Uro=1:4). The brown mixed phase was then characterized via FTIR spectroscopic measurements and the presence of BaCO_3 was confirmed (Figure 85). Notwithstanding, at around 1586 cm^{-1} the stretching vibration of an alkene-type group was identified due to the shift towards a pure BaCO_3 sample and the comparatively broad band.

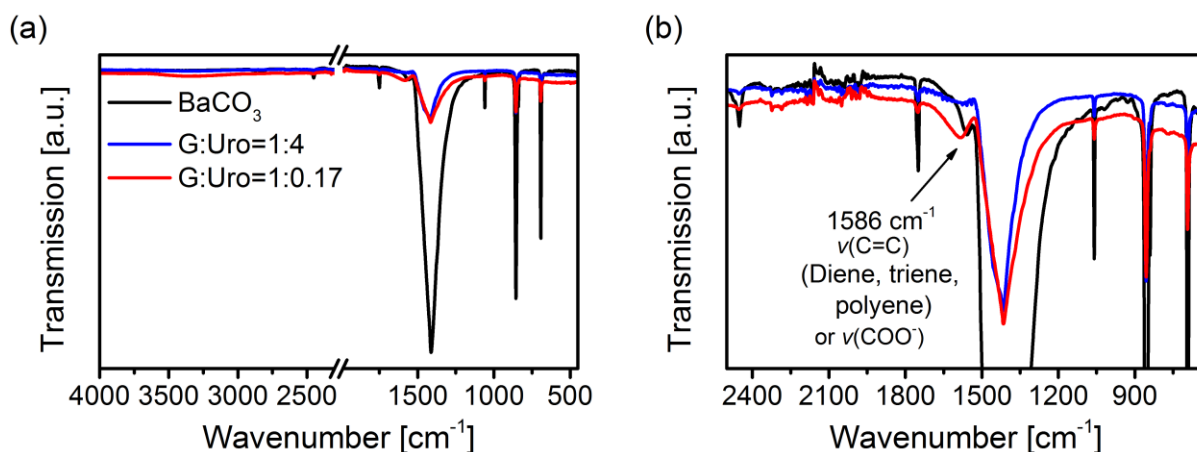


Figure 85: (a) Entire and (b) enlarged FTIR spectrum of the brown mixed phase for G:Uro=1:4 and G:Uro=1:0.17 in comparison with BaCO₃.

Raman spectrum verifies the findings of the FTIR spectroscopic measurement. The characteristic signals of BaCO₃ are observed. Moreover, two pronounced bands arise at 1340 cm^{-1} and 1558 cm^{-1} (Figure 86).

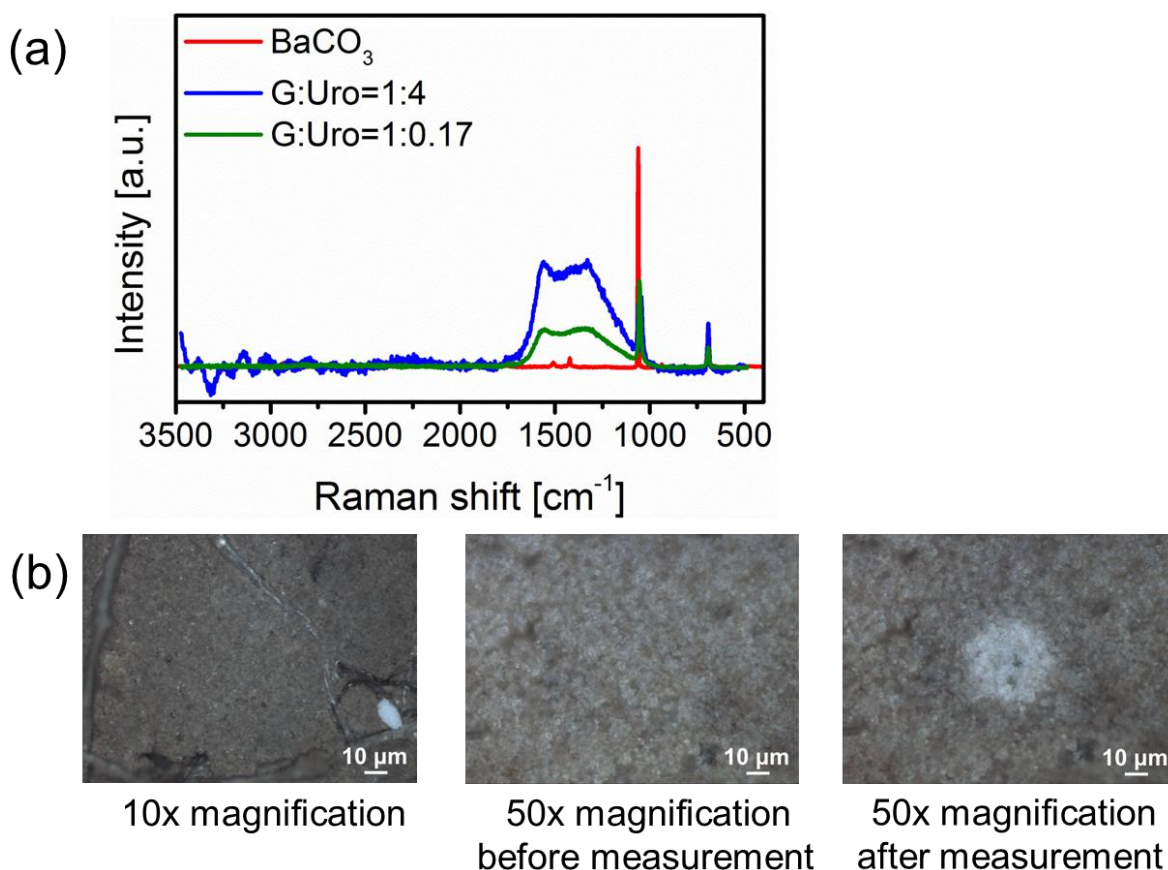


Figure 86: (a) Raman spectrum of brown mixed phase in comparison with BaCO₃ and (b) optical micrographs of brown mixed phase before and after measurement.

These bands are an evidence for the amorphous character of the brown mixed phase and can be put down to molecular excitations. But harsh Raman conditions are needed to measure the brown mixed phase (9 mW, 40 scans) and a burn of the spot that was measured cannot be avoided as proved by optical micrograph. By contrast, the Raman measurement of BaCO_3 was conducted at milder conditions of only 3 mW utilizing 2 scans.

TG-MS analyses of brown mixed phase were performed in order to get an idea about possible functional groups evolving at different temperatures (Figure 87).

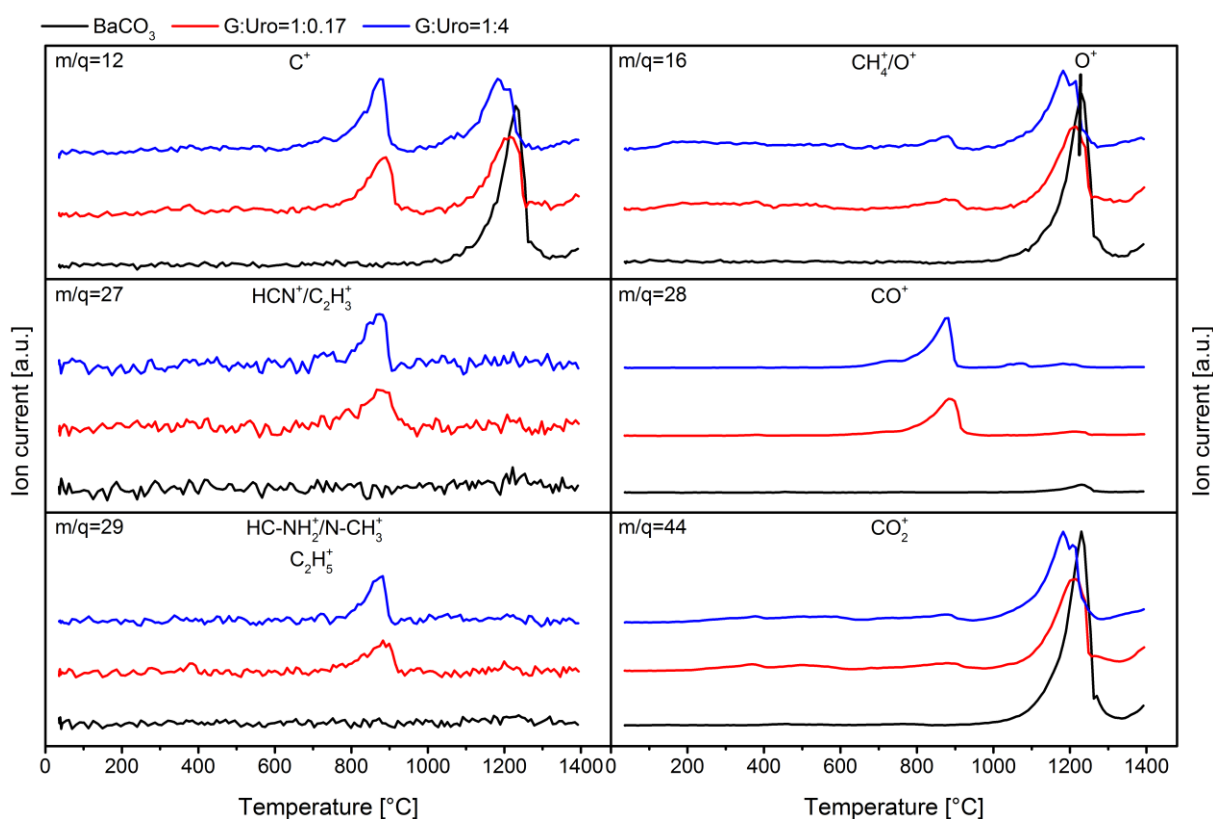


Figure 87: TG-MS spectra of brown mixed phase for G:Uro=1:0.17 and G:Uro=1:4 in comparison with BaCO_3 utilizing a heating rate of $20 \text{ K}\cdot\text{min}^{-1}$ within a temperature range between 40 and 1400 °C.

It should be noted that decomposition of BaCO_3 of the mixed phase starts at ca. 1192 °C which is in accordance with a commercially supplied BaCO_3 sample (Figure 87). Based on this result analyses have been performed to discriminate between different types of oxygen-functional groups.

As it is stated in literature that humic acid can be a possible corrosion by-product during CA of carbon samples, commercially available humic acid has

been purchased which acted as reference sample. Humic acid is a polymeric organic compound and the major constituent of soil, peat or coal materials and hence composed of a variety of structural motifs including organic components such as quinone, catechol, phenol, benzoic acid as well as sugar and peptide entities.^[263] The TG-MS spectrum of humic acid confirms the evolution of a large number of structural entities (Figure 88).

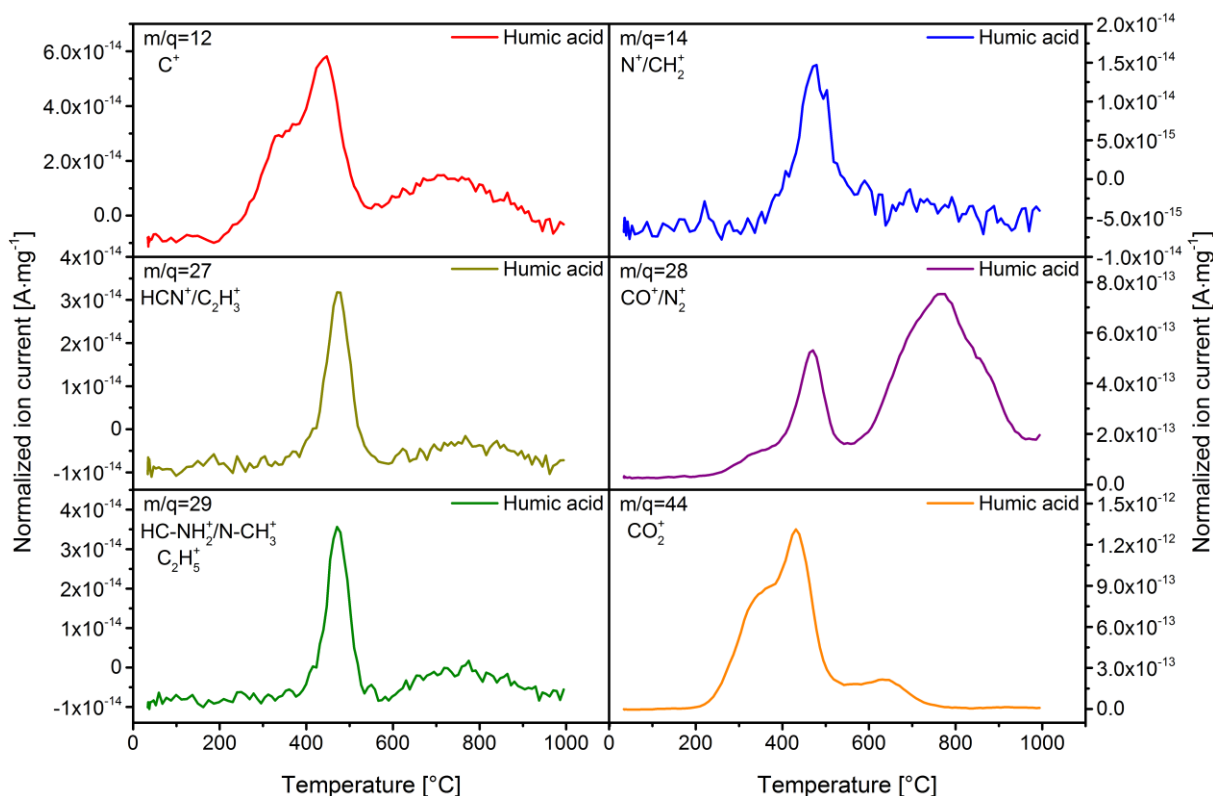


Figure 88: TG-MS spectra of humic acid at a heating rate of 20 K·min⁻¹.

In contrast to Figure 87, the TG-MS spectra of humic acid are completely different. One important aspect is the richness of functional groups humic acid is composed of meaning that functional groups degrade and release over the whole temperature window. The isolated brown mixed phase consists of more thermostable functional groups which start to decompose and evolve at around 800-900 °C (Figure 87). These functional groups include phenol, ether, quinone or keto groups.^[142a, 264] So, only within this temperature region the TG-MS spectra of humic acid can be compared with Figure 88. In fact, all MS spectra of humic acid except of m/q=44 substantiate the existence of these O-functional

groups since they indicate a more or less pronounced bump in this temperature range.

To summarize, similar observations can be made as it has been published in a previous work albeit glassy carbon (GC) was used as object of investigation.^[254] GC behaves in a similar way as a HTC disc in alkaline environment (0.1 M KOH). Stability tests were also conducted for 24 h. It turned out that GC remains stable just like the N-containing HTC disc electrodes. At high anodic potential the carbon surface undergoes tremendous changes induced by the generation of surface oxide functionalities. SEM micrographs corroborate morphological changes to the GC surface caused by electrochemical measurements in alkaline media. Electrochemical oxidation results in heavy surface and impairments of the carbon surface due to carbon dissolution. This goes hand with an increase in the surface area and thus a sudden rise of the electrochemical capacitance. Additionally, the abrupt potential onset can be accounted for the dissolution of the GC pellet. The accompanied brown coloration is a hint for dissolution of carbon particles in the electrolyte.

4.23. Concluding Remarks

Binder-free and biomass-derived disc electrodes from N-functionalized hydrothermal carbon powder materials of spherical morphology were successfully synthesized exhibiting a remarkable mechanical stability without the usage of any binders. After thermal annealing still a high N-portion of 8 wt% was achieved. At the same time, the carbon content increased to 96 wt% while the hydrogen content was detected to below 1 wt%, indicating the high degree of internal condensation of the carbonaceous material. X-ray diffractograms, apart from confirming the amorphousness of all N-HTC samples, emphasize an

occurrence of pregraphitization presuming a turbostratic-like structure independent on the N-content.

For electrochemical analyses, a modified version of an already published standardization protocol was successfully introduced. Electrochemical corrosion tests at high and constant current densities of $10 \text{ mA}\cdot\text{cm}^{-2}$ within OER conditions were performed in 0.1 M KOH. It turns out that N-free disc electrodes are most vulnerable to carbon corrosion. The introduction of N-functional groups enhances the material properties. The higher the N-content is, the higher the electrochemical activity and stability. Importantly, after at least 24 h N-containing pellets are more stable than N-free discs. Likewise, an improved stability towards carbon degradation with N-content is attained. The electrolyte is accompanied with a brown coloration during electrochemical measurements. The brown material in KOH was isolated in two ways, by lyophilization and precipitation as mixed phase composed of the major part of BaCO_3 . The isolated brown material is rich in oxygen-functional groups and can be assumed to be a humic acid-like organic polymeric compound.

To conclude, this synthetic strategy is advantageous since it enables the development of stable electrode materials without utilizing any binder which can perturb and influence significantly the electrochemical measurements.

The N-HTC disc electrodes are suitable for applications as (electro)catalyst support since hydrothermal carbons are electrical conductive and mechanically stable. As this material is N-functionalized they indicate intrinsic catalytic properties and provide stabilization. Due to N-functionalization they have the potential to exhibit a high anchoring ability towards nanoparticles. Thus, the synergetic effect of nanoparticles can provide efficient catalytic active materials for the oxygen reduction reaction (ORR) in fuel cell applications.

5. CONCLUSIONS

Our efforts in understanding the molecular structure of HTC chars were rewarded with the finding that they are basically lignite, meaning coal-like structures, classified as the lowest rank of coal according to the enormous variety of analytical methods that have been utilized.

The incorporation of N by means of urotropine as N-precursor seems to stabilize the polymeric carbonaceous network by strengthening and enhancing the cross-linking density due to the synergetic effects of O- and N-functional groups, structural motifs and organic compounds. By the addition of a mass fraction of 3 wt% of urotropine, higher degree of internal condensation of the polymeric network can be achieved as well as an improved HTC yield and carbon efficiency. Herein, the pH plays a decisive role depending on the reaction pathway. The combined reductive and oxidative synthesis routes in the presence of urotropine causes an activating effect referring to cross-linking of the polymeric carbon network resulting in higher carbon efficiencies.

The preparative success of hydrochars also reflects on the electrochemical measurements, in which a standardization protocol was successfully introduced. N-HTC pellets have been proven to be most stable to carbon corrosion. The introduction of N improves the material properties considerably. The higher the N-content is (up to 8 wt%), the higher the electrochemical activity and stability.

In conclusion, the hydrothermal synthetic strategy is beneficial as it allows the development of disc electrodes with a remarkable mechanical stability without the usage of any binder. The addition of N is most advantageous since the pellets reveal an enhanced electrochemical activity and stability.

6. OUTLOOK

Despite the great achievements that have been reached, still a lot of optimizations need to be done.

Next steps in hydrothermal synthesis optimizations are changing parameters, such as pressure, temperature, solvent, pH or reaction time. An important factor would be to investigate the impact and influence of pressure on the final molecular structure of HTC chars due to the lack of pressure studies in literature. Apart from that, as the pH plays a major role during synthesis, it still can be influenced in another way and not only by adjusting the pH by means of varying the molar ratio of the precursor. For example, the pH of the reaction solution can be directly tuned by the addition of an alkaline (e.g. NaOH) or acidic (e.g. H₂SO₄) solution. This has definitely a serious effect on the already introduced roadmap and can probably lead to other reaction pathways.

Open questions are also the systematic variation of the surface area by, for instance, introducing porosity or the systematic investigation of temperature beyond 900 °C in which the carbon materials starts to turn into a graphitic-like structure. Herein, it is reasonable to perform graphitization studies.

Concerning the starting materials, other N-precursors should be tested and examined referring to their practical usefulness and comparability with N-precursors that have been applied so far.

In terms of electrochemistry, measurements not only in alkaline medium but also in acidic electrolyte can be carried out. Another idea would be to replace the nail polish with another agent in future.

7. REFERENCES

- [1] a) F. Bergius, *Z. Elektrochem.* **1912**, *18*, 660-662; b) F. Bergius, *Z. Elektrochem.* **1913**, *19*, 858-860; c) F. Bergius, *J. Soc. Chem. Ind.* **1913**, *32*, 462-467.
- [2] a) F. Bergius, *Naturwissenschaften* **1928**, *16*, 1-10; b) F. Bergius, in *Nobel Lecture: Chemical reactions under high pressure* (http://www.nobelprize.org/nobel_prizes/chemistry/laureates/1931/bergius-lecture.html) (Ed.: Nobelprize.org), retrieved on September 18, 2017, The Nobel Foundation, Royal Swedish Academy of Sciences, Stockholm, Sweden, **1932**.
- [3] a) F. Bergius, *Z. VDI (Z. Ver. dtsh. Ing.)* **1925**, *69*, 1313-1320; b) F. Bergius, *Z. VDI (Z. Ver. dtsh. Ing.)* **1925**, *69*, 1359-1362.
- [4] E. Berl, A. Schmidt, *Justus Liebigs Ann. Chem.* **1928**, *461*, 192-220.
- [5] a) E. Berl, A. Schmidt, *Justus Liebigs Ann. Chem.* **1932**, *493*, 97-123; b) E. Berl, A. Schmidt, *Justus Liebigs Ann. Chem.* **1932**, *493*, 124-135; c) E. Berl, A. Schmidt, *Justus Liebigs Ann. Chem.* **1932**, *496*, 283-303.
- [6] E. Berl, A. Schmidt, H. Koch, *Angew. Chem.* **1932**, *45*, 517-519.
- [7] M. W. Haenel, *Fuel* **1992**, *71*, 1211-1223.
- [8] a) J. P. Schuhmacher, H. A. van Vucht, M. P. Groenewege, L. Blom, D. W. van Krevelen, *Fuel* **1956**, *35*, 281-290; b) J. P. Schuhmacher, F. J. Huntjens, D. W. van Krevelen, *Fuel* **1960**, *39*, 223-234.
- [9] Q. Wang, H. Li, L. Q. Chen, X. J. Huang, *Carbon* **2001**, *39*, 2211-2214.
- [10] X. M. Sun, Y. D. Li, *Angew. Chem. Int. Ed.* **2004**, *43*, 597-601.
- [11] S.-H. Yu, X. J. Cui, L. L. Li, K. Li, B. Yu, M. Antonietti, H. Cölfen, *Adv. Mater.* **2004**, *16*, 1636-1640.
- [12] H.-S. Qian, S.-H. Yu, L.-B. Luo, J.-Y. Gong, L.-F. Fei, X.-M. Liu, *Chem. Mater.* **2006**, *18*, 2102-2108.
- [13] a) A. Rabenau, *Angew. Chem. Int. Ed.* **1985**, *24*, 1026-1040; b) S.-H. Feng, G.-H. Li, in *Modern Inorganic Synthetic Chemistry*, 2nd ed. (Eds.: R. Xu, Y. Xu), Elsevier B.V., Amsterdam, Netherlands, **2017**, pp. 73-104.
- [14] H. Zhao, Z.-R. Qu, H.-Y. Ye, R.-G. Xiong, *Chem. Soc. Rev.* **2008**, *37*, 84-100.
- [15] a) S. H. Feng, R. R. Xu, *Acc. Chem. Res.* **2001**, *34*, 239-247; b) G. Demazeau, *J. Mater. Chem.* **1999**, *9*, 15-18.
- [16] R. Nacken, *Chem. Ztg.* **1950**, *74*, 745-749.
- [17] a) H. Zhao, S. H. Feng, *Chem. Mater.* **1999**, *11*, 958-964; b) G. S. Li, L. P. Li, S. H. Feng, M. Q. Wang, L. Y. Zhang, X. Yao, *Adv. Mater.* **1999**, *11*, 146-149; c) G. S. Pang, S. H. Feng, Y. C. Tang, C. H. Tan, R. R. Xu, *Chem. Mater.* **1998**, *10*, 2446-2449.
- [18] S. H. Feng, M. Greenblatt, *Chem. Mater.* **1992**, *4*, 1257-1262.

- [19] Q. W. Chen, Y. T. Qian, Z. Y. Chen, K. B. Tang, G. E. Zhou, Y. H. Zhang, *Physica C* **1994**, *224*, 228-230.
- [20] a) Y. C. Mao, G. S. Li, W. Xu, S. H. Feng, *J. Mater. Chem.* **2000**, *10*, 479-482; b) C. Y. Zhao, S. H. Feng, Z. C. Chao, C. S. Shi, R. Xu, J. Z. Ni, *Chem. Commun.* **1996**, 1641-1642.
- [21] D. Wang, R. Yu, H. Wang, M. Takano, S. Feng, W. Theng, *J. Ceram. Soc. Jpn.* **2004**, *112*, S30-S32.
- [22] C. Y. Zhao, S. H. Feng, R. R. Xu, C. S. Shi, J. Z. Ni, *Chem. Commun.* **1997**, 945-946.
- [23] a) H. Y. Chen, J. Wydra, X. Y. Zhang, P.-S. Lee, Z. P. Wang, W. Fan, M. Tsapatsis, *J. Am. Chem. Soc.* **2011**, *133*, 12390-12393; b) C. S. Cundy, P. A. Cox, *Microporous Mesoporous Mater.* **2005**, *82*, 1-78; c) A. K. Cheetham, G. Férey, T. Loiseau, *Angew. Chem. Int. Ed.* **1999**, *38*, 3268-3292; d) X. H. Bu, P. Y. Feng, T. E. Gier, D. Y. Zhao, G. D. Stucky, *J. Am. Chem. Soc.* **1998**, *120*, 13389-13397; e) D. E. Akporiaye, I. M. Dahl, A. Karlsson, R. Wendelbo, *Angew. Chem. Int. Ed.* **1998**, *37*, 609-611; f) P. Y. Feng, X. H. Bu, G. D. Stucky, *Nature* **1997**, *388*, 735-741.
- [24] a) P. J. Hagrman, D. Hagrman, J. Zubieta, *Angew. Chem. Int. Ed.* **1999**, *38*, 2639-2684; b) S. R. Batten, R. Robson, *Angew. Chem. Int. Ed.* **1998**, *37*, 1460-1494; c) O. M. Yaghi, H. L. Li, C. Davis, D. Richardson, T. L. Groy, *Acc. Chem. Res.* **1998**, *31*, 474-484; d) C. Janiak, *Angew. Chem. Int. Ed.* **1997**, *36*, 1431-1434.
- [25] a) Y. Liang, W.-G. Yuan, S.-F. Zhang, Z. He, J. R. Xue, X. Zhang, L.-H. Jing, D.-B. Qin, *Dalton Trans.* **2016**, *45*, 1382-1390; b) Y. Qi, F. Luo, Y. X. Che, J. M. Zhen, *Cryst. Growth Des.* **2008**, *8*, 606-611; c) O. M. Yaghi, H. L. Li, *J. Am. Chem. Soc.* **1995**, *117*, 10401-10402.
- [26] J. A. Darr, J. Y. Zhang, N. M. Makwana, X. L. Weng, *Chem. Rev.* **2017**, *117*, 11125-11238.
- [27] a) N. Brun, S. A. Wohlgemuth, P. Osiceanu, M. M. Titirici, *Green Chem.* **2013**, *15*, 2514-2524; b) T.-P. Fellingner, R. J. White, M.-M. Titirici, M. Antonietti, *Adv. Funct. Mater.* **2012**, *22*, 3254-3260; c) R. J. White, N. Yoshizawa, M. Antonietti, M.-M. Titirici, *Green Chem.* **2011**, *13*, 2428-2434.
- [28] a) V. V. Kondalkar, R. R. Kharade, S. S. Mali, R. M. Mane, P. B. Patil, P. S. Patil, S. Choudhury, P. N. Bhosale, *Superlattices Microstruct.* **2014**, *73*, 290-295; b) Z. N. Urgessa, O. S. Oluwafemi, J. R. Botha, *Mater. Lett.* **2012**, *79*, 266-269; c) N. P. Padture, X. Z. Wei, *J. Am. Ceram. Soc.* **2003**, *86*, 2215-2217.
- [29] X.-Z. Zhao, R. Roy, K. A. Cherian, A. Badzian, *Nature* **1997**, *385*, 513-515.
- [30] S. H. Feng, H. M. Yuan, Z. Shi, Y. Chen, Y. W. Wang, K. K. Huang, C. M. Hou, J. X. Li, G. S. Pang, Y. Hou, *J. Mater. Sci.* **2008**, *43*, 2131-2137.
- [31] a) J. J. Lu, Y. Xu, N. K. Goh, L. S. Chia, *Chem. Commun.* **1998**, 2733-2734; b) K.-H. Lii, *J. Chem. Soc., Dalton Trans.* **1996**, 815-818.

- [32] D. A. Bruce, A. P. Wilkinson, M. G. White, J. A. Bertrand, *J. Solid State Chem.* **1996**, *125*, 228-233.
- [33] a) H. W. Jannasch, M. J. Mottl, *Science* **1985**, *229*, 717-725; b) J. A. Baross, J. W. Deming, *Nature* **1983**, *303*, 423-426.
- [34] a) A. Aimable, H. Muhr, C. Gentric, F. Bernard, F. Le Cras, D. Aymes, *Powder Technol.* **2009**, *190*, 99-106; b) Y. Matsumura, T. Nunoura, T. Urase, K. Yamamoto, *J. Hazard. Mater.* **2000**, *73*, 245-254; c) S. Gopalan, P. E. Savage, *AIChE J.* **1995**, *41*, 1864-1873.
- [35] H. Y. Chen, D. M. Hiller, J. E. Hudson, C. J. A. Westenbroek, *IEEE Trans. Magn.* **1984**, *20*, 24-26.
- [36] a) H. Rau, Rabenau, *Solid State Commun.* **1967**, *5*, 331-332; b) V. A. Nikitenko, V. I. Popolitov, S. G. Stoyukhin, A. Ya. Shapiro, A. N. Lobachev, A. I. Tereshchenko, V. G. Kolotilova, *Pis'ma v Zhurnal Tekhnicheskoi Fiziki* **1979**, *5*, 1177-1181.
- [37] R. Kniep, A. Rabenau, *Top. Curr. Chem.* **1983**, *111*, 145-192.
- [38] K. Byrappa, M. Yoshimura, in *Handbook of Hydrothermal Technology: A Technology for Crystal Growth and Materials Processing*, Noyes Publications / William Andrews Publishing, LLC, Norwich, New York, United States of America, **2001**, pp. 691-753.
- [39] H. S. Kambo, A. Dutta, *Renew. Sust. Energ. Rev.* **2015**, *45*, 359-378.
- [40] a) J. Ming, Y. Wu, G. Liang, J.-B. Park, F. Zhao, Y.-K. Sun, *Green Chem.* **2013**, *15*, 2722-2726; b) S.-A. Wohlgemuth, F. Vilela, M.-M. Titirici, M. Antonietti, *Green Chem.* **2012**, *14*, 741-749.
- [41] S. Reiche, N. Kowalew, R. Schlögl, *ChemPhysChem* **2015**, *16*, 579-587.
- [42] a) L. H. Yu, C. Falco, J. Weber, R. J. White, J. Y. Howe, M.-M. Titirici, *Langmuir* **2012**, *28*, 12373-12383; b) M.-M. Titirici, M. Antonietti, *Chem. Soc. Rev.* **2010**, *39*, 103-116; c) B. Hu, K. Wang, L. H. Wu, S.-H. Yu, M. Antonietti, M.-M. Titirici, *Adv. Mater.* **2010**, *22*, 813-828.
- [43] a) S. K. Hoekman, A. Broch, C. Robbins, B. Zielinska, L. Felix, *Biomass Conv. Bioref.* **2013**, *3*, 113-126; b) J. Mumme, L. Eckervogt, J. Pielert, M. Diakité, F. Rupp, J. Kern, *Bioresour. Technol.* **2011**, *102*, 9255-9260; c) J. A. Libra, K. S. Ro, C. Kammann, A. Funke, N. D. Berge, Y. Neubauer, M.-M. Titirici, C. Fühner, O. Bens, J. Kern, K.-H. Emmerich, *Biofuels* **2011**, *2*, 71-106.
- [44] a) I. Pavlovič, Z. Knez, M. Škerget, *J. Agric. Food. Chem.* **2013**, *61*, 8003-8025; b) A. A. Peterson, F. Vogel, R. P. Lachance, M. Fröling, M. J. Antal, J. W. Tester, *Energy Environ. Sci.* **2008**, *1*, 32-65.
- [45] V. Benavente, E. Calabuig, A. Fullana, *J. Anal. Appl. Pyrolysis* **2015**, *113*, 89-98.
- [46] W. Yan, J. T. Hastings, T. C. Acharjee, C. J. Coronella, V. R. Vásquez, *Energy Fuels* **2010**, *24*, 4738-4742.
- [47] M.-M. Titirici, A. Thomas, M. Antonietti, *New J. Chem.* **2007**, *31*, 787-789.

- [48] N. D. Berge, K. S. Ro, J. D. Mao, J. R. V. Flora, M. A. Chappell, S. Y. Bae, *Environ. Sci. Technol.* **2011**, *45*, 5696-5703.
- [49] a) A. Gajić, in *Einfluss von HTC-Biokohle auf chemische und physikalische Bodeneigenschaften und Pflanzenwachstum*, Institut für Zuckerrübenforschung, Göttingen, Germany, **2012**, pp. 1-10; b) H.-G. Ramke, D. Blöhse, in *Fachgespräch Feststoffuntersuchung 2010 – Neue Entwicklungen in der Abfall- und Altlastenuntersuchung*, Bildungsstätte Essen des Bildungszentrum für Entsorgungs- und Wasserwirtschaft GmbH, Ministerium für Umwelt und Naturschutz, Landwirtschaft und Verbraucherschutz des Landes NRW, Essen, Germany, **2010**, pp. 1-21.
- [50] G. Trif-Tordai, I. Ionel, in *Alternative Fuel* (Ed.: M. Manzanera), InTech, Rijeka, Croatia, **2011**, pp. 285-306.
- [51] a) M. Sevilla, M. M. Titirici, *Bol. Grupo Español Carbón* **2012**, *25*, 7-17; b) N. Baccile, G. Laurent, F. Babonneau, F. Fayon, M.-M. Titirici, M. Antonietti, *J. Phys. Chem. C* **2009**, *113*, 9644-9654.
- [52] M. Sevilla, A. B. Fuertes, *Chem. Eur. J.* **2009**, *15*, 4195-4203.
- [53] a) C. Falco, N. Baccile, M.-M. Titirici, *Green Chem.* **2011**, *13*, 3273-3281; b) C. Falco, F. Perez Caballero, F. Babonneau, C. Gervais, G. Laurent, M.-M. Titirici, N. Baccile, *Langmuir* **2011**, *27*, 14460-14471.
- [54] a) M. Möller, P. Nilges, F. Harnisch, U. Schröder, *ChemSusChem* **2011**, *4*, 566-579; b) A. Gandini, M. N. Belgacem, *Prog. Polym. Sci.* **1997**, *22*, 1203-1379.
- [55] M.-M. Titirici, M. Antonietti, N. Baccile, *Green Chem.* **2008**, *10*, 1204-1212.
- [56] M. Sevilla, A. B. Fuertes, *Carbon* **2009**, *47*, 2281-2289.
- [57] a) P. Kumar, D. M. Barrett, M. J. Delwiche, P. Stroeve, *Ind. Eng. Chem. Res.* **2009**, *48*, 3713-3729; b) R. Rinaldi, F. Schüth, *ChemSusChem* **2009**, *2*, 1096-1107; c) M. Sasaki, Z. Fang, Y. Fukushima, T. Adschiri, K. Arai, *Ind. Eng. Chem. Res.* **2000**, *39*, 2883-2890; d) M. Sasaki, B. Kabyemela, R. Malaluan, S. Hirose, N. Takeda, T. Adschiri, K. Arai, *J. Supercrit. Fluids* **1998**, *13*, 261-268; e) O. Bobleter, *Prog. Polym. Sci.* **1994**, *19*, 797-841.
- [58] a) K. David, Y. Q. Pu, M. Foston, J. Muzzy, A. Ragauskas, *Energy Fuels* **2009**, *23*, 498-501; b) M. Bardet, S. Hediger, G. Gerbaud, S. Gambarelli, J. F. Jacquot, M. F. Foray, A. Gadelle, *Fuel* **2007**, *86*, 1966-1976.
- [59] a) D. Knežević, W. van Swaaij, S. Kersten, *Ind. Eng. Chem. Res.* **2010**, *49*, 104-112; b) J. B. Wooten, J. I. Seeman, M. R. Hajaligol, *Energy Fuels* **2004**, *18*, 1-15; c) E. B. Sanders, A. I. Goldsmith, J. I. Seeman, *J. Anal. Appl. Pyrolysis* **2003**, *66*, 29-50; d) I. Pastorova, R. E. Botto, P. W. Arisz, J. J. Boon, *Carbohydr. Res.* **1994**, *262*, 27-47.
- [60] a) K. Tekin, S. Karagöz, S. Bektaş, *Renew. Sust. Energ. Rev.* **2014**, *40*, 673-687; b) A. Funke, F. Ziegler, *Biofuels, Bioprod. Bioref.* **2010**, *4*, 160-177.
- [61] X. Q. Zhang, J. Golding, I. Burgar, *Polymer* **2002**, *43*, 5791-5796.

- [62] a) M.-M. Titirici, R. J. White, L. Zhao, *Green* **2012**, *2*, 25-40; b) T. J. Bandoz, in *Carbon Materials for Catalysis*, 1st ed. (Eds.: P. Serp, J. L. Figueiredo), John Wiley & Sons, Inc., Hoboken, New Jersey, United States of America, **2009**, pp. 45-92; c) H.-P. Boehm, in *Carbon Matreials for Catalysis*, 1st ed. (Eds.: P. Serp, J. L. Figueiredo), John Wiley & Sons, Inc., Hoboken, New Jersey, United States of America, **2009**, pp. 219-266; d) Y. Y. Shao, J. H. Sui, G. P. Yin, Y. Z. Gao, *Appl. Catal., B* **2008**, *79*, 89-99.
- [63] a) M. Glerup, J. Steinmetz, D. Samaille, O. Stéphan, S. Enouz, A. Loiseau, S. Roth, P. Bernier, *Chem. Phys. Lett.* **2004**, *387*, 193-197; b) R. Droppa, P. Hammer, A. C. M. Carvalho, M. C. dos Santos, F. Alvarez, *J. Non-Cryst. Solids* **2002**, *299*, 874-879.
- [64] a) J. C. Hummelen, B. Knight, J. Pavlovich, R. González, F. Wudl, *Science* **1995**, *269*, 1554-1556; b) S. Glenis, S. Cooke, X. Chen, M. M. Labes, *Chem. Mater.* **1994**, *6*, 1850-1853.
- [65] a) M. Terrones, H. Terrones, N. Grobert, W. K. Hsu, Y. Q. Zhu, J. P. Hare, H. W. Kroto, D. R. M. Walton, P. Kohler-Redlich, M. Rühle, J. P. Zhang, A. K. Cheetham, *Appl. Phys. Lett.* **1999**, *75*, 3932-3934; b) M. Yudasaka, R. Kikuchi, Y. Ohki, S. Yoshimura, *Carbon* **1997**, *35*, 195-201.
- [66] a) M. Glerup, M. Castignolles, M. Holzinger, G. Hug, A. Loiseau, P. Bernier, *Chem. Commun.* **2003**, 2542-2543; b) M. Terrones, R. Kamalakaran, T. Seeger, M. Rühle, *Chem. Commun.* **2000**, 2335-2336.
- [67] S. Maldonado, S. Morin, K. J. Stevenson, *Carbon* **2006**, *44*, 1429-1437.
- [68] E.-G. Wang, *Adv. Mater.* **1999**, *11*, 1129-1133.
- [69] a) D. Srivastava, M. Menon, C. Daraio, S. Jin, B. Sadanadan, A. M. Rao, *Phys. Rev. B: Condens. Matter* **2004**, *69*, 153414; b) C. C. Tang, Y. Bando, D. Golberg, F. F. Xu, *Carbon* **2004**, *42*, 2625-2633; c) M. Terrones, P. Redlich, N. Grobert, S. Trasobares, W. K. Hsu, H. Terrones, Y. Q. Zhu, J. P. Hare, C. L. Reeves, A. K. Cheetham, M. Rühle, H. W. Kroto, D. R. M. Walton, *Adv. Mater.* **1999**, *11*, 655-658; d) M. Terrones, N. Grobert, J. Olivares, J. P. Zhang, H. Terrones, K. Kordatos, W. K. Hsu, J. P. Hare, P. D. Townsend, K. Prassides, A. K. Cheetham, H. W. Kroto, D. R. M. Walton, *Nature* **1997**, *388*, 52-55.
- [70] a) L. Zhao, R. Crombez, F. Pérez Caballero, M. Antonietti, J. Texter, M.-M. Titirici, *Polymer* **2010**, *51*, 4540-4546; b) L. Zhao, N. Baccile, S. Gross, Y. Zhang, W. Wei, Y. Sun, M. Antonietti, M.-M. Titirici, *Carbon* **2010**, *48*, 3778-3787; c) N. Baccile, M. Antonietti, M.-M. Titirici, *ChemSusChem* **2010**, *3*, 246-253.
- [71] a) C. B. Cao, F. L. Huang, C. T. Cao, J. Li, H. Zhu, *Chem. Mater.* **2004**, *16*, 5213-5215; b) Q. X. Guo, Y. Xie, X. J. Wang, S. Y. Zhang, T. Hou, S. C. Lv, *Chem. Commun.* **2004**, 26-27.
- [72] G. Lota, B. Grzyb, H. Machnikowska, J. Machnikowski, E. Frackowiak, *Chem. Phys. Lett.* **2005**, *404*, 53-58.

- [73] H. Zengin, W. S. Zhou, J. Y. Jin, R. Czerw, D. W. Smith, L. Echegoyen, D. L. Carroll, S. H. Foulger, J. Ballato, *Adv. Mater.* **2002**, *14*, 1480-+.
- [74] L. J. Zhi, T. Gorelik, R. Friedlein, J. S. Wu, U. Kolb, W. R. Salaneck, K. Müllen, *Small* **2005**, *1*, 798-801.
- [75] J. Lahaye, G. Nansé, A. Bagreev, V. Strelko, *Carbon* **1999**, *37*, 585-590.
- [76] A. Bagreev, S. Bashkova, T. J. Bandosz, *Langmuir* **2002**, *18*, 1257-1264.
- [77] D. Hulicova, J. Yamashita, Y. Soneda, H. Hatori, M. Kodama, *Chem. Mater.* **2005**, *17*, 1241-1247.
- [78] R. Sen, B. C. Satishkumar, S. Govindaraj, K. R. Harikumar, M. K. Renganathan, C. N. R. Rao, *J. Mater. Chem.* **1997**, *7*, 2335-2337.
- [79] a) F. Jaouen, M. Lefèvre, J. P. Dodelet, M. Cai, *J. Phys. Chem. B* **2006**, *110*, 5553-5558; b) R. A. Sidik, A. B. Anderson, N. P. Subramanian, S. P. Kumaraguru, B. N. Popov, *J. Phys. Chem. B* **2006**, *110*, 1787-1793; c) L. Q. Jiang, L. Gao, *Carbon* **2003**, *41*, 2923-2929; d) S. C. Roy, A. W. Harding, A. E. Russell, K. M. Thomas, *J. Electrochem. Soc.* **1997**, *144*, 2323-2328; e) B. Stöhr, H. P. Boehm, R. Schlögl, *Carbon* **1991**, *29*, 707-720; f) H.-P. Boehm, A. R. Derincon, T. Stohr, B. Tereczki, A. Vass, *J. Chim. Phys. Phys.-Chim. Biol.* **1987**, *84*, 1449-1455.
- [80] S. Biniak, G. Szymański, J. Siedlewski, A. Świątkowski, *Carbon* **1997**, *35*, 1799-1810.
- [81] Y. Komatsubara, S. Ida, H. Fujitsu, I. Mochida, *Fuel* **1984**, *63*, 1738-1742.
- [82] Y. El-Sayed, T. J. Bandosz, *Langmuir* **2002**, *18*, 3213-3218.
- [83] a) A. Gajić, H.-J. Koch, *J. Environ. Qual.* **2012**, *41*, 1067-1075; b) A. Gajić, H.-J. Koch, B. Märlander, *Sugar Ind.* **2011**, *136*, 791-799.
- [84] a) M. M. Tusi, N. S. de Oliveira Polanco, M. Brandalise, O. V. Correa, J. C. Villalba, F. J. Anaissi, A. O. Neto, E. V. Spinacé, *Int. J. Electrochem. Sci.* **2011**, *6*, 484-491; b) M. Sevilla, C. Sanchís, T. Valdés-Solís, E. Morallón, A. B. Fuertes, *Electrochim. Acta* **2009**, *54*, 2234-2238; c) Z. H. Wen, J. Liu, J. H. Li, *Adv. Mater.* **2008**, *20*, 743-747; d) Z. H. Wen, Q. Wang, J. H. Li, *Adv. Funct. Mater.* **2008**, *18*, 959-964; e) J. B. Joo, Y. J. Kim, W. Kim, P. Kim, J. Yi, *Catal. Commun.* **2008**, *10*, 267-271; f) M. Sevilla, G. Lota, A. B. Fuertes, *J. Power Sources* **2007**, *171*, 546-551; g) Z. H. Wen, Q. Wang, Q. Zhang, J. H. Li, *Electrochem. Commun.* **2007**, *9*, 1867-1872; h) P. Kim, J. B. Joo, W. Kim, J. Kim, I. K. Song, J. Yi, *Catal. Lett.* **2006**, *112*, 213-218; i) R. Z. Yang, X. P. Qiu, H. R. Zhang, J. Q. Li, W. T. Zhu, Z. X. Wang, X. J. Huang, L. Q. Chen, *Carbon* **2005**, *43*, 11-16.
- [85] a) N. Brun, K. Sakaushi, L. Yu, L. Giebeler, J. Eckert, M. M. Titirici, *Phys. Chem. Chem. Phys.* **2013**, *15*, 6080-6087; b) Y.-S. Hu, R. Demir-Cakan, M.-M. Titirici, J.-O. Müller, R. Schlögl, M. Antonietti, J. Maier, *Angew. Chem. Int. Ed.* **2008**, *47*, 1645-1649.
- [86] a) C. Falco, J. M. Sieben, N. Brun, M. Sevilla, T. van der Maelen, E. Morallón, D. Cazorla-Amorós, M.-M. Titirici, *ChemSusChem* **2013**, *6*,

- 374-382; b) L. Zhao, L.-Z. Fan, M.-Q. Zhou, H. Guan, S. Qiao, M. Antonietti, M.-M. Titirici, *Adv. Mater.* **2010**, *22*, 5202-5206.
- [87] a) M. Soorholtz, R. J. White, T. Zimmermann, M.-M. Titirici, M. Antonietti, R. Palkovits, F. Schüth, *Chem. Commun.* **2013**, *49*, 240-242; b) G. B. Yu, B. Sun, Y. Pei, S. H. Xie, S. R. Yan, M. H. Qiao, K. N. Fan, X. X. Zhang, B. N. Zong, *J. Am. Chem. Soc.* **2010**, *132*, 935-937; c) S. Y. Wu, Y. S. Ding, X. M. Zhang, H. O. Tang, L. Chen, B. X. Li, *J. Solid State Chem.* **2008**, *181*, 2171-2177; d) P. Makowski, R. Demir Cakan, M. Antonietti, F. Goettmann, M.-M. Titirici, *Chem. Commun.* **2008**, 999-1001.
- [88] a) P. Zhang, X. Li, C. Shao, Y. Liu, *J. Mater. Chem. A* **2015**, *3*, 3281-3284; b) P. Zhang, C. L. Shao, M. Y. Zhang, Z. C. Guo, J. B. Mu, Z. Y. Zhang, X. Zhang, P. P. Liang, Y. C. Liu, *J. Hazard. Mater.* **2012**, *229*, 265-272; c) Y. Zhang, P. Zhang, Y. N. Huo, D. Q. Zhang, G. S. Li, H. X. Li, *Appl. Catal., B* **2012**, *115*, 236-244; d) J. D. Zhuang, Q. F. Tian, H. Zhou, Q. Liu, P. Liu, H. M. Zhong, *J. Mater. Chem.* **2012**, *22*, 7036-7042; e) J.-W. Shi, X. Zong, X. Wu, H.-J. Cui, B. Xu, L. Z. Wang, M.-L. Fu, *ChemCatChem* **2012**, *4*, 488-491; f) P. Zhang, C. L. Shao, Z. Y. Zhang, M. Y. Zhang, J. B. Mu, Z. C. Guo, Y. Y. Sun, Y. C. Liu, *J. Mater. Chem.* **2011**, *21*, 17746-17753; g) J. Zhong, F. Chen, J. L. Zhang, *J. Phys. Chem. C* **2010**, *114*, 933-939; h) L. Zhao, X. F. Chen, X. C. Wang, Y. J. Zhang, W. Wei, Y. H. Sun, M. Antonietti, M.-M. Titirici, *Adv. Mater.* **2010**, *22*, 3317-3321.
- [89] a) M. Sevilla, C. Falco, M.-M. Titirici, A. B. Fuertes, *RSC Adv.* **2012**, *2*, 12792-12797; b) M. Sevilla, A. B. Fuertes, *Energy Environ. Sci.* **2011**, *4*, 1765-1771; c) L. Zhao, Z. Bacsik, N. Hedin, W. Wei, Y. H. Sun, M. Antonietti, M.-M. Titirici, *ChemSusChem* **2010**, *3*, 840-845; d) N. Hedin, L. J. Chen, A. Laaksonen, *Nanoscale* **2010**, *2*, 1819-1841.
- [90] a) M. Sevilla, A. B. Fuertes, R. Mokaya, *Energy Environ. Sci.* **2011**, *4*, 1400-1410; b) Y. Yürüm, A. Taralp, T. N. Veziroglu, *Int. J. Hydrogen Energy* **2009**, *34*, 3784-3798.
- [91] a) S. Kumar, V. A. Loganathan, R. B. Gupta, M. O. Barnett, *J. Environ. Manage.* **2011**, *92*, 2504-2512; b) Z. G. Liu, F.-S. Zhang, J. Z. Wu, *Fuel* **2010**, *89*, 510-514; c) Z. G. Liu, F.-S. Zhang, *J. Hazard. Mater.* **2009**, *167*, 933-939; d) R. Demir-Cakan, N. Baccile, M. Antonietti, M.-M. Titirici, *Chem. Mater.* **2009**, *21*, 484-490.
- [92] J. B. Zhou, C. Tang, B. Cheng, J. G. Yu, M. Jaroniec, *ACS Appl. Mater. Interfaces* **2012**, *4*, 2174-2179.
- [93] a) W. B. Lu, X. Y. Qin, S. Liu, G. H. Chang, Y. W. Zhang, Y. L. Luo, A. M. Asiri, A. O. Al-Youbi, X. P. Sun, *Anal. Chem.* **2012**, *84*, 5351-5357; b) F. J. Xia, M. Pan, S. C. Mu, M. D. Jones, D. Wolverson, F. Marken, *Electroanalysis* **2012**, *24*, 1703-1708.
- [94] a) Z. Guo, J. Y. Liu, Y. Jia, X. Chen, F. L. Meng, M. Q. Li, J. H. Liu, *Nanotechnology* **2008**, *19*, 345704; b) C. H. Wang, X. F. Chu, M. M. Wu,

- Sens. Actuators, B* **2007**, *120*, 508-513; c) X.-L. Li, T.-J. Lou, X.-M. Sun, Y.-D. Li, *Inorg. Chem.* **2004**, *43*, 5442-5449.
- [95] a) J. L. Gu, S. S. Su, Y. S. Li, Q. J. He, J. L. Shi, *Chem. Commun.* **2011**, *47*, 2101-2103; b) G. Gao, H. X. Wu, Y. X. Zhang, K. Wang, P. Huang, X. Q. Zhang, S. W. Guo, D. X. Cui, *J. Mater. Chem.* **2011**, *21*, 12224-12227; c) B. R. Selvi, D. Jagadeesan, B. S. Suma, G. Nagashankar, M. Arif, K. Balasubramanyam, M. Eswaramoorthy, T. K. Kundu, *Nano Lett.* **2008**, *8*, 3182-3188.
- [96] a) H.-W. Li, Y. Li, Y.-Q. Dang, L.-J. Ma, Y. Q. Wu, G. F. Hou, L. X. Wu, *Chem. Commun.* **2009**, 4453-4455; b) S.-R. Guo, J.-Y. Gong, P. Jiang, M. Wu, Y. Lu, S.-H. Yu, *Adv. Funct. Mater.* **2008**, *18*, 872-879; c) Y.-P. Sun, B. Zhou, Y. Lin, W. Wang, K. A. S. Fernando, P. Pathak, M. J. Meziani, B. A. Harruff, X. Wang, H. F. Wang, P. J. G. Luo, H. Yang, M. E. Kose, B. L. Chen, L. M. Veca, S.-Y. Xie, *J. Am. Chem. Soc.* **2006**, *128*, 7756-7757.
- [97] A. P. Zeng, Y. B. Yin, M. Bilek, D. McKenzie, *Surf. Coat. Technol.* **2005**, *198*, 202-205.
- [98] Y. F. Jia, B. Xiao, K. M. Thomas, *Langmuir* **2002**, *18*, 470-478.
- [99] a) G. G. Stavropoulos, P. Samaras, G. P. Sakellaropoulos, *J. Hazard. Mater.* **2008**, *151*, 414-421; b) A. Vinu, S. Anandan, C. Anand, P. Srinivasu, K. Ariga, T. Mori, *Microporous Mesoporous Mater.* **2008**, *109*, 398-404.
- [100] a) Y. Shao, J. Sui, G. Yin, Y. Gao, *Appl. Catal., B* **2008**, *79*, 89-99; b) H. Yoon, S. Ko, J. Jang, *Chem. Commun.* **2007**, 1468-1470.
- [101] a) M. Kawaguchi, A. Itoh, S. Yagi, H. Oda, *J. Power Sources* **2007**, *172*, 481-486; b) C. O. Ania, V. Khomenko, E. Raymundo-Piñero, J. B. Parra, F. Béguin, *Adv. Funct. Mater.* **2007**, *17*, 1828-1836; c) D. Hulicova, M. Kodama, H. Hatori, *Chem. Mater.* **2006**, *18*, 2318-2326.
- [102] a) P. S. D. Brito, C. A. C. Sequeira, *J. Power Sources* **1994**, *52*, 1-16; b) E. Yeager, *Electrochim. Acta* **1984**, *29*, 1527-1537.
- [103] W. J. Weydanz, B. M. Way, T. van Buuren, J. R. Dahn, *J. Electrochem. Soc.* **1994**, *141*, 900-906.
- [104] A. Arenillas, T. C. Drage, K. Smith, C. E. Snape, *J. Anal. Appl. Pyrolysis* **2005**, *74*, 298-306.
- [105] B. Kamm, M. Kamm, *Chem. Ing. Tech.* **2007**, *79*, 592-603.
- [106] B. Kamm, *Angew. Chem. Int. Ed.* **2007**, *46*, 5056-5058.
- [107] F. W. Lichtenthaler, *Carbohydr. Res.* **1998**, *313*, 69-89.
- [108] S. Yu, H. M. Brown, X. W. Huang, X. D. Zhou, J. E. Amonette, Z. C. Zhang, *Appl. Catal., A* **2009**, *361*, 117-122.
- [109] I. R. Sitepu, L. A. Garay, R. Sestric, D. Levin, D. E. Block, J. B. German, K. L. Boundy-Mills, *Biotechnol. Adv.* **2014**, *32*, 1336-1360.
- [110] D. M. Alonso, S. G. Wettstein, J. A. Dumesic, *Chem. Soc. Rev.* **2012**, *41*, 8075-8098.
- [111] J. S. Van Dyk, B. I. Pletschke, *Biotechnol. Adv.* **2012**, *30*, 1458-1480.

- [112] a) F. M. Gírio, C. Fonseca, F. Carvalheiro, L. C. Duarte, S. Marques, R. Bogel-Lukasik, *Bioresour. Technol.* **2010**, *101*, 4775-4800; b) Q. K. Beg, M. Kapoor, L. Mahajan, G. S. Hoondal, *Appl. Microbiol. Biotechnol.* **2001**, *56*, 326-338.
- [113] W. G. T. Willats, J. P. Knox, J. D. Mikkelsen, *Trends Food Sci. Technol.* **2006**, *17*, 97-104.
- [114] K.-E. L. Eriksson, H. Bermek, *Appl. Microbiol. Ind.* **2009**, 373-384.
- [115] J. Bidlack, M. Malone, R. Benson, *Proc. Okla. Acad. Sci.* **1992**, *72*, 51-56.
- [116] a) N. Kaur, D. Kishore, *J. Iran. Chem. Soc.* **2013**, *10*, 1193-1228; b) J. M. Dreyfors, S. B. Jones, Y. Sayed, *Am. Ind. Hyg. Assoc. J.* **1989**, *50*, 579-585; c) N. Blažević, D. Kolbah, B. Belin, V. Šunjić, F. Kajfež, *Synthesis* **1979**, 161-176.
- [117] a) H. Stetter, *Angew. Chem.* **1954**, *66*, 217-229; b) A. M. Kirillov, *Coord. Chem. Rev.* **2011**, *255*, 1603-1622.
- [118] T. Schultheis, E. Schindler, in *Handbuch der Urologie: Die urologische Begutachtung und Dokumentation, Vol. VII/2*, 1st ed., Springer-Verlag, Berlin, Germany, **1965**, pp. 82-151.
- [119] L. Liu, Q.-F. Deng, X.-X. Hou, Z.-Y. Yuan, *J. Mater. Chem.* **2012**, *22*, 15540.
- [120] a) R. J. van Putten, J. C. van der Waal, E. de Jong, C. B. Rasrendra, H. J. Heeres, J. G. de Vries, *Chem. Rev.* **2013**, *113*, 1499-1597; b) E. F. L. J. Anet, *Adv. Carbohydr. Chem.* **1964**, *19*, 181-218.
- [121] a) C. J. Knill, J. F. Kennedy, *Carbohydr. Polym.* **2003**, *51*, 281-300; b) Z. Srokol, A.-G. Bouche, A. van Estrik, R. C. J. Strik, T. Maschmeyer, J. A. Peters, *Carbohydr. Res.* **2004**, *339*, 1717-1726.
- [122] a) D. J. Hayes, S. Fitzpatrick, M. H. B. Hayes, J. R. H. Ross, in *Biorefineries-Industrial Processes and Products: Status Quo and Future Directions, Vol. 1* (Eds.: B. Kamm, P. R. Gruber, M. Kamm), Wiley-VCH Verlag GmbH, Weinheim, Germany, **2006**, pp. 139-164; b) B. V. Timokhin, V. A. Baransky, G. D. Eliseeva, *Russ. Chem. Rev.* **1999**, *68*, 73-84; c) J. Horvat, B. Klaić, B. Metelko, V. Šunjić, *Croat. Chem. Acta* **1986**, *59*, 429-438; d) J. Horvat, B. Klaić, B. Metelko, V. Šunjić, *Tetrahedron Lett.* **1985**, *26*, 2111-2114.
- [123] S. K. R. Patil, C. R. F. Lund, *Energy Fuels* **2011**, *25*, 4745-4755.
- [124] S. Wohlgemuth, H. Urakami, L. Zhao, M.-M. Titirici, in *Sustainable Carbon Materials from Hydrothermal Processes*, 1st ed. (Ed.: M.-M. Titirici), John Wiley & Sons, Ltd., Chichester, West Sussex, United Kingdom, **2013**, pp. 125-150.
- [125] a) N. Baccile, G. Laurent, C. Coelho, F. Babonneau, L. Zhao, M.-M. Titirici, *J. Phys. Chem. C* **2011**, *115*, 8976-8982; b) M. A. Glomb, in *Moderne Lebensmittelchemie*, 1st ed. (Eds.: M. Fischer, M. A. Glomb), Behr's Verlag GmbH & Co. KG, Hamburg, Germany, **2015**, pp. 133-198.

- [126] a) M.-M. Titirici, R. J. White, C. Falco, M. Sevilla, *Energy Environ. Sci.* **2012**, *5*, 6796-6822; b) E. Capuano, V. Fogliano, *LWT-Food Sci. Technol.* **2011**, *44*, 793-810; c) J. Koch, M. Pischetsrieder, K. Polborn, T. Severin, *Carbohydr. Res.* **1998**, *313*, 117-123; d) N. Baccile, J. Weber, C. Falco, M.-M. Titirici, in *Sustainable Carbon Materials from Hydrothermal Processes*, 1st ed. (Ed.: M.-M. Titirici), John Wiley & Sons, Ltd., Chichester, West Sussex, United Kingdom, **2013**, pp. 151-212.
- [127] J. C. Sowden, *Adv. Carbohydr. Chem.* **1957**, *12*, 35-79.
- [128] a) I. Forsskåhl, T. Popoff, O. Theander, *Carbohydr. Res.* **1976**, *48*, 13-21; b) O. Theander, D. A. Nelson, *Adv. Carbohydr. Chem. Biochem.* **1988**, *46*, 273-326.
- [129] a) J. M. de Bruijn, A. P. G. Kieboom, H. van Bekkum, P. W. van der Poel, *Sugar Technol. Rev.* **1986**, *13*, 21-52; b) J. M. de Bruijn, A. P. G. Kieboom, H. van Bekkum, *Starch* **1987**, *39*, 23-28; c) J. M. de Bruijn, F. Touwslager, A. P. G. Kieboom, H. van Bekkum, *Starch* **1987**, *39*, 49-52; d) J. M. de Bruijn, A. P. G. Kieboom, H. van Bekkum, P. W. van der Poel, N. H. M. de Visser, M. A. M. de Schutter, *Int. Sugar J.* **1987**, *89*, 208-210; e) A. V. Ellis, M. A. Wilson, *J. Org. Chem.* **2002**, *67*, 8469-8474.
- [130] B. Y. Yang, R. Montgomery, *Carbohydr. Res.* **1996**, *280*, 27-45.
- [131] a) J. M. de Bruijn, A. P. G. Kieboom, H. van Bekkum, *Recl. Trav. Chim. Pays-Bas* **1986**, *105*, 176-183; b) J. M. de Bruijn, A. P. G. Kieboom, H. van Bekkum, *Recl. Trav. Chim. Pays-Bas* **1987**, *106*, 35-43; c) G. de Wit, A. P. G. Kieboom, H. van Bekkum, *Carbohydr. Res.* **1979**, *74*, 157-175.
- [132] H. Steinhart, *Angew. Chem. Int. Ed.* **2005**, *44*, 7503-7504.
- [133] a) P. Buonora, J. C. Olsen, T. Oh, *Tetrahedron* **2001**, *57*, 6099-6138; b) R. Demir-Cakan, P. Makowski, M. Antonietti, F. Goettmann, M.-M. Titirici, *Catal. Today* **2010**, *150*, 115-118.
- [134] H. Schiff, *Justus Liebigs Ann. Chem.* **1864**, *131*, 118-119.
- [135] F. Micheel, I. Dijong, *Justus Liebigs Ann. Chem.* **1962**, *658*, 120-127.
- [136] a) R. Leuckart, *Ber. Dtsch. Chem. Ges.* **1885**, *18*, 2341-2344; b) O. Wallach, *Justus Liebigs Ann. Chem.* **1893**, *272*, 99-122.
- [137] a) W. Eschweiler, *Ber. Dtsch. Chem. Ges.* **1905**, *38*, 880-882; b) H. T. Clarke, H. B. Gillespie, S. Z. Weisshaus, *J. Am. Chem. Soc.* **1933**, *55*, 4571-4587.
- [138] C. Mannich, W. Krösche, *Arch. Pharm.* **1912**, *250*, 647-667.
- [139] a) C. Schotten, *Ber. Dtsch. Chem. Ges.* **1884**, *17*, 2544-2547; b) E. Baumann, *Ber. Dtsch. Chem. Ges.* **1886**, *19*, 3218-3222.
- [140] a) C. Paal, *Ber. Dtsch. Chem. Ges.* **1885**, *18*, 367-371; b) L. Knorr, *Ber. Dtsch. Chem. Ges.* **1885**, *18*, 299-311; c) V. Amarnath, D. C. Anthony, K. Amarnath, W. M. Valentine, L. A. Wetterau, D. G. Graham, *J. Org. Chem.* **1991**, *56*, 6924-6931.

- [141] a) C. Paal, *Ber. Dtsch. Chem. Ges.* **1884**, *17*, 2756-2767; b) L. Knorr, *Ber. Dtsch. Chem. Ges.* **1884**, *17*, 2863-2870; c) V. Amarnath, K. Amarnath, *J. Org. Chem.* **1995**, *60*, 301-307.
- [142] a) K. Friedel Ortega, R. Arrigo, B. Frank, R. Schlögl, A. Trunschke, *Chem. Mater.* **2016**, *28*, 6826-6839; b) S. Kundu, W. Xia, W. Busser, M. Becker, D. A. Schmidt, M. Havenith, M. Muhler, *Phys. Chem. Chem. Phys.* **2010**, *12*, 4351-4359.
- [143] a) A. E. Chichibabin, *J. Russ. Phys. Chem. Soc.* **1906**, *37*, 1229; b) R. L. Frank, R. P. Seven, *J. Am. Chem. Soc.* **1949**, *71*, 2629-2635; c) Z. Wang, in *Comprehensive Organic Name Reactions and Reagents, Vol. 1-3*, 1st ed., John Wiley & Sons, Inc., Hoboken, New Jersey, United States of America, **2009**, pp. 635-638.
- [144] W. Staedel, L. Rügheimer, *Ber. Dtsch. Chem. Ges.* **1876**, *9*, 1758-1761.
- [145] a) V. K. LaMer, R. H. Dinegar, *J. Am. Chem. Soc.* **1950**, *72*, 4847-4854; b) A. Laaksonen, V. Talanquer, D. W. Oxtoby, *Annu. Rev. Phys. Chem.* **1995**, *46*, 489-524.
- [146] B. M. Hunter, H. B. Gray, A. M. Müller, *Chem. Rev.* **2016**, *116*, 14120-14136.
- [147] a) N.-T. Suen, S.-F. Hung, Q. Quan, N. Zhang, Y.-J. Xu, H. M. Chen, *Chem. Soc. Rev.* **2017**, *46*, 337-365; b) R. L. Doyle, M. E. G. Lyons, in *Photoelectrochemical Solar Fuel Production: From Basic Principles to Advanced Devices* (Eds.: S. Giménez, J. Bisquert), Springer International Publishing AG, Switzerland, **2016**, pp. 41-104.
- [148] a) X. J. Zhang, C. Bauer, C. L. Mutel, K. Volkart, *Appl. Energy* **2017**, *190*, 326-338; b) R. Krishna, E. Titus, M. Salimian, O. Okhay, S. Rajendran, A. Rajkumar, J. M. G. Sousa, A. L. C. Ferreira, J. Campos Gil, J. Gracio, in *Hydrogen Storage* (Ed.: J. Liu), InTech, Rijeka, Croatia, **2012**, pp. 243-266; c) M. Ni, D. Y. C. Leung, M. K. H. Leung, *Int. J. Hydrogen Energy* **2007**, *32*, 3238-3247.
- [149] a) M. Bououdina, D. Grant, G. Walker, *Int. J. Hydrogen Energy* **2006**, *31*, 177-182; b) Q. K. Wang, C. C. Zhu, W. H. Liu, T. Wu, *Int. J. Hydrogen Energy* **2002**, *27*, 497-500; c) M. Kruk, M. Jaroniec, *Chem. Mater.* **2001**, *13*, 3169-3183.
- [150] J. Ohi, *J. Mater. Res.* **2005**, *20*, 3180-3187.
- [151] a) M. Grätzel, *Chem. Lett.* **2005**, *34*, 8-13; b) J. A. Turner, *Science* **2004**, *305*, 972-974.
- [152] N. S. Lewis, D. G. Nocera, *Proc. Natl. Acad. Sci. U.S.A.* **2006**, *103*, 15729-15735.
- [153] R. Schlögl, *ChemSusChem* **2010**, *3*, 209-222.
- [154] K. Zeng, D. K. Zhang, *Prog. Energy Combust. Sci.* **2010**, *36*, 307-326.
- [155] a) S. Marini, P. Salvi, P. Nelli, R. Pesenti, M. Villa, M. Berrettoni, G. Zangari, Y. Kiros, *Electrochim. Acta* **2012**, *82*, 384-391; b) H. Dau, C. Limberg, T. Reier, M. Risch, S. Roggan, P. Strasser, *ChemCatChem* **2010**, *2*, 724-761; c) D. E. Hall, *J. Electrochem. Soc.* **1983**, *130*, 317-321.

- [156] a) W. C. Sheng, H. A. Gasteiger, Y. Shao-Horn, *J. Electrochem. Soc.* **2010**, *157*, B1529-B1536; b) N. M. Marković, P. N. Ross, *Surf. Sci. Rep.* **2002**, *45*, 121-229.
- [157] J. Greeley, N. M. Markovic, *Energy Environ. Sci.* **2012**, *5*, 9246-9256.
- [158] a) I. Katsounaros, S. Cherevko, A. R. Zeradjanin, K. J. J. Mayrhofer, *Angew. Chem. Int. Ed.* **2014**, *53*, 102-121; b) A. Michas, F. Andolfatto, M. E. G. Lyons, R. Durand, *Key Eng. Mater.* **1992**, 72-74, 535-550.
- [159] R. Kötzt, H. J. Lewerenz, S. Stucki, *J. Electrochem. Soc.* **1983**, *130*, 825-829.
- [160] a) E. Antolini, *ACS Catal.* **2014**, *4*, 1426-1440; b) R. Kötzt, H. Neff, S. Stucki, *J. Electrochem. Soc.* **1984**, *131*, 72-77.
- [161] S. Cherevko, S. Geiger, O. Kasian, N. Kulyk, J.-P. Grote, A. Savan, B. R. Shrestha, S. Merzlikin, B. Breitbach, A. Ludwig, K. J. J. Mayrhofer, *Catal. Today* **2016**, *262*, 170-180.
- [162] a) K. G. Qu, Y. Zheng, S. Dai, S. Z. Qiao, *Nano Energy* **2016**, *19*, 373-381; b) J. T. Zhang, Z. H. Xia, L. M. Dai, *Sci. Adv.* **2015**, *1*, 1-19.
- [163] W. He, C. Jiang, J. Wang, L. Lu, *Angew. Chem. Int. Ed.* **2014**, *53*, 9503-9507.
- [164] a) M.-M. Titirici, R. J. White, N. Brun, V. L. Budarin, D. S. Su, F. del Monte, J. H. Clark, M. J. MacLachlan, *Chem. Soc. Rev.* **2015**, *44*, 250-290; b) Z. Y. Lin, M.-K. Song, Y. Ding, Y. Liu, M. L. Liu, C.-p. Wong, *Phys. Chem. Chem. Phys.* **2012**, *14*, 3381-3387; c) L.-F. Chen, X.-D. Zhang, H.-W. Liang, M. G. Kong, Q.-F. Guan, P. Chen, Z.-Y. Wu, S.-H. Yu, *ACS Nano* **2012**, *6*, 7092-7102; d) S. Maldonado, K. J. Stevenson, *J. Phys. Chem. B* **2005**, *109*, 4707-4716.
- [165] K. N. Wood, R. O'Hayre, S. Pylypenko, *Energy Environ. Sci.* **2014**, *7*, 1212-1249.
- [166] a) G. Wu, R. Swaidan, D. Y. Li, N. Li, *Electrochim. Acta* **2008**, *53*, 7622-7629; b) G. Wu, D. Y. Li, C. S. Dai, D. L. Wang, N. Li, *Langmuir* **2008**, *24*, 3566-3575; c) S. Maldonado, K. J. Stevenson, *J. Phys. Chem. B* **2004**, *108*, 11375-11383; d) J. R. Pels, F. Kapteijn, J. A. Moulijn, Q. Zhu, K. M. Thomas, *Carbon* **1995**, *33*, 1641-1653.
- [167] a) D.-W. Wang, D. S. Su, *Energy Environ. Sci.* **2014**, *7*, 576-591; b) I.-Y. Jeon, H.-J. Choi, S.-M. Jung, J.-M. Seo, M.-J. Kim, L. M. Dai, J.-B. Baek, *J. Am. Chem. Soc.* **2013**, *135*, 1386-1393; c) K. L. Ai, Y. L. Liu, C. P. Ruan, L. H. Lu, G. Q. Lu, *Adv. Mater.* **2013**, *25*, 998-1003; d) J. Liang, Y. Zheng, J. Chen, J. Liu, D. Hulicova-Jurcakova, M. Jaroniec, S. Z. Qiao, *Angew. Chem. Int. Ed.* **2012**, *51*, 3892-3896; e) K. P. Gong, F. Du, Z. H. Xia, M. Durstock, L. M. Dai, *Science* **2009**, *323*, 760-764; f) B. Winther-Jensen, O. Winther-Jensen, M. Forsyth, D. R. MacFarlane, *Science* **2008**, *321*, 671-674; g) S. Chen, J. Duan, M. Jaroniec, S.-Z. Qiao, *Adv. Mater.* **2014**, *26*, 2925-2930; h) P. Chen, T.-Y. Xiao, Y.-H. Qian, S.-S. Li, S.-H. Yu, *Adv. Mater.* **2013**, *25*, 3192-3196; i) L. Chen, X. Cui, Y. Wang, M. Wang, F. Cui, C. Wei, W. Huang, Z. Hua, L. Zhang, J. Shi, *Chem. Asian*

- J.* **2014**, *9*, 2915-2920; j) Z. Lin, G. H. Waller, Y. Liu, M. Liu, C.-p. Wong, *Nano Energy* **2013**, *2*, 241-248.
- [168] Z. Lin, G. H. Waller, Y. Liu, M. Liu, C.-p. Wong, *Carbon* **2013**, *53*, 130-136.
- [169] a) K. K. R. Datta, V. V. Balasubramanian, K. Ariga, T. Mori, A. Vinu, *Chem. Eur. J.* **2011**, *17*, 3390-3397; b) C. M. Lieber, Z. J. Zhang, *Adv. Mater.* **1994**, *6*, 497-499; c) A. Y. Liu, M. L. Cohen, *Science* **1989**, *245*, 841-842.
- [170] a) C. H. Choi, S. H. Park, M. W. Chung, S. I. Woo, *Carbon* **2013**, *55*, 98-107; b) A. V. Okotrub, L. G. Bulusheva, A. G. Kudashov, V. V. Belavin, D. V. Vyalikh, S. L. Molodtsov, *Appl. Phys. A* **2009**, *94*, 437-443.
- [171] a) Y. Jiao, Y. Zheng, M. Jaroniec, S. Z. Qiao, *J. Am. Chem. Soc.* **2014**, *136*, 4394-4403; b) Y. Zheng, Y. Jiao, J. Chen, J. Liu, J. Liang, A. Du, W. M. Zhang, Z. H. Zhu, S. C. Smith, M. Jaroniec, G. Q. Lu, S. Z. Qiao, *J. Am. Chem. Soc.* **2011**, *133*, 20116-20119; c) Y. F. Tang, B. L. Allen, D. R. Kauffman, A. Star, *J. Am. Chem. Soc.* **2009**, *131*, 13200-13201; d) D. S. Yu, E. Nagelli, F. Du, L. M. Dai, *J. Phys. Chem. Lett.* **2010**, *1*, 2165-2173; e) Z. Jin, J. Yao, C. Kittrell, J. M. Tour, *ACS Nano* **2011**, *5*, 4112-4117; f) H. Zhong, C. Deng, Y. Qiu, L. Yao, H. Zhang, *J. Mater. Chem. A* **2014**, *2*, 17047-17057; g) Z. Liu, G. Zhang, Z. Lu, X. Jin, Z. Chang, X. Sun, *Nano Research* **2013**, *6*, 293-301; h) X. Y. Chen, C. Chen, Z. J. Zhang, D. H. Xie, X. Deng, J. W. Liu, *J. Power Sources* **2013**, *230*, 50-58.
- [172] G. Wu, A. Santandreu, W. Kellogg, S. Gupta, O. Ogoke, H. G. Zhang, H.-L. Wang, L. M. Dai, *Nano Energy* **2016**, *29*, 83-110.
- [173] a) C. H. Choi, S. H. Park, S. I. Woo, *Appl. Catal., B* **2012**, *119*, 123-131; b) R. L. Liu, D. Q. Wu, X. L. Feng, K. Müllen, *Angew. Chem. Int. Ed.* **2010**, *49*, 2565-2569.
- [174] a) L. F. Lai, J. R. Potts, D. Zhan, L. Wang, C. K. Poh, C. H. Tang, H. Gong, Z. X. Shen, L. Y. Jianyi, R. S. Ruoff, *Energy Environ. Sci.* **2012**, *5*, 7936-7942; b) C. V. Rao, C. R. Cabrera, Y. Ishikawa, *J. Phys. Chem. Lett.* **2010**, *1*, 2622-2627; c) K. A. Kurak, A. B. Anderson, *J. Phys. Chem. C* **2009**, *113*, 6730-6734.
- [175] a) J. J. Duan, S. Chen, M. Jaroniec, S. Z. Qiao, *ACS Catal.* **2015**, *5*, 5207-5234; b) Y. F. Li, Z. Zhou, P. W. Shen, Z. F. Chen, *ACS Nano* **2009**, *3*, 1952-1958; c) S. Majeed, J. Zhao, L. Zhang, S. Anjum, Z. Liu, G. Xu, *Nanotechnol. Rev.* **2013**, *2*, 615-635.
- [176] P. H. Matter, L. Zhang, U. S. Ozkan, *J. Catal.* **2006**, *239*, 83-96.
- [177] C. H. Zhang, L. Fu, N. Liu, M. H. Liu, Y. Y. Wang, Z. F. Liu, *Adv. Mater.* **2011**, *23*, 1020-1024.
- [178] Z. Y. Lin, G. Waller, Y. Liu, M. L. Liu, C.-P. Wong, *Adv. Energy Mater.* **2012**, *2*, 884-888.
- [179] a) E. J. Biddinger, D. von Deak, U. S. Ozkan, *Top. Catal.* **2009**, *52*, 1566-1574; b) P. H. Matter, E. Wang, M. Arias, E. J. Biddinger, U. S. Ozkan, *J.*

- Mol. Catal. A: Chem.* **2007**, *264*, 73-81; c) P. H. Matter, E. Wang, J.-M. M. Millet, U. S. Ozkan, *J. Phys. Chem. C* **2007**, *111*, 1444-1450; d) E. J. Biddinger, U. S. Ozkan, *Top. Catal.* **2007**, *46*, 339-348; e) P. H. Matter, E. Wang, U. S. Ozkan, *J. Catal.* **2006**, *243*, 395-403; f) J. A. R. van Veen, J. F. van Baar, K. J. Kroese, *J. Chem. Soc., Faraday Trans. 1* **1981**, *77*, 2827-2843.
- [180] H. Kim, K. Lee, S. I. Woo, Y. Jung, *Phys. Chem. Chem. Phys.* **2011**, *13*, 17505-17510.
- [181] a) Z.-H. Sheng, L. Shao, J.-J. Chen, W.-J. Bao, F.-B. Wang, X.-H. Xia, *ACS Nano* **2011**, *5*, 4350-4358; b) J. Zhang, X. Liu, R. Blume, A. H. Zhang, R. Schlögl, D. S. Su, *Science* **2008**, *322*, 73-77; c) L. S. Panchalkarla, A. Govindaraj, C. N. R. Rao, *ACS Nano* **2007**, *1*, 494-500.
- [182] D. S. Su, J. Zhang, B. Frank, A. Thomas, X. C. Wang, J. Paraknowitsch, R. Schlögl, *ChemSusChem* **2010**, *3*, 169-180.
- [183] a) S. van Dommele, K. P. de Jong, J. H. Bitter, *Chem. Commun.* **2006**, 4859-4861; b) F. G. Souza, L. Sirelli, R. C. Michel, B. G. Soares, M. H. Herbst, *J. Appl. Polym. Sci.* **2006**, *102*, 535-541; c) M.-C. Huang, H. S. Teng, *Carbon* **2003**, *41*, 951-957; d) V. V. Strelko, V. S. Kuts, P. A. Thrower, *Carbon* **2000**, *38*, 1499-1503.
- [184] a) Y.-H. Li, T.-H. Hung, C.-W. Chen, *Carbon* **2009**, *47*, 850-855; b) R. Arrigo, S. Wrabetz, M. E. Schuster, D. Wang, A. Villa, D. Rosenthal, F. Girsgdies, G. Weinberg, L. Prati, R. Schlögl, D. S. Su, *Phys. Chem. Chem. Phys.* **2012**, *14*, 10523-10532.
- [185] C. H. Choi, S. H. Park, S. I. Woo, *Green Chem.* **2011**, *13*, 406-412.
- [186] H. L. Guo, Q. M. Gao, *J. Power Sources* **2009**, *186*, 551-556.
- [187] a) S. Giraudet, Z. H. Zhu, X. D. Yao, G. Q. Lu, *J. Phys. Chem. C* **2010**, *114*, 8639-8645; b) L. F. Wang, R. T. Yang, *J. Phys. Chem. C* **2009**, *113*, 21883-21888; c) T. Kwon, H. Nishihara, H. Itoi, Q. H. Yang, T. Kyotani, *Langmuir* **2009**, *25*, 11961-11968; d) M. Deifallah, P. F. McMillan, F. Corà, *J. Phys. Chem. C* **2008**, *112*, 5447-5453; e) E. Kroke, M. Schwarz, *Coord. Chem. Rev.* **2004**, *248*, 493-532; f) L. Hultman, J. Neidhardt, N. Hellgren, H. Sjöström, J.-E. Sundgren, *MRS Bull.* **2003**, *28*, 194-202.
- [188] a) Z. Chen, A. P. Yu, R. Ahmed, H. J. Wang, H. Li, Z. W. Chen, *Electrochim. Acta* **2012**, *69*, 295-300; b) P. Kichambare, J. Kumar, S. Rodrigues, B. Kumar, *J. Power Sources* **2011**, *196*, 3310-3316; c) L. G. Bulusheva, A. V. Okotrub, A. G. Kurennya, H. K. Zhang, H. J. Zhang, X. H. Chen, H. H. Song, *Carbon* **2011**, *49*, 4013-4023; d) Y. Y. Shao, X. Q. Wang, M. Engelhard, C. M. Wang, S. Dai, J. Liu, Z. G. Yang, Y. H. Lin, *J. Power Sources* **2010**, *195*, 4375-4379.
- [189] a) C. H. Choi, S. H. Park, S. I. Woo, *Int. J. Hydrogen Energy* **2012**, *37*, 4563-4570; b) G. Wu, K. L. More, C. M. Johnston, P. Zelenay, *Science* **2011**, *332*, 443-447.
- [190] a) J. D. Wiggins-Camacho, K. J. Stevenson, *J. Phys. Chem. C* **2009**, *113*, 19082-19090; b) Z. R. Ismagilov, A. E. Shalagina, O. Y. Podyacheva, A.

- V. Ischenko, L. S. Kibis, A. I. Boronin, Y. A. Chesalov, D. I. Kochubey, A. I. Romanenko, O. B. Anikeeva, T. I. Buryakov, E. N. Tkachev, *Carbon* **2009**, *47*, 1922-1929.
- [191] C. Domínguez, F. J. Pérez-Alonso, M. Abdel Salam, S. A. Al-Thabaiti, A. Y. Obaid, A. A. Alshehri, J. L. Gómez de la Fuente, J. L. G. Fierro, S. Rojas, *Appl. Catal., B* **2015**, *162*, 420-429.
- [192] a) H. B. Li, W. J. Kang, L. Wang, Q. L. Yue, S. L. Xu, H. S. Wang, J. F. Liu, *Carbon* **2013**, *54*, 249-257; b) D. C. Wei, Y. Q. Liu, Y. Wang, H. L. Zhang, L. P. Huang, G. Yu, *Nano Lett.* **2009**, *9*, 1752-1758.
- [193] a) L. S. Panchokarla, K. S. Subrahmanyam, S. K. Saha, A. Govindaraj, H. R. Krishnamurthy, U. V. Waghmare, C. N. R. Rao, *Adv. Mater.* **2009**, *21*, 4726-4730; b) T. Ikeda, M. Boero, S.-F. Huang, K. Terakura, M. Oshima, J. Ozaki, *J. Phys. Chem. C* **2008**, *112*, 14706-14709.
- [194] a) G. Wu, C. M. Johnston, N. H. Mack, K. Artyushkova, M. Ferrandon, M. Nelson, J. S. Lezama-Pacheco, S. D. Conradson, K. L. More, D. J. Myers, P. Zelenay, *J. Mater. Chem.* **2011**, *21*, 11392-11405; b) S. Yasuda, L. Yu, J. Kim, K. Murakoshi, *Chem. Commun.* **2013**, *49*, 9627-9629; c) L. G. Bulusheva, A. V. Okotrub, I. A. Kinloch, I. P. Asanov, A. G. Kurennya, A. G. Kudashov, X. Chen, H. Song, *Phys. Status Solidi B* **2008**, *245*, 1971-1974; d) K. Artyushkova, P. Atanassov, *ChemPhysChem* **2013**, *14*, 2071-2080; e) D. H. Deng, X. L. Pan, L. A. Yu, Y. Cui, Y. P. Jiang, J. Qi, W.-X. Li, Q. A. Fu, X. C. Ma, Q. K. Xue, G. Q. Sun, X. H. Bao, *Chem. Mater.* **2011**, *23*, 1188-1193; f) S. van Dommele, A. Romero-Izquierdo, R. Brydson, K. P. de Jong, J. H. Bitter, *Carbon* **2008**, *46*, 138-148.
- [195] a) L. P. Zhang, J. B. Niu, L. Dai, Z. H. Xia, *Langmuir* **2012**, *28*, 7542-7550; b) Z. Q. Luo, S. H. Lim, Z. Q. Tian, J. Z. Shang, L. F. Lai, B. MacDonald, C. Fu, Z. X. Shen, T. Yu, J. Y. Lin, *J. Mater. Chem.* **2011**, *21*, 8038-8044; c) Y. Y. Shao, S. Zhang, M. H. Engelhard, G. S. Li, G. C. Shao, Y. Wang, J. Liu, I. A. Aksay, Y. H. Lin, *J. Mater. Chem.* **2010**, *20*, 7491-7496; d) L. T. Qu, Y. Liu, J.-B. Baek, L. M. Dai, *ACS Nano* **2010**, *4*, 1321-1326.
- [196] a) K. R. Lee, K. U. Lee, J. W. Lee, B. T. Ahn, S. I. Woo, *Electrochem. Commun.* **2010**, *12*, 1052-1055; b) P. Wang, Z. K. Wang, L. X. Jia, Z. L. Xiao, *Phys. Chem. Chem. Phys.* **2009**, *11*, 2730-2740.
- [197] C. C. Ma, X. H. Shao, D. P. Cao, *J. Mater. Chem.* **2012**, *22*, 8911-8915.
- [198] a) J. Yan, H. Meng, F. Y. Xie, X. L. Yuan, W. D. Yu, W. R. Lin, W. P. Ouyang, D. S. Yuan, *J. Power Sources* **2014**, *245*, 772-778; b) D. S. Yu, Q. Zhang, L. M. Dai, *J. Am. Chem. Soc.* **2010**, *132*, 15127-15129; c) S. Kundu, T. C. Nagaiah, W. Xia, Y. M. Wang, S. Van Dommele, J. H. Bitter, M. Santa, G. Grundmeier, M. Bron, W. Schuhmann, M. Muhler, *J. Phys. Chem. C* **2009**, *113*, 14302-14310.
- [199] H. Niwa, K. Horiba, Y. Harada, M. Oshima, T. Ikeda, K. Terakura, J. Ozaki, S. Miyata, *J. Power Sources* **2009**, *187*, 93-97.

- [200] H. M. Jeong, J. W. Lee, W. H. Shin, Y. J. Choi, H. J. Shin, J. K. Kang, J. W. Choi, *Nano Lett.* **2011**, *11*, 2472-2477.
- [201] a) A. L. Shen, Y. Q. Zou, Q. Wang, R. A. W. Dryfe, X. B. Huang, S. Dou, L. M. Dai, S. Y. Wang, *Angew. Chem. Int. Ed.* **2014**, *53*, 10804-10808; b) W. J. Yuan, Y. Zhou, Y. R. Li, C. Li, H. L. Peng, J. Zhang, Z. F. Liu, L. M. Dai, G. Q. Shi, *Sci. Rep.* **2013**, *3*, 1-7.
- [202] C. Song, J. Zhang, in *PEM Fuel Cell Electrocatalysts and Catalyst Layers: Fundamentals and Applications* (Ed.: J. Zhang), Springer-Verlag Limited, London, United Kingdom, **2008**, pp. 89-134.
- [203] a) M. Li, L. Zhang, Q. Xu, J. Niu, Z. Xia, *J. Catal.* **2014**, *314*, 66-72; b) L. P. Zhang, Z. H. Xia, *J. Phys. Chem. C* **2011**, *115*, 11170-11176.
- [204] a) G. Wu, N. H. Mack, W. Gao, S. G. Ma, R. Q. Zhong, J. T. Han, J. K. Baldwin, P. Zelenay, *ACS Nano* **2012**, *6*, 9764-9776; b) L. Sun, L. Wang, C. G. Tian, T. X. Tan, Y. Xie, K. Y. Shi, M. T. Li, H. G. Fu, *RSC Adv.* **2012**, *2*, 4498-4506; c) R. Czerw, M. Terrones, J.-C. Charlier, X. Blase, B. Foley, R. Kamalakaran, N. Grobert, H. Terrones, D. Tekleab, P. M. Ajayan, W. Blau, M. Rühle, D. L. Carroll, *Nano Lett.* **2001**, *1*, 457-460.
- [205] a) W. Koch, M. C. Holthausen, *A Chemist's Guide to Density Functional Theory*, 1st ed., Wiley-VCH Verlag GmbH, Weinheim, Germany, **2000**; b) R. G. Parr, W. Yang, *Density-Functional Theory of Atoms and Molecules*, Oxford University Press, Inc., New York City, New York, United States of America, **1994**.
- [206] P. J. Stephens, F. J. Devlin, C. F. Chabalowski, M. J. Frisch, *J. Phys. Chem.* **1994**, *98*, 11623-11627.
- [207] F. Weigend, R. Ahlrichs, *Phys. Chem. Chem. Phys.* **2005**, *7*, 3297-3305.
- [208] a) S. Grimme, *J. Comput. Chem.* **2006**, *27*, 1787-1799; b) S. Grimme, J. Antony, S. Ehrlich, H. Krieg, *J. Chem. Phys.* **2010**, *132*, 154104.
- [209] a) A. D. Becke, E. R. Johnson, *J. Chem. Phys.* **2005**, *123*, 154101; b) E. R. Johnson, A. D. Becke, *J. Chem. Phys.* **2005**, *123*, 024101; c) E. R. Johnson, A. D. Becke, *J. Chem. Phys.* **2006**, *124*, 174104.
- [210] a) F. Neese, F. Wennmohs, A. Hansen, U. Becker, *Chem. Phys.* **2009**, *356*, 98-109; b) R. Izsák, F. Neese, *J. Chem. Phys.* **2011**, *135*, 144105.
- [211] K. Eichkorn, F. Weigend, O. Treutler, R. Ahlrichs, *Theor. Chem. Acc.* **1997**, *97*, 119-124.
- [212] F. Neese, *WIREs Comput. Mol. Sci.* **2012**, *2*, 73-78.
- [213] a) A. B. Jorge, D. J. Martin, M. T. S. Dhanoa, A. S. Rahman, N. Makwana, J. Tang, A. Sella, F. Corà, S. Firth, J. A. Darr, P. F. McMillan, *J. Phys. Chem. C* **2013**, *117*, 7178-7185; b) Y. Li, J. Zhang, Q. Wang, Y. Jin, D. Huang, Q. Cui, G. Zou, *J. Phys. Chem. B* **2010**, *114*, 9429-9434.
- [214] a) J. Liu, Y. Liu, N. Y. Liu, Y. Z. Han, X. Zhang, H. Huang, Y. Lifshitz, S. T. Lee, J. Zhong, Z. H. Kang, *Science* **2015**, *347*, 970-974; b) X. C. Wang, K. Maeda, A. Thomas, K. Takanabe, G. Xin, J. M. Carlsson, K. Domen, M. Antonietti, *Nature Materials* **2009**, *8*, 76-80.

- [215] a) X. Li, J. Zhang, L. Shen, Y. Ma, W. Lei, Q. Cui, G. Zou, *Appl. Phys. A* **2009**, *94*, 387-392; b) C. Li, X. Yang, B. Yang, Y. Yan, Y. Qian, *Mater. Chem. Phys.* **2007**, *103*, 427-432; c) V. N. Khabashesku, J. L. Zimmerman, J. L. Margrave, *Chem. Mater.* **2000**, *12*, 3264-3270.
- [216] W. Rüetschi, PhD thesis, Eidgenössische Technische Hochschule Zürich (Switzerland), **1941**.
- [217] Z. Y. Liu, C. L. Zhang, L. Luo, Z. Chang, X. M. Sun, *J. Mater. Chem.* **2012**, *22*, 12149-12154.
- [218] a) A. Kruse, A. Gawlik, *Ind. Eng. Chem. Res.* **2003**, *42*, 267-279; b) W. S.-L. Mok, M. J. Antal, *Ind. Eng. Chem. Res.* **1992**, *31*, 1157-1161.
- [219] T. Rogalinski, T. Ingram, G. Brunner, *J. Supercrit. Fluids* **2008**, *47*, 54-63.
- [220] E. Fuente, J. A. Menéndez, M. A. Díez, D. Suárez, M. A. Montes-Morán, *J. Phys. Chem. B* **2003**, *107*, 6350-6359.
- [221] R. J. White, C. Antonio, V. L. Budarin, E. Bergström, J. Thomas-Oates, J. H. Clark, *Adv. Funct. Mater.* **2010**, *20*, 1834-1841.
- [222] *NIST Chemistry WebBook, NIST Standard Reference Database Number 69*, National Institute of Standards and Technology, Gaithersburg, Maryland, United States of America.
- [223] S. Glenis, M. Benz, E. LeGoff, J. L. Schindler, C. R. Kannewurf, M. G. Kanatzidis, *J. Am. Chem. Soc.* **1993**, *115*, 12519-12525.
- [224] M.-M. Titirici, A. Thomas, M. Antonietti, *J. Mater. Chem.* **2007**, *17*, 3412-3418.
- [225] M. J. González-Tejera, E. Sánchez de la Blanca, I. Carrillo, *Synth. Met.* **2008**, *158*, 165-189.
- [226] P. Dungen, M. Prenzel, C. Van Stappen, N. Pfänder, S. Heumann, R. Schlögl, *Materials Sciences and Applications* **2017**, *8*, 628-641.
- [227] R. Arrigo, M. Hävecker, R. Schlögl, D. S. Su, *Chem. Commun.* **2008**, 4891-4893.
- [228] K.-M. Hansson, J. Samuelsson, L.-E. Åmand, C. Tullin, *Fuel* **2003**, *82*, 2163-2172.
- [229] J. Żurakowska-Orszàgh, T. Chreptowicz, *Eur. Polym. J.* **1981**, *17*, 877-880.
- [230] a) K. Chen, J. C. Mackie, D. Wojtalewicz, E. M. Kennedy, B. Z. Dlugogorski, *J. Hazard. Mater.* **2011**, *187*, 407-412; b) Sonya-T-Etemad-Rad, E. Metcalfe, *Fire Mater.* **1993**, *17*, 33-37.
- [231] a) G. Choudhary, A. M. Cameron, R. A. Back, *J. Phys. Chem.* **1968**, *72*, 2289-2292; b) D. J. Bogan, C. W. Hand, *J. Phys. Chem.* **1971**, *75*, 1532-1536.
- [232] a) X. Hong, L. Zhang, T. Zhang, F. Qi, *J. Phys. Chem. A* **2009**, *113*, 5397-5405; b) E. Ikeda, J. C. Mackie, *J. Anal. Appl. Pyrolysis* **1995**, *34*, 47-63; c) B. Xiao, J. P. Boudou, K. M. Thomas, *Langmuir* **2005**, *21*, 3400-3409.
- [233] Z. Xing, Z. C. Ju, Y. L. Zhao, J. L. Wan, Y. B. Zhu, Y. H. Qiang, Y. T. Qian, *Sci. Rep.* **2016**, *6*, 1-10.

- [234] A. Sadezky, H. Muckenhuber, H. Grothe, R. Niessner, U. Pöschl, *Carbon* **2005**, *43*, 1731-1742.
- [235] a) R. Atchudan, T. N. J. I. Edison, S. Perumal, Y. R. Lee, *Appl. Surf. Sci.* **2017**, *393*, 276-286; b) M. Asadullah, S. Zhang, Z. Min, P. Yimsiri, C.-Z. Li, *Ind. Eng. Chem. Res.* **2009**, *48*, 9858–9863; c) M. Chhowalla, A. C. Ferrari, J. Robertson, G. A. J. Amaratunga, *Appl. Phys. Lett.* **2000**, *76*, 1419.
- [236] a) Y. M. Lin, X. L. Pan, W. Qi, B. S. Zhang, D. S. Su, *J. Mater. Chem. A* **2014**, *2*, 12475-12483; b) A. Braun, *J. Environ. Monit.* **2005**, *7*, 1059-1065; c) J. Robertson, *Semicond. Sci. Technol.* **2003**, *18*, S12-S19.
- [237] a) H. Daniels, R. Brydson, B. Rand, A. Brown, *Philos. Mag.* **2007**, *87*, 4073-4092; b) J. Bruley, P. Madakson, J. C. Liu, *Nucl. Instrum. Methods Phys. Res., Sect. B* **1990**, *45*, 618-621.
- [238] a) J. Stöhr, *NEXAFS Spectroscopy*, Vol. 25, Springer-Verlag GmbH, Heidelberg, Germany, **1992**; b) G. Comelli, J. Stöhr, C. J. Robinson, W. Jark, *Phys. Rev. B: Condens. Matter* **1988**, *38*, 7511-7519.
- [239] J. Robertson, C. A. Davis, *Diamond Relat. Mater.* **1995**, *4*, 441-444.
- [240] C. Wang, Z. H. Huang, L. Zhan, Y. L. Wang, W. M. Qiao, X. Y. Liang, L. C. Ling, *Diamond Relat. Mater.* **2011**, *20*, 1353-1356.
- [241] J. A. Franz, R. Garcia, J. C. Linehan, G. D. Love, C. E. Snape, *Energy Fuels* **1992**, *6*, 598-602.
- [242] a) I. van Zandvoort, E. J. Koers, M. Weingarth, P. C. A. Bruijninx, M. Baldus, B. M. Weckhuysen, *Green Chem.* **2015**, *17*, 4383-4392; b) J. D. Mao, X. Y. Cao, D. C. Olk, W. Y. Chu, K. Schmidt-Rohr, *Prog. Nucl. Magn. Reson. Spectrosc.* **2017**, *100*, 17-51.
- [243] a) M. Begtrup, J. Elguero, R. Faure, P. Camps, C. Estopá, D. Ilavský, A. Fruchier, C. Marzin, J. de Mendoza, *Magn. Reson. Chem.* **1988**, *26*, 134-151; b) D. C. G. A. Pinto, C. M. M. Santos, A. M. S. Silva, in *Research Developments in Heterocyclic Chemistry* (Eds.: T. M. V. D. Pinho e Melo, A. M. d. A. Rocha Gonsalves), Research Signpost, Trivandrum, Kerala, India, **2007**, pp. 397-475.
- [244] S. Hayashi, K. Hayamizu, *Bull. Chem. Soc. Jpn.* **1991**, *64*, 688-690.
- [245] a) J. A. Theron, E. le Roux, *J. South. Afr. Inst. Min. Metall.* **2015**, *115*, 339-348; b) M. S. Masoudian, D. W. Airey, A. El-Zein, *Geomech. Geoengin.* **2013**, *8*, 229-243; c) A. Marzec, *J. Anal. Appl. Pyrolysis* **1985**, *8*, 241-254; d) J. H. Shinn, *Fuel* **1984**, *63*, 1187-1196; e) D. G. Levine, R. H. Schlosberg, B. G. Silbernagel, *Proc. Natl. Acad. Sci. U.S.A.* **1982**, *79*, 3365-3370; f) W. H. Wiser, in *Proceedings of the Electric Power Research Institute Conference on Coal Catalysis*, Palo Alto, California, United States of America, **1973**, pp. 3-53; g) P. H. Given, *Fuel* **1960**, *39*, 147-153.
- [246] M. R. Dong, X. L. Mao, J. J. Gonzalez, J. D. Lu, R. E. Russo, *J. Anal. At. Spectrom.* **2012**, *27*, 2066-2075.

- [247] a) B. J. Arnold, in *The coal handbook: Towards cleaner production, Vol. 1: Coal production* (Ed.: D. Osborne), Woodhead Publishing Limited, Sawston, Cambridge, United Kingdom, **2013**, pp. 31-52; b) J. Hoinkis, E. Lindner, *Chemie für Ingenieure*, 13th ed., Wiley-VCH Verlag GmbH, Weinheim, Germany, **2007**.
- [248] Q. Wang, X. Y. Liang, W. M. Qiao, C. J. Liu, X. J. Liu, L. A. Zhan, L. C. Ling, *Fuel Process. Technol.* **2009**, *90*, 381-387.
- [249] a) X. S. Zhao, F. Su, Q. Yan, W. Guo, X. Y. Bao, L. Lv, Z. Zhou, *J. Mater. Chem.* **2006**, *16*, 637-648; b) H. Eckert, Y. A. Levendis, R. C. Flagan, *J. Phys. Chem.* **1988**, *92*, 5011-5019.
- [250] Y. H. Liu, J. S. Xue, T. Zheng, J. R. Dahn, *Carbon* **1996**, *34*, 193-200.
- [251] I. Spanos, A. A. Auer, S. Neugebauer, X. H. Deng, H. Tüysüz, R. Schlögl, *ACS Catal.* **2017**, *7*, 3768-3778.
- [252] a) K. J. May, C. E. Carlton, K. A. Stoerzinger, M. Risch, J. Suntivich, Y.-L. Lee, A. Grimaud, Y. Shao-Horn, *J. Phys. Chem. Lett.* **2012**, *3*, 3264-3270; b) F. Song, X. L. Hu, *J. Am. Chem. Soc.* **2014**, *136*, 16481-16484.
- [253] a) S. I. Bailey, I. M. Ritchie, *Electrochim. Acta* **1985**, *30*, 3-12; b) P. S. Guin, S. Das, P. C. Mandal, *J. Phys. Org. Chem.* **2010**, *23*, 477-482; c) P. S. Guin, S. Das, P. C. Mandal, *Int. J. Electrochem.* **2011**, *2011*, 1-22.
- [254] Y. Yi, G. Weinberg, M. Prenzel, M. Greiner, S. Heumann, S. Becker, R. Schlögl, *Catal. Today* **2017**, *295*, 32-40.
- [255] K. Kinoshita, in *Carbon: Electrochemical and Physicochemical Properties*, John Wiley & Sons, Inc., New York City, New York, United States of America, **1988**, pp. 293-387.
- [256] Y. Yi, J. Tornow, E. Willinger, M. G. Willinger, C. Ranjan, R. Schlögl, *ChemElectroChem* **2015**, *2*, 1929-1937.
- [257] M. Pourbaix, in *Atlas of Electrochemical Equilibria in Aqueous Solutions*, 2nd ed., National Association of Corrosion Engineers, Houston, Texas, United States of America, **1974**, pp. 95-626.
- [258] O. S. Ksenzhek, V. M. Chaikovskaya, *J. Appl. Chem. USSR* **1962**, *35*, 1713.
- [259] a) G. N. Kokhanov, N. G. Milova, *Elektrokhimiya* **1969**, *5*, 93-96; b) P. N. Ross, H. Sokol, *J. Electrochem. Soc.* **1984**, *131*, 1742-1750; c) N. Staud, P. N. Ross, *J. Electrochem. Soc.* **1986**, *133*, 1079-1084.
- [260] H. Binder, A. Köhling, K. Richter, G. Sandstede, *Electrochim. Acta* **1964**, *9*, 255-274.
- [261] K. Kinoshita, J. Bett, *Carbon* **1973**, *11*, 237-247.
- [262] a) H. H. Heller, *Trans. Electrochem. Soc.* **1945**, *87*, 501-510; b) M. Janes, *Trans. Electrochem. Soc.* **1947**, *92*, 23-44; c) M. Janes, N. J. Johnson, E. B. Pilcher, *J. Electrochem. Soc.* **1955**, *102*, 474-478; d) S. Wawzonek, D. S. P. Eftax, *J. Electrochem. Soc.* **1957**, *104*, 494-497; e) T. I. Balkaş, Ö. Bastürk, A. F. Gaines, I. Salihoğlu, A. Yilmaz, *Fuel* **1983**, *62*, 373-379; f) Y. Fujita, H. Nakamura, *Denki Kagaku oyobi Kogyo Butsuri Kagaku* **1984**, *52*, 346-350.

- [263] F. J. Stevenson, *Humus Chemistry: Genesis, Composition, Reactions*, 2nd ed., John Wiley & Sons, Inc., New York City, New York, United States of America, **1994**.
- [264] J. L. Figueiredo, M. F. R. Pereira, M. M. A. Freitas, J. J. M. Órfão, *Carbon* **1999**, 37, 1379-1389.

8. APPENDIX

8.1. List of Abbreviations

2D NMR	Two-dimensional nuclear magnetic resonance
^{13}C 2D SQ–DQ	Carbon-13 two-dimensional single-quantum double-quantum
^{13}C CP	Carbon-13 cross-polarization
^{13}C DP	Carbon-13 direct polarization
^{13}C NMR	Carbon-13 nuclear magnetic resonance
ATR	Attenuated total reflection
BET	Brunauer-Emmett-Teller
CA	Chronoamperometry
CE	Counter electrode
CNFs	Carbon nanofibers
CNTs	Carbon nanotubes
CP	Chronopotentiometry
CV	Cyclic voltammetry
CQDs	Carbon quantum dots
CVD	Chemical vapor deposition
DFT	Density functional theory
DOS	Density of states
E°	Standard electrode potential
EELS	Electron energy loss spectroscopy
ELS	Electrophoretic light scattering
EPM	Electrophoretic mobility
EtOH	Ethanol

FTIR	Fourier-transform infrared spectroscopy
GC	Glassy carbon
HER	Hydrogen evolution reaction
HMF	5-hydroxymethylfurfural
HMX	Octogen
HMTA	Hexamethylenetetramine, urotropine
HOR	Hydrogen oxidation reaction
HPLC	High-Performance Liquid Chromatography
HTC	Hydrothermal carbonization
HTG	Hydrothermal gasification
HTL	Hydrothermal liquefaction
HTV	Hydrothermal vaporization
(HR)TEM	(High-resolution) transmission electron microscopy
IEP	Isoelectric point
iR	Internal resistance
IR	Infrared
LSV	Linear sweep voltammetry
MAS	Magic angle spinning
MOF	Metal-organic framework
MP	Modular potentiometry
MPa	Megapascal
MS	Mass spectrometry
mW	Milliwatt
NIR	Near-infrared
N-HTC	N-containing hydrothermal carbon
NMR	Nuclear magnetic resonance
NTA	Nitrilotriacetic acid
OCP	Open circuit potential
OER	Oxygen evolution reaction

ORR	Oxygen reduction reaction
PAHs	Polycyclic aromatic hydrocarbons
PALS	Phase analysis light scattering
PVDF	Polyvinylidene fluoride
pH	Potential of hydrogen
RDE	Rotating disk electrode
RDX	Hexogen
RE	Reference electrode
RF	Radiofrequency
RHE	Reversible hydrogen electrode
SCF	Self-consistent field
SCWG	Supercritical water gasification
SCWO	Supercritical water oxidation
SEM	Scanning electron microscopy
SHE	Standard hydrogen electrode
TG-MS	Thermogravimetric-mass spectrometry
TOC	Total organic carbon
UV	Ultraviolet
UV/VIS	Ultraviolet-visible spectroscopy
WE	Working electrode
XPS	X-ray photoelectron spectroscopy
XRD	X-ray diffraction

8.2. List of Publications

Referenced Publication

J. W. Straten, P. Schleker, M. Krasowska, E. Veroutis, J. Granwehr, A. A. Auer, W. Hetaba, S. Becker, R. Schlögl and S. Heumann, N-Functionalized Hydrothermal Carbon Materials by using Urotropine as the Nitrogen Precursor, *Chem. Eur. J.* **2018**, *24*, 1-21. DOI: [10.1002/chem.201800341](https://doi.org/10.1002/chem.201800341).

Concept and experimental design: Sylvia Becker, Saskia Heumann, Jan Willem Straten

Data collection and analysis:

Synthesis and characterization (HPLC, pH, acid-base titrations, FTIR spectroscopy, Raman spectroscopy, TG-MS, Zeta-potential, optical microscopy): Jan Willem Straten

Elemental analysis: Mikrolab Kolbe (Höhenweg 17, 45470 Mülheim an der Ruhr)

UV/Vis spectroscopy: Jutta Kröhnert

SEM: Wiebke Frandsen

TEM: Liudmyla Masliuk

XRD: Frank Girgsdies

BET: Maike Hashagen

Solid-state NMR: Philipp Schleker, Emmanouil Veroutis, Josef Granwehr

HRTEM/EELS: Walid Hetaba

Theoretical calculations: Małgorzata Krasowska, Alexander A. Auer

Drafting of the manuscript: Jan Willem Straten, Sylvia Becker, Saskia Heumann

Critical revision of the article for important intellectual content: Sylvia Becker, Saskia Heumann, Robert Schlögl

Corresponding author: Saskia Heumann

The order of the author's names in the row shows the contribution; the first in the row means the greatest contribution

Intended Publication

J. W. Straten, A. K. Mechler, S. Becker, R. Schlögl and S. Heumann, Binder-free N-functionalized Carbon Disc Electrode Materials for Application as Oxygen Evolution Catalysts in (Alkaline) Water Splitting Process.

Concept and experimental design: Sylvia Becker, Anna K. Mechler, Saskia Heumann, Jan Willem Straten

Data collection and analysis:

Synthesis, pelletization and characterization (TG-MS, geometrical analyses, FTIR spectroscopy, Raman spectroscopy, electrical conductivity, UV/Vis spectroscopy, optical microscopy): Jan Willem Straten

Electrochemistry: Jan Willem Straten, Anna K. Mechler, Sylvia Becker, Saskia Heumann

Elemental analysis: Mikrolab Kolbe (Höhenweg 17, 45470 Mülheim an der Ruhr)

SEM: Wiebke Frandsen, Norbert Pfänder

XRD: Frank Girgsdies

BET: Maike Hashagen

Liquid ^1H and ^{13}C NMR: Christina Römelt, Dagmar Merkl

Drafting of the manuscript: Anna K. Mechler, Saskia Heumann, Jan Willem Straten

Critical revision of the article for important intellectual content: Anna K. Mechler, Saskia Heumann, Robert Schlögl

Corresponding author: Saskia Heumann

The order of the author's names in the row shows the contribution; the first in the row means the greatest contribution

Oral presentations

1. J. W. Straten, S. Becker, S. Buller, R. Schlögl, Binder-free N-functionalized hydrothermal carbon-based disc-electrode materials. *Electrochemistry Day 2016*, Fritz-Haber-Institut der Max-Planck-Gesellschaft, Berlin, Deutschland, 26. September 2016.
2. J. W. Straten, Y. Yi, S. Becker, S. Buller, R. Schlögl, Binder-free N-functionalized carbon disc electrode materials for electrochemical applications. *1st International Symposium on Hydrothermal Carbonisation: Possibilities and Limits for Feedstock, Processes and Applications*, Queen Mary, University of London, London, Großbritannien, 3.-4. April 2017.
3. J. W. Straten, A. K. Mechler, S. Heumann, R. Schlögl, OER studies of N-functionalized hydrothermal carbon disc electrodes. *Electrochemistry Day 2017*, Fritz-Haber-Institut der Max-Planck-Gesellschaft, Berlin, Deutschland, 21. August 2017.

Posters

1. J. W. Straten, R. Rameker, N. Kowalew, S. Reiche, R. Schlögl, Electrodes from N-functionalized hydrothermal carbon – N-precursor urotropine. *International Symposium: Catalytic Systems for Chemical Energy Conversions*, Max-Planck-Institut für Chemische Energiekonversion, Mülheim an der Ruhr, Deutschland, 23.-25. Juli 2014.
2. J. W. Straten, R. Rameker, N. Kowalew, S. Reiche, R. Schlögl, Electrodes from N-functionalized hydrothermal carbon – N-precursor urotropine. *Summer School 2014: Methods in Molecular Energy Research: Theory and Spectroscopy*, Wissenschaftspark, Gelsenkirchen, Deutschland, 31. August-6. September 2014.
3. J. W. Straten, R. Rameker, N. Kowalew, S. Reiche, R. Schlögl, Carbon-based electrode materials – N-functionalization with urotropine. *3rd Ertl Symposium on Surface Analysis and Dynamics*, Fritz-Haber-Institut der Max-Planck-Institut- Gesellschaft, Berlin, Deutschland, 9.-12. November 2014.
4. J. W. Straten, R. Rameker, S. Reiche, R. Schlögl, Nitrogen-rich carbon-based electrode materials by hydrothermal synthesis. *48. Jahrestreffen Deutscher Katalytiker*, Weimar, Deutschland, 11.-13. März 2015.
5. J. W. Straten, S. Reiche, R. Schlögl, N-functionalized carbon-based electrode materials with urotropine. *CARBON 2015*, Internationales Congress Center, Dresden, Deutschland, 12.-17. Juli 2015.
6. J. W. Straten, S. Becker, R. Schlögl, N-functionalized carbon-disc materials by hydrothermal process using urotropine as precursor for electrolysis. *49. Jahrestreffen Deutscher Katalytiker*, Weimar, Deutschland, 16.-18. März 2016.
7. J. W. Straten, S. Becker, R. Schlögl, N-functionalized carbon-disc materials using glucose and urotropine as precursor for electrocatalysis.

Manfred-Eigen-Nachwuchswissenschaftlertgespräche: Physical Chemistry of Solar Fuels Catalysis, Max-Planck-Institut für Chemische Energiekonversion, Mülheim an der Ruhr, Deutschland, 6.-8. April 2016.

8. J. W. Straten, S. Becker, S. Buller, R. Schlögl, Binder-free N-functionalized hydrothermal carbon-based disc electrode materials using urotropine and glucose as precursors. *CARBON 2016*, The Penn Stater Conference Center Hotel, State College, Pennsylvania, USA, 10.-15. Juli 2016.

8.3. Lebenslauf (Curriculum Vitae)

Der Lebenslauf ist in der Online-Version aus Gründen des Datenschutzes nicht enthalten.

8.4. Erklärung (Statement)

Hiermit versichere ich, dass ich die vorliegende Arbeit mit dem Titel

**„Carbon-based Electrode Materials for Application in the Electrochemical
Water Splitting Process“**

selbständig verfasst und keine außer den angegebenen Hilfsmitteln und Quellen benutzt habe. Alle wörtlich oder inhaltlich übernommenen Stellen sind als solche gekennzeichnet. Die Doktorarbeit wurde in dieser oder ähnlicher Form noch bei keiner anderen Universität eingereicht.

Mülheim an der Ruhr, den 24.05.2018



(Jan Willem Straten)

8.5. Acknowledgments

The present doctoral thesis of the title “Carbon-based Electrode Materials for Application in the Electrochemical Water Splitting Process” was carried out at the Max Planck Institute for Chemical Energy Conversion, Mülheim an der Ruhr, Germany.

First of all, I am grateful to all the chairmen – Prof. Dr. Robert Schlögl, Prof. Dr. Malte Behrens and Prof. Dr. Stefan Rumann – who accepted reviewing my doctoral thesis.

I would like to take this opportunity to thank my group leaders Dr. Sylvia Becker and Dr. Saskia Heumann for tireless support which they unconditionally shared with me as well as the colleagues and members of my group. Special thanks to Prof. Dr. Robert Schlögl. Without his promise to join the Max Planck Institute for Chemical Energy Conversion, none of this work would be possible. I am so grateful, in particular, for the scientific and the financial support of my experiments. Likewise, I am so lucky that I have been able to attend various conferences and symposia, both in Germany and abroad. The financing and funding that have enabled the participations have been provided by the Max Planck Institute. The technical and administrative staff at the institute have been of excellent assistance, too.

I also would like to also mention that the whole Schlögl group in Mülheim an der Ruhr was a great team and very helpful whenever I encountered various problems, not only on scientific basis. Especially many thanks to Dr. Yang-Ming Lin and Dr. Yuxiao Ding for thorough proofreading of my doctoral thesis plus, more particularly, many thanks to all the other scientific members of the group. I had a lot of fun with them all in the open-plan office including a number of fruitful discussions.

My biggest thanks go of course to my beloved family; my parents and two brothers. They all, each in their own way, contribute to my motivation and their

kind words gave me ongoing encouragement. I am so thankful for all their spiritual support.

Jan Willem Straten